Supercapacitor development from transition metal-integrated spinel manganese oxide-carbon nanotubes composite materials

By

Christopher Nolly

(BSc Honours)

A mini-thesis submitted in partial fulfilment of the requirements for the degree of

Magister Scientiae in Nanoscience

Faculty of Science

University of the Western Cape

Bellville, Cape Town, South Africa

Supervisor: Dr. Chinwe Ikpo

Co-supervisor(s): Prof. Emmanuel Iwuoha,

Dr. Unathi Sidwaba

December 2019

KEY WORDS

Supercapacitors

Asymmetric pseudocapacitors

Swagelok

Hybrid composite

Multi-walled carbon nanotubes

Activated carbon

Mn_3O_4

$CuMn_2O_4$

Specific capacitance

Energy density

Power density

Cycles

Conductivity

ABSTRACT

Supercapacitor development from transition metal-integrated spinel manganese oxide-carbon nanotubes composite materials

Christopher Nolly

MSc. Nanoscience, Department of Chemistry, University of the Western Cape

December 2019

Supercapacitors are electrochemical energy storage devices, much like Li-ion batteries, that have expeditiously been improved over the years through extensive research conducted in material sciences and nanotechnology. Since supercapacitors are mostly known for their high power densities and extended lifecycle, they are therefore mainly employed in applications where large quantities of energy is required to be stored and/or released within quick time periods and energy outputs. In the modern technological era, supercapacitors are predominantly employed in hybrid electric vehicles (HEVs), trains, trams, cranes, cell phones, as uninterrupted power supplies (UPS devices), and in memory backup units for computer systems. Apart from these conventional application areas, the application field of energy storage that ultimately makes supercapacitors blossom, is the field of storing harvested renewable energy from self-sustaining power sources such as solar cells and/or wind turbines. However, the unfortunate disadvantage associated with supercapacitors is its low energy density compared to batteries. Therefore, this research work presents the study of multi-walled carbon nanotubes (MWCNTs) integrated with spinel nanostructured $CuMn_2O_4$ nanoparticles as composite electrode materials towards enhancing the energy performance in asymmetric pseudocapacitors. The hybrid composite ($CuMn_2O_4$/MWCNT) development process initially started with the synthesis of the pristine (hausmannite-type) Mn_3O_4 material, upon modification thereafter with copper and carbon nanoparticles. The synthetic procedure that was used to develop the pristine and spinel materials is a versatile high-pressure

hydrothermal method, where the hybrid composite material was synthesized via a more energy efficient reflux heating system. The copper integrated with the pristine Mn_3O_4 material formulates a more stable spinel face-centered-cubic (FCC) $CuMn_2O_4$ crystal structured material, with additional tetrahedral and octahedral interstitial sites as electron vacancies. The integration of MWCNTs to $CuMn_2O_4$ was intended to enhance its electrochemical conductivity, thermal stability, and surface-electrolyte contact area. Physical properties of the synthesized electrode materials were investigated using various microscopic and spectroscopic techniques such as scanning electron microscopy (SEM), high-resolution transmission electron microscopy (HR-TEM), energy dispersive X-ray spectroscopy (EDS), Fourier transform-infrared spectroscopy (FT-IR), and Raman spectroscopy. Crystallite size, particle size distribution, as well as thermal stability analysis were conducted through X-ray diffraction (XRD), small-angle X-ray scattering (SAXS), and thermo-gravimetric analysis (TGA). Electrochemical properties of the synthesized electrode materials were studied through employing cyclic voltammetric (CV), galvanostatic charge/discharge (GCD), and electrochemical impedance spectroscopic (EIS) analysis. Microscopic analysis revealed that the synthesized materials displayed regular morphologies from SEM images, as well as rectangular box and cubic structures for Mn_3O_4 and $CuMn_2O_4$, respectively, from HR-TEM figures. XRD and SAXS analysis indicated that the average crystallite size and particle size distribution for the hybrid composite material was the smallest compared to the pristine and spinel materials. TGA analysis additionally confirmed the superior thermal stability of $CuMn_2O_4$/MWCNT over that of Mn_3O_4 and $CuMn_2O_4$. Electrochemical analysis was conducted on all electrode materials utilizing both three-electrode (half cell) and two-electrode (full cell) testing devices, where 3 M KOH and 3 M LiOH were tested as aqueous electrolyte solutions for the half cell, of which the best suited electrolyte (3 M LiOH) was used for the full cell analysis. The maximum specific capacitance values for the Mn_3O_4 ‖ AC, $CuMn_2O_4$ ‖ AC, and $CuMn_2O_4$/MWCNT ‖ AC full cell devices were obtained as 994.373 F/g, 1608.523 F/g, and 2234.460 F/g, respectively. The ragone plot from the results section illustrated that the $CuMn_2O_4$/MWCNT ‖ AC cell device retained a relatively high energy of 35.068 Wh/kg, with a maximum power density of 2449.942 W/kg. Cycling stability analysis impressively revealed that the $CuMn_2O_4$/MWCNT ‖ AC electrochemical cell exhibited a specific capacitance of 948.388 F/g together with a capacitance retention and coulombic efficiency of 88.571 % and 92 %, respectively after 3000 cycles.

DECLARATION

I declare that "*Supercapacitor development from transition metal-integrated spinel manganese oxide-carbon nanotubes composite materials"* is my own work and that it has not been submitted before for any degree or examination in any other university, and all the sources I have used or quoted have been indicated or acknowledged as complete references.

Christopher Nolly

Signed:  December 2019

DEDICATION

This research work is dedicated to my dear parents, Mr & Mrs Keith Nolly and Charmain Nolly, as well as to my late grandmother Frances Nolly.

ACKNOWLEDGEMENTS

I would like to gracefully give thanks to my creator Almighty God and his son Lord Jesus Christ for blessing me with the mental and physical strength to complete this research work at my utmost best academic performance.

Secondly, to the outstanding people responsible for making this opportunity and experience a reality; I want to sincerely bestow my humble gratuity to my supervisor (Dr. Chinwe Ikpo) and co-supervisor (Prof. Emmanuel Iwuoha) for their impeccable mentorship and guidance towards completing this research work. I especially want to thank Dr. Ntuthuko Wonderboy Hlongwa and Ms. Miranda Mengwi Ndipingwi for their assistance with electrochemical instrumentation analysis and laboratory work.

To my beloved parents, Mr & Mrs Keith and Charmain Nolly, who continually supported me throughout the beginning of my academic journey. Thank you so much for never giving up on me and always believing in me to accomplish great things. I also want to thank my little brother, Liam Nolly, for looking up to me as a role model, as that gave me motivation to fulfil my goals.

I would like to give my appreciation to the Department of Chemistry staff and Nanoscience colleagues for always making SensorLab a welcoming place of work. Finally, I want to thank the administration organizers of the Nanoscience and Nanotechnology Postgraduate Teaching and Training program, especially to Mrs. Valencia Jamalie, for their continuous support. One final thank you is to the Department of Science and Technology for granting me this MSc Nanoscience bursary award.

TABLE OF CONTENTS

ACRONYMS AND ABBREVIATIONS

EDLC	Electric Double Layer Capacitor
PC	Pseudocapacitor
HC	Hybrid Capacitor
MWCNTs	Multi-Walled Carbon Nanotubes
CB	Carbon Black
PVDF	Polyvinylidene Fluoride
NMP	N-methyl-2-pyrrolidone
Mn_3O_4	Manganese Oxide
$CuMn_2O_4$	Spinel Copper Oxide
$CuMn_2O_4$/MWCNT	Hybrid Spinel Copper Oxide/Multi-Walled Carbon Nanotubes
XRD	X-ray Diffraction
SEM	Scanning Electron Microscopy
HR-TEM	High-Resolution Transmission Electron Microscopy
FT-IR	Fourier Transform Infra-Red Spectroscopy
TGA	Thermo-Gravimetric Analysis
SAXS	Small-Angle X-ray Scattering
CV	Cyclic Voltammetry
EIS	Electrochemical Impedance Spectroscopy
GCD	Galvanostatic Charge-Discharge

LIST OF FIGURES

LIST OF TABLES

LIST OF SCHEMES

CHAPTER 1

Chapter Overview

Chapter 1 presents a concise introduction on the research background of the project, emphasizing on the transition towards sustainable and renewable energy sources and energy storage technologies. In addition, it briefly explores the current research pursued in supercapacitor technology and its contribution towards supercapacitor performance. This chapter also states the problems associated with current research in supercapacitor electrode materials as well as the motivation, aims, objectives, and outline of this research project.

1.0 Introduction

1.1 Research Background

The reliance of modern civilization on the use of non – renewable energy sources such as fossil fuels (coal, petroleum, and natural gas) in road transportations systems, manufacturing, and electrical power industries has given rise to significant environmental and human safety concerns [1]. The continuous combustion of fossil fuels during electricity production, results in the abundant emission of poisonous carbon dioxide (CO_2), carbon monoxide (CO), and hydrocarbon gases, which are toxic to environmental and human exposure [2]. The concerns regarding environmental exposure of CO_2 is driven by the knowledge of it being a major greenhouse gas, contributing towards a gradual overall temperature increase in the earth's atmosphere, thus resulting in global warming occurrence and harsh climate change [3]. Human safety concerns of CO exposure at moderate and high concentration levels over extended periods potentially increase the risk of people experiencing toxic diseases [4]. It is additionally anticipated for future global energy demands to continuously rise in proportion to the current increase in the world's economic and population growth. This

particular concern is propelled by the increase in consumption quantity of fossil fuels each year. Therefore, it is required for modern society to transition from an economy based on fossil fuels to renewable self-sustaining energy sources as well as efficient energy storage technologies. Due to this requirement, there has recently been immense interest in the development of high power and high energy density storage devices suitable for use in mobile electronics, hybrid electric automobiles, and smart grids.

1.1.1 Transition towards renewable energy resources

The general origin of sustainable and renewable energy sources come from resources that are not diminished when used overtime such as solar, wind, biomass, geothermal, and hydropower [5]. The advantage of these resources over fossil fuels is that we do not compromise the safety of our planet in order to harness it. According to the BP Statistical Review of Energy, since the year 2013, Africa's petroleum reserve has decreased from an average quantity of 6.3 million to 5.2 million barrels of crude oil per day [6]. Since South Africa is known to be the seventh largest coal producer in the world, approximately 77% of the country's electricity generation is derived from coal [7]. As a result of the many coal mining activities and large coal consumption quantities, 396.78 tonnes of toxic carbon dioxide (CO_2) gases are emitted each year, thus making South Africa's greenhouse gas emissions the highest in Africa [7]. The South African Department of Minerals and Energy (SADME) developed a renewable energy policy, setting specific electricity targets for renewable energy contribution [6]. Solar power is one of the most popular forms of renewable energy resources used in South Africa as it provides a great theoretical supply potential in the production of electrical energy from solar radiation. The technological principle of solar energy is employed through photovoltaic panels, which convert solar radiation from the sun directly into electrical energy, thus providing power to light home electrical appliances, and telecommunication devices. The Northern Cape region, apart from other provincial regions in South Africa, amounts to an approximate total area of 194,000 km^2 available for accumulation of highly concentrated solar radiation [8]. It is therefore scientifically estimated that if every square kilometre of solar panel surface in a solar power plant could generate 30.2 Megawatts of electricity, then only 1% of the total geographical area of radiation would be available for solar energy generation [8]. This estimation would therefore result in a potential generation of 64 Gigawatts, thus indicating that approximately

1.25% of the total area of radiation would meet the projected electricity demand target of 80 Gigawatts by 2025 [8]. Despite these promising estimates, the major downside of electricity production from solar power technology is energy efficiency, storage, and transportation. In order to overcome these obstacles, solar power plants must be located in areas receiving highly concentrated solar radiation. However, these solar plants are located far away from densely populated areas where energy demand is high. This in turn applies to other forms of renewable energy sources such as wind, hydroelectric, geothermal, and biomasses concerning availability and location. Therefore, energy storage technologies such as fuel cells, enhanced rechargeable batteries, and high performance supercapacitors could potentially provide a solution. These next generation technological devices could potentially store the excess energy generated by solar power plants and transport it whenever and wherever it is needed.

1.1.2 The need for electrochemical energy storage systems

Energy storage technologies are the key solution to managing the intermittent nature of renewable energy sources [1]. This implies that these electricity storage systems could be used to store the excess energy generated from renewable energy sources such as wind and solar power plants, and transmit it into the power grid during demanding times when climate change results in the less availability of wind and solar radiation. One additional advantage of using these energy storage systems is that not only are they environmentally friendly, but they could also potentially reduce the electrical marketing costs for consumers and distributors [9-10]. The various types of energy storage systems used for electric energy applications and that are currently under research and development include the following: SMES (superconducting magnetic energy storage), FES (flywheel energy storage), ECES (electrochemical energy storage such as batteries, supercapacitors, electrolytic capacitors, and film capacitors) [1, 10]. These storage technologies are classified according to their lifetime period, number of charge/discharge cycles, storage capacity, and energy response time. The figure below illustrates a ragone plot, which represents the comparison between the various principle energy storage systems mentioned above according to their energy and power densities as well as their energy response times.

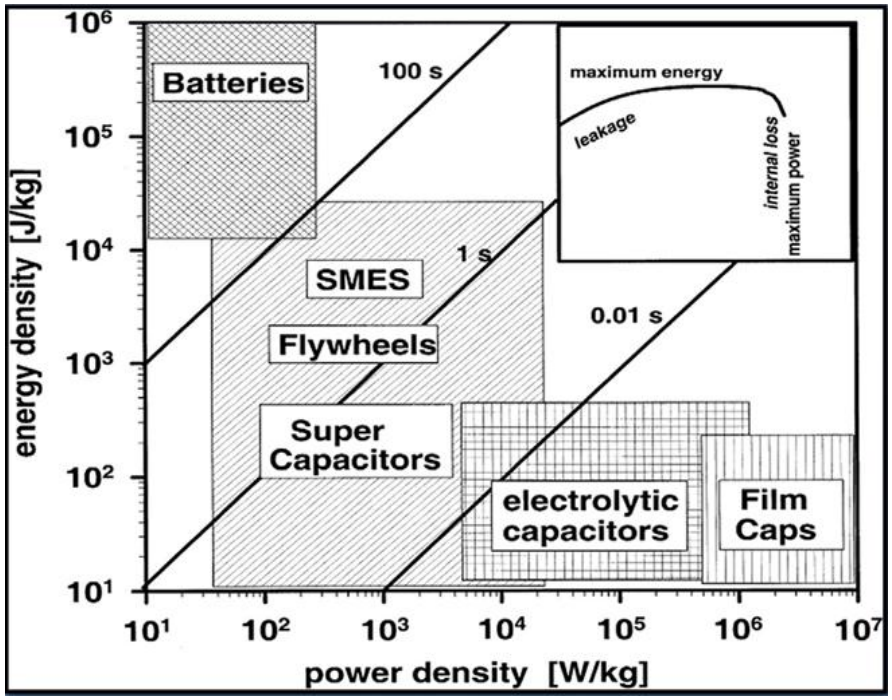

Figure 1.1: Comparison of different energy storage technologies with respect to their energy and power densities [1].

Antecedent research pursued in electrochemical energy storage technologies such as batteries, electrochemical capacitors, and fuel cells, has proven it to be the best performing storage systems used for providing support to photovoltaic and wind generators regarding short and long time scale energy storage [10]. These energy storage devices are similar concerning their electrochemical operating systems, but are distinguishable according to their application, energy storage capacity, and power conversion mechanisms. Electrochemical capacitors, also known as supercapacitors, are energy storage devices with similar designing and manufacturing attributes to that of batteries and fuel cells [11]. However, the difference of supercapacitors to batteries and fuel cells is that supercapacitors store charge non-faradaically, meaning that electrons are not transferred across the electrode interface and electrostatic forces allows for the storage of electrical energy to occur [11]. This type of supercapacitor is known as an electrical double-layer capacitor (EDLC), where during its charging process, the electrons and ions are stored at the interface between the high surface area conductive solid material electrodes and the liquid electrolyte, thus generating an electrical field near the electrodes which holds the positive and negative ions together [11]. Electrical energy is then generated when the electrons are removed through the external

circuit, and the counter-ions (positive ions) are repelled from the negative electrode at the electrode/electrolyte interface. A pseudocapacitor is another type of supercapacitor; however, it relies on faradaic processes to store charge. This implies that the charge storage process involves the transfer of electrons via redox reactions at the positive and negative electrodes [11]. These types of supercapcitors possess a greater specific capacitance as opposed to EDLCs, however, the redox reactions causes high internal resistance within the cell, thus resulting in a decreased specific power density [11]. In the case of fuel cells, fuels such as hydrogen and hydrocarbon gases are required for energy storage and conversion [12].

Since the year 1990, supercapacitor devices became well known within the application of hybrid electric vehicles [11]. The efficiency of a vehicle requires kinetic energy to be stored within a compartment of the vehicle when it reduces speed or remains stationary [1]. Batteries have been regarded as suitable technological devices for successfully performing these energy storage operations [1]. However, due to the low – specific power density of batteries, additional energy storage technologies such as supercapacitors can boost the battery in a hybrid electric vehicle, thus providing efficient power for the acceleration and regenerative braking of the vehicle [11]. Supercapacitors have mostly been recognized for this particular application as a result of their high power rate capabilities and extended lifecycle, thus providing an improvement in the development and manufacturing of more advanced hybrid electric vehicles [1]. The figure below presents various electrochemical energy storage and conversion devices in terms of their specific energy and power [11]. From our knowledge of batteries and capacitors, batteries are able to store large quantities of energy; however, they do take a long time to charge. Capacitors, on the other hand, can charge very quickly; however, they do not store as much energy. Supercapacitors fill in the gap between batteries and conventional capacitors, as they are able to store more energy than capacitors and charge more quickly than batteries [11]. Ideally, we desire to develop supercapacitor technologies with the ability to store large amounts of energy as well as charge very quickly. This research work is therefore aimed at developing a high performance supercapacitor electrode material that has the potential to store a large quantity of charge, undergo many chemical reactions without breaking down, and possess a high electrical conductivity.

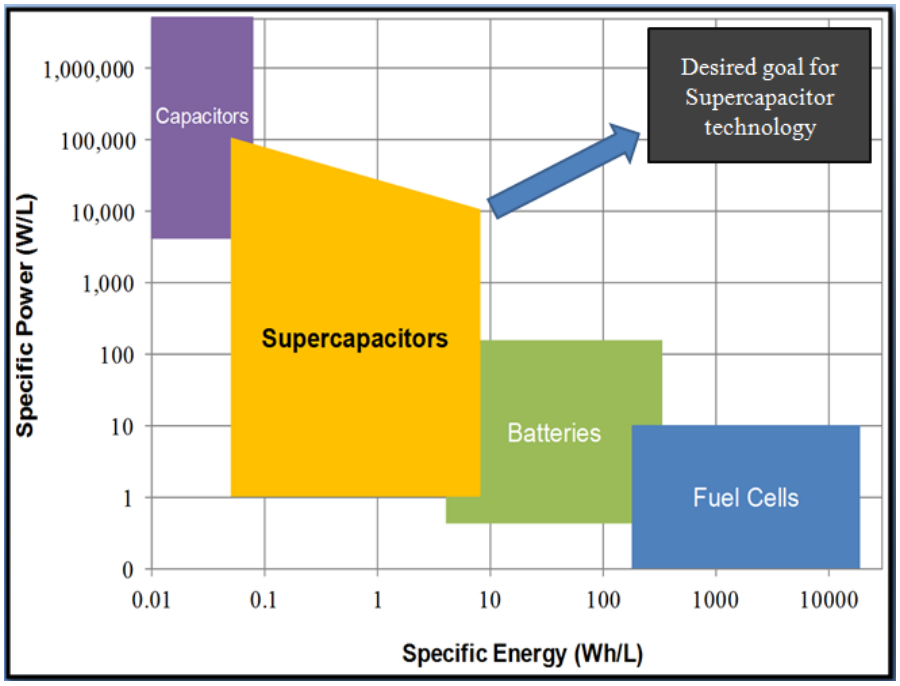

Figure 1.2: Ragone plot illustrating general guidelines for various electrochemical energy storage and conversion devices [11].

The current electrode materials generally used in today's supercapacitor devices are mainly categorized according to the following types: carbon-based materials; conducting polymers; and metal oxide materials such as RuO_2, IrO_2, MnO_2, NiO, Co_2O_3, Fe_2O_3, Mn_3O_4, SnO_2, V_2O_5, and MoO [11]. Carbon materials such as activated carbons, carbon nanotubes (CNTs), and graphene have been immensely studied in the application of supercapacitor electrode materials due to their large surface area, rich pore structures, and high electrical conductivity [13]. However, it is prominent that these types of carbon materials have their own unique advantages and disadvantages. Extensive research have been conducted on activated carbon materials for EDLC electrodes due to their large surface area (ranging from 1000-3000 m^2/g) [11] and relatively low cost [13]. However, its electrochemical analysis revealed an undesirable specific capacitance value of about 60 F/g [14] at low current densities [13]. Carbon nanotubes have also been employed as high energy density EDLC electrode materials due to their satisfactory electronic conductivity; however, they do possess a lower surface area of 430 m^2/g [11] as compared to activated carbon [13]. Despite the disadvantage of CNTs to activated carbons regarding surface area, the entanglement formation of the nanotube structures allows for easier access of electrolyte ions to the electrode/electrolyte interface during the charging process of the EDLC [11].

A research group evaluated the electrochemical performance of a hybrid activated carbon and carbon nanotube nanocomposite material in an organic electrolyte [14]. The results obtained from electrochemical analysis revealed that the synthesized material achieved a specific capacitance value of 90 F/g, indicating an improvement as compared to the pure activated carbon-based electrode material [14]. Recently, many research groups have shown intensive interest in the development of graphene electrode materials for EDLCs as they exhibit a theoretical specific surface area of 2630 m^2/g and a theoretical specific capacitance of 550 F/g [13]. However, the downfall to graphene is that when few-layered graphene sheets are stacked together during electrode preparation, they experience strong Van der Waals forces between the layers [13]. This interaction reduces the accessible surface area of the densely stacked graphene layers for the accumulation of electrolyte ions [13]. Innovative research aimed at solving this problem have been implemented by incorporating an activation methodology involving the development of activated graphene nanostructures [13]. This research resulted in the formation of graphene materials possessing an even greater specific surface area ranging between 2400-3100 m^2/g [13]. Although these materials showed promising results regarding surface area, they only managed to achieve a specific capacitance ranging between 120-165 F/g [13]. This implies that there are certain sections of the specific surface area that are not electrochemically accessible to the electrolyte ions [13]. Nevertheless, activated graphene still exhibits a greater specific surface area and capacitance than that of activated carbon and carbon nanotubes combined.

Second on the list of supercapacitor electrode materials is conducting polymers. These types of materials possess interesting characteristics that make them acceptable candidates for supercapacitor applications such as their relatively low cost, low toxicity, high electrical conductivity, and large energy storage capacity [11]. Conducting polymers are mostly employed as electrode materials for pseudocapacitors as they produce the capacitive response via fast-moving redox reactions occurring within the polymer matrix [13]. The two types of conducting polymers which are predominantly investigated include polyaniline (PANI) and polypyrrole (PPy) [13]. They exhibit specific capacitance values ranging between 150-190 F/g (for PANI) and 80-100 F/g (for PPy) in both aqueous and non-aqueous electrolytes [13]. However, these values are still undesirable for achieving the prerequisites of experimental application because conducting polymers tends to experience instability during charging/discharging cycling processes, which results from the swelling and shrinking

formation of the conducting polymer structures [13]. Therefore, researchers have performed numerous efforts on developing nanostructured conducting polymers to moderately enhance its capacitance and cycling stability [13].

Metal oxides are additional types of electrode materials employed in pseudocapacitors and they include RuO_2, IrO_2, MnO_2, SnO_2, Co_2O_3, Fe_2O_3, Mn_3O_4, and etc [13]. Ruthenium(IV) oxide (RuO_2) is one of the most vastly explored electrode materials, due to it having the highest theoretical specific capacitance among pseudocapacitive materials (about 2000 F/g) [13]. In addition, it also exhibits a high electrical conductivity, good chemical and thermal stability, long cycle life, and high rate capabilities [13]. However, it has a considerably high cost and toxicity, thus limiting its applications to aerospace and military use where the budget is not an issue. Therefore, researchers are traversing their attention to developing cheaper and more environmentally friendly metal oxide materials which still retains the desired supercapacitive properties [13].

Researchers have, however, considered manganese oxide (MnO_2) as alternative pseudocapacitive energy storage materials due to their desired low cost, low toxicity, environmental safety, and high theoretical specific capacitance values ranging between 1100-1300 F/g [13]. Scientists have also pondered upon developing other metal oxides with different morphologies to that of pure MnO_2, such as Co_2O_3, Fe_2O_3, and Mn_3O_4 [13]. Additionally, a specific research group innovatively proposed the development of binary transition metal oxides with AB_2O_4 (A = Co, Ni, Mn, and Zn; B = Co, Mn, and Fe) structures as pseudocapacitive energy storage and conversion electrode materials [2, 13]. An example of such material types that have been developed and studied is $NiCo_2O_4$, which was proven to exhibit an electrical conductivity far greater than single metal oxides (NiO and Co_3O_4), and with specific capacitances ranging between 400-1600 F/g [13].

This research study will involve the development of a $CuMn_2O_4$ spinel nanostructured binary metal oxide electrode material via a hydrothermal synthetic route. The $CuMn_2O_4$ nanoparticles will also be strongly anchored to the outer walls and inner cores of carboxylic

acid functionalized multi-walled carbon nanotubes (MWCNTs) to accommodate stability of the $CuMn_2O_4$ active material at the surface of the electrode/electrolyte interface. The additional purpose of binding the $CuMn_2O_4$ nanoparticles to MWCNTs is also to enhance its electrical conductivity, induce a high capacity, extend its cycle life, and enforce a good rate capability. For comparison purposes, the pristine Mn_3O_4 nanoparticles will also be synthesized according to the same hydrothermal synthetic route. The electrochemical performance of the Mn_3O_4 and $CuMn_2O_4$ electrode materials will be compared to that of the hybrid $CuMn_2O_4$/MWCNT composite electrode material [15].

1.2 Problem Statement

The spinel $CuMn_2O_4$ is an appealing material in relation to ecological and economical sustainability due to the environmental compatibility, low cost, and high natural abundance of its individual elemental components. The distinctive advantage of spinel $CuMn_2O_4$ nanoparticles is that its charge storage mechanism, which is based on the adsorption and desorption of alkaline electrolyte anions onto the $CuMn_2O_4$ surface, is contributed by the valence translation of Mn^{3+}/Mn^{2+} [16]. This particular phenomenon therefore renders a specific capacitance value of 577.9 F/g, which is about three orders of magnitude greater than that of its Mn_3O_4 correspondent [17]. However, the unfortunate disadvantage of spinel $CuMn_2O_4$ nanoparticles is that its specific capacitance drastically decays during charging/discharging processes at current densities $\geq$10 A/g [16]. This downside is attributed by the morphology of the particle surfaces as it contains limited active sites for electrolyte ions, thus restricting the ion diffusion processes within the electrodes resulting in ineffective charge transfer channels [15]. This proposed study addresses the above-mentioned disadvantage by developing electrochemically active composites of spinel $CuMn_2O_4$ nanoparticles agglutinated onto the surface of multi-walled carbon nanotubes (MWCNTs). The incorporation purpose of MWCNTs to the spinel $CuMn_2O_4$ nanoparticles is to enhance its specific capacitance, increase its specific surface area for the promotion of additional redox active sites, and provide structural stability under high-rate charge/discharge processes [15].

1.3 Rationale and motivation of research

The economical dependence of South Africa on fossil fuel energy sources has evoked consequential concerns towards environmental sustainability. This therefore encourages the need for developing renewable and self-sustaining energy generation systems such as solar cells, wind, and hydroelectric turbines. However, due to the intermittent nature of solar and wind resources, their efficiency is not equivalent with current energy demands. Additionally, due to the high construction cost of hydropower stations, government officials are therefore enticed to invest in further development of energy storage technologies. Therefore, it is a crucial requirement for employing additional development of high performance electrochemical energy storage devices such as lithium-ion batteries and supercapacitors. These technologies could potentially store the energy generated from solar and wind power, and supply it to wherever, whenever needed. However, the implementation of these technologies within large-scale applications is restricted by the electrochemical performance induced from their electrode materials. This therefore provides motive to develop supercapacitor electrode materials capable of generating enhanced energy storage capacities, potentially suitable for large-scale clean energy systems such as solar, wind, and electric vehicles.

In recent literatures of supercapacitor electrode materials, Lina Chen and co-authors designed a spinel structured composite material by integrating $LiMn_2O_4$ nanoparticles with graphene/carbon nanotube networks, thus formulating $LiMn_2O_4$/CNTs/graphene [233]. This material was employed as a cathode electrode material for hybrid capacitors, and exhibited overall energy and power densities of 62.77 Wh/kg and 2967.96 W/kg, respectively [233]. Transition metals such as copper and/or nickel can become more conductive when incorporated with manganese oxides into a spinel-structured formation. Additionally, introducing carbon type materials such as graphene or carbon nanotubes, would improve the conductivity of the spinel-structured material. A reduced graphene oxide/$NiMn_2O_4$ composite material, developed by Zhongbing Wang and co-workers for high-performance supercapacitors, exhibited a specific capacitance of 693 F/g at a 1 A/g current density [252]. From the results and insights of these recently researched materials, the development of spinel $CuMn_2O_4$ electrode materials provided an interest due to its relatively high conductivity, low cost, high relative abundance, and environmental benignity. In the attempt

to further improve its electronic conductivity, structural, and thermal stability, multi-walled carbon nanotubes (MWCNTs) would provide a lower interfacial resistance along the electrode/electrolyte interface, thus inducing a lower energy loss during charge/discharge cycles [15]. Composite electrode materials in recent literatures are often composed of combined structural networks of graphene@CNTs [232]. Graphene increases the number of electro-active sites for binding with the spinel component of the composite, thus benefitting its electrolyte ion diffusion mechanisms [234]. However, due to the time consuming synthetic procedure of graphene, as well as low yield production of reduced graphene oxide, functionalized MWCNTs provide a suitable alternative with similar physical and chemical characteristics. Asymmetric supercapacitors, using $NiCo_2O_4$/rGO/MWCNTs as the cathode and activated carbon (AC) as the anode, delivered energy densities of 13.3 Wh/kg – 38.1 Wh/kg at low (58.1 W/kg) and high (797.8 W/kg) power densities [246]. This type of device configuration is therefore more optimal for use in researching supercapacitor electrode materials.

1.4 Research aims and objectives

The aim of this research project is to develop a nanostructured spinel copper manganese oxide ($CuMn_2O_4$) nanocomposite electrode material, modified with multi-walled carbon nanotube (MWCNT) networks. Additionally, the aim is also to explore the energy and power density properties of this composite material with high performance supercapacitor applications.

This research study involves the following objectives:

1. Synthesis of the pristine manganese oxide (Mn_3O_4) nanoparticles via a high temperature hydrothermal heating method.
2. Synthesis of the spinel copper manganese oxide ($CuMn_2O_4$) nanoparticles similarly via the hydrothermal heating method.
3. Purification and chemical oxidation process of multi-walled carbon nanotubes (MWCNTs).
4. Incorporation of $CuMn_2O_4$ nanoparticles onto MWCNT surfaces via a reflux heating method to form the hybrid $CuMn_2O_4$/MWCNT composite material.
5. Microscopic, elemental, and particle size analysis of the synthesized electrode materials via High-Resolution Transmission Electron Microscopy (HR-TEM), Scanning Electron Microscopy (SEM), Energy Dispersive X-ray Spectroscopy (EDS), and Small-Angle X-ray Scattering (SAXS).
6. Crystallographic and functional group analysis of the electrode materials via X-ray Diffraction (XRD) and Fourier Transform-InfraRed Spectroscopy (FT-IR). Raman Spectroscopic analysis, to study the molecular vibrations of each electrode materials as well as Thermo-Gravimetric Analysis (TGA) towards investigating the thermal stability of said electrode materials.
7. Fabrication of nickel-foam electrodes with the nanocomposite materials and assembly of the Swagelok device to perform electrochemical characterization using Cyclic Voltammetry (CV), Galvanostatic charge/discharge (GCD), and Electrochemical Impedance Spectroscopy (EIS).

1.5 Research framework

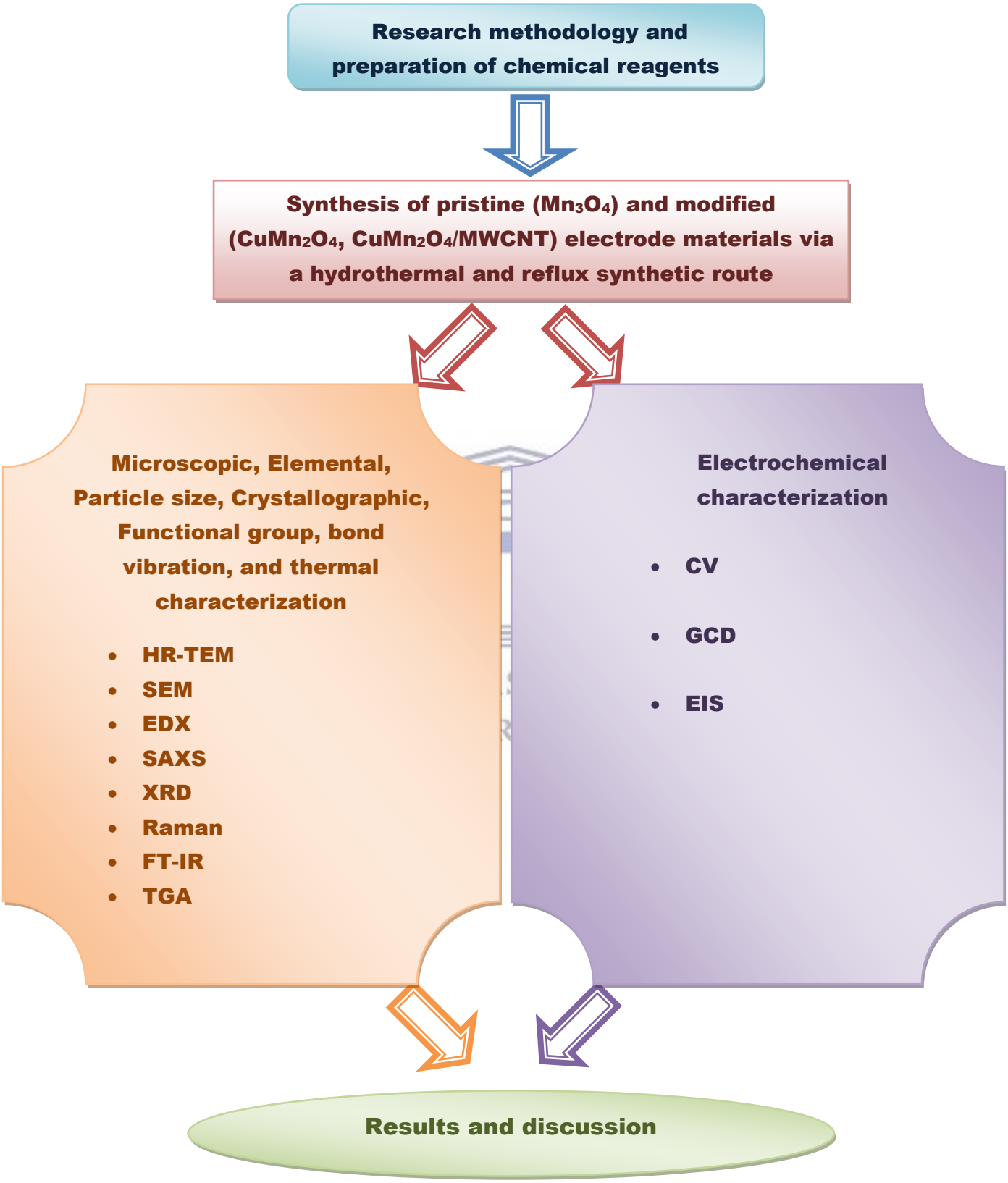

Scheme 1.1: Flowchart illustrating the research framework.

1.6 Thesis outline

The broad context of this research project is to design and develop a modified electrode material ($CuMn_2O_4$/MWCNT), from previous materials that have already been tested (Mn_3O_4 and $CuMn_2O_4$), that would exhibit an improved electrochemical performance in the application of supercapacitor devices. Additionally, the objective is to scientifically understand how the modified elemental and structural components on the $CuMn_2O_4$/MWCNT material (i.e. how the Cu^{2+} atoms and MWCNTs alter the physical, structural, and electrochemical properties of the pristine Mn_3O_4 material) influences its electrochemical performance. The results and key findings of all the experiments conducted on each synthesized electrode material, is presented as an outline below.

Chapter 1, as previously mentioned, presents as concise introduction on the research background knowledge of the project, as well as, an overlook on recent advances on electrode materials used in supercapacitor devices. The research motivation, aims, objectives, and outline of the project, is additionally stated in this chapter.

Chapter 2 provides a literature review relating to the elementary concepts concerned with electrochemical energy storage and capacitor systems. This chapter initially presents a descriptive definition of capacitance and continues to provide a better understanding of the physical, chemical, and structural properties of the modified $CuMn_2O_4$/MWCNT electrode material.

Chapter 3 initially presents the chemical reagents and experimental procedures used for the synthesis of Mn_3O_4, $CuMn_2O_4$, and $CuMn_2O_4$/MWCNT electrode materials. This chapter additionally provides a brief background knowledge on the characterization techniques and instrumentation used during the investigation.

Chapter 4 provides the results and discussion of the analyzed electrode materials illustrating the morphological, structural, spectroscopic, and electrochemical properties.

Chapter 5 provides a brief but comprehensive summary of all the research findings and additionally offers an overview description of potential future improvements and recommendations.

The absolute final section of this research project is the reference section, which is ascribed to the list of references utilized for this investigative study.

CHAPTER 2

Chapter Overview

Chapter 2 provides an extensive overview of the elementary concepts concerned with electrochemical energy storage and capacitor systems, placing emphasis on the prospective demand for supercapacitor devices. The classification of capacitor systems, underlining the various types of supercapacitor technologies, as well as, the materials associated with these types of supercapacitor devices are additionally discussed in this chapter. The importance of nanotechnology on the development of superior electrode materials for high performance supercapacitors, is finally studied and portrayed as the last section of the literature review. This particular end segment is of essential significance as it elucidates the broad context of the research work.

2.0 Literature Review

2.1 Elementary concepts of capacitor systems

Renewable energy resources such as wind, water, and solar power have continuously contributed towards electricity generation for global energy demands [18]. As a result of the increasing growth in energy contribution from these renewable and intermittent energy sources, the demand for energy storage technologies is becoming increasingly indispensable [18]. The required characteristics that these energy storage systems should attain, is the ability to store substantial amounts of energy and be able to deliver it over extended periods of time [18]. However, in applications where quick energy bursts is required, technologies such as capacitors are suitable for addressing this particular requirement. In contrast, conventional capacitors are able to store up to 0.15 Wh/kg of energy, which is insufficient for applications requiring considerable energy outputs in short durations such as vehicle engine starting mechanisms [18-19]. This advanced energy storage technology, known as

supercapacitors, exhibit energy densities exceeding that of conventional capacitors, and power densities exceeding that of batteries [18]. These technological devices are mainly utilized in electric vehicle applications due to their lightweight, zero maintenance, fast charging times, and virtual limitless cycle life characteristics [19]. In order to fully understand the scientific fundamentals of electrochemical supercapacitors, it is imperative to understand the elementary concepts of conventional capacitor systems.

A capacitor can be described as an electronic component capable of storing electrical potential energy in the form of charge within an electric field existing between two parallel oppositely charged conducting plates called electrodes [20]. The electrical field between the plates of a capacitor is affected by a thin layer of insulating material, e.g. vacuum, air, glass, paper, etc, known as a dielectric [21]. This material, which is inserted between the parallel plates, is generally designed to prevent the transfer of charges from occurring between the plates, in order to ensure that electric charge of equal magnitude, but opposite polarity, accumulates on each plate [21]. These conventional capacitor devices are commonly utilized in the electrical circuitry of radio applications for fine-tuning the frequency of radio receivers, in the circuitry of electronic calculators, additionally in automobile ignition systems for preventing the occurrence of sparking, and ultimately in electronic flashing units as energy storing devices [21].

The figures below represents (a) a circuit diagram of a parallel-plate capacitor consisting of two parallel plates each with area {A} separated by a distance {D}, where the two plates sustain equal and opposite charges [21]. Additionally, it also represents (b) an image of a cylindrical shape capacitor consisting of a cylindrical conductor of radius {a} and length {L}, surrounded by a coaxial cylindrical shell of radius {b} [21].

(a) **(b)**

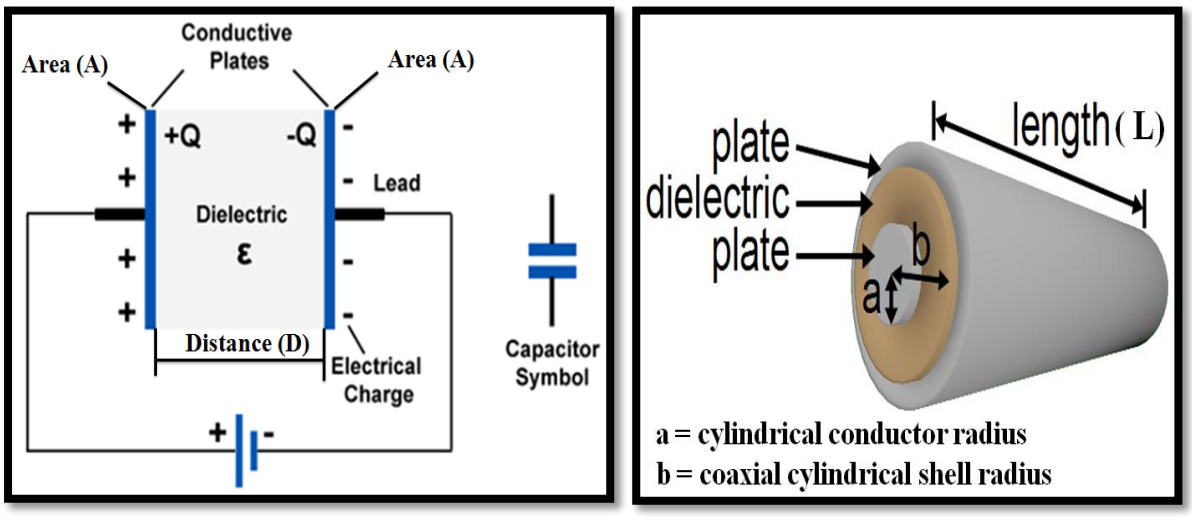

Figures 2.1: (a) A parallel-plate capacitor connected to an energy source (i.e. a battery cell), and (b) a cylindrical shape capacitor [22-23].

2.1.1 Definition of capacitance

Defining the concept of capacitance, we could consider an isolated metallic sphere conductor with an arbitrary radius illustrated as {R}, where charge can be stored on the surface of the spherical conductor [24]. If we also consider the quantity of charge stored on the surface of the sphere as {Q}, then the electrical potential of the sphere can be illustrated as the following equation:

$$V = \frac{1}{4\pi\varepsilon_0}\frac{Q}{R} \qquad (2.1)$$

Where ε_0 = Permittivity constant {8.85 x 10^{-12} $C^2/(N.m^2)$} , Q = quantity of charge stored on the spherical conductor, and R = radius of the spherical conductor [24]. From **equation (2.1)**, we can therefore deduce that the quantity of charge stored on the spherical conductor is directly proportional to its electrical potential [25]. The relation of charge with potential is generally true for any arbitrary shaped conductor [26]. The charge accumulated and stored on the surface of the conductor induces an electrical field with an electric field strength directly

proportional to the charge stored on the conductor surface [27]. This electrical field generates an electrical potential that is directly proportional to the electric field strength, thus providing the indication of charge being directly proportional to the potential [28]. From this deduction, we can therefore formulate the following expression:

$$Q = CV \tag{2.2}$$

Where, C is defined as the constant of proportionality, which is fundamentally known as the capacitance of the conductor [24]. Additionally, it is quite important to note that the capacitance would undoubtedly increase in magnitude if the conductor is able to store a large quantity of charge at a relatively low electrical potential [24]. For a spherical conductor, the capacitance value would increase in correlation with its radius and it can be calculated using the following mathematical equation:

$$C = \frac{Q}{V} = \frac{Q}{\left(1/4\pi\varepsilon_0\right)\left(Q/R\right)} = 4\pi\varepsilon_0 R \tag{2.3}$$

Where the unit for capacitance is farad (F), and 1 farad = 1 F = 1 coulomb/volt [24].

2.1.2 Calculation of capacitance

2.1.2.1 The Parallel-Plate Capacitor

The most customary variation of capacitor systems is comprised of two metallic parallel plate conductors, separated from one another by an insulating material called a dielectric, where individually, the plates carry opposite magnitudes of electric charge [29]. The capacitance value of such a capacitor configuration can be described by the following expression bellow, which incorporates the difference of potential between the two metallic parallel plate conductors [30].

$$C = \frac{Q}{\Delta V} \tag{2.4}$$

Where Q = the quantity of charge on each plate, ΔV = the change in potential between the two plates [31]. It is also important to note that for this expression, both Q and ΔV are considered as positive quantities, and that the net charge within the metallic parallel plate capacitor is zero [24].

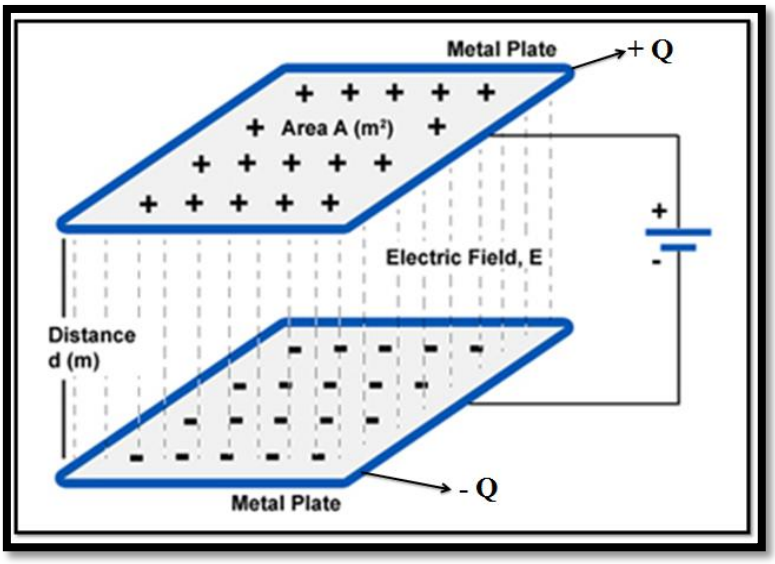

Figure 2.2: Diagram of a two metallic parallel-plate capacitor, each of area A (m^2), separated by a distance d (m), with respective charges of +Q and –Q [32].

The electric field and the potential difference between the two metallic parallel plates is described by the following two expressions bellow (given in **equation 2.5** and **2.6**). It is imperative to note that for these expressions, the electric field lines at the edge of the plates, which are not considered as straight lines, are neglected as we only consider the electric field lines between the plates when calculating capacitance [33].

$$E = \frac{\sigma}{\varepsilon_0} = \frac{Q}{\varepsilon_0 A} \tag{2.5}$$

$$\Delta V = Ed = \frac{Qd}{\varepsilon_0 A} \tag{2.6}$$

From these expressions, we can therefore finally formulate a mathematical equation (illustrated in **equation 2.7**) that can be used to calculate the capacitance value of a parallel plate capacitor configuration [33].

$$C = \frac{Q}{\Delta V} = \frac{Q}{Qd/\varepsilon_0 A} = \frac{\varepsilon_0 A}{d} \tag{2.7}$$

2.1.2.2 The Cylindrical Capacitor

A cylindrical capacitor device consists of a cylindrical wire with radius R_1, which is additionally surrounded by a cylindrical shell of inner radius R_2. Both the cylindrical wire and the shell have equal lengths, as portrayed in the following diagram below. During the charging process of the capacitor, the inner wire and outer shell continually receive equal but opposite charges until they reach their maximum capacitance. The calculation for the capacitance of the cylindrical capacitor is methodically illustrated below the displayed diagram of the cylindrical capacitor.

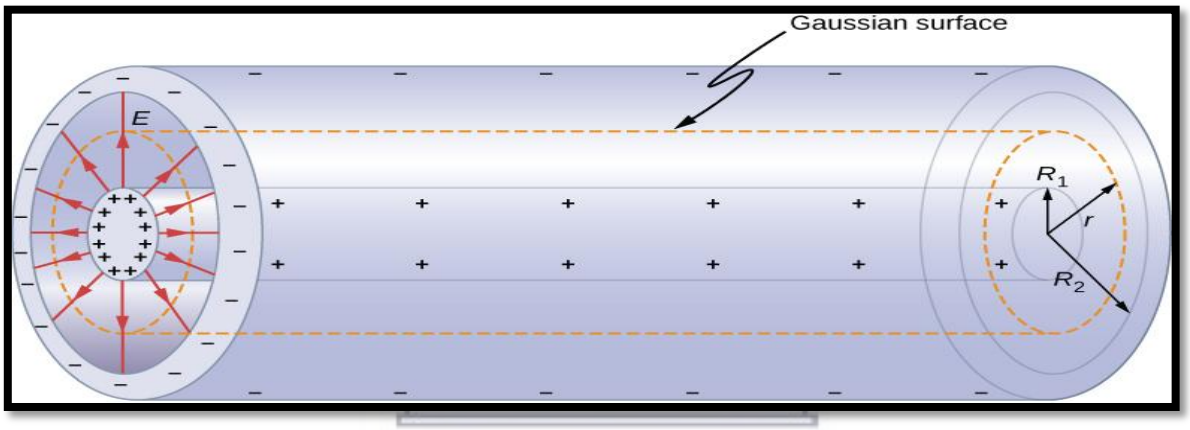

Figure 2.3: Pictorial representation of a cylindrical capacitor consisting of a cylindrical conductor of radius R_1 and length L, surrounded by a coaxial cylindrical shell of radius R_2, where the dashed line, in the diagram, represents the end of the cylindrical Gaussian surface [34].

The capacitance calculation of the cylindrical capacitor is progressively displayed in the following set of mathematical equations:

Step 1: Initially, it is required to calculate the electric field generated between the two cylindrical conductors (E), by using the integral form of Gauss's Law (which states the following; the total electric flux, Φ, through any closed surface is equivalent to the charge stored, divided by the permittivity constant) [35] .

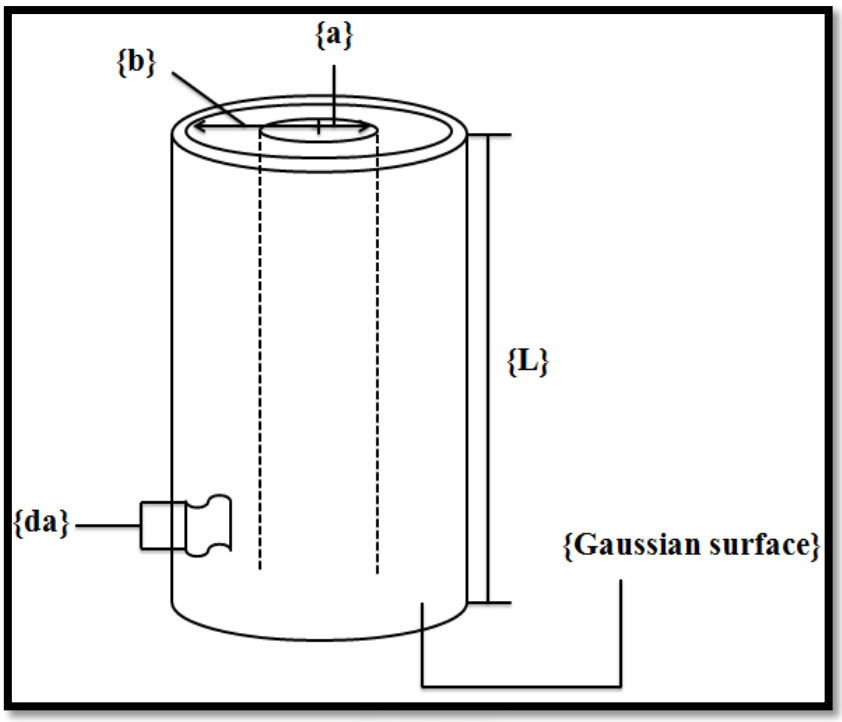

Scheme 2.1: Schematic diagram displaying a drawing representing a Gaussian surface [35].

$$\oint \mathrm{E}.da = \frac{Q}{\varepsilon_0} \tag{2.8}$$

$$\mathrm{E}.2\pi r.L = \frac{Q}{\varepsilon_0} \tag{2.9}$$

Where 2πr = the circumference of the ring shell, and L = the length of the ring shell. When solving for E in **equation (2.9)**, we obtain the following expression:

$$E = \frac{Q}{2\pi L\varepsilon_0} \tag{2.10}$$

For the radius between *a* and *b*, additionally represented as (a$< r <$ *b*).

In physics, the charge per unit length is also represented as lambda (λ). This can be used in the above expression by substituting λ = Q/L (charge per unit length).

$$\therefore \quad E = \frac{\lambda}{2\pi r \varepsilon_0} \tag{2.11}$$

Step 2: Secondly, part 2 of the calculation include the use of the expression for (E), in order to determine the potential difference (V) between the two shells.

$$V = \int dv \tag{2.12}$$

$$dv = -Edr$$

$$\frac{dv}{dr} = -E$$ Standard electromagnetics equations (2.13 & 2.14)

$$V = -\int_b^a \mathrm{E}.dr \tag{2.15}$$

With the use of the expression for (E), we have the integral form of (V) as follows:

$$V = -\int_b^a \frac{\lambda}{2\pi r \varepsilon_0}.dr \tag{2.16}$$

The next sub-step would be to rearrange the integral variables, cancel out the negative sign, and use the fundamental calculus theorem to obtain the complete expression for (V).

$$V = \frac{\lambda}{2\pi\varepsilon_0}\int_a^b \frac{1}{r}\,dr \tag{2.17}$$

According to the natural logarithm theorem, $\frac{d}{dx}\ln|x| = \frac{1}{x}, if\ x > 0$. In this case, $\frac{d}{dx}\ln|r| = \frac{1}{r}, if\ r > 0$ [36]. From the derivative of $\ln|r|$, the integral result can be obtained as follows:

$$V = \frac{\lambda}{2\pi\varepsilon_0}\ln|r|\Big|_a^b \tag{2.18}$$

The upper and the lower limits are illustrated as (a) and (b). Applying "The Fundamental Theorem of Calculus", we obtain the following expression:

$$V = \frac{\lambda}{2\pi\varepsilon_0}\left(\ln|b| - \ln|a|\right) \tag{2.19}$$

Using the rules of logarithms, we can simplify the above expression to formulate the complete mathematical expression for the potential difference (V) between the inner and outer cylindrical shells.

$$V = \frac{\lambda}{2\pi\varepsilon_0}\ln\left(\frac{b}{a}\right) \tag{2.20}$$

Step 3: The third and final part of the calculation would be to determine the actual capacitance of the cylindrical capacitor. This can be performed by using the equation below:

$$C = \frac{Q}{V} \tag{2.21}$$

Next would be to find the expression for charge (Q), by using the equations λ=Q/L $\Rightarrow$ Q=λL. This expression for (Q) can then be used to find the expression for the capacitance.

$$C = \frac{2\pi L\varepsilon_0}{\ln\left(b/a\right)} \tag{2.22}$$

Additionally, it is important to note that the magnitude of the potential difference (V) is a positive quantity since the inner cylinder possesses a greater potential than that of the outer cylinder. The expression shown in **equation (2.22)**, illustrating the capacitance of a cylindrical capacitor, is now well understood as it also indicates that the capacitance is proportional to the length of the cylinders (C$\propto$ L) [37]. This therefore implies that, as the length of the cylinders increases, its capacitance also increases. An extra detail to note is that the capacitance also depends on the radii of the two cylindrical conductors [38].

2.1.2.3 The Spherical Capacitor

A spherical capacitor device is generally comprised of a spherical conducting shell of radius {r_b} and charge {-Q}, that is concentric with a smaller conducting sphere of radius {r_a} and charge {+Q} [21]. The electric field {E} between the two conducting spheres is radiating outward, due to the positive charge retained by the inner sphere. The capacitance of a spherical capacitor can be calculated by initially evaluating the potential difference {ΔV} between the spherical conductors for a given charge on each sphere. The following and final step is to apply Gauss's Law as well as the definition of capacitance, in order the complete the calculation.

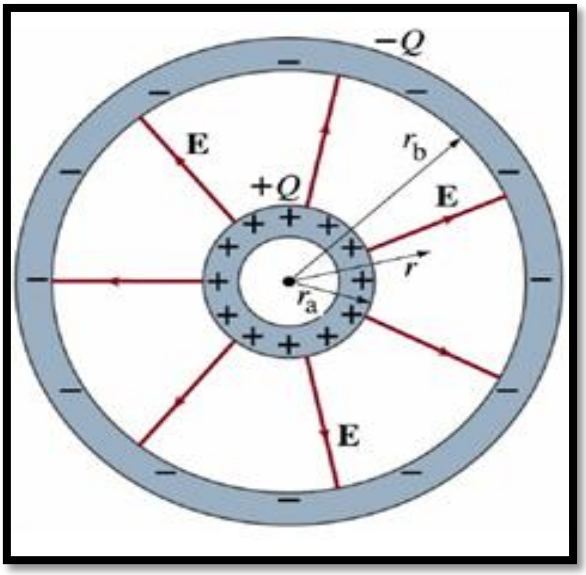

Figure 2.4: Diagram of a spherical capacitor consisting of two concentric conducting spheres [38].

By definition: $$C = \frac{Q}{V}$$

In order to obtain the potential difference between the two spheres, it is essential to initially, determine the electric field outside of the inner sphere. Since the electric field is only determined by the charge on the inner sphere and not the outer sphere, we therefore have the following expression for the electric field (E_1-the electric field caused by the inner sphere):

$$E_1 = \frac{kQ}{r^2} \tag{2.23}$$

The main objective is to obtain the potential difference between $\{r_a\}$ and $\{r_b\}$, by using the following relationship, illustrated below, between the potential difference (ΔV) and the electric field (E_1):

$$E_1 = \frac{V}{r} \Rightarrow V = E_1 r \tag{2.24}$$

It is crucial to note that the relationship, illustrated above, is only true if the electric field (E_1) is constant. In the case of the spherical capacitor, the electric field (E_1) is not constant, as it is a function represented as $E_1(r) = \frac{1}{r^2}$. Therefore, we can present the relationship between the potential difference and the electric field in a differential form expression, as illustrated below:

$$V = E_1 r$$

$$dV = E_1 dr \tag{2.25 \& 2.26}$$

The dV derivative notation is similar to the change in potential notation (ΔV) between the inner and outer spheres, which is also additionally implied as the potential difference (V).

$$\therefore \quad dV = E_1 dr$$

$$\Rightarrow \quad V = -\int_{r_b}^{r_a} E_1 dr \tag{2.27 \& 2.28}$$

The negative sign is included before the integral, due to the decrease in potential occurrence as the radius of the spheres increases, i.e. as the radius of the spheres increases, the potential decreases. The purpose of the negative sign is to compensate for that, thus the continued integral expressions are illustrated below:

$$\Delta V_{r_b \to r_a} = V = -\int_{r_b}^{r_a} \frac{kQ}{r^2} dr \tag{2.29}$$

$$\Delta V_{r_b \to r_a} = V = -\int_{r_b}^{r_a} \frac{Q}{4\pi\varepsilon_0 r^2} dr \tag{2.30}$$

$$\Delta V_{r_b \to r_a} = V = -\frac{Q}{4\pi\varepsilon_0}\int_{r_b}^{r_a} r^{-2} dr \tag{2.31}$$

$$\Delta V_{r_b \to r_a} = V = -\frac{Q}{4\pi\varepsilon_0}\left[\frac{r^{-1}}{-1}\right]\Bigg|_{r_b}^{r_a} = \frac{Q}{4\pi\varepsilon_0}\left[\frac{1}{r}\right]\Bigg|_{r_b}^{r_a} \tag{2.32}$$

$$\Delta V_{r_b \to r_a} = V = \frac{Q}{4\pi\varepsilon_0}\left[\frac{1}{r_a} - \frac{1}{r_b}\right] \tag{2.31}$$

Before continuing with the calculation, it is vital to note that ΔV is a positive quantity, since $r_b > r_a$. This notification, therefore, implies that $\frac{1}{r_a} - \frac{1}{r_b} > 0$. The above expression, in **equation (2.31)**, is further simplified below to obtain the complete expression for the potential difference (ΔV).

$$\Delta V_{r_b \to r_a} = V = \frac{Q}{4\pi\varepsilon_0}\left[\frac{r_b - r_a}{r_a r_b}\right] \tag{2.32}$$

The final expression for the capacitance of the spherical capacitor is illustrated as follows by relating the definition of capacitance, C = Q/V, with the above expression for the potential difference, to formulate the capacitance expression in its simplest mathematical form.

$$C = 4\pi\varepsilon_0\left[\frac{r_a\, r_b}{r_b - r_a}\right] \tag{2.33}$$

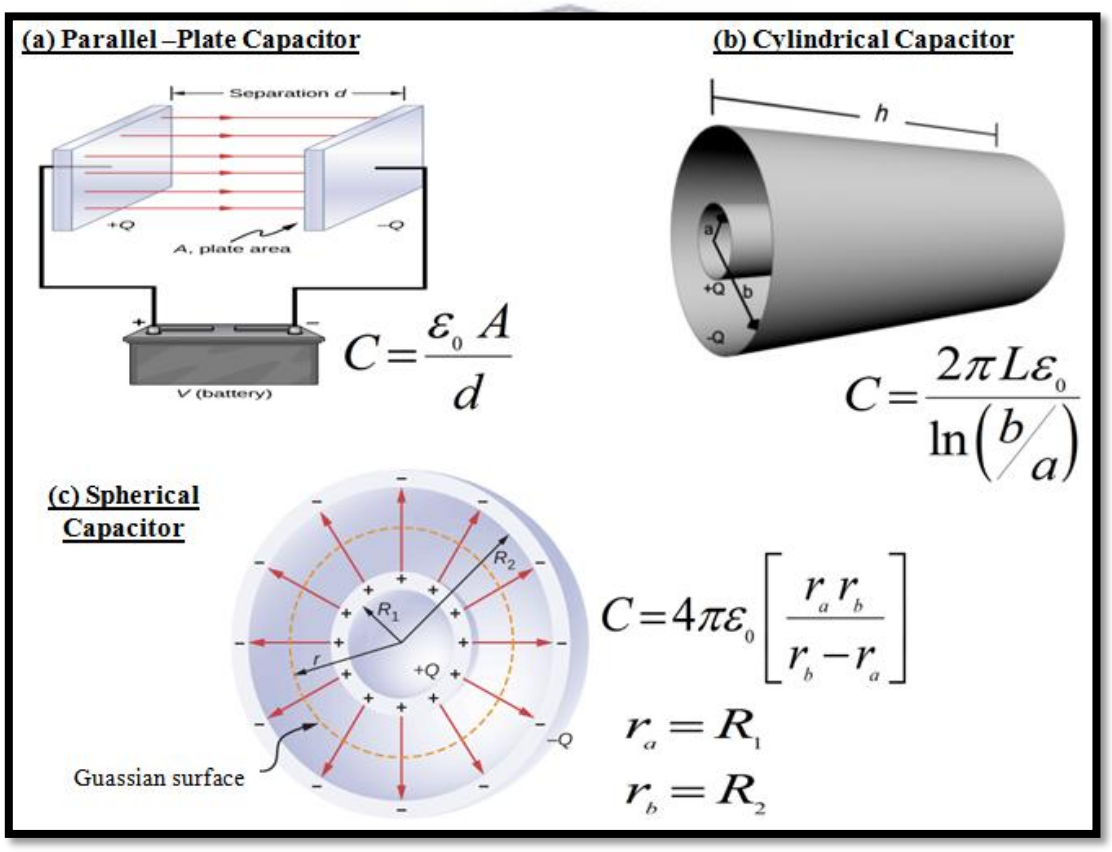

Figure 2.5: Summary of the three geometrical capacitor designs with their respective capacitance derived expressions [39].

2.1.3 Energy stored in a charged capacitor

The energy stored on a capacitor in the form of charge, can also be considered as the energy stored in the form of electrical potential energy. However, in order for the capacitor to store charge, a power source (for example a battery) must be connected to it. The battery cell performs work (W) by mobilizing the positive and negative charges from one plate to the other. Additionally, it is significant to take into account that this discussion is considered for a parallel-plate capacitor system. However, the derived electrochemical potential energy expression, which is illustrated below, is generally valid for any electrostatic field configuration.

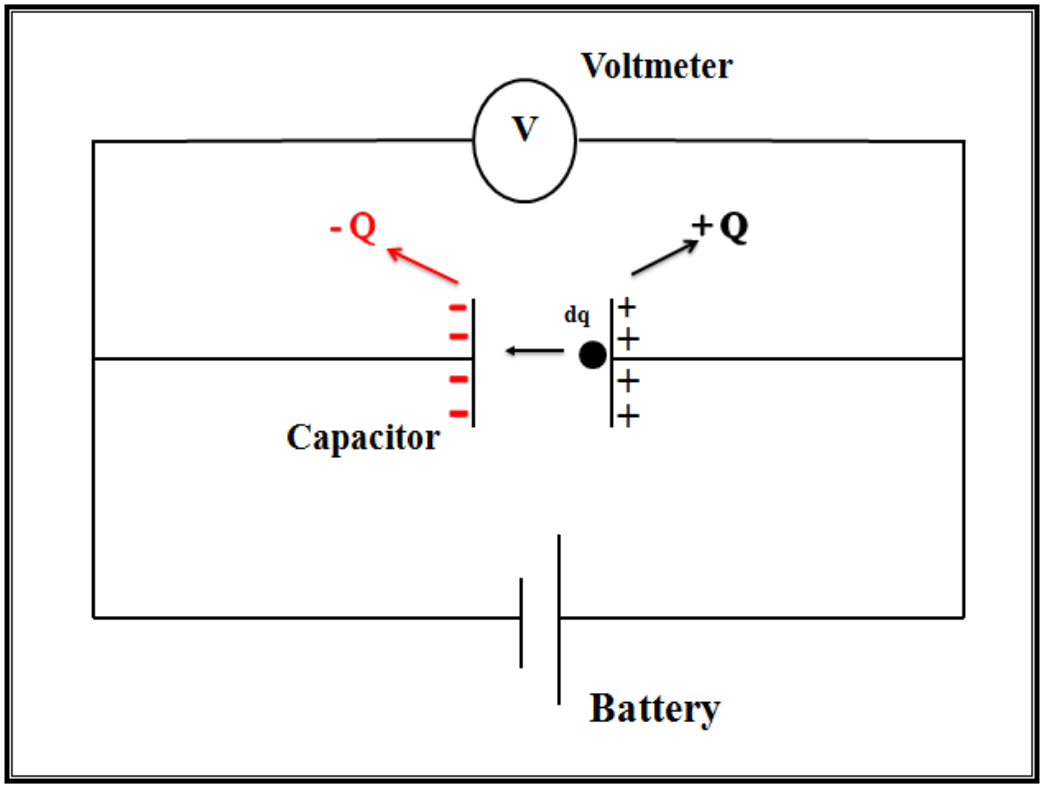

Scheme 2.2: Schematic of a capacitor circuit diagram connected to a battery cell and a voltmeter, to measure the voltage across the capacitor during its charging process [40].

During the charging process of the capacitor, when the battery cell is in connection with the closed circuit, the positive and negative charges separate from one plate to the other. This occurs by virtue of the battery cell performing work by transporting the negative charges to the negative plate. Once the capacitor is fully charge up, all the positive and negative charges are stored, in the form of electrical potential energy, on the positive and negative plates. If we were to, hypothetically, consider an infinitesimally small charge on the negative plate electrode as (dq); the work (U) required to transport the charge element (dq) from the negative plate to the positive plate involves the following formula:

$$dU = V\,dq \tag{2.34}$$

It is additionally important to note that the energy stored on a capacitor can also be expressed in relation to the work done by the battery cell. As each differential charge (dq) moves towards the capacitor plate, the voltage across the capacitor progressively increases toward the voltage of the battery cell. This implies that during the energy storing process, it requires more work to move each successive elemental differential charge (dq) from one capacitor plate to the other. The culmination of all the amounts of work done by the movement of all the dq charges, until the capacitor plate attains its total maximum charge, requires an infinite summation calculation, for which the integration tool is famously essential. Below is the mathematical interpretation of the definite polynomial capacitor energy integral:

$$U_{\text{Total}} = \int_0^{Q_f} V\,dq \tag{2.35}$$

Using the basic definition of capacitance for all capacitor configuration types, C = q/V (which also implies) V = q/C, we can rewrite the potential energy expression with the use of some additional substitutions.

$$U_{\text{Total}} = \int_0^{Q_f} \frac{q}{C}\, dq \tag{2.36}$$

The upper and lower limits of the integral is the charge variable of the capacitor, i.e in this case, the capacitor is being charged up from zero coulomb to (Q_f) coulombs. Thereafter, it is just a matter of solving the integral to obtain the final expression for the electrical potential energy stored on the parallel-plate capacitor.

$$U_{\text{Total}} = \frac{1}{C}\int_0^{Q_f} q\, dq = \frac{1}{C}\frac{q^2}{2}\Big|_0^{Q_f} \tag{2.37}$$

Becomes zero

$$U_{\text{Total}} = \frac{1}{2}\frac{q^2}{C}\Big|_0^{Q_f} = \frac{1}{2}\left[\frac{(Q_f)^2}{C} - \frac{(0)^2}{C}\right] \tag{2.38}$$

$$U_{\text{Total}} = \frac{1}{2}\frac{Q_f^2}{C} \tag{2.39}$$

2.2 Classification of capacitor systems

2.2.1 Electrostatic capacitors

Electrostatic capacitors, which are generally considered as conventional capacitors, are constructed of two conductive electrodes, onto which electric charge is stored, each separated by a thin layer of non-conducting insulating material called the dielectric. When a dielectric is inserted between the parallel-plates of a charged capacitor, and completely fills the space between the plates, the quantity of charge on the plates will remain unchanged. However, the potential difference across the capacitor, as well as, the electric field strength within the capacitor plates is drastically reduced from what it would be in a vacuum (i.e. in a capacitor without a dielectric). Additionally, during this process, the capacitance of the capacitor increases by a specific dimensionless factor denoted as (K), called the dielectric constant. All known dielectric materials each possess their own unique dielectric constant (K), and dielectric strength (V/m) values. The dielectric strength of an insulating material can be described as the maximum electric field that can exist within the dielectric material without it experiencing any electrical malfunction.

An important statement previously mention with regard to how the capacitance changes due to the presence of a dielectric material, states that the capacitance increases and the voltage decreases by the dielectric constant factor (K). Since the charge (Q_0) on the capacitor remains unchanged, we conclude that the capacitance must change to the following expression:

$$C = \frac{Q_0}{V} = \frac{Q_0}{V_0 / K} = K \frac{Q_0}{V_0} \tag{2.40}$$

$$\therefore \quad C = K C_0 \tag{2.41}$$

Where (C_0) = the capacitance of a capacitor in the absence of the dielectric material. For a parallel-plate capacitor configuration, where $C_0 = \varepsilon_0 A/d$, we can express the capacitance of the capacitor containing a dielectric as the following expression:

$$C = K\frac{\varepsilon_0 A}{d} \tag{2.42}$$

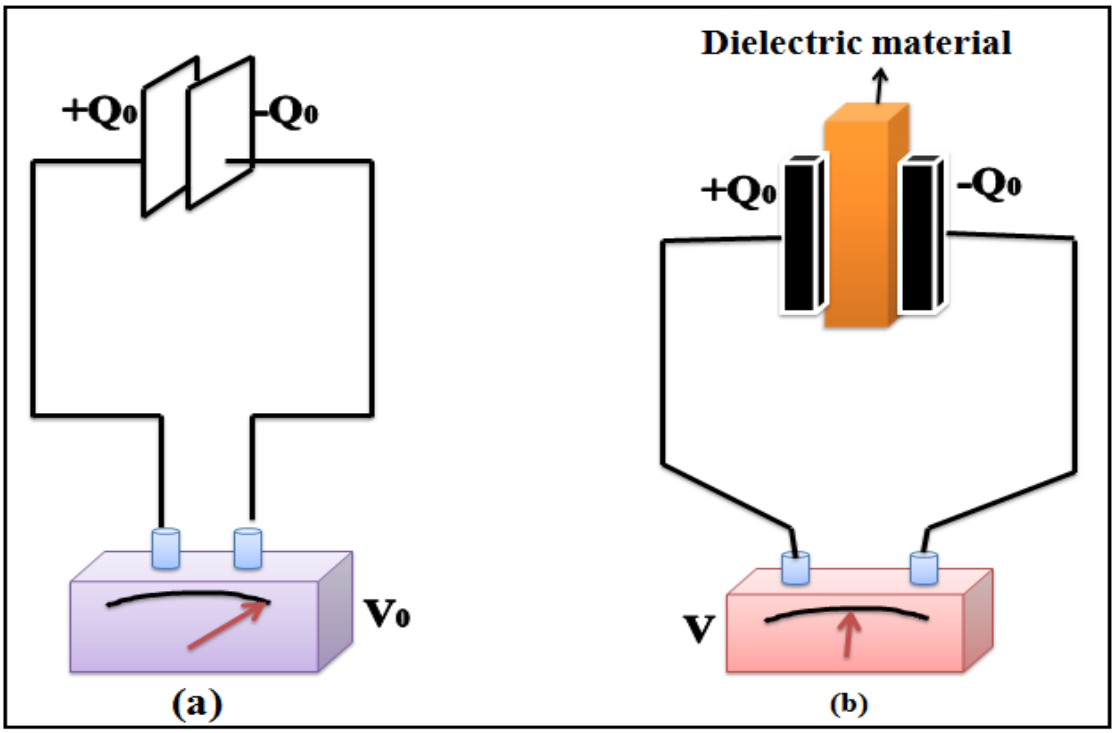

Scheme 2.3: Circuit diagrams illustrating how the potential difference, as recorded by an electrostatic voltmeter, for capacitors without (a) and with (b) a dielectric material, is reduced from V_0 to V by a factor of K (which implies that $V = V_0 / K$) [41].

Table 2.1: Table showing the dielectric constants and dielectric strengths of various materials at room temperature [42].

Material	Dielectric Constant (K)	Dielectric Strength (V/m)
Vacuum	1,00000	-
Air	1,00059	3×10^6
Bakelite	4,9	24×10^6
Fused quartz	3,78	8×10^6
Pyrex glass	5,6	14×10^6
Polystyrene	2,56	24×10^6
Teflon	2,1	60×10^6
Neoprene rubber	6,7	12×10^6
Nylon	3,4	14×10^6
Paper	3,7	16×10^6
Strontium titanate	233	8×10^6
Water	80	-
Silicone oil	2,5	15×10^6

The list presented below describes what advantages a dielectric material would offer a capacitor within a vacuum or air.

- The dielectric material would increase the capacitance value of the capacitor by the dimensionless factor K.
- The dielectric material would also increase the maximum operating voltage within which the capacitor could function.
- Lastly, the dielectric material could/would possibly provide mechanical support between the plates, thus allowing the plates to have a shorter distance (d) from one another, thereby causing an increase in the capacitor's capacitance.

Commercial grade electrostatic capacitors are frequently constructed of metal foil layers, intertwined with thin sheets of paraffin-impregnated paper or mylar, which is utilized as the dielectric material. These alternating layers and sheets of metal foil and dielectric are then rolled into the shape of a cylinder to form a small packaged electrostatic cylindrical capacitor (shown in the figure below). High-voltage capacitors commonly consist of numeral parallel interwoven metallic plates submerged in silicone oil, which serves as the dielectric material (as shown in the figure below). Small commercial capacitors of today are often constructed of ceramic and thin film materials.

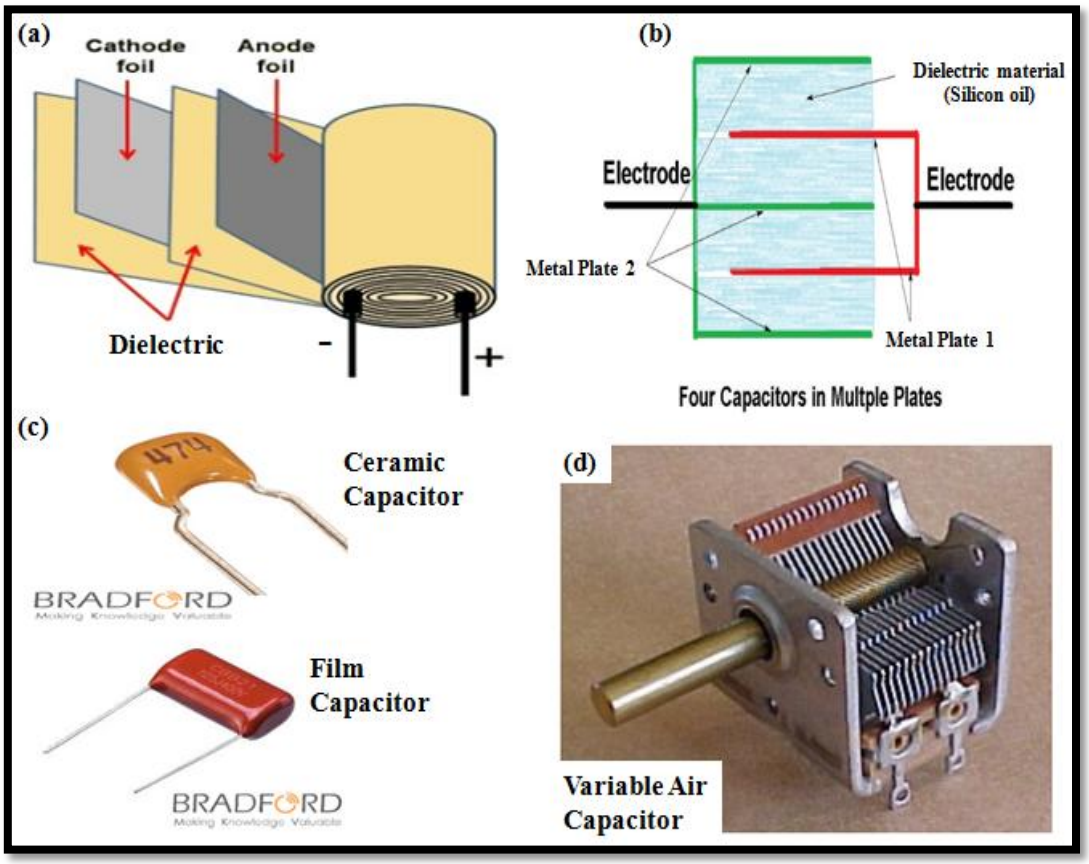

Figure 2.6: Image displaying (a) the basic construction of a cylindrical electrostatic capacitor, (b) a high-voltage multi-plate capacitor containing a silicon oil dielectric, (c) commercial grade ceramic and film capacitors, and (d) a variable air electrostatic capacitor [43-44].

2.2.2 Electrolytic capacitors

Electrolytic capacitors are conventionally employed as DC power supplies in electronic circuits due to their superior capacitances over that of electrostatic capacitors [45]. In this capacitor design, one of the two electrodes (usually the positive/cathode electrode) contains a very thin film layer (less than 10 μm) which serves as the dielectric material of the capacitor, with both electrodes separated by a semi-fluid electrolyte material in the form of a slurry paste [46]. These electrolytic type capacitors are primarily polarised, implying that the DC voltage applied to the capacitor terminals must be of correct polarity, as the incorrect polarisation will cause the film material on the cathode electrode to deteriorate [47]. The figure below displays the basic interior designs on an aluminium electrolytic capacitor, together with an image of a commercially packaged electrolytic capacitor.

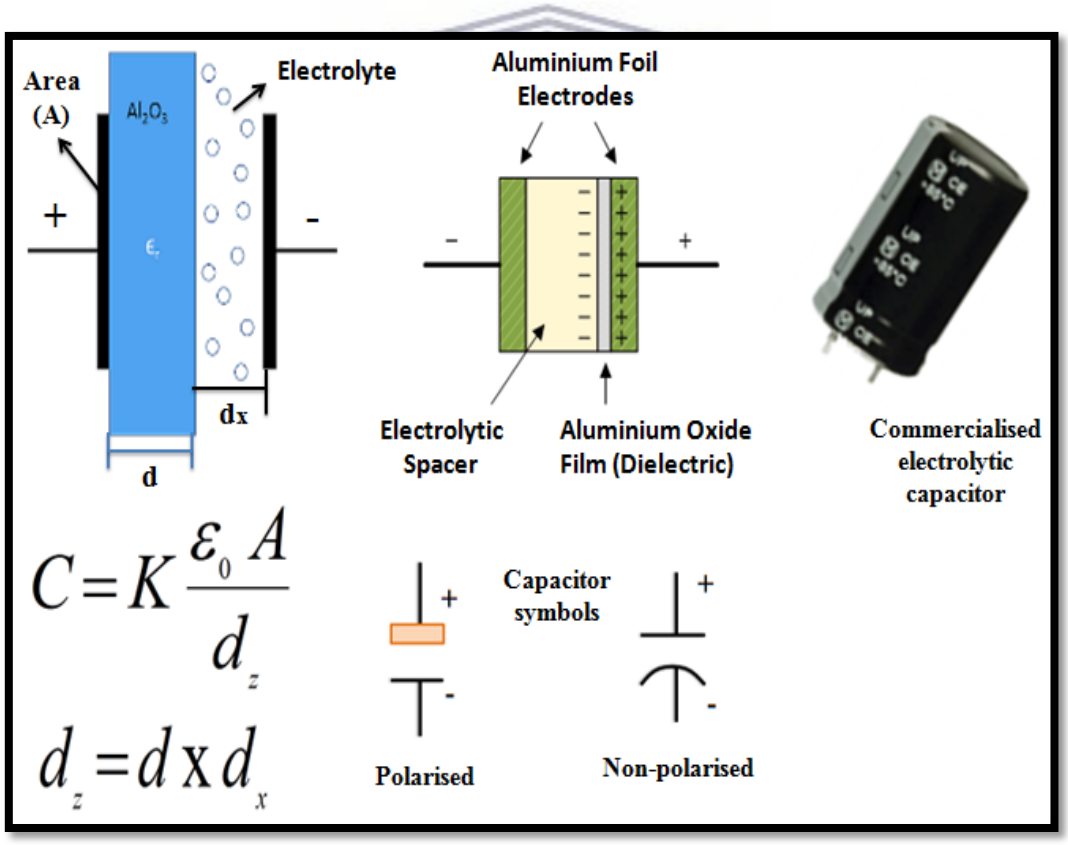

Figure 2.7: Diagram displaying interior designs of an aluminium electrolytic capacitor, as well as an image of a packaged commercial grade electrolytic capacitor [48].

2.2.3 Electrochemical capacitors

Electrochemical capacitors, also known as supercapacitors or ultra-capacitors, are fast energy storage devices capable of reaching over 1 million deep charge/discharge cycles [49]. In comparison to the famous Tesla graphite NMC lithium-ion battery manufactured by Panasonic, it is capable of achieving approximately 3000 – 5000 cycles [50]. However, the total energy content in supercapacitors is smaller than that in batteries meaning that energy can be supplied very quickly, which is a unique aspect for some applications. The more widely applied research field in energy storage technologies is the combination of supercapacitor and battery systems. This hybrid configuration would attain a greater energy efficiency and cycle life, as the supercapacitor component would sustain high peak potentials, which, in single lithium ion batteries, do potentially cause punctures in the separator thus resulting to overheating occurrence [51]. Additionally, the life cycle of the battery component of the hybrid system would, in-turn, be extended twice as long.

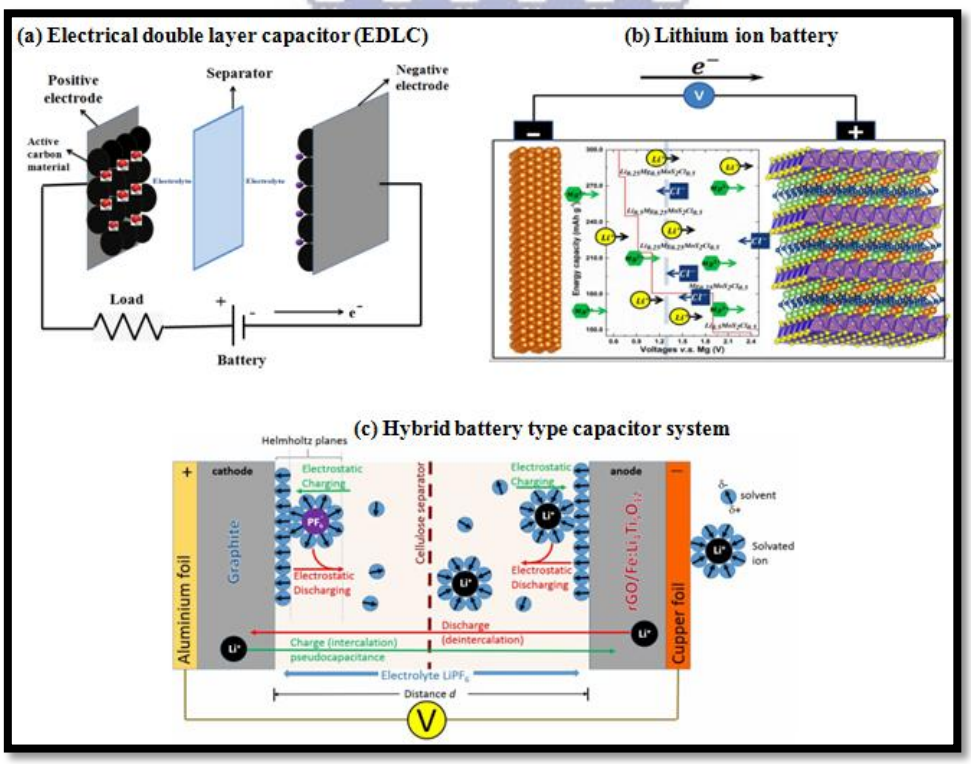

Figure 2.8: Diagram displaying interior designs of an (a) electrical double layer capacitor (EDLC), (b) lithium ion battery, and (c) hybrid battery type capacitor system [52-53].

2.2.3.1 Types of electrochemical capacitor technologies

2.2.3.1.1 Electrical Double Layer Capacitors (EDLCs)

Electrochemical capacitors (ECs) are classified into three unique categories, namely, electrical double layer capacitors (EDLCs), pseudocapacitors, and hybrid capacitors [54]. The main property that makes these EC devices distinguishable from one another is their unique energy storage mechanism. The EDLC uses a reversible electrostatic adsorption of electrolyte ions onto the electrode surface (containing the active electrode material) to mechanistically store energy in the form of charge [55]. This electrostatic force across the electrode/electrolyte interface is generated by an intense electric field from the applied voltage during charging processes of the device. Although EDLCs have lower operating performances than that of pseudocapacitors, they do possess a superior life expectancy due to their electrostatic energy storage mechanism [56]. As displayed in **Fig. 2.8** above, the interior construction of EDLCs is much like that of Li-ion batteries. However, EDLCs store energy by the separation of minuscule ionic charges at the electrode/electrolyte interface, as represented by the Helmholtz Model envisioned by Hermann von Helmholtz in 1879 [57].

Hermann von Helmholtz, a German physician and physicist, discovered that charged electrodes immersed within an electrolyte solution would attract counter-ions and repel co-ions, thus formulating two compact layers of charges at the electrode/electrode interface, hence the formation of an electric double layer at the electrochemical interface [58]. The Helmholtz model structure is analogous to that of a conventional electrostatic parallel-plate capacitor, with planar electrodes separated by distance (d_H), containing a dielectric material between the electrode plates [59]. Form this analogy, the specific capacitance $\left(C_s^H\right)$ of the Helmholtz layer is given by the following expression:

$$C_s^H = \varepsilon_0 \, \varepsilon_r \left(\frac{A}{d_H} \right) \tag{2.43}$$

Where ε_0 and ε_r are the free space and relative permittivity of the electrolyte solution, respectively, together with A being the electrode surface area [58]. The thickness (d_H) of the Helmholtz double layer can be approximated as the radius of the solvated ions [58]. Later, Gouy and Chapman designed an electric double layer model that introduces the thermal motion of solvated cations and anions within the electrolyte solution [60]. These mobile ions are driven by diffusion kinetics and electrostatic forces, thus formulating the "diffuse layer" as illustrated in **Fig. 2.9**. Thereafter, Stern later developed the Gouy-Chapman-Stern model, where he combined the Helmholtz model and the Gouy-Chapman model and described the inner compact layer (of immobilized ions) as the Stern layer and the outer region (containing mobile solvated ions) as the diffuse layer, thus formulating the two layers of the electric double layer model [61].

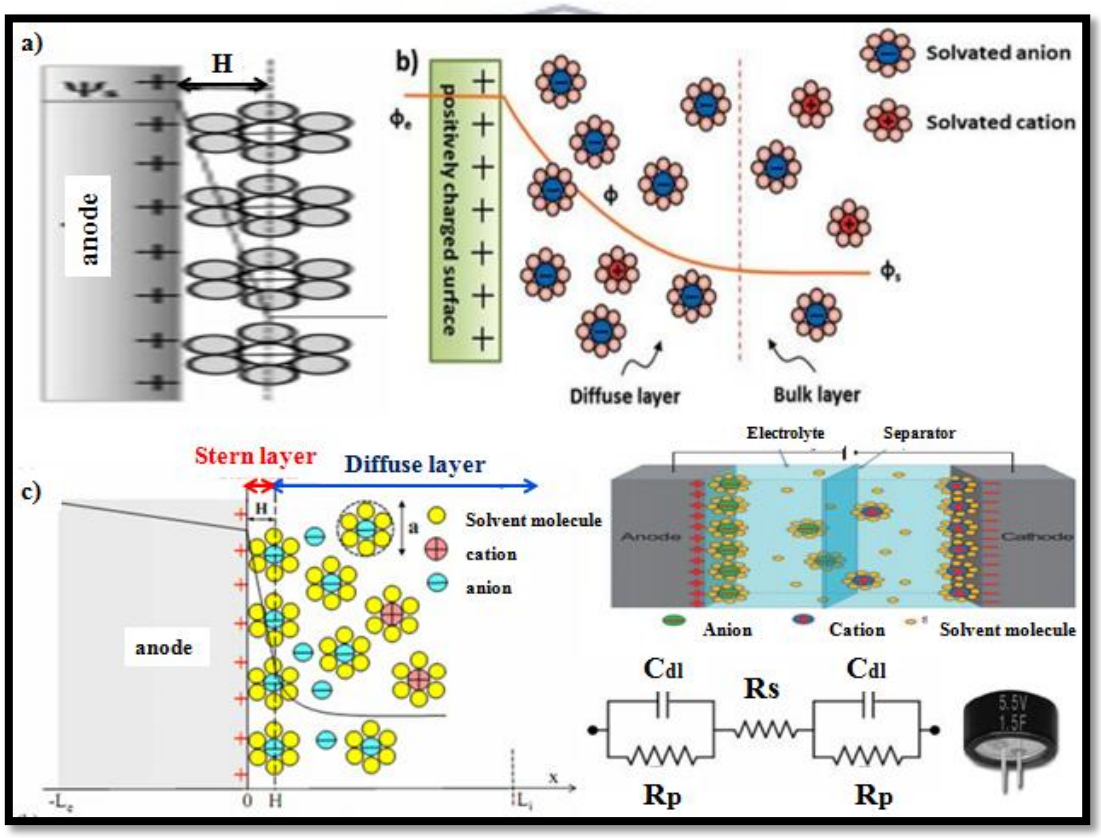

Figure 2.9: Models of the electric double layer structure illustrating the orientation of solvated cations and anions at the electrode/electrolyte interface within the Stern and diffuse layer, respectively: a) Helmholtz model, b) Gouy-Chapman model, and c) Gouy-Chapman-Stern model [58, 62-63].

2.2.3.1.2 Pseudocapacitors (PCs)

Pseudocapacitors, another type of EC, operate through a different energy storage mechanism to that of EDLCs. The general principle behind its charge storage mechanism involves rapid reversible faradaic charge transfer processes, through redox reactions, occurring throughout the active electrode material surface [64]. The required physical and chemical property that these active materials should exhibit is a high electrical conductivity and specific surface area, for it to be a suitable electrode material candidate in pseudocapacitor applications [65]. Pseudocapacitors can be constructed as symmetric PCs, much like EDLCs, where both electrodes contain the same active material, and asymmetric PCs, where the electrodes are coated with different active materials. In this research work, an asymmetric pseudocapacitor design was implemented for the performance investigative study of the synthesized cathode (positive) electrode materials, against activated carbon as the negative active electrode material. The diagram below (**Fig. 2.10**) illustrates three different Faradaic charge transfer mechanisms, which pseudocapacitors use to store energy, namely: a) underpotential deposition, b) redox pseudocapacitance, and c) intercalation pseudocapacitance [65-66].

The underpotential deposition mechanism occurs when metal ions (e.g., Pd^{2+}) adsorb onto the surface of a metallic (e.g., gold) electrode, thus forming a monolayer at the electrode/electrolyte interface [64]. These ions adsorb at electrical potentials greater than their reversible redox potentials [65]. Redox pseudocapacitance occurs when electrolyte ions are electrochemically adsorbed onto or in close-proximity to the electrode material surface, accompanied by a faradaic charge-transfer process [65]. Classic examples of these types of electrode materials include RuO_2, MnO_2, and conducting polymers [64, 67]. Intercalation pseudocapacitance occurs when the electrolyte ions intercalate between the atomic planes or layers of the active material's crystal lattices [68]. During intercalation processes, the crystal lattice phase remains unchanged throughout the concomitant faradaic transfer of electric charge [65].

The synthesized electrode materials investigated in this study utilizes a combination of two energy storage mechanisms, namely: i) redox pseudocapacitance and ii) intercalation pseudocapacitance [69]. It was calculated (from XRD data) that the crystal lattice sizes of the

researched electrode materials ranged between 0.5762 – 0.7708 nm. These values are a great deal larger than the ionic radii of a Li^+ atom or ion, theoretically determined as 0.068 nm [70]. From these findings, it is factual to state that both intercalation and redox pseudocapacitance processes govern the energy storage mechanisms of the proposed electrode materials. The diagram in **Fig. 2.10** additionally displays 3D and 2D images of the interior design for an asymmetric pseudocapacitor system (full cell device), where the positive and negative electrodes are coated with the active material and activated carbon, respectively.

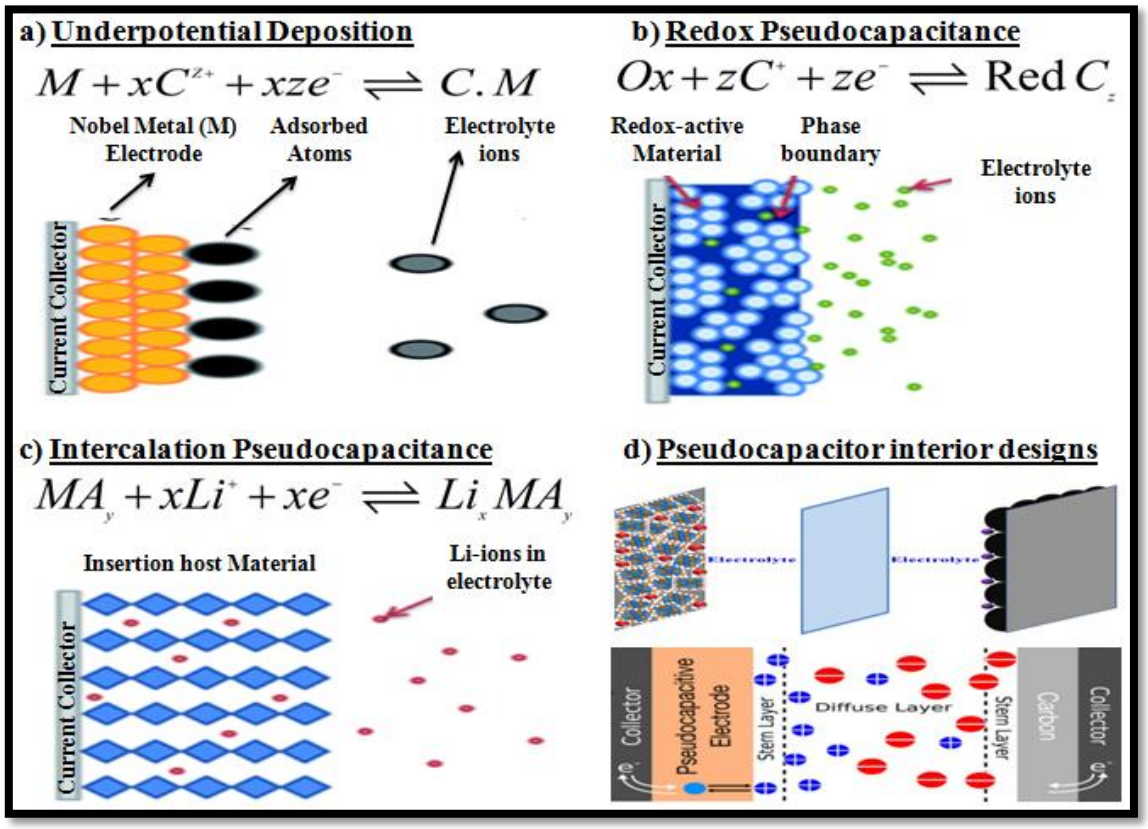

Figure 2.10: Diagram illustrating various types of reversible charge-storage mechanisms for pseudocapacitive electrode materials: a) underpotential deposition, b) redox pseudocapacitance, and c) intercalation pseudocapacitance. The diagram additionally displays 3D and 2D images of an asymmetric pseudocapacitor design [64].

2.2.3.1.3 Hybrid capacitors (HCs)

The fundamental aspects of hybrid capacitors are comprised of a unique characteristic of asymmetric pseudocapacitor devices [71]. This characteristic entails hybrid capacitors utilizing two energy storage mechanisms, much like pseudocapacitors, in order to store electric charge [72]. The positive electrode, containing the active material, utilizes the generic faradaic pseudocapacitance mechanism; while the negative electrode (containing any carbon type material, e.g; porous carbon, graphene, and/or carbon nanotubes) utilizes the electric double-layer capacitance mechanism [73]. Depending on the elemental construction and crystallographic nature of the active electrode material, it could possibly utilize additional charge storage mechanisms such as intercalation pseudocapacitance, commonly used by battery-type electrode materials [74]. The diagram below, **Fig. 2.11**, provides a structured illustration of the various electrode materials employed in specific supercapacitor or EC systems.

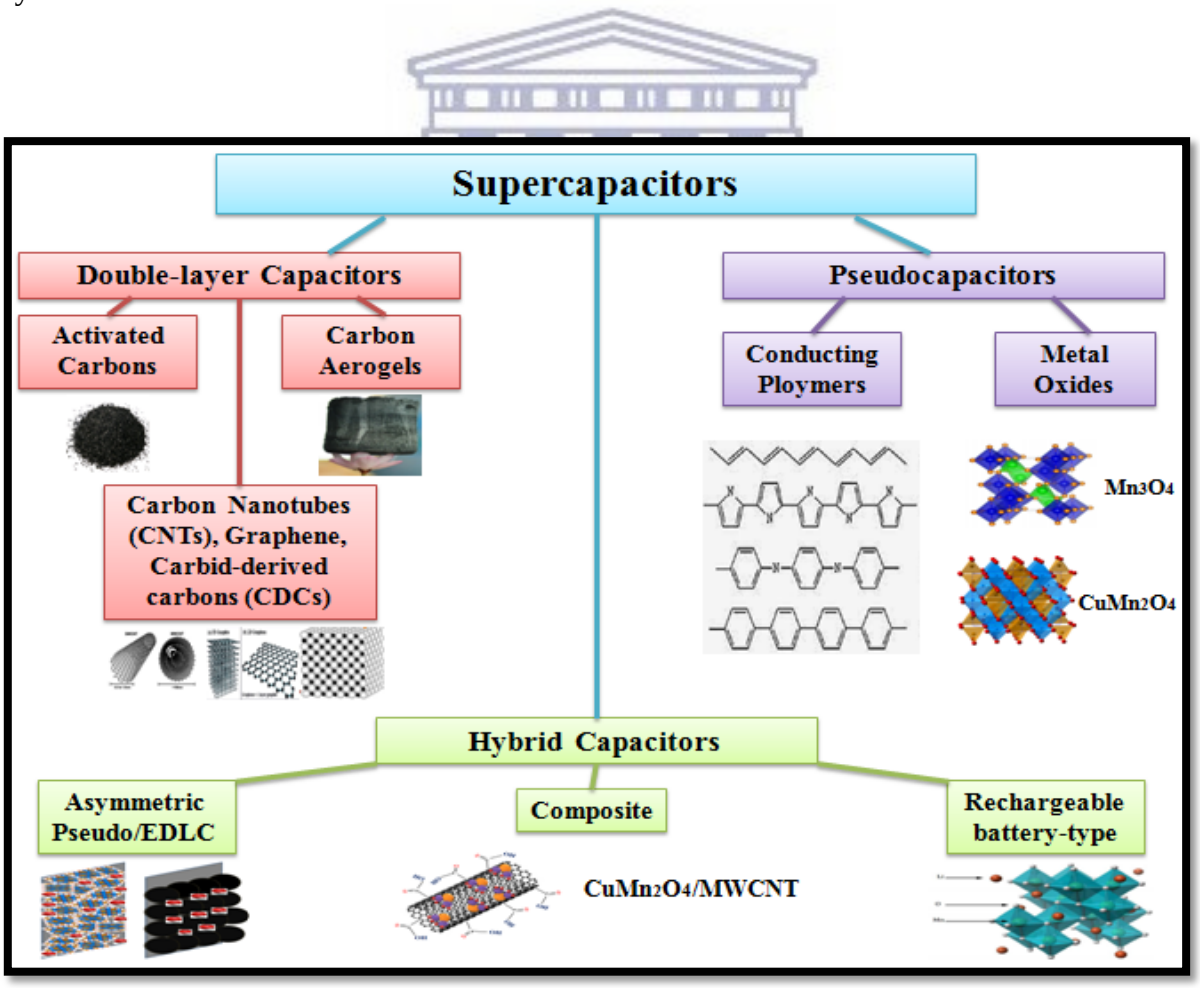

Figure 2.11: Flow diagram illustrating the taxonomy of ECs [62, 75-76].

2.3 Electrode materials utilized in the classified supercapacitor devices

It is essential to understand that the taxonomy of supercapacitor devices, illustrated in **Fig. 2.11** above, each employs electrode materials that only use specific energy storage mechanisms to function, according to the respective EC device operation specifications. The materials labelled Mn_3O_4, $CuMn_2O_4$, and $CuMn_2O_4$/MWCNT (in **Fig. 2.11**) are the synthesized electrode materials investigated in this research project. According to the flow diagram, both Mn_3O_4 and $CuMn_2O_4$ are metal oxide type materials, which utilize faradaic pseudocapacitance mechanisms to store charge. The composite $CuMn_2O_4$/MWCNT electrode material is illustrated as a hybrid capacitor type material, comprised of a combination of heteroatoms from its metal oxide and carbon constituents [77]. In order to understand the energy storage mechanism of this hybrid composite material, it was necessary to research various metal oxide and carbon based materials currently found in literature.

2.3.1 Carbon-based electrode materials employed in EDLCs

In the modern field of energy storage technologies, extensive research has been conducted on carbon as the most suitable electrode material for EC application [77]. Research findings from literature reported various carbon based materials possessing impressive supercapacitive properties such as high electrical conductivity, high surface area, high thermal stability, and low internal resistance [78]. This family of carbon-incorporated materials include activated carbons, carbon aerogels, graphene, carbon nanotubes, carbide-derived carbons, and more. However, brief and constructive information concerning chemical, physical, and electrical properties of the listed carbon-based materials is presented in the following section.

2.3.1.1 Activated Carbons

Activated carbons can be synthetically manufactured through treating carbonaceous raw materials (e.g., coal and/or pine wood) with a mild oxidation process called the activation process, which involves the carbonization and activation of organic molecules) [62, 77]. The main purpose of this activation process is to formulate a network of micro-pores, which would increase the carbon surface area. The pore size and distribution of carbons can be

controlled by manipulating various experimental parameters such as temperature, reaction time, and reagents used [77]. This pore size distribution of activated carbons has become a major focus in the research field of EDLC devices. Literature reports activated carbons processing a surface area exceeding 1000 m^2/g determined by gas adsorption/desorption techniques [77, 79]. A team of researchers, who conducted this study, published their findings in a high impact factor journal. In summary, they conducted a scientific investigation upon measuring the adsorption capacity of CO_2 onto the surface of activated carbon fibers (ACFs) [80]. This particular research aspect of activated carbons is what highlights its focus in the field of electrochemical capacitors, as having the ability to control the form and morphology of an electrode material, could aid in the diffusion of electrolyte ions for enhanced supercapacitive performance.

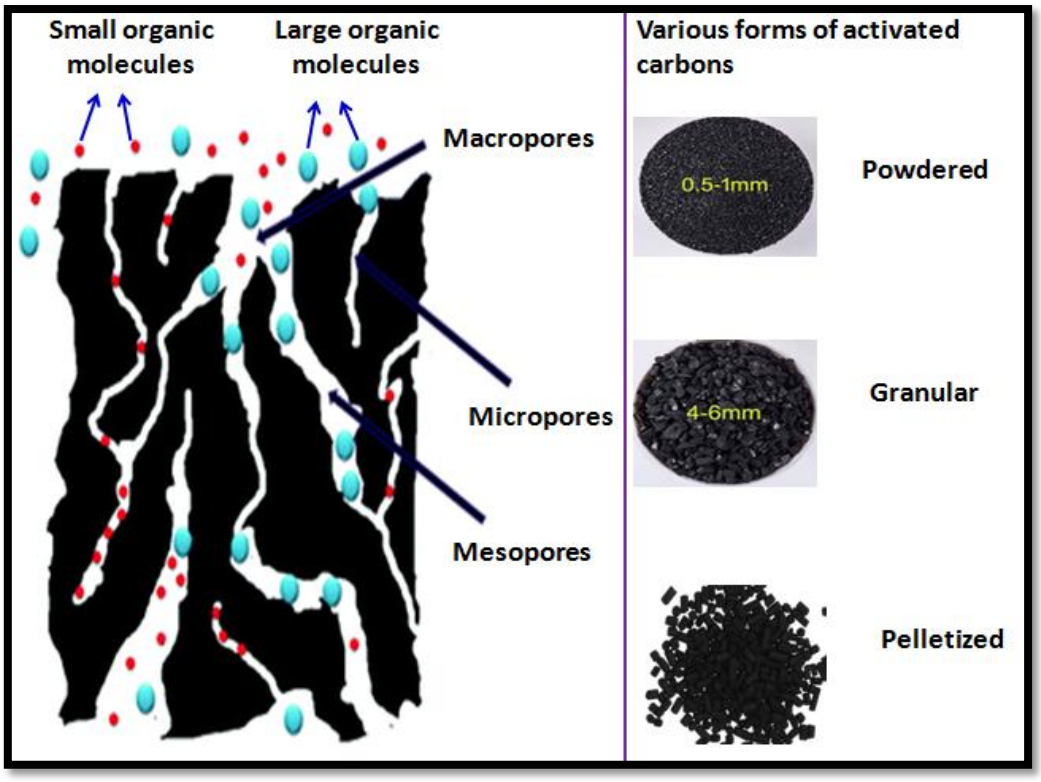

Figure 2.12: Diagram displaying a nano-scaled representation of activated carbon illustrating the various internal pore sizes responsible for the diffusion of large and small organic particles. Additional images of various forms of activated carbons are also displayed in the diagram [62, 81-82].

2.3.1.2 Carbon Aerogels

Carbon aerogels consist of carbon nanoparticles bonded together covalently, with a uniform distribution of mesopores across its surface area [79]. They retain a high but lower surface area compared to activated carbons, in the range of 400 – 800 m^2/g, together with a pore size distribution of less than 100 nm [83]. Due to the satisfactory specific capacitance exhibited by carbon aerogels, ranging between 20 – 100 F/g, they have been under close examination as potential electrode materials suitable for symmetric and asymmetric EDLC and pseudocapacitor devices [79, 84]. A synthetic advantage of carbon aerogels is that they do not require a binder additive during electrode preparation, as they are originally in a self-binding state [79]. This leads to carbon aerogels processing a much lower electron paramagnetic resonance (EPR) than that of activated carbons; thus promoting the generation of higher power density outputs [84].

2.3.1.3 Carbide-derived carbons

Carbide-derived carbons form part of a specific classification of carbon materials developed from ceramic precursors such as titanium carbide, silicon carbide, vanadium carbide, and molybedenum carbide, through the removal of metallic atoms under chemical or physical processes [77, 85]. These physical and chemical processes are introduced as thermal decomposition and halogenations, respectively [77]. Similar to activated carbons, carbide derived carbons can also have their pore size and distribution factors controlled through monitoring and altering various synthetic parameters [86]. Historic research conducted by Otis Hutchins in 1918, designed a method involving the chlorination of silicon carbide, for the development of carbide-derived carbon materials [77, 87]. This development embarked the beginning of these carbon-type materials into the employment of EDLC and pseudocapacitor devices as electrode materials.

2.3.1.4 Graphene and Carbon Nanotubes

Graphene is one of the most famously used carbon-type electrode material employed in all fields of supercapacitor technologies. Its two dimensional structure is composed of single-layered carbon atoms co-ordinated into a 2D honeycomb network of hexagonal crystal lattices [62, 77, 79]. It can additionally be modified into various physical and chemical forms such as graphene oxide, graphene-doped metal oxide composites, carbon nanotubes, and fullerenes [88]. Electrochemical analysis reports, found in literature, illustrated a modified 3D graphene electrode material, exhibiting impressive specific capacitance and energy density values of 341 F/g and 16.2 Wh/Kg, respectively [79, 89]. The diagram in **Fig. 2.13** shows the synthetic route to formulating chemically derived graphene from natural grade graphite [62]. Carbon nanotubes are graphene's most famous derivative constructed of sp^2 hybridized carbon atoms, rolled up into single/multi-walled cylindrical tubes [62]. **Fig. 2.13** additionally shows images of single and multi-walled carbon nanotubes. Performance analysis reported carbon nanotube supercapacitor electrodes achieving specific capacitance and energy density values of 160 F/g and 50 Wh/kg, respectively [90].

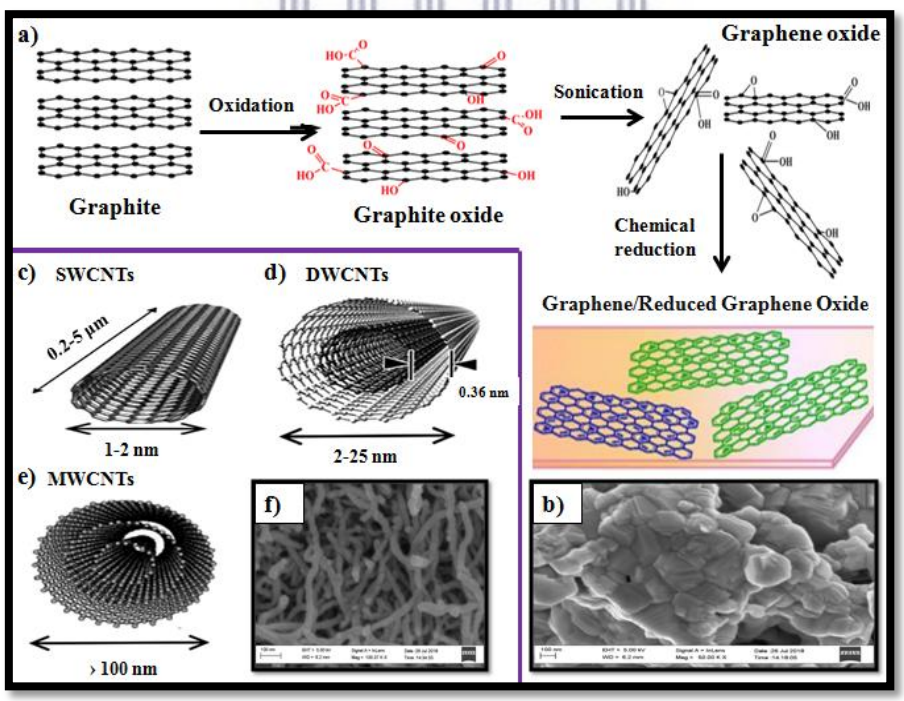

Figure 2.13: Diagram illustrating a) the synthetic route to developing graphene from commercial grade graphite, b) SEM image of graphene, c) single, d) double, and e) multi-walled CNTs, and f) SEM image of MWCNTs [62, 91-92].

2.3.2 Metal oxides and Conducting Polymers employed in pseudocapacitors

Transition metal oxides are the best-suited electrode materials for pseudocapacitor development due to its exceptional exhibited specific capacitance and low charge transfer resistance, thus leading towards high power and energy density outputs [93]. Examples of these materials include RuO_2, MnO_2, IrO_2, CoO, NiO, TiO_2, Fe_3O_4, etc [79]. Electrochemical analysis reported RuO_2, incorporated with mesoporous activated carbon, exhibiting a specific capacitance of 188 F/g, together with energy and power densities within the range of 14-24 Wh/kg and 400-10000 W/kg, respectively [94]. Despite the performance advantages provided by ruthenium (IV) oxide, there are some drawbacks involved such as high production cost, low abundance, and low operating potentials [95]. In this research review, manganese (IV) oxide, with no applied modifications, was utilized as the core metal oxide precursor due to its inexpensive cost, relatively high abundance, and low toxicity [96]. Due to the astonishingly high specific capacitance and conductivity exhibited by conducting polymers, these materials have also gained considerable attention in the development of improved EDLCs [97]. Conducting polymers utilize both faradaic and double-layer capacitance mechanisms to store charge, thus exhibiting better performance results than that of carbon type materials. In addition, a team of researchers innovatively developed graphene/CNT/polyaniline (PANI) composites as electrode materials, which exhibited improved specific capacitances within the range of 1000-1035 F/g [79, 98].

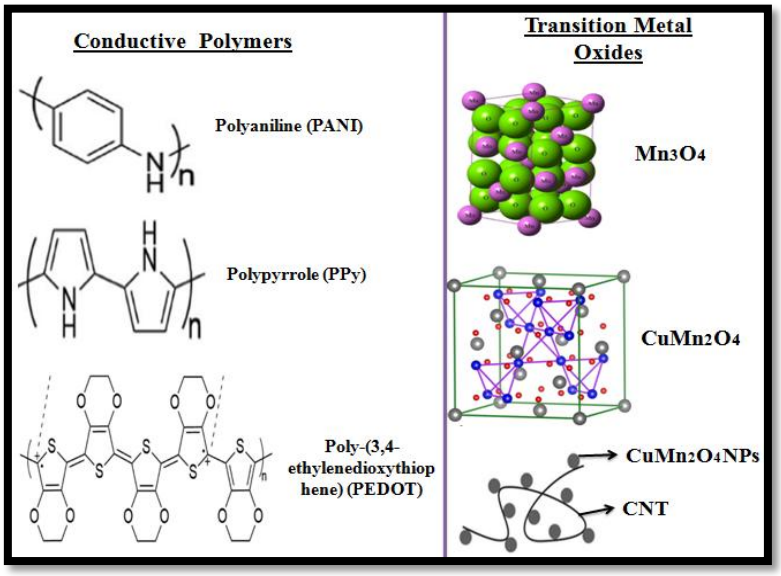

Figure 2.14: Various conductive polymers and related metal oxide materials [99-100].

2.3.3 The use of nanotechnology towards the development of hybrid composite pseudocapacitor electrode materials

It is well aware that pseudocapacitors mainly store charge through redox reaction mechanisms, occurring on the surface of the active electrode materials. Therefore, synthetic methods implementing nanotechnology towards the development of nanoscaled pseudocapacitor materials, are employed to improve their specific capacitance [62]. The size reduction of the material provides a greater surface contact area between the electrode (containing the active material) and the electrolyte, thus reducing the ionic transport length during diffusion processes at the electrode/electrolyte interface [101]. A researcher named Xiao and co-workers reported their findings of a monolithic NiO/Ni nanocomposite material exhibiting an astonishing specific capacitance value of 900 F/g [102]. Although these findings were only reported back in 2011, researchers are continuing to improve the electrochemical performance of metal oxides through modification with various carbon materials and/or conductive polymers. The purpose of these modifications is to alter the physical, chemical, and mechanical properties of the metal oxides towards enhancing their overall electrochemical performance [103]. As displayed before, in **Fig.2.14**, the proposed electrode materials were investigated in order to discover how its significant physical and electrochemical properties changes with the respective applied modification. The results section, in chapter 4, illustrates reduced particle size, high thermal stability, and satisfactory electrochemical performance achieved from each modification employed on the parent (Mn_3O_4) material towards formulating the spinel $CuMn_2O_4$/MWCNT hybrid composite electrode material.

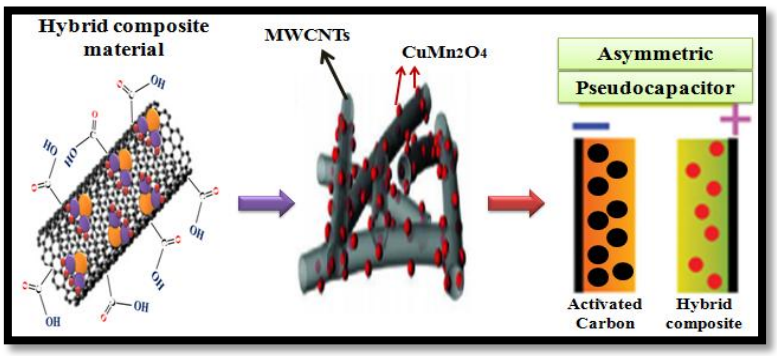

Figure 2.15: Two and three-dimensional illustrations of the hybrid composite material and its application in pseudocapacitors [104-105].

2.3.4 Summary

In order to realize the full potential impact factor of composite electrode materials in supercapacitor applications, a good understanding of material chemistry and elementary capacitor concepts is required. The main incentive is to improve the energy density capabilities of supercapacitors through employing material property modification. However, having the suitable electrode material also requires the suitable electrode configuration. In this work, an asymmetric pseudocapacitor electrode configuration, used as the testing device, delivered optimal performance results. This electrode system also provides improved thermal and structural stability during charge/discharge cycles. The combination of $CuMn_2O_4$/MWCNT and activated carbon as positive and negative materials for this device displayed enhanced performance compared to $CuMn_2O_4$/rGO reported in literature. However, the composite material integrating rGO@MWCNTs with $CuMn_2O_4$ is yet to be extensively researched in supercapacitor applications. To reduce the quantity level of electrode material used during fabrication, smaller electrode configurations such as coin cells are an ideal implementation. However, this limits its use to small-scale applications. Copper is one of many transition metals such as Ni, Zn, V, Cr, and Fe, which are suitable implementations for this research study.

CHAPTER 3

Chapter Overview

Chapter 3 commences by recapitulating the miscellaneous reagents used in the laboratory design and fabrication of the pristine (Mn_3O_4), and spinel-type binary ($CuMn_2O_4$) transition metal oxide electrode materials. This also includes the reagents used to synthesize the modified hybrid spinel-type binary metal oxide material incorporated with functionalized multi-walled carbon nanotubes ($CuMn_2O_4$/MWCNT). This chapter additionally presents a detailed discussion on the synthetic procedures used during the synthesis of the pristine and newly modified electrode materials. In relation to the synthetic procedures, the methodology used during the fabrication process of the electrode with the active electrode material, as well as the construction process of the supercapacitor cell device (Swagelok), is additionally included in this chapter. Finally presented in this chapter, is a brief description on all the characterization techniques used to analyze the electrode materials.

3.0 Experimental Section

3.1 List of chemical reagents used

All chemicals used in the synthetic procedures include: potassium permanganate ($KMnO_4$, ACS reagent grade, ≥ 99.0%), diethylene glycol ($C_4H_{10}O_3$, ≥ 99.0%), ethanol (CH_3CH_2OH, absolute grade, ≥ 99.8%), copper(II) nitrate trihydrate ($Cu(NO_3)_2$. $3H_2O$, purity 99%), manganese(II) nitrate tetrahydrate ($Mn(NO_3)_2$. $4H_2O$, purity 99%), dilute nitric acid (55%, HNO_3), citric acid monohydrate ($C_6H_8O_7.H_2O$, purity 99.5%), ammonium hydroxide (25%, NH_4OH), multi-walled carbon nanotubes (MWCNTs, purity degree > 95%), sulphuric acid (98%, H_2SO_4), nitric acid (65%, HNO_3), polyvinylpyrrolidone (PVP, average mol wt 40,000), hydrazine hydrate (N_2H_4. H_2O, reagent grade, N_2H_4 50-60%), carbon black (CB), polyvinylidene fluoride (PVDF), N-methyl-2-pyrollidone (NMP, anhydrous, 99.5%),

activated carbon (AC), potassium hydroxide (KOH, 85%), and lithium hydroxide (LiOH, reagent grade powder, 98%). These chemicals were all purchased from Sigma Aldrich and used without further purification. In addition, the nickel foam substrate sheets were purchased from MTI corp.

3.2 Synthetic Procedures

3.2.1 Synthesis of the pristine manganese oxide (Mn_3O_4) electrode material

This pristine electrode material was fabricated using a temperature controlled hydrothermal heating method, which is commonly used for the synthesis of crystalline phased materials. In this typical synthetic procedure, 1.50 g of $KMnO_4$ was initially dispersed in 50 mL of ultra-pure water. The suspension was additionally stirred and subjected to ultrasonic treatment for 30 min respectively. This step was done to ensure uniform dispersion of the $KMnO_4$ metal precursor with the water solvent. Subsequently, 10 mL of diethylene glycol was added to the above solution mixture, in addition to repeating the stirring and ultrasonic treatment step. Upon commencement of the hydrothermal heating process, the resulting suspension was carefully transferred into a 100 mL stainless steel hydrothermal autoclave reactor. This device was tightly sealed and placed in a silicon oil bath, where the oil was heated on a hotplate at 180 ℃ for 12 h. Thereafter, the reactor vessel was allowed to cool down naturally to room temperature, followed by filtration of the reactor contents via centrifugation and washing via ethanol and distilled water. The obtained solid product appeared to have a brown-red coloration, after it was dried in a vacuum oven at 60 ℃ overnight [106-107].

The purpose of adding diethylene glycol was to stabilize the Mn_3O_4 nanoparticles, thus preventing the occurrence of nanoparticle agglomeration. It also acted as a protecting agent to ensure the preservation of the transition metal based nanostructures. It is well known that out of all the most common oxidation states for manganese (which are Mn^{+2}, Mn^{+3}, Mn^{+4}, Mn^{+6}, and Mn^{+7}), Mn^{+2} is the most stable one from the list. Therefore, compounds containing manganese ions with an oxidation state of 2+ would possess impressive oxidative properties.

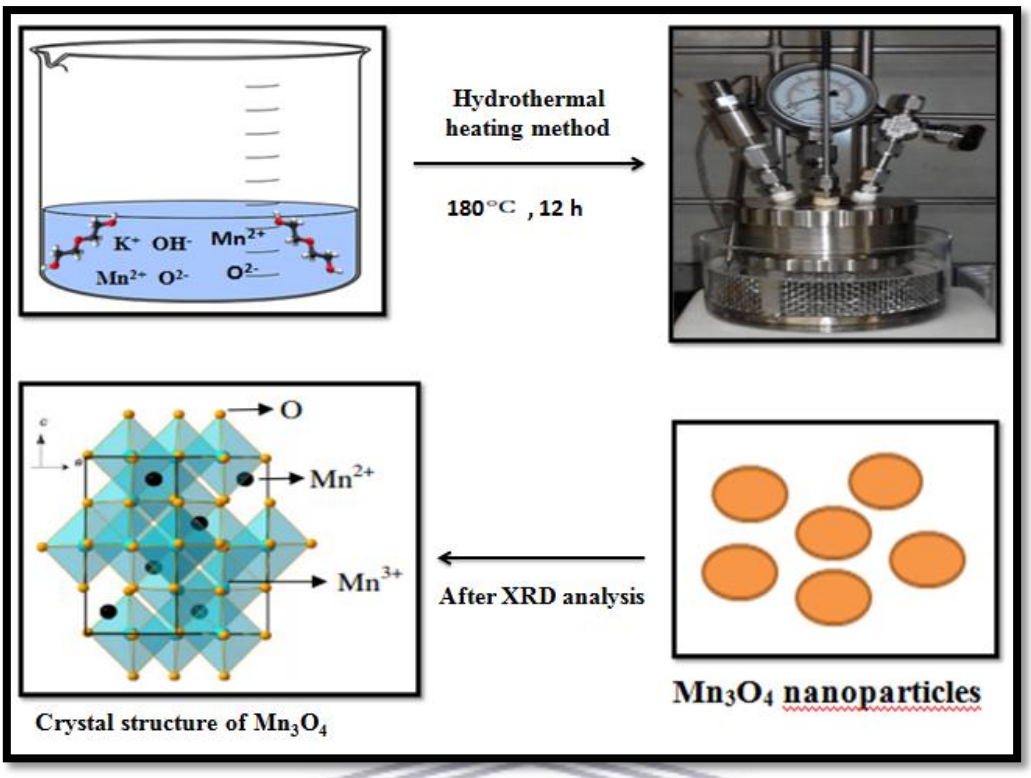

Scheme 3.1: Schematic diagram illustrating the synthetic procedure for Mn_3O_4 nanoparticles [106-107].

3.2.2 Synthesis of the spinel copper manganese oxide ($CuMn_2O_4$) electrode material

The spinel electrode material was similarly synthesized via the hydrothermal method under ambient conditions. Initially in this synthetic procedure, 1.55 g of $Cu(NO_3)_2.\ 3H_2O$ was dissolved in 6 ml of dilute HNO_3. This was followed by the addition of 2.5 g of $Mn(NO_3)_2.\ 4H_2O$, 0.67 g of $C_6H_8O_7.H_2O$, and 40 ml of ultra-pure water. The mixing process was done in a round bottom flask under continuous magnetic stirring for 30 min at room temperature. Thereafter, the pH of the solution mixture was converted from acidic to basic (pH of 8/9) via drop wise addition of NH_4OH to the solution contents. After reaching the desired pH, the solution mixture was magnetically stirred for another 30 min at room temperature. During the heating process, initially the obtained homogeneous solution was cautiously transferred into a 100 mL stainless steel autoclave vessel under autogeneous pressure. Secondly, the reactor

vessel was heated and maintained at a temperature of 180 °C for 12 h. After heating, the resulting precipitate was then collected by means of centrifugation and washed several times with deionised water and ethanol. Thereafter, it was dried at 60 °C in a vacuum oven overnight. The recovered product was finally annealed in a muffle furnace at 400 °C for 4 h in air (ramped at 15 °C/min) to obtain the $CuMn_2O_4$ spinel nanoparticles [108-109].

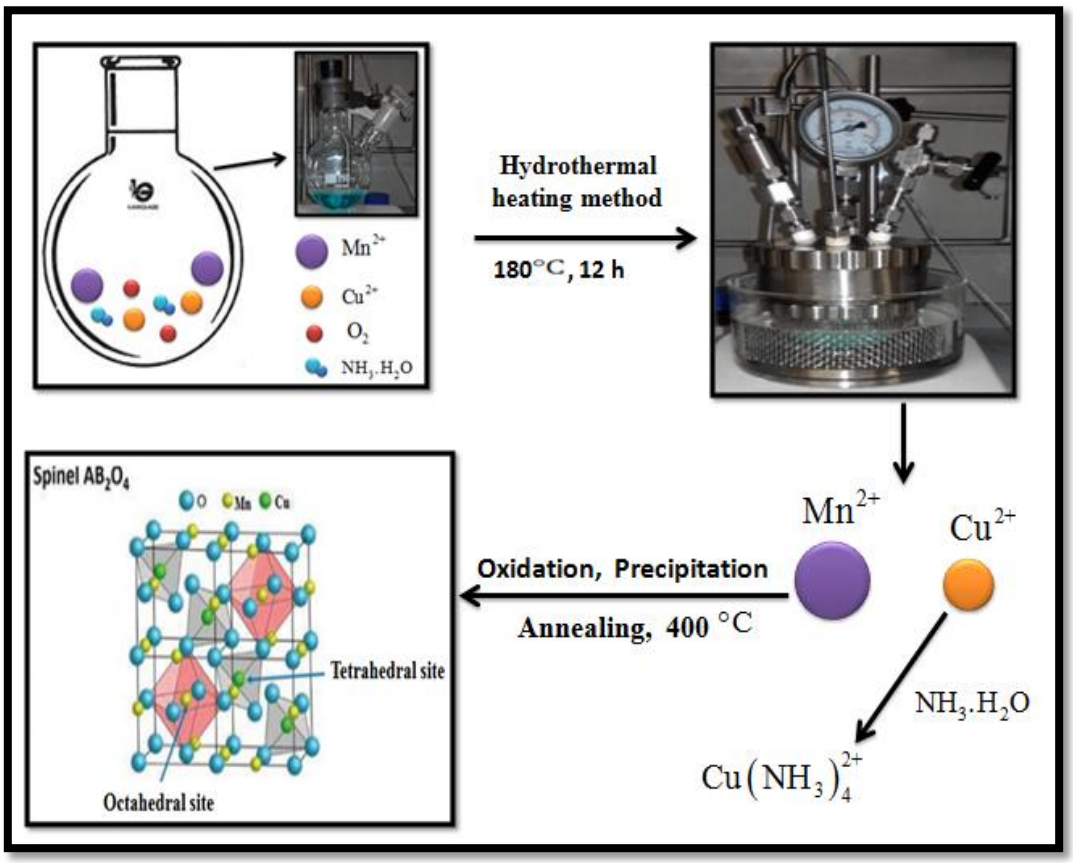

Scheme 3.2: Schematic diagram illustrating the synthetic procedure for $CuMn_2O_4$ nanoparticles [108-109].

3.2.3 Acid pre-treatment process for the functionalization of MWCNTs

The oxidation process of the MWCNTs was done as follows. Firstly, 5 mg of raw MWCNTs was added to a 10 mL acid mixture of 3:1 concentration of sulphuric acid (98%) and concentrated nitric acid (65%). The actual volumes of the acids were 7.5 mL for H_2SO_4 and 2.5 mL for HNO_3. The acid mixture containing the MWCNTs was then sonicated in a DC 200 Hz ultra-sonicator for 3 h. The purpose of the acid pre-treatment process was to purify the MWCNTs by removing the amorphous carbon and most of the catalyst particles. An additional purpose was also to shorten the MWCNTs, in order to generate oxygenated groups such as carboxylic acid groups at the ends for providing detection sites on the MWCNT surfaces. After ultra-sonication, the reaction mixture was then diluted with 100 mL of deionised water. The resulting suspension was lastly filtered and washed 10 times with deionised water, where it was then left to stand and dry overnight in order to form the oxidized MWCNTs [110, 150].

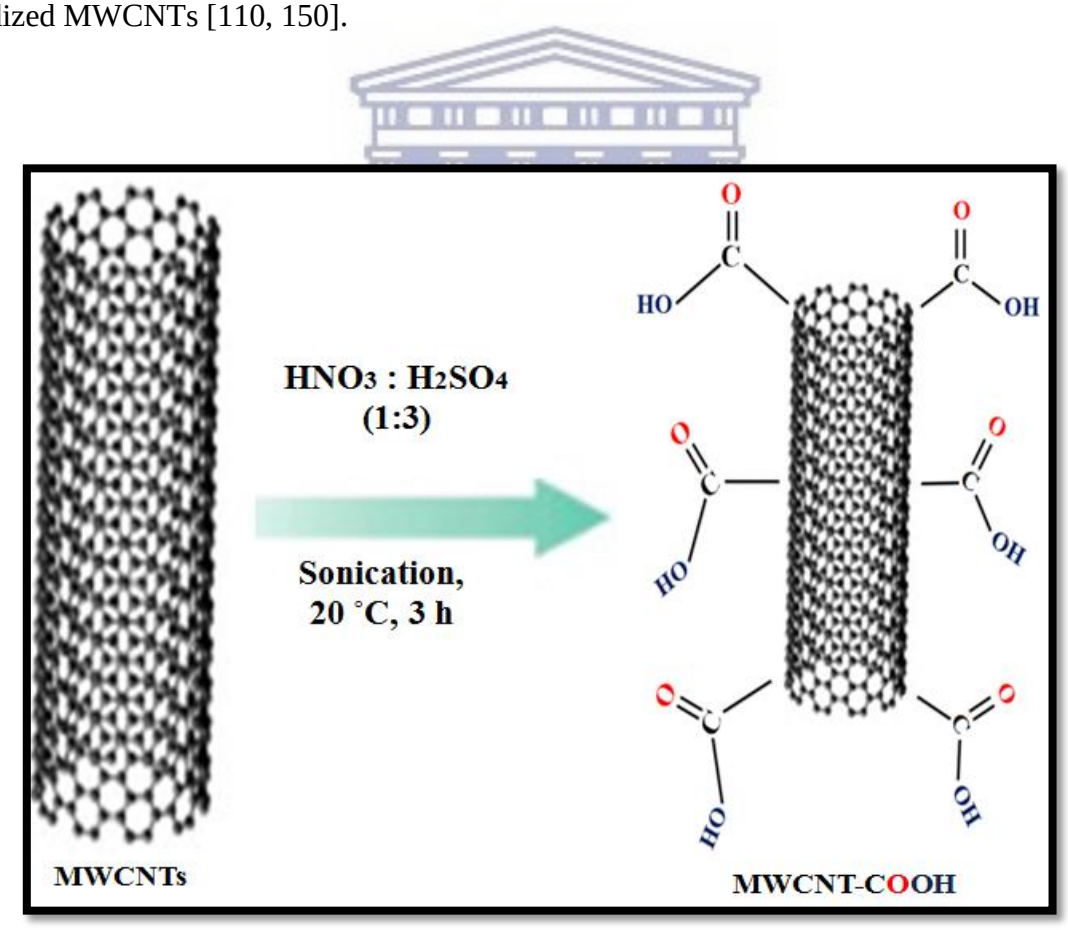

Scheme 3.3: Schematic diagram illustrating the acid pre-treatment process for functionalized MWCNTs [110].

3.2.4 Synthesis of the final hybrid ($CuMn_2O_4$/MWCNT) nanocomposite electrode material

The final hybrid material was synthesized via a high temperature and low-pressure reflux heating method. Firstly, 100 mg of acid treated MWCNTs were uniformly dispersed in 60 mL of diethylene glycol, upon the assistance of ultrasonication for 1 h. This mixture was labelled as solution A. Separately, solution B was obtained by dissolving 1.55 g of $Cu(NO_3)_2.3H_2O$, 2.5 g of $Mn(NO_3)_2.4H_2O$, and 0.4 g of PVP in 40 mL of ultra-pure water under magnetic stirring for 30 min. Solution B was then subsequently added to solution A and while stirring, the pH value of the mixture was adjusted to pH 8 via drop wise addition of a 10 mL $N_2H_4.H_2O$ solution. Once the desired pH value was reached, the solution mixture was attentively transferred into a clean round bottom flask, where thereafter the flask was connected to a reflux system for heating. The solution mixture was then heated to 180 ℃ and maintained at that temperature for 4 h. After refluxing, the resulting suspension was allowed to cool down to room temperature. The light black precipitate was then collected via centrifugation and washed several times with deionised water and ethanol. Thereafter, it was dried at 60 ℃ in a vacuum oven overnight, and finally annealed in a muffle furnace at 500 ℃ for 5 h in air (ramped at 17 ℃/min) to obtain the hybrid $CuMn_2O_4$/MWCNT nanoparticles.

The PVP polymer reagent was additionally added to the metal precursors as a stabilizing agent in order to ensure successful modification of the MWCNT surface with the spinel $CuMn_2O_4$ nanoparticles. The use of diethylene glycol as a solvent was also intended to provide additional support for the decoration of MWCNTs with $CuMn_2O_4$ nanoparticles.

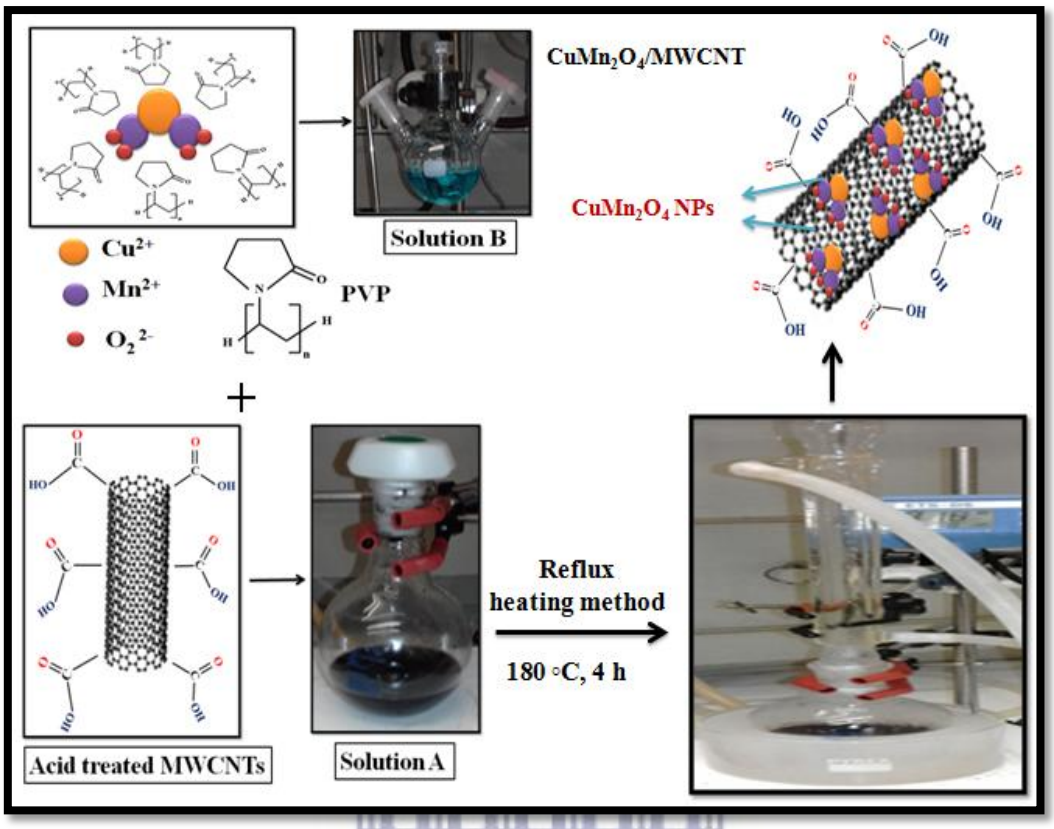

Scheme 3.4: Schematic diagram illustrating synthetic procedure for the hybrid $CuMn_2O_4$/MWCNT composite.

3.2.5 Preparation of electrochemical cells for material performance testing

The electrochemical analyses were conducted using a Bio-Logic VMP 300 potentiostat/galvanostat instrument, integrated with an EC-Lab software for data analysis and processing. The electrochemical cells that were configured for testing was a half cell (three-electrode system) and a full cell (two-electrode system). The half cell consisted of the working electrode (active material coated onto a nickel foam substrate), the reference electrode (Ag/AgCl in 3M KCl), and the counter electrode (platinum wire). The full cell configuration was assembled in a Swagelok device as an asymmetric cell configuration. This cell consisted of a paper separator, soaked in electrolyte solution, which is then sandwiched between the positive (active material) and negative (activated carbon) electrodes [75].

3.2.5.1 Electrode preparation for half cell (three-electrode) configuration

The pristine Mn_3O_4, spinel $CuMn_2O_4$, and hybrid $CuMn_2O_4$/MWCNT working electrodes were prepared firstly by mixing the active materials with carbon black (CB) and polyvinylidene fluoride (PVDF) in a mass ratio of 70:20:10, respectively. The powdered mixture was then converted into a homogeneous slurry paste using anhydrous N-methyl-2-pyrrolidine (NMP) as the solvent. Thereafter, the resulting paste was coated on a nickel foam (1cm x 0.5 cm) substrate current collector, utilizing a spatula to flatten out the grooves of the nickel foam surface for allowing a uniform dispersion. The as prepared electrode was then finally dried in a vacuum oven at 60 ℃ for 10 h to remove nonreactive solvent residues. The electrolytes used for this electrode system was 3M KOH and 3M LiOH, upon which the best performing electrolyte was used for the two-electrode system [75].

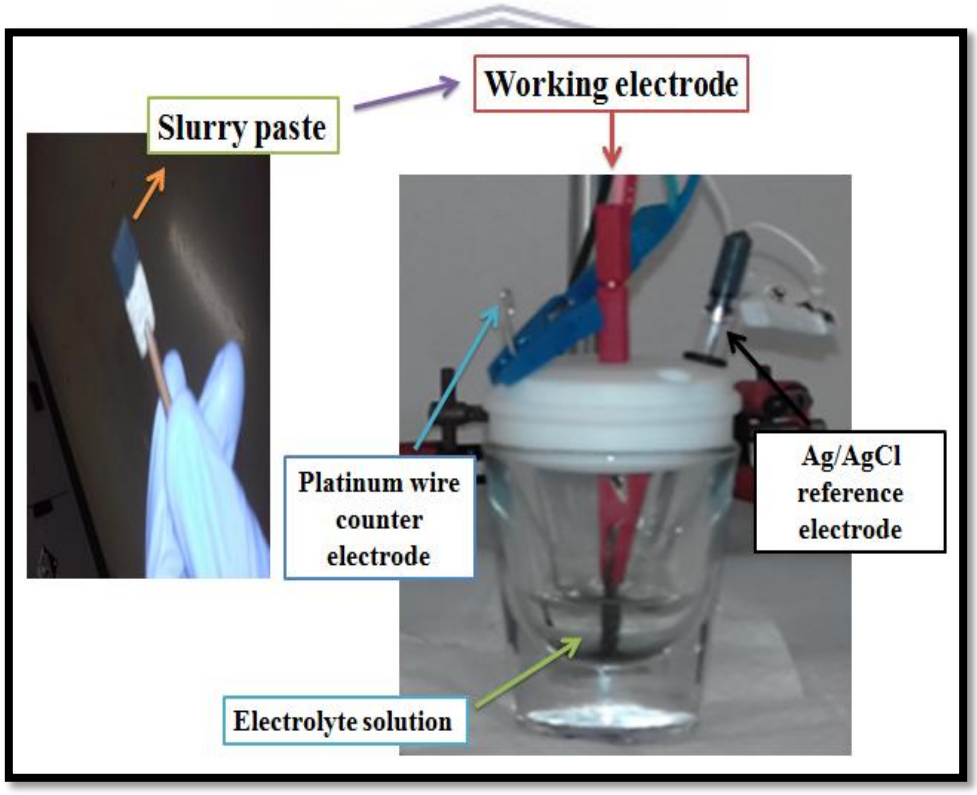

Figure 3.1: Diagram illustrating the half cell (three-electrode) configuration.

3.2.5.2 Electrode preparation for the full cell (two-electrode) configuration

The nickel foam substrates were initially cut into 20 mm diameter discs (3.14 cm^2) and then coated with the prepared slurry paste. The positive electrode contained a paste made up of 70 wt% active electrode material, 20 wt% carbon black (CB), and 10 wt% polyvinylidene fluoride (PVDF) with anhydrous N-methyl-2-pyrrolidone (NMP) as the solvent [75]. The slurry paste for the negative electrode contained a similar mixture with, instead, activated carbon used as the active material. The electrochemical cell was then finally assembled with the Swagelok device and left to stand for 24 h prior to conducting performance tests. The best-suited electrolyte used for this electrode system was 3M LiOH.

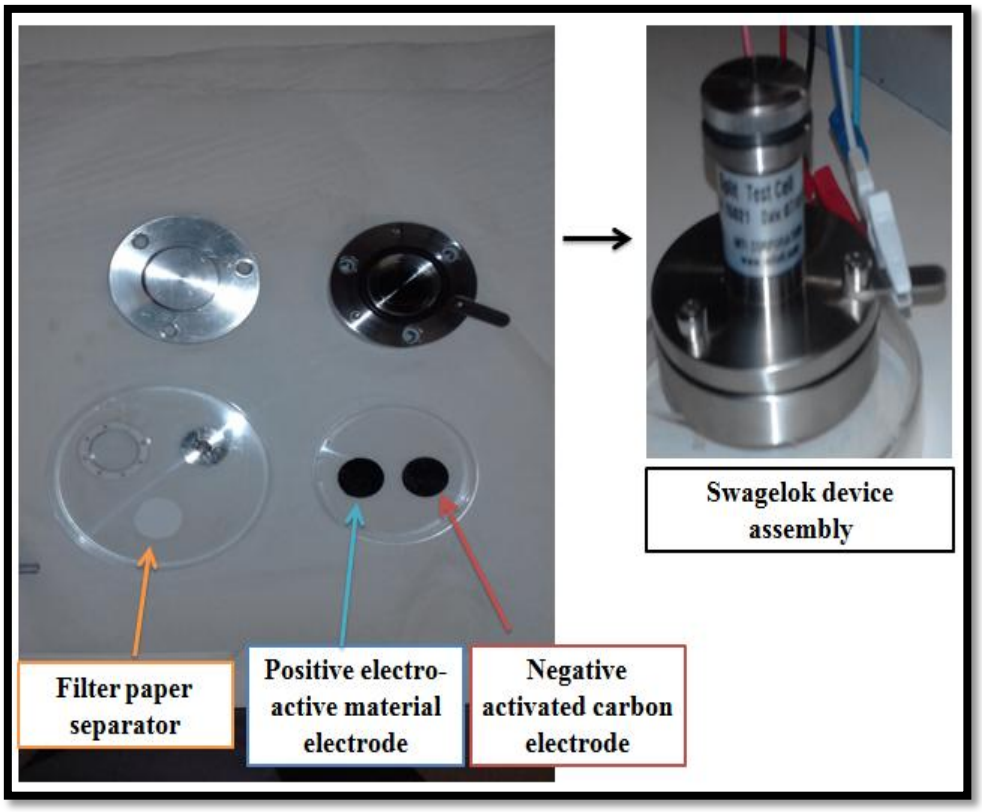

Figure 3.2: Diagram illustrating the full cell (two-electrode) configuration.

3.3 Electrode material characterisation techniques used

The crystallographic structural and morphological studies of the pristine, spinel, and hybrid electrode materials were systematically investigated by employing scanning electron microscopic (SEM), high-resolution transmission electron microscopic (HR-TEM), and X-ray diffraction (XRD) analysis. The high-resolution transmission electron microscope instrument was equipped with an energy-dispersive X-ray spectroscope (EDS) for elemental composition and mapping analysis. The functional group detection and particle size distribution measurements were additionally performed by conducting Fourier transform-infrared (FT-IR) spectroscopic and small-angle X-ray scattering (SAXS) analysis. Bond vibration analysis and thermal stability testing of the synthesized electrode materials were also performed using Raman spectroscopic and thermo-gravimetric analysis (TGA) techniques. Lastly, the electrochemical performance and properties of the active electrode materials were studied through conducting cyclic voltammetric (CV), electrochemical impedance spectroscopic (EIS), and galvanostatic charge-discharge (GCD) analysis.

3.3.1 Structural, morphological, and spectroscopic characterisation techniques

3.3.1.1 Crystal structure and crystallite size determination by X-ray diffraction (XRD) analysis

The X-ray diffraction technique is predominately used for diagnosing the structure of crystal lattices within a powdered or thin film material. The technique was performed using a focused D8 advanced diffractometer purchased from Bruker AXS. This machine is equipped with an evacuated copper K-alpha radiation X-ray tube, operated at 40 kV and 40 mA. The X-ray tube functions similarly to that of a cathode ray tube. The X-rays are produced inside the tube when an applied current heats up a tungsten filament, thus liberating electrons that are additionally accelerated by a high voltage towards a copper target. This copper target, thereafter, emits copper X-rays through a beryllium X-ray window (for maximum X-ray flux transmission). The X-rays then exit the tube and are incident on the sample from which they are diffracted into a scintillating type detector. The diffracted X-ray beam passes through a slit, which determines the angular width of the beam, and a nickel filter, for removing the K-

alpha energy, before reaching the detector. During an X-ray scan, the detector is rotated over a range of 2θ- angles, in this case a range of $10° - 90°$ was used, to detect diffracted X-ray bands produced by the precisely aligned crystal lattices within the sample.

The powdered electrode materials, at the nano-scale, consist of numerous crystal lattices located at random angles. It is, therefore, essential for the crystals to be correctly oriented in order for the X-ray beam, crystals, and detector to satisfy Bragg's Law. This implies that the scattered X-rays must be in-phase with the incident X-rays for constructive interference to occur, which in turn obeys the conditions of Bragg's Law.

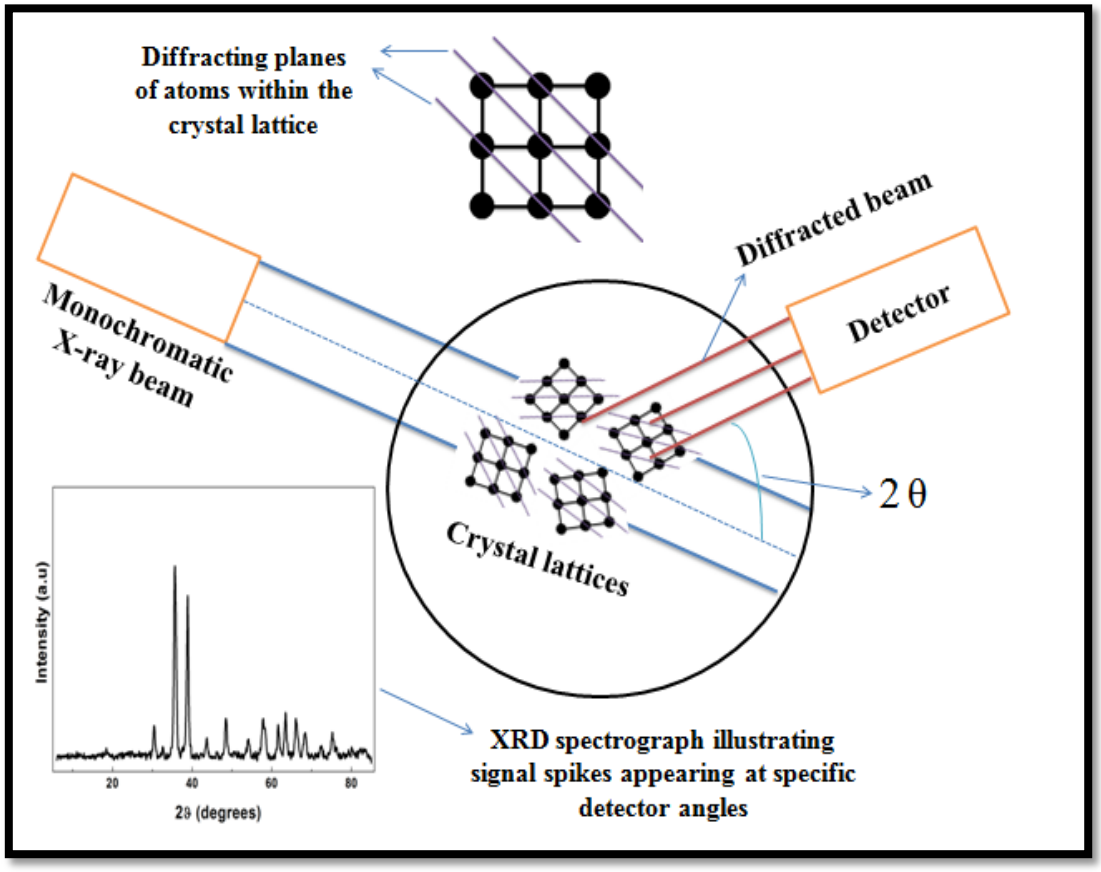

Scheme 3.5: Schematic diagram illustrating the generic principle of X-ray diffraction [112].

In 1912, a German physicist by the name of Max von Laue displayed that X-rays could be diffracted by crystal lattices within crystalline type materials. This work awarded von Laue the Nobel Prize in Physics during the year 1914. In 1912 – 1913, Henry Bragg (a British physicist) built an X-ray spectrometer in order to continue his research on the properties of X-rays. Lawrence Bragg, son of Henry Bragg, was interested in X-ray diffraction and began to examine X-ray patterns generated by various crystalline materials. From his analysis, he discovered a simplified and ingenious way to solve Laue's diffraction problem and formulated the famous Bragg's Law. Lawrence Bragg was only 22 years of age when he made this discovery as a research student at Cambridge University.

The derivation of Bragg's Law is initially done by considering the conditions required to ensure that the incident and scattered X-rays are in-phase with one another. It is schematically shown below that when the first ray hits the top atomic plane at atom Z, the second ray continues to the next atomic plane and is scattered by atom B. This results in the second beam having to travel an extra distance $(AB+BC)$, in order for the two reflecting beams to be in-phase with one another. Therefore, if this extra distance is equivalent to an integer (n) multiple of the wavelength (λ), then constructive interference will occur.

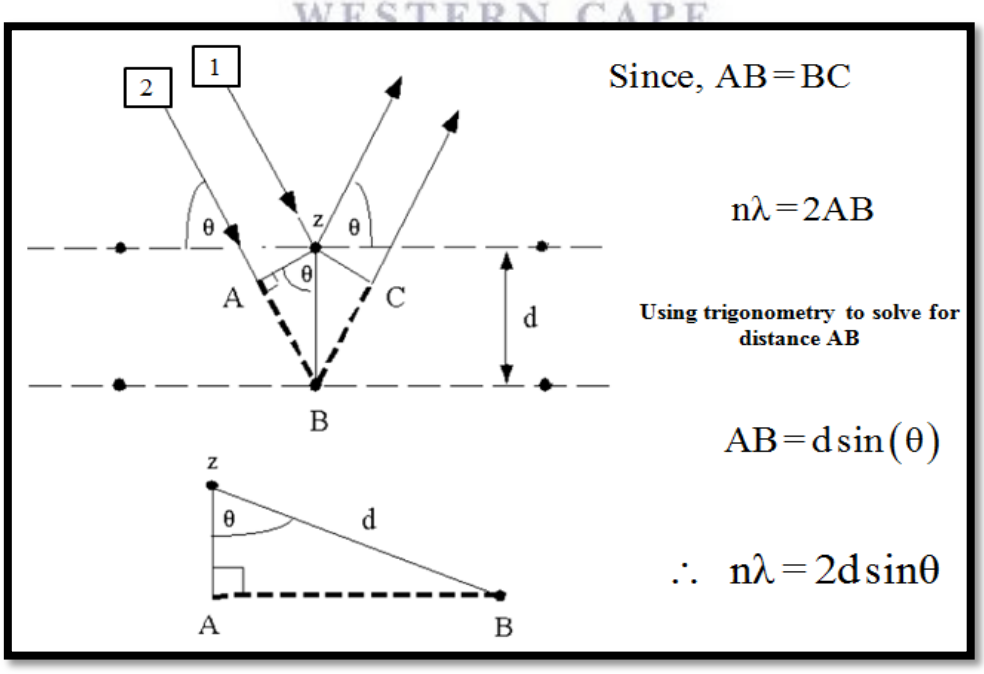

Scheme 3.6: Derivation of Bragg's Law [113].

3.3.1.2 Morphological characterisation by SEM and HR-TEM techniques

3.3.1.2.1 Scanning Electron Microscopy

The scanning electron microscope (SEM) utilizes a focused electron beam to scan the surface morphology of a material in order to generate a photographic image of the analyzed specimen [114]. The main components of which the microscope is constructed of include an electron gun (as electron source), electromagnetic lenses, apertures, and detectors. In **Fig. 3.3** below, it illustrates that the electron beam passes through a condenser lens, objective lens, and scan coil before reaching the surface of the specimen. These components are responsible for controlling the intensity of the electron beam, concentrating the beam into a focused fine probe, and scanning the electrons over the x-y plane of the specimen. The incident electron beam interacts with the surface atoms of the specimen by penetrating it into a region known as the interaction volume. Various interactions occur within this region of the specimen and depending on how far the electron beam penetrates into the region, will result in the energy magnitude of the emitted electrons. The low energy electrons are emitted as secondary electrons, where as the high energy electrons are emitted as backscattered electrons [115-116]. The secondary electrons are detected by the secondary detector, which provides informational data describing the surface topography of the specimen. Similarly, the backscatter detector detects the backscattered electrons; however, elemental composition data is obtained.

The elemental composition analysis is performed with an energy dispersive spectrometer (EDS) detection system, which is incorporated into many scanning electron microscopes [117]. In this research study, the microscope used to employ SEM analysis was a ZEISS ULTRA scanning electron microscope. This type of microscope is equipped with a field emission electron beam source and is capable of obtaining a 1-nanometre SEM imaging resolution. The sample preparation procedure involved it initially being deposited onto a carbon support, and then placed inside a sputter coater for the coating of a gold-palladium alloy onto the material surface. The coating process was initiated to ensure that the material was conductive for electron absorption during analysis.

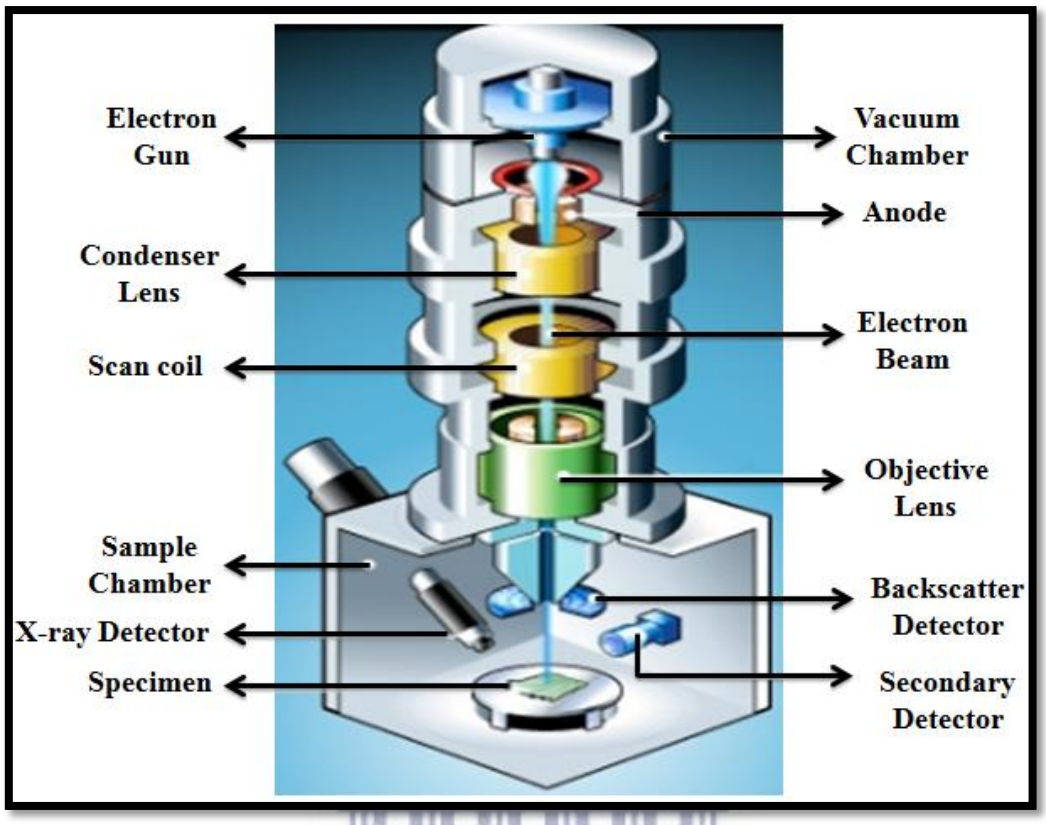

Figure 3.3: Diagram illustrating the basic operating components of the SEM instrument [118].

3.3.1.2.2 High-Resolution Transmission Electron Microscopy

HR-TEM analysis is a famous microscopic characterisation technique used to image the crystalline nature, nanotube morphology, and elemental composition of the interested material specimen. The basic operation of the HR-TEM instrument, much like the SEM instrument, begins with an electron source generating an electron beam, which passes through a series of electromagnetic lenses that condense the beam before it interacts with the material specimen. The beam's interaction with the specimen transmits scattered electrons to a detector system that displays a two-dimensional projection of the specimen onto a fluorescent screen or digital camera. Selected area electron diffraction (SAED) and energy dispersive X-ray spectroscopy (EDS) data can also be obtained from HR-TEM analysis. The SAED image displays a reflection that is indicative of the crystalline make-up of a specific scanned area of the specimen. These reflections are imaged as vertical coloumns of dots that can be indexed,

much like in XRD analysis, to represent the atomic planes within the crystalline structure of the specimen.

The HR-TEM instrument allows scientists to view materials at the atomic scale, thus providing photographic evidence of atomic lattice planes and additional nanostructures present within the analyzed material. The instrument also operates at a higher accelerating voltage (normally at 180 kV or greater), thus generating a denser electron beam containing more electrons to produce more data and images with high quality spatial resolutions as compared to the SEM instrument. Atomic defects, such as linear defects (irregular groups of atoms) and planar defects (grain boundaries), can also be detected from HR-TEM analysis. Despite its advantages, it also tends to manipulate the mechanical properties of the material's crystal structure by increasing the number of dislocations (distorted crystal lattice planes) per unit volume. This manipulation, however, does yields a higher hardness and tensile strength for the metals present within the material's crystal structure, which could be a useful technique in the development of strong crystalline materials.

EDS results were reported from HR-TEM analysis as more data points were collected in order to provide a complete spectrum of the material's elemental composition. The sample preparation procedure involved initially dissolving the synthesized material in a solvent, preferably ethanol, then drop casting it on a copper-nickel grid. The grid was dried under a lamp to evaporate the solvent before the commencement of analysis. In this research study, high-resolution transmission electron microscopic images were obtained from a Tecnai G^2F_2O X-Twin MAT 200 kV field emission HR-TEM instrument [114, 116].

3.3.1.2.3 Energy Dispersive X-ray Spectroscopy (EDS)

Energy dispersive X-ray spectroscopy (EDS, EDX, or XEDS) is an analytical tool generally used for elemental compositional mapping, which involves the generation of a spectrograph illustrating elemental data of a given sample [119]. The EDS technique can not only measure relative elemental composition, but also the distribution of atoms present within the analyzed sample, which can then be mapped on an energy spectrograph [120]. EDS systems are generally integrated into SEM and HR-TEM instruments and for this research work, EDS analysis was performed using the HR-TEM instrument to acquire a more accurate elemental composition interpretation spectra for each of the synthesized powdered electrode materials [121]. During EDS analysis, the sample is initially bombarded with electrons from a high-energy focused electron beam, thus causing the sample to be excited and emit X-rays, as illustrated in **Scheme 3.7(a)** [122]. These individual X-rays are detected by the X-ray detector and then converted into corresponding electrical potentials [123]. The signals produced at specific binding energies, in other words potentials (measured in keV), are indicative to the elements of which the analyzed sample is constructed [124].

The schematic diagram represented in **Scheme 3.7(b)**, illustrates how a focused electron beam can cause X-ray emission from a sodium atomic nucleus surrounded by electrons in its inner and outer most electron shells [125]. When the incident electron beam strikes the atom within the specimen, it then excites an electron in the inner most electron shell, thus vacating it from the shell (as a secondary electron), and causing an electron hole to be left behind in its original position [62]. At this state, the atomic nucleus is highly unstable; therefore, an electron from a higher-energy level will then descend to fill the electron hole in the lower-energy level [126]. The change in energy between the higher and lower-energy level is emitted in the form of an X-ray, which is then measured and projected on an EDS spectrograph [127]. The quantity of energy emitted from the electron is equally dependent on the energy difference between the shells as it is on the atomic structure of the element. As illustrated in **Scheme 3.7(c)**, the nomenclature of the electron shells starts with the inner most shell denoted as K, followed by L, M, N, O, P, and Q [128]. EDS analysis is predominately concerned with the K, L, M, and N shells of the investigated element. It is schematically shown below that if electrons descend in energy to fill a vacant electron hole from the nearest electron shell of the atomic nucleus, then it is denoted as an alpha signal (K_α, L_α, and M_α)

[129]. However, if the electrons come from a shell that is two shells away from the atomic nucleus, then it is known as a beta signal (K_β, L_β, and M_β) [129]. It should be noted that the electrons residing in the shell furthest away from the atomic nucleus, possess the lowest ionisation energy [130]. Therefore, it would require a large amount of energy to remove an electron from the K-shell of the atomic structure. The quantity of energy required to remove electrons from specific shells of certain elements, presented on the periodic table, have been obtained through extensive research [131]. These references can be used when identifying characteristic elemental signals from the obtained EDS spectrograph.

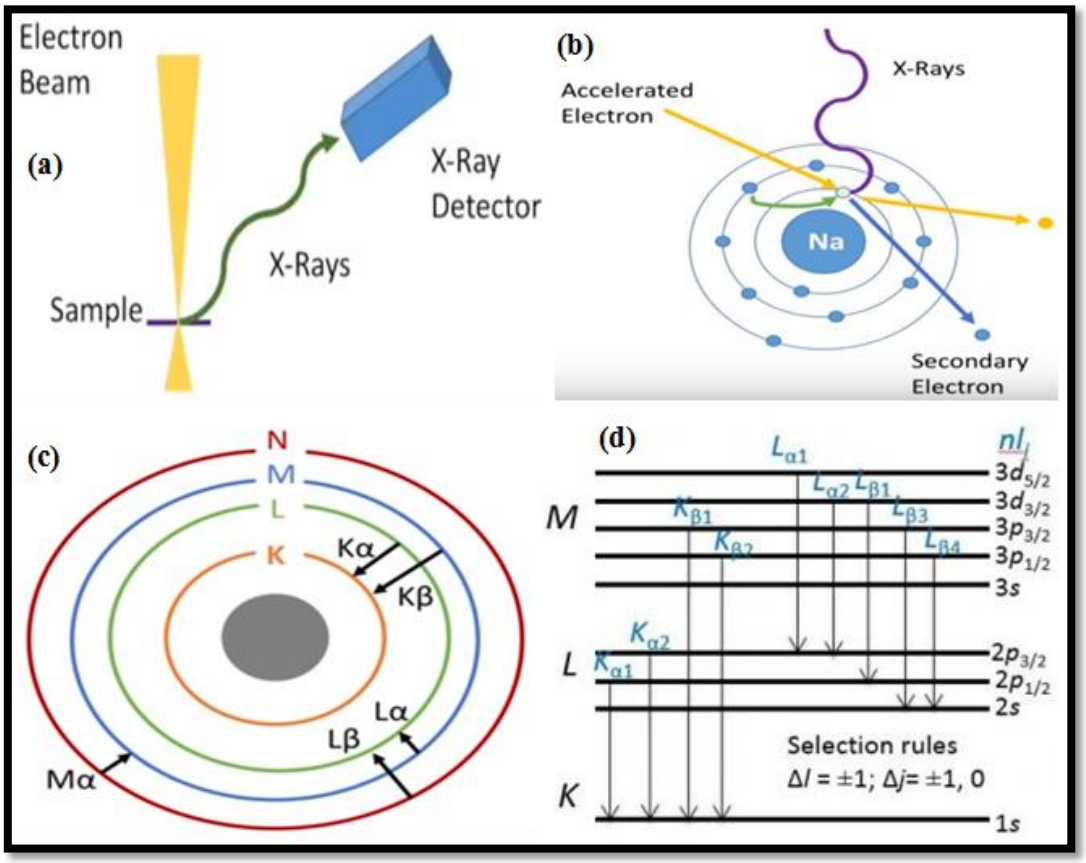

Scheme 3.7: Schematic diagram representing various operating principles of EDS [132].

3.3.1.2.4 Fourier Transform-Infrared Spectroscopy (FT-IR)

FT-IR spectroscopy is a resourceful technique that allows researchers to obtain information concerning the stretching and bending vibrations of molecular bonds of functional groups present within the investigated solid, liquid, or gas sample. The FT-IR spectroscopy technique initially involves irradiating the sample with polychromatic infrared electromagnetic radiation, which is then partially absorbed by the sample during analysis. The FT-IR spectrum generated from the data of the transmitted infrared radiation is utilized to identify specific structural units that make up the studied sample material. During FT-IR analysis, as the sample absorbs the exciting electromagnetic radiation, it causes the molecular bonds of the sample to vibrate in a specific motion/mode. **Fig. 3.4** displays the various vibration modes, which molecular bonds could experience. It is additionally important to note that only specific wavelengths of exciting radiation is required to initiate each of the displayed vibrations. This discussion is better understood by comparing the FT-IR spectrum of the exciting IR radiation to that of the transmitted IR radiation. The observation made from these two spectra is that on the transmitted spectrum, the intensity of the IR radiation at certain wavelengths or wave numbers significantly drop due to the absorbed IR radiation by the sample, thus causing the occurrence of specific bond-vibrations.

The Fourier transform infrared spectrometer is composed of unique system components namely a radiation source, a beam splitter, two mirrors (static mirror and moving mirror), and a photodetector. In majority of FT-IR spectrometer configurations, the sample is generally placed in front of the detector. The operating principles of the instrument include the following: firstly infrared radiation is emitted from the source to the beam splitter (partially transparent mirror), where some of the radiation is transmitted through the splitter and the rest is reflected. The transmitted and reflected beams are then reflected back towards the splitter by the fixed and moving mirrors, where both beams are split again causing the partially reflected radiation beams to recombine into a single beam that is transmitted through the sample into the detector. Initially, both mirrors are positioned at an equal distance from the splitter, thus causing the two beams reaching the detector to be in-phase with one another. This is known as constructive interference and at this point, the radiation reaching the detector possesses the highest intensity. However, the radiation intensity suddenly drops if one of the mirrors is moved a short distance away from the detector. This is a result of the

two recombined radiation beams at the detector not being in-phase with one another, and therefore cancelling each other out. Alternatively, this phenomenon is known as destructive interference. Therefore, in order to conduct the desired FT-IR experimental measurements, the mirrors must be positioned in a way that will promote the occurrence of constructive interference and generate an interferogram, which measures the intensity of the radiation that reaches the detector. Finally, this interferogram is then converted into a spectrum through a mathematical theorem known as the Fourier transform.

$$F(s)=\int_{-\infty}^{\infty} f(x)e^{-i2\pi sx}\,dx \tag{3.1}$$

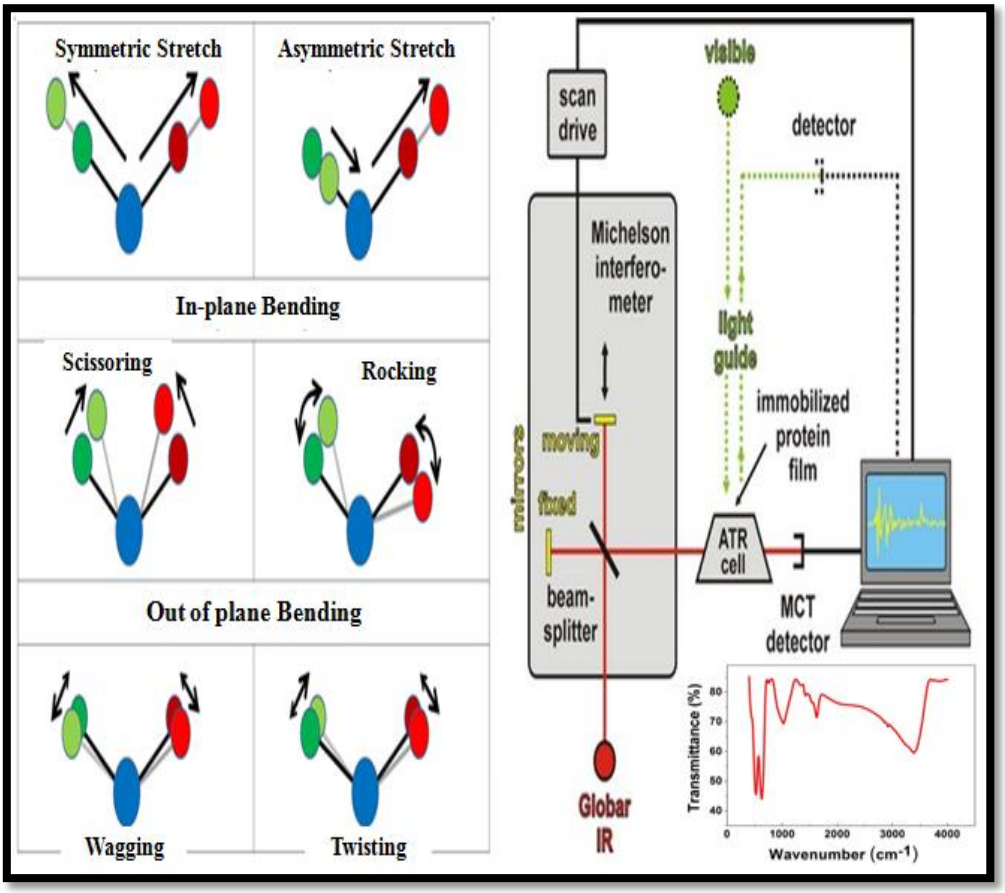

Figure 3.4: Illustrating modes of bond vibration and the operating principles involved in FT-IR spectroscopy [133].

3.3.1.2.5 Raman Spectroscopy

The Raman spectroscopic technique was firstly developed by an Indian scientist named C.V. Raman in 1928. In 1930, C.V. Raman was awarded the Nobel Prize in Physics for the famous technique, which is also occasionally known as the Raman Effect. Although the technique was developed over 80 years ago, it still required advanced technological and scientific developments over time for the technique to really blossom in the field of scientific research and development. The one critical and central development that is ultimately linked with the Raman spectroscopic technique is the laser that was built in 1960 by Theodore H. Maiman, based on theoretical work done by Charles Hard Townes and Arthur Leonard Schawlow. In other known branches of spectroscopic techniques such as FT-IR, UV-Visible, NMR, and etc, the absorption of radiation by the sample is studied where the molecules within the sample gets excited and undergoes a transition from a lower to a higher energy level. However, in Raman spectroscopy the scattering of the radiation from the sample is analysed and studied to observe the vibrational and rotational modes exhibited by the molecular structure of the sample.

The principle of this scattering phenomenon entails when monochromatic light, such as the laser radiation, is subjected onto the sample, where most of the radiation is transmitted through the sample, while some of the radiation is scattered at an angle 90° to that of the incident radiation. The two different types of scattering observed in Raman spectroscopy is generally known as Elastic and Inelastic scattering. Elastic scattering, also known in scientific language as Rayleigh scattering, is perceived when the scattered radiation has the same frequency as that of the incident radiation ($\nu_i = \nu_s$), thus implying that there is no net change in the energy of the radiation after the scattering occurrence. The most important type of scattering, which is predominately analysed in Raman spectroscopy, is the Inelastic scattering (scientifically known as Raman scattering). Inelastic scattering is perceived when there is a change in the frequency (approximately 1%) of the radiation after the scattering ($\nu_i \neq \nu_s$). Raman scattering is additionally categorized into two types. One where the scattering radiation has a lower frequency as compared to that of the incident radiation ($\nu_i > \nu_s$) and the peaks observed on the spectrum are called Stokes lines, thus indicating Stokes Raman scattering. The other type of scattering is referred as Anti-Stokes Raman scattering, where the scattered radiation has a higher frequency than that of the incident radiation ($\nu_i < \nu_s$), and the

peaks are illustrated as Anti-Stokes lines on the Raman spectrum. The diagram illustrated in **Fig. 3.5(a)**, displays a schematic representation of how the incident radiation interacts with the molecules of the analysed sample. In the case of Raman scattering, after irradiating the sample with photons, the molecule is then excited from its ground state (low energy) to an unstable excited virtual state. Due to the instability of the virtual state, the excited photon will then drop down to a (higher energy) vibrational state, where the scattered photon has less energy and a longer wavelength than that of the incident photon. As previously mentioned, this is characteristic to Stokes Raman scattering. However, if the molecule returns to a vibrational state that is below its original ground state after scattering, then the scattered photon has a greater energy level and shorter wavelength as compared to the incident photon. This phenomenon is attributable to Anti-Stokes Raman scattering. As observed in the Raman spectrum for the carbon tetrachloride molecule (CCl_4), illustrated in **Fig. 3.5(b)**, the Raman shift is due to the Raman Effect which is determined by the spacing distance between the vibrational and ground states of the scattered photons. The Stokes and Anti-Stokes scattered photons is shifted an equal distance on opposite sides of the Rayleigh scattered photons, as can be seen on the CCl_4 spectrum.

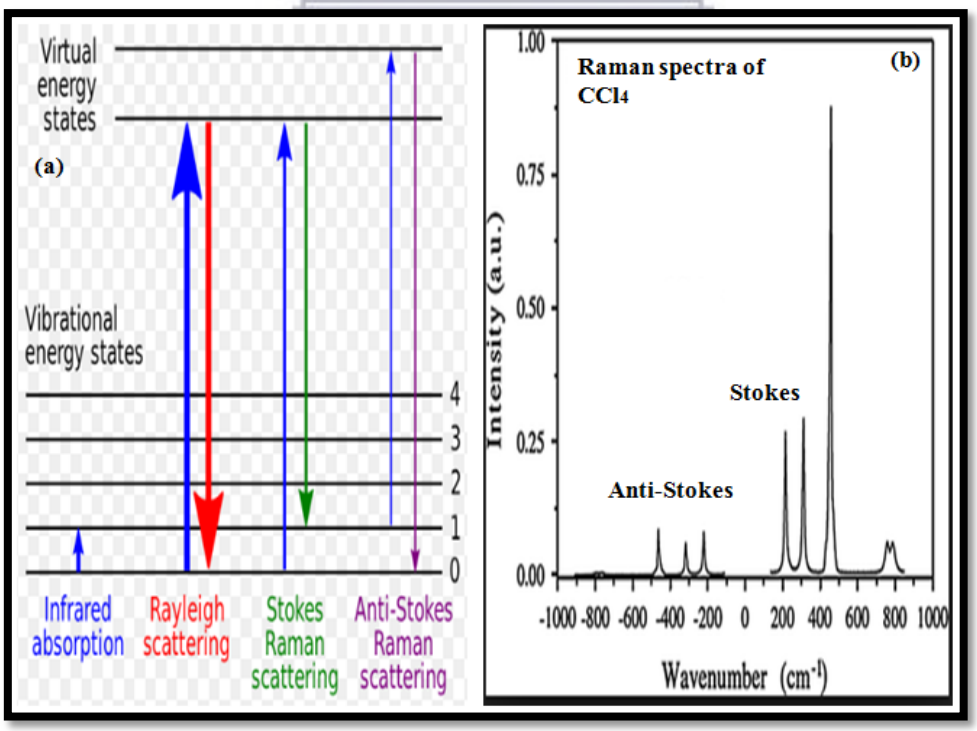

Figure 3.5: Diagram illustrating a schematic representation of energy transitions for Rayleigh and Raman scattering [134-135].

3.3.1.2.6 Thermo-Gravimetric Analysis (TGA)

Thermo-gravimetric analysis is an analytical technique that was used to analyse the thermal stability of the investigated supercapacitor electrode materials, by measuring the change in mass of the materials as a function of increasing temperature at a scanning mode with constant heating rate. The mass loss can also be measured as a function of time, which is described as an isothermal mode. This mass loss is due to the alteration of physical and chemical properties through oxidation/reduction, vaporisation, and decomposition processes occurring consequentially due to highly subjected temperatures to the electrode materials of interest. There are three classifications of thermo-gravimetric analysis (TGA), where one is known as dynamic TGA, the second as isothermal TGA, and the third as quasi-static TGA. The quasi-static TGA technique was selected and employed to perform thermal stability analysis on the electrode materials, as it entails the sample being heated until it reaches a constant weight (in mg) at each of the increasing temperature intervals through a linearly constant heating rate.

The principle behind thermo-gravimetric analysis is initially comprised of a sensitive microbalance that is used to continually measure the change in mass of the sample as it is bombarded with heat waves from the furnace. The computer program, with respect to the applied heating rate and inert gas flow, generally controls the experimental system. The microbalance is designed in a manner where it systematically generates an electrical signal corresponding to a particular weight change proportionate to a specific temperature interval. The schematic diagram, illustrated in **Scheme 3.8**, displays the various operating components of a TGA/DSC instrument. The instrument configuration involves a horizontally designed furnace, displayed in the centre of the scheme, configured with a highly sensitive balance on the right side of the furnace. The balance beam is connected to the heat and temperature sensors of the TGA/DSC instrument. The horizontal design of the furnace minimizes the occurrence of potential thermal buoyancies arising from a high density of gas particles levitating inside the furnace chamber. The furnace is well protected on both left and right sides by baffles. The volatile and gaseous combustion residues, together with the purged gas and reactive gas, excite the furnace through a gas outlet located on the left side of the furnace. Additional analytical instruments, for example a gas chromatography instrument, can be connected to this gas outlet to perform more advanced analytical analysis.

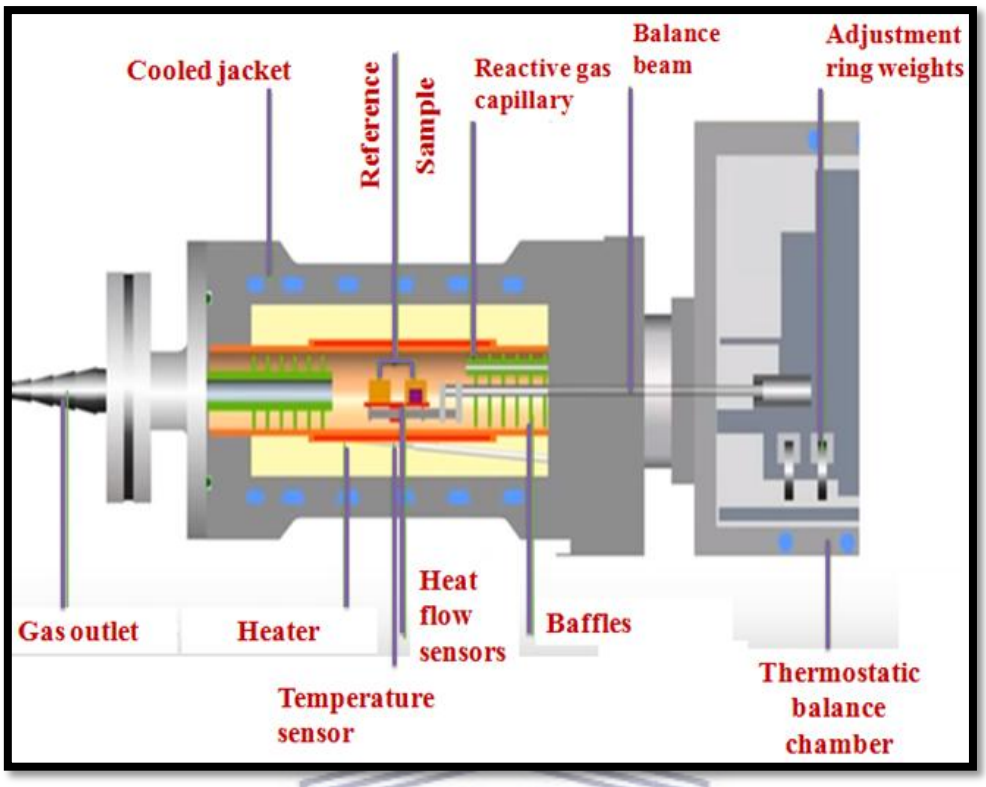

Scheme 3.8: Schematic diagram illustrating the various operating components of a TGA/DSC instrument [136].

3.3.1.2.7 Small-Angle X-ray Scattering (SAXS)

Small-Angle X-ray Scattering (SAXS) is a non-destructive analytical technique utilized for investigating the nanostructures of the material ranging from 1-200 nm in size. This technique additionally supplies information on a wide variety of aspects such as aggregation occurrence, particle size distribution, radius of gyration, folding and un-folding of the macromolecules within the material sample, and many more. The radius of gyration is mathematically considered as the square root of the sum of the distances of all the atoms from the centre of mass of the sample. In a basic SAXS experiment, the incident X-rays impinge upon the solution state sample (in the case of this research a powdered sample was analysed) where a spherically averaged intensity is recorded. This therefore generates an isotropic pattern of which a radial integration is taken from that pattern in order to produce a one-dimensional profile. The analysis of this 1D profile is what essentially provides information concerning the size and shape of the nanostructures within the sample material. It is

additionally noted that in SAXS analysis, larger particles scatter at smaller angles and smaller particles scatter at larger angles. In the case of anisotropic particles, the scattering for each orientation is calculated and recorded as an average result. The particle distance distribution function (PDDF), which is generally obtained from the geometrical considerations of the particles, is used to perform the calculation of the scattering curves. Smaller structures such as atomic crystal lattices can also be analysed by resolving the scattered profile. Wide angle X-ray scattering is used for X-rays with angles $2\theta > 10°$. During SAXS analysis, the X-rays are initially collimated into either a line or a point collimation, where both collimated beams possess unique advantages. Line collimation is preferably suited for analysing non-oriented isotropic systems, especially samples exhibiting weak scattering such as diluted dispersions and immersions. Point collimation is an ideal choice for analysing oriented samples such as solids containing in-homogeneous nanostructures. This type of collimation was best suited for performing analysis on the composite electrode materials investigated in this research work.

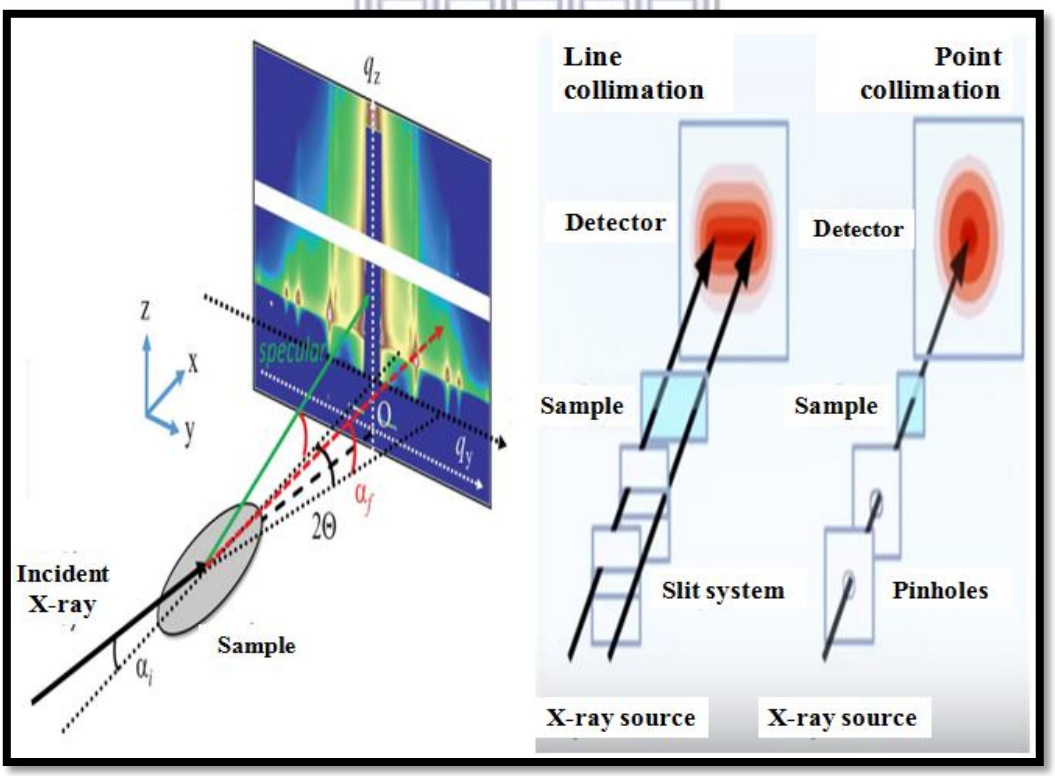

Scheme 3.9: Schematic diagram illustrating scattering patterns obtained with a GISAXS instrument, together with the two modes of beam collimation [137].

3.3.2 Electrochemical characterisation techniques

3.3.2.1 Cyclic Voltammetry (CV)

Cyclic Voltammetry is often described as a type of potentiodynamic polarization technique, where we observe the effect of an applied current to the electrode through an electrolyte species at varied electrical potentials of selected scan rates. CV experiments are predominately conducted for determining electrochemical data such as electrode potentials, reaction kinetics, and reversibility information of the analyzed electrode materials assembled in a half cell configuration device. In the case of the half cell (three-electrode) design assembly, CV analysis examines electrochemical processes occurring at a single working electrode containing the investigated electro-active material. The three-electrode cell design is also mainly used to identify whether the electrode material behaves as the anode or cathode, depending on the selected potential and scan rates. This information is essential to obtain for when performing CV analysis on a full cell (two-electrode) device.

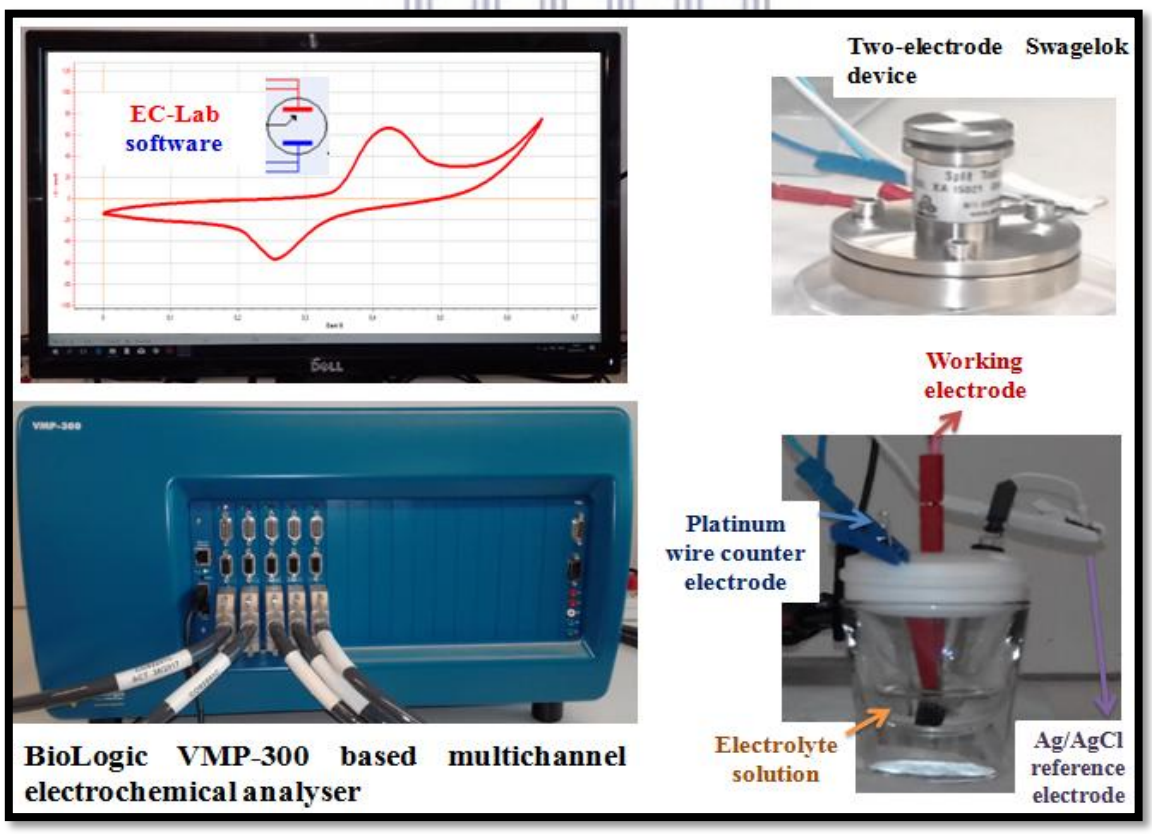

Figure 3.6: Experimental workstation of half cell (three-electrode) and full cell (two-electrode) electrochemical devices for CV analysis [138].

The Swagelok device assembly, as displayed in **Fig. 3.6**, was used to test the synthesized electrode materials at the application stage in order to completely evaluate their electrochemical performance. In a typical CV experiment, as illustrated in the generic potential (V) versus time (s) plot in **Fig. 3.7(a)**, a constant rate of potential is swept up to a maximum value and then back down to zero potential at the same inverse rate. The cell is initially allowed to equilibrate at the start and end of the potential sweeps. In the corresponding current versus potential curve, as expected the current increases as the potential increases. However, a rapid change in current is observed on the reversal potential scan, thus resulting in a significant curve shape. These curves can be used to calculate the standard electrode potential (E^0) of the cell, which is known to be the point equidistant between the oxidation and reduction peaks. The shape of the curves can additionally be analysed in order to obtain information relating to the electrochemical kinetics of the investigated electro-active material at the electrode surface. The voltammogram illustrated in **Fig. 3.7(b)** is a typical representation of a fully reversible system. A diagnostic test can be performed on the CV voltammogram to absolutely confirm the reversibility of the process by analysing vital parameters that signifies a particular electron transfer process. In the case of a reversible process, the diagnostic criterion, which each parameter must obey, is listed as follows:

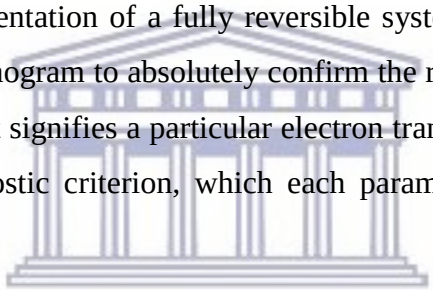

- The $\Delta E_p = E_{pa} - E_{pc}$ values (representing the peak-to-peak separation potentials) must be approximately 59/n mV, at 25 ℃. Note that n is considered as the number of electrons transferred during the oxidation/reduction process.

- E_p does not change with a change in scan rates (mV/s).

- $I_{pa}/I_{pc} = 1$ (slope extrapolated from the i_{pa}/i_{pc} versus $v^{1/2}$ linear plot).

- I_p is proportional to $v^{1/2}$

An important aspect to consider when performing CV analysis is the timescale of the potential sweep, which additionally affects the results of the analysis. This implies that potential sweeps initialized at speeds that are too fast, might cause a miss in the subtleties of diffusion/migration kinetics, thus resulting in insufficient experimental data obtained.

However, sufficient information can be inferred by slowing down the rate of potential sweeps to values below 10 mV/s.

The cyclic voltammograms illustrated in **Fig. 3.7(c)** and **(d)**, are typical examples of asymmetric electrochemical processes. The CV curve in **Fig. 3.7(c)** represents an irreversible oxidation process, as no reduction peak is observed in the reverse potential sweep. This, however, could imply that the process possesses slow reduction kinetics attributed by uncharged oxidants present within the electrode material matrix. The diagnostic criterion for the electrochemical parameters associated with an irreversible oxidation process is observably different to that of a reversible process from their respective voltammograms.

- Firstly, no reverse peak is visible on the voltammogram.

- E_p shifts by a factor of $30/\alpha n_a$ mV, where α is known to be the charge transfer coefficient. Additionally, $(E_p-E_{p/2})$ is approximately equivalent to $47.7/\alpha n_a$ mV for a 10-fold increase in potential.

- I_p is proportional to $v^{1/2}$

The CV plot illustrated in **Fig. 3.7(d)** is for a MnO_2 material coated electrode, operated in a three-electrode cell at high scan rates between 200-100 mV/s. Observably it can be deduced from the plot that the current responses for both oxidation and reduction peaks, increase with an increase in scan rate. At a more in-depth perspective, it can additionally be observed that E_{pa} shifts positively and E_{pc} shifts negatively, respectively, with an increase in scan rate. These are, in fact, diagnostic criterion for the E_p parameter of this particular electrochemical process, which is known to be a quasi-reversible electron transfer process. Additional diagnostic tests for CV curves of quasi-reversible processes proceeds in the following list below:

- As mentioned before, the I_p increases with the increase in scan rate. However, it is not considered as being directly proportional to the scan rate.

- The $\Delta E_p = E_{pa} - E_{pc}$ values are greater than 59/n mV and increases with increase in scan rate.

- $I_p/v^{1/2}$ is virtually independent of the scan rate.

It is later, experimentally, illustrated and discussed in the results section of this research work that the investigated electrode materials exhibited cyclic voltammograms resembling that of reversible and quasi-reversible electron transfer processes.

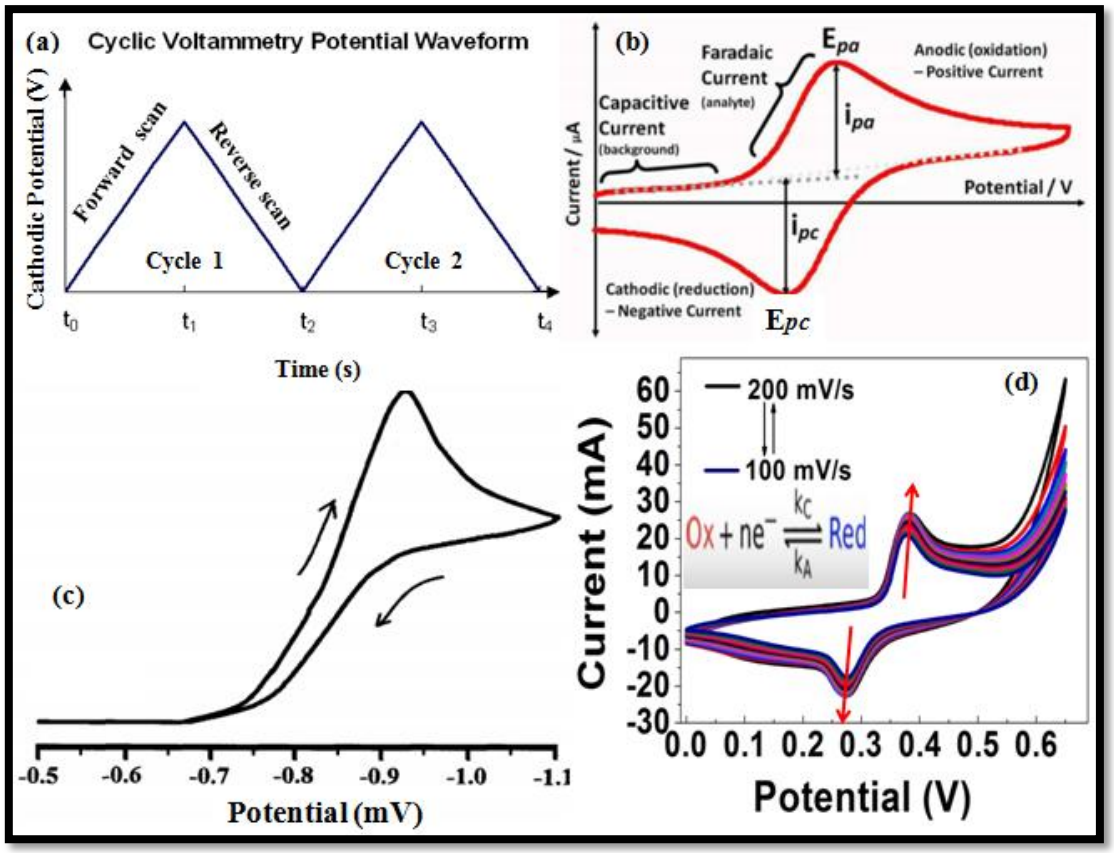

Figure 3.7: Diagram illustrating (a) an experimental potential (V) versus time (s) profile for two cyclic voltammetry scans, (b) a typical CV representation of a fully reversible process, (c) a CV analysed plot of an irreversible oxidation process, and (d) a CV interpreted plot of a purely synthesized MnO_2 electrode material [139-140].

3.3.2.2 Electrochemical Impedance Spectroscopy (EIS)

Electrochemical impedance spectroscopy is a versatile technique primarily employed in the research field of batteries, supercapacitors, fuel cells, corrosion, electroplating, photovoltaic cells, biosensors, and many more. The main concept behind the analytical process of EIS analysis deals with the initial understanding of the diffusion model (mechanistic motion of electrolyte ions at the electrode/electrolyte interface) best suited for data fitting and interpretation. The diffusion model type predominately utilized in electrochemical experiments for supercapacitor applications is called the double layer capacitance. The schematic diagram, illustrated in **Scheme 3.10(a)**, displays the double layer capacitance model indicating the associated diffusion planes/layers at the negative electrode/electrolyte interface of a hypothetical electrochemical cell.

In order to discuss the mechanistic function of the double layer capacitance model, it initially involves the understanding of how the solvated ions and partially solvated (solvent) molecules interact with the charged electrode surface. Due to the electrostatic attraction of the partially positive dipole moment of the solvent molecules with that of the negatively charged electrode surface, a monolayer of the solvent molecules adsorb onto the surface of the electrode. This monolayer of solvent molecules is what formulates the Inner Helmholtz plane (IHP), which also serves as a dielectric medium between the opposite charges of the electrode and solvated electrolyte ions. The Outer Helmholtz plane (OHP) extends to the centre of the positively charged electrolyte ions, and the combination of the two planes formulate the single layer of the double layer capacitance model. During electrochemical testing, the potential variation across the Helmholtz planes progresses linearly; however, it becomes exponential along the diffuse layer in the bulk electrolyte solution. The double layer capacitance model is therefore comprised of the capacitance of the Helmholtz plane or Stern layer (another term for the Helmholtz plane), in combination with the capacitance of the diffuse layer, as illustrated in **Scheme 3.10(b)**, connected in series.

$$\frac{1}{C} = \frac{1}{C_S} + \frac{1}{C_D} \tag{3.2}$$

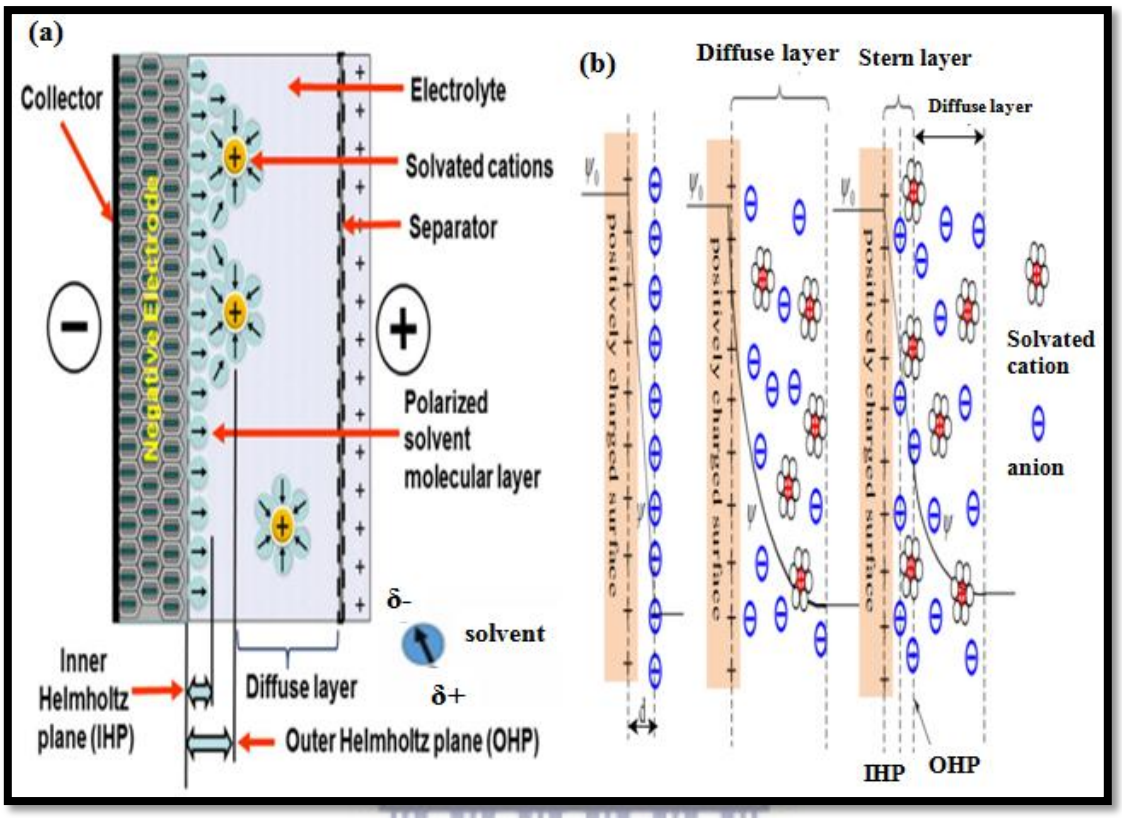

Scheme 3.10: Schematic diagram illustrating (a) the double layer capacitance model, and (b) a more detailed model displaying the potential variation across the diffuse and Stern layers [79].

The expression illustrated in **Equation (3.2)** represents the total capacitance of the double layer model, where C_S = capacitance of the Stern layer and C_D = capacitance of the diffuse layer. Since both layers experience a capacitance, they also experience a resistance at varied electrical potentials. This resistance is measured as electrochemical impedance upon conducting an EIS experiment. The impedance of an electrochemical cell is generally analysed by utilizing a small potential or current excitation signal obtained by subjecting a sinusoidal AC current or voltage of known amplitude and frequency to the cell. The amplitude and phase responses of the cell are measured as AC current or potential signals, and the sum of the AC sinusoidal functions is obtained mathematically by employing a Fourier series.

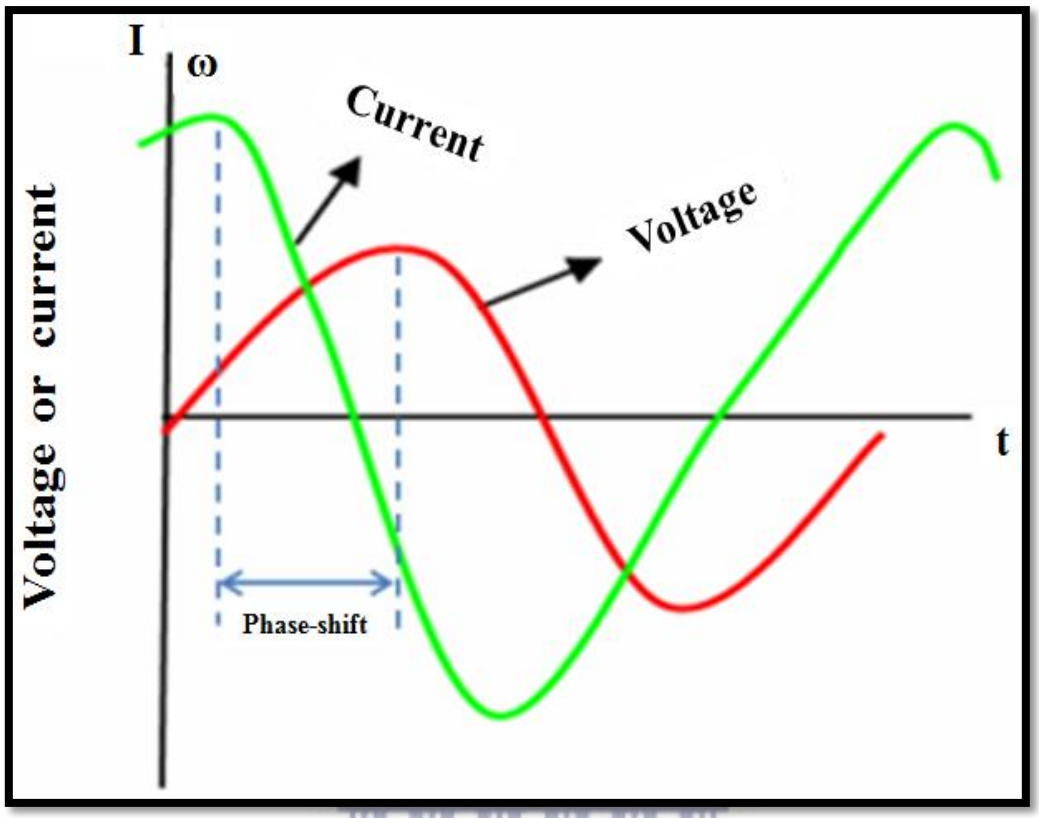

Figure 3.8: Graph illustrating two functions, which represent a current response signal obtained from a subjected sinusoidal voltage [62].

The mathematical expression representing the potential (voltage) excitation signal is shown below as a function of time.

$$V(t) = V_0 \sin(\omega t) \tag{3.3}$$

Where V(t) = potential at time (t), V_0 = signal amplitude, and $\omega = 2\pi f$ implies the radial frequency. The expression for the corresponding current response signal is also presented below as a function of time.

$$I(t) = I_0 \sin(\omega t + \varphi) \tag{3.4}$$

Where I(t) = current response signal at time t, I_0 = signal amplitude, and φ = phase shift between the applied AC voltage sinusoidal waveform and the AC current response curve. From the use of Ohm's law, the analogy of calculating resistance can also be applied to calculating impedance, as illustrated in the expression below:

$$Z = \frac{V(t)}{I(t)} = \frac{V_0 \sin(\omega t)}{I_0 \sin(\omega t + \varphi)} = Z_0 \left(\frac{\sin(\omega t)}{\sin(\omega t + \varphi)} \right) \tag{3.5}$$

The impedance, as illustrated in **Equation (3.5)**, is expressed in terms of a magnitude (Z_0) and a phase shift (φ). However, from the use of Euler's relation:

$$\exp(j\varphi) = \cos(\varphi) + j\sin(\varphi) \tag{3.6}$$

The impedance can additionally be expressed as a complex function:

$$Z(\omega) = Z_0 \left(\frac{\sin(\omega t)}{\sin(\omega t + \varphi)} \right) = Z_0 \exp(j\varphi) = Z_0 \left[\cos(\varphi) + j\sin(\varphi) \right] \tag{3.7}$$

The expression for the complex impedance function, Z(ω), illustrated in **Equation (3.7)**, is constructed of in-phase and out-of phase impedances, commonly referred to as real (Z') and imaginary (Z") impedances. As mentioned before, these impedances are attributable by the capacitance and resistance experienced by the diffusion reactions occurring at the positive and negative electrode/electrolyte interfaces. A representative example of a generic "Nyquist plot" illustrating the imaginary, -Im(Z")/Ω, part versus the real, Re(Z')/Ω, part is displayed in **Fig. 3.9(a).** The "Bode frequency" plot, presented in **Fig. 3.9(b)**, illustrates the logarithm of the magnitude of impedance and phase angle versus the logarithm of frequency. This plot is essential as it coincides with the Nyquist plot, and provides additional information

concerning the diffusion kinetics of electrolyte ions at the electrode surface. The red dots displayed on the Nyguist spectrograph indicate the fitted EIS data, where the data points are fitted onto the appropriately selected equivalent electrical circuit model, which was analysed using the Z-fit integrated EC-Lab analysis and interpretation software. The equivalent circuit model ideally measures the complex impedances in terms of circuit elements such as resistors (R_S and R_{ct}), capacitors (C_{dl}), and distributed Warburg (W_S) impedances. The solution resistance, denoted as R_S, is the resistance that occurs between the working electrode and the Ag/AgCl reference electrode. R_{ct} is called the charge transfer resistance associated with the transfer of electrons at the electrode interface. The double layer capacitance (C_{dl}) element of the equivalent circuit model is measured as a constant phase element (CPE) impedance. Lastly, the Warburg-impedance (W_S) distribution is a measure of resistance due to the diffusion of electrolyte ions across the electrode/electrolyte interface.

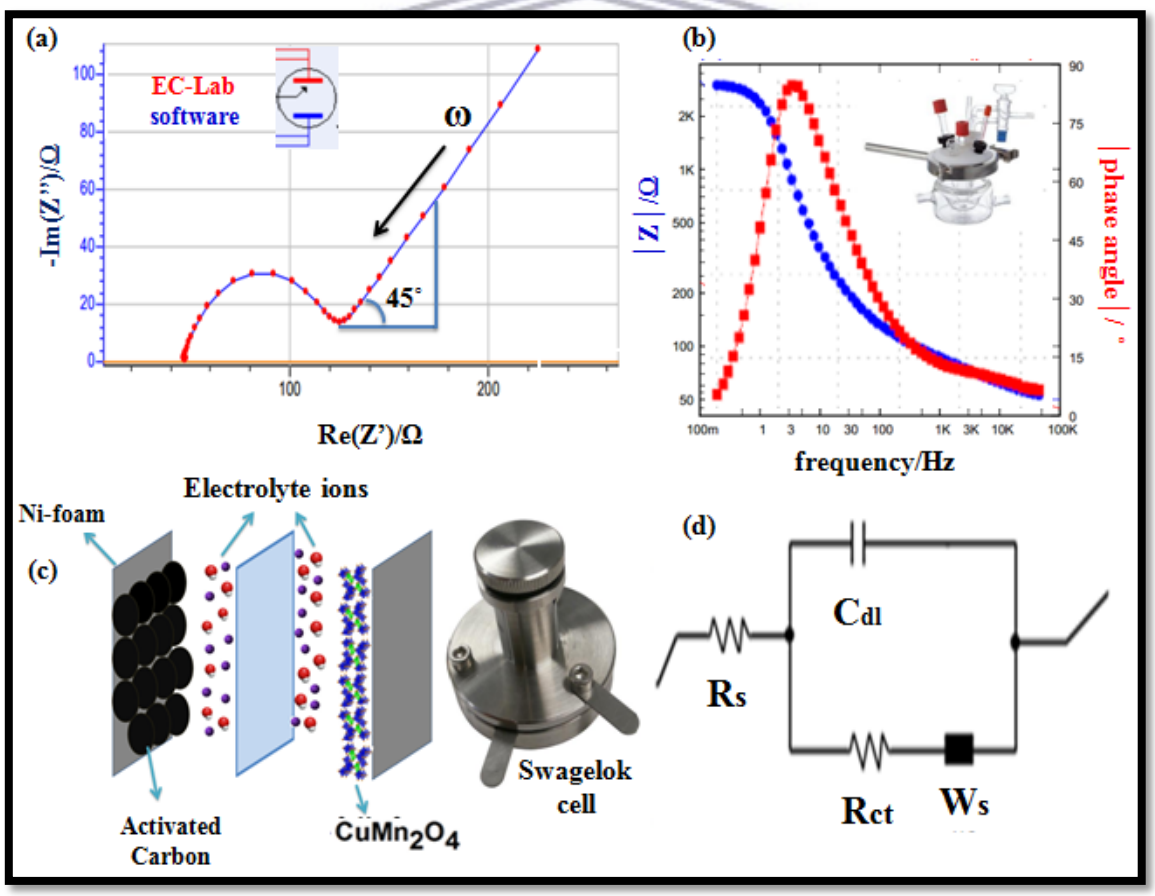

Figure 3.9: Illustrating (a) typical Nyquist plot, (b) corresponding Bode plot, and (d) the Randles equivalent circuit model used during data fitting and interpretation [141].

3.3.2.3 Galvanostatic Charge-Discharge (GCD) analysis

The galvanostatic charge-discharge (GCD) technique is well considered as the expansive electrochemical method employed in the research field of supercapacitor performance analysis and application. The GCD technique is also considered as a more accurate tool used for the evaluation of the specific capacitance of synthesized active electrode materials, over that of the CV technique. Additional information such as energy and power density, as well as cycling stability is also obtainable from the use of this technique. In a typical GCD experiment, constant positive and negative currents (obtained from selected current densities) are applied across the working electrode (to charge and discharge the electrode), where its potential relative to the reference (Ag/AgCl) electrode is monitored with respect to time. Similar to the CV and EIS experimental workstations, GCD analysis was performed on the three-electrode (half cell) and two-electrode (full cell) electrochemical devices, as displayed in **Fig. 3.10**.

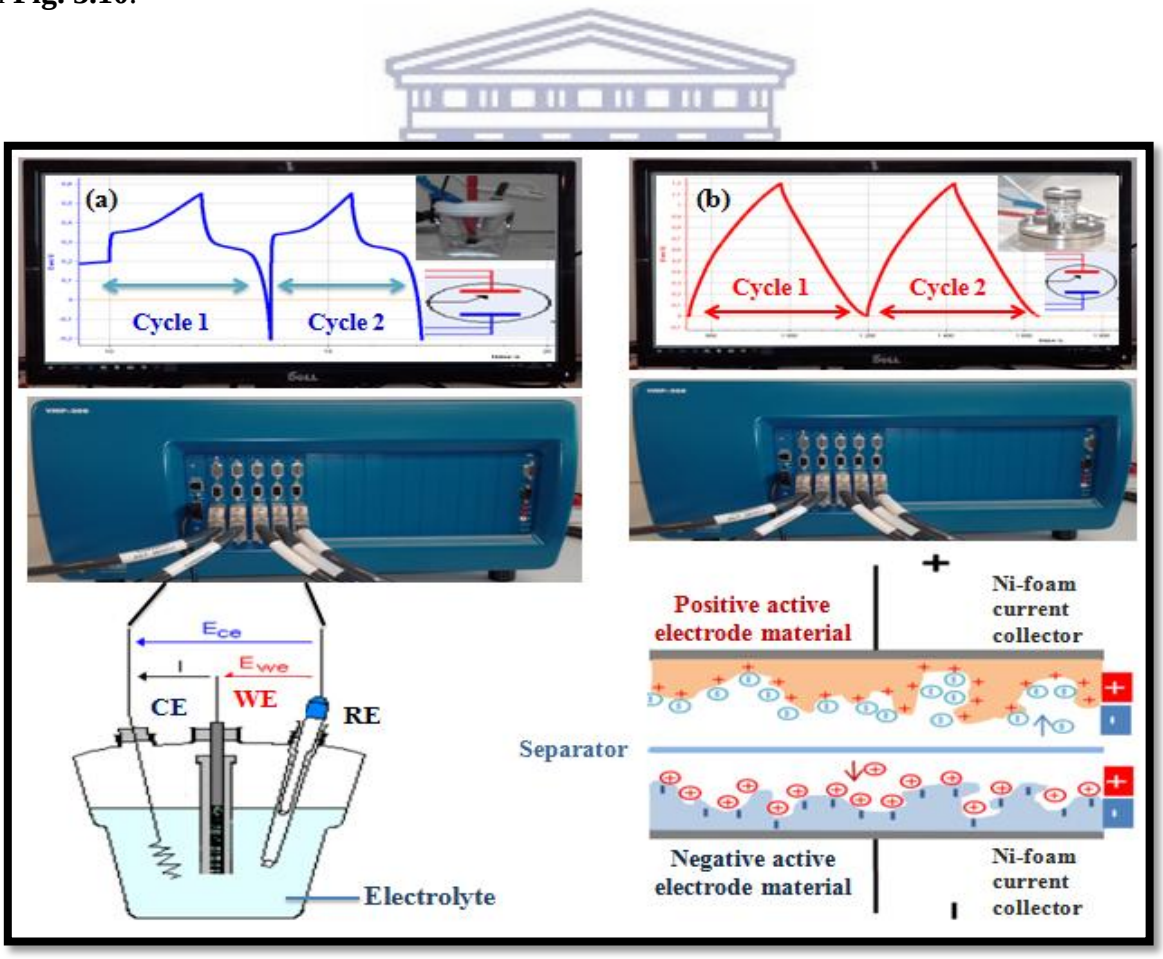

Figure 3.10: GCD experimental workstations of (a) three-electrode (half cell) and (b) two-electrode (full cell) electrochemical devices [79, 142].

The following section illustrates theoretical terminology of how a capacitor undergoes charging and discharging processes. In order to understand this concept, it is required to perceive the charging/discharging processes at a practical level (i.e. involving a conventional parallel-plate capacitor connected to an RC-circuit, as displayed in **Scheme 3.11**). During the charging process of the capacitor, as current (I) flows through the RC-circuit, positive charges begin to build up on the one plate, thus repelling positive charges on the other plate to formulate a fully charged parallel-plate capacitor containing positive and negative charges on the respective plates. The current continues to flow until the voltage across the capacitor is equivalent to the emf (ε) of the battery cell (at which point the current will stop flowing). Graphical representations of the charge/discharge processes, as illustrated in **Scheme 3.11**, can be used to deduce mathematical expressions, which describe relevant circuit elements such as the voltage (V_C) and charge (q) across the capacitor. However, in order to perform these deductions, it is initially required to have a brief knowledge of the following key math expressions.

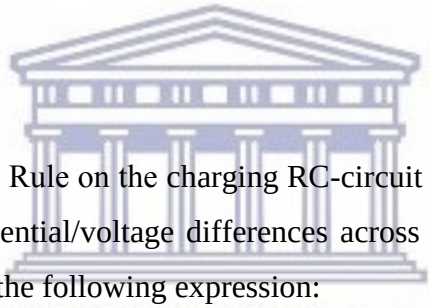

Utilizing the Kirchhoff's Loop Rule on the charging RC-circuit in **Scheme 3.11**, which states that the summation of the potential/voltage differences across all the circuit components is equivalent to zero, formulates the following expression:

$$\varepsilon - V_R - V_C = 0 \tag{3.8}$$

Where ε = the emf (electromotive force) of the battery cell, V_R = the voltage across the resistor, and V_C = the voltage across the capacitor. Re-arranging the equation and making ε the subject, gives the following expression:

$$\varepsilon = V_R + V_C \tag{3.9}$$

As the capacitor begins to charge up, its voltage (V_C) starting at zero will gradually increase until it reaches its maximum potential or charge capacitance. However, the voltage on the resistor (V_R) will not start at zero, as the sum of V_R and V_C equals the emf of the battery from the Kirchhoff's Loop Rule. Therefore, during charging, V_R experiences an exponential decay due to a complex feedback phenomenon occurring between V_R and V_C, namely as V_C increases V_R decreases. The following expression mathematically describes the potential decay across the resistor with respect to time.

$$V_R = \varepsilon e^{-t/RC} \tag{3.10}$$

Substituting the expression for V_R into the Kirchhoff's Loop Rule, in **Equation (3.9)**, and solving for V_C, gives the expression describing the exponential potential increase across the capacitor, as illustrated in the graphical representation of the capacitor charging process.

$$V_C = \varepsilon\left(1 - e^{-t/RC}\right) \tag{3.11}$$

The definition of capacitance is mathematically defined by the following formula:

$$C = \frac{Q}{V} \tag{3.12}$$

This definition can then be related to the RC-circuit and used to formulate the expression describing the charge accumulated on the capacitor.

$$\Rightarrow \quad q = CV_C \tag{3.13}$$

$$\therefore \quad q = C\varepsilon\left(1 - e^{-t/RC}\right) \tag{3.14}$$

During discharging, as illustrated in the circuit diagram, the battery is disconnected and the capacitor now functions as the emf energy source for the resistor. Initially the capacitor has its maximum voltage (V_0) and as current flows through the circuit and the resistor in a loop, the capacitor will gradually lose its voltage over time. Since initially $V_C = V_R$, the voltage across the resistor will also decay over time, much like in the case of the capacitor. The mathematical expression describing the V_C exponential decay is illustrated in the corresponding graphical representation of the capacitor discharging process. Since, V_C decays, the charge (q) on the capacitor plate will also decay, thus giving an expression for q similar to that of V_C (except with the capacitance multiplied to it).

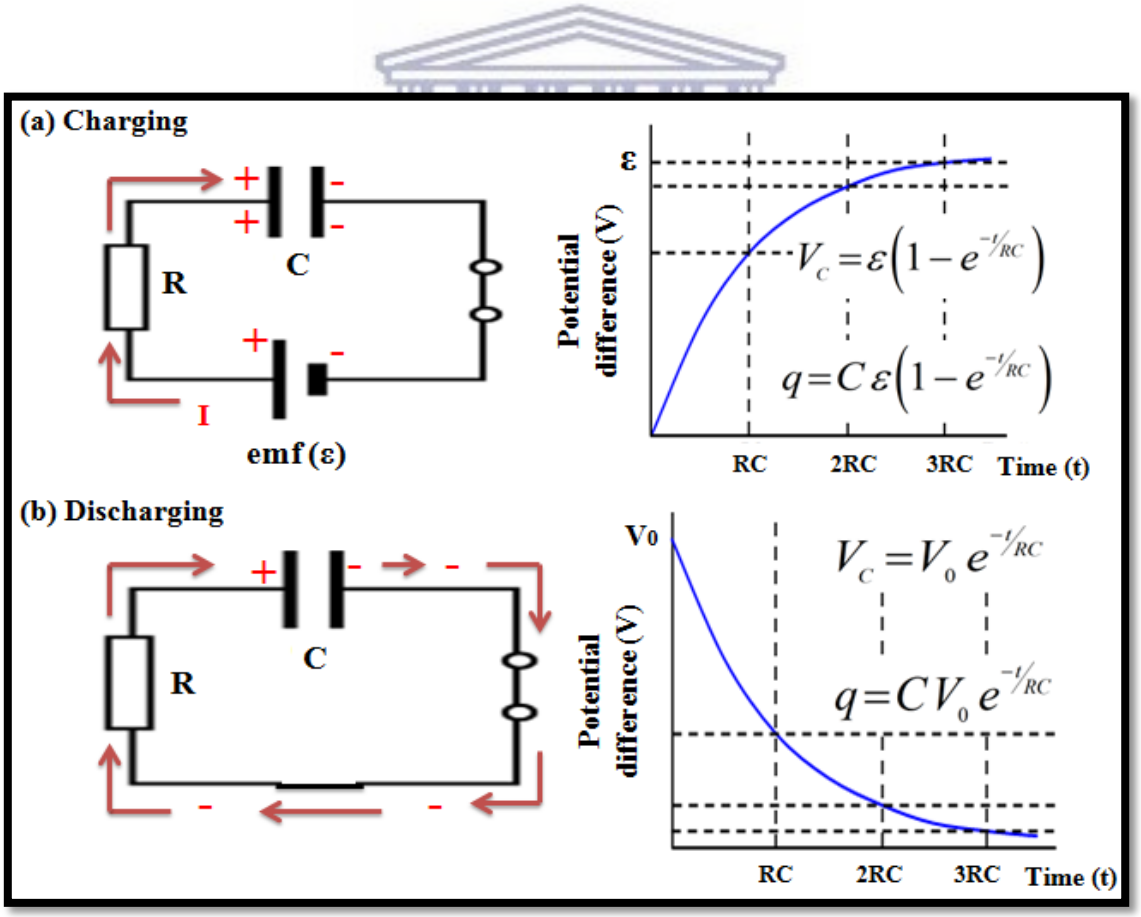

Scheme 3.11: Schematic diagram illustrating the RC-circuit diagrams and graphical representations of the (a) charging and (b) discharging processes of a parallel-plate capacitor system [143].

CHAPTER 4

Chapter Overview

This chapter critically discusses the characterization results of the pristine manganese oxide Mn_3O_4, spinel-type copper manganese oxide $CuMn_2O_4$, and modified hybrid $CuMn_2O_4$/MWCNT supercapacitor electrode materials. The discussion entails a complete understanding of the results obtained via microscopic (SEM and HR-TEM), spectroscopic, and crystallographic (FT-IR, Raman, and XRD) techniques. In addition to these techniques, highly sensitive techniques such as SAXS and TGA were used for obtaining information on the particle size and thermal stability of the electrode materials. Finally discussed in this chapter involves results obtained from electrochemical analysis via cyclic voltammetric (CV), galvanostatic charge/discharge (GCD), and electrochemical impedance spectroscopic (EIS) techniques.

4.0 Results and Discussion

4.1 Compositional and Microscopic Characterization

4.1.1 Scanning Electron Microscopic analysis

The scanning electron microscopy technique was used to investigate the micro-structures, surface morphology, and average/mean particle size distribution of the synthesized pristine Mn_3O_4, spinel $CuMn_2O_4$, and hybrid $CuMn_2O_4$/MWCNT electrode materials [144]. The Mn_3O_4 morphologies displayed in the SEM image titled (**Fig. 4.1)** portrayed uniformly agglomerated spherical shaped nanostructures. Particle size analysis and calculations were performed using ImageJ (an image processing software) [116], and the results obtained revealed average particle sizes ranging between 65-105 nm. These morphological findings were evidently analogous to the SAXS obtained results. An additional morphological

observation of the pristine Mn_3O_4 material, was that its SEM image displayed large secondary agglomerated particles (~ 145 nm) originating from the aggregation of smaller primary particles (~ 73 nm) [114]. This observation was also correspondent to its XRD structural characterisation results.

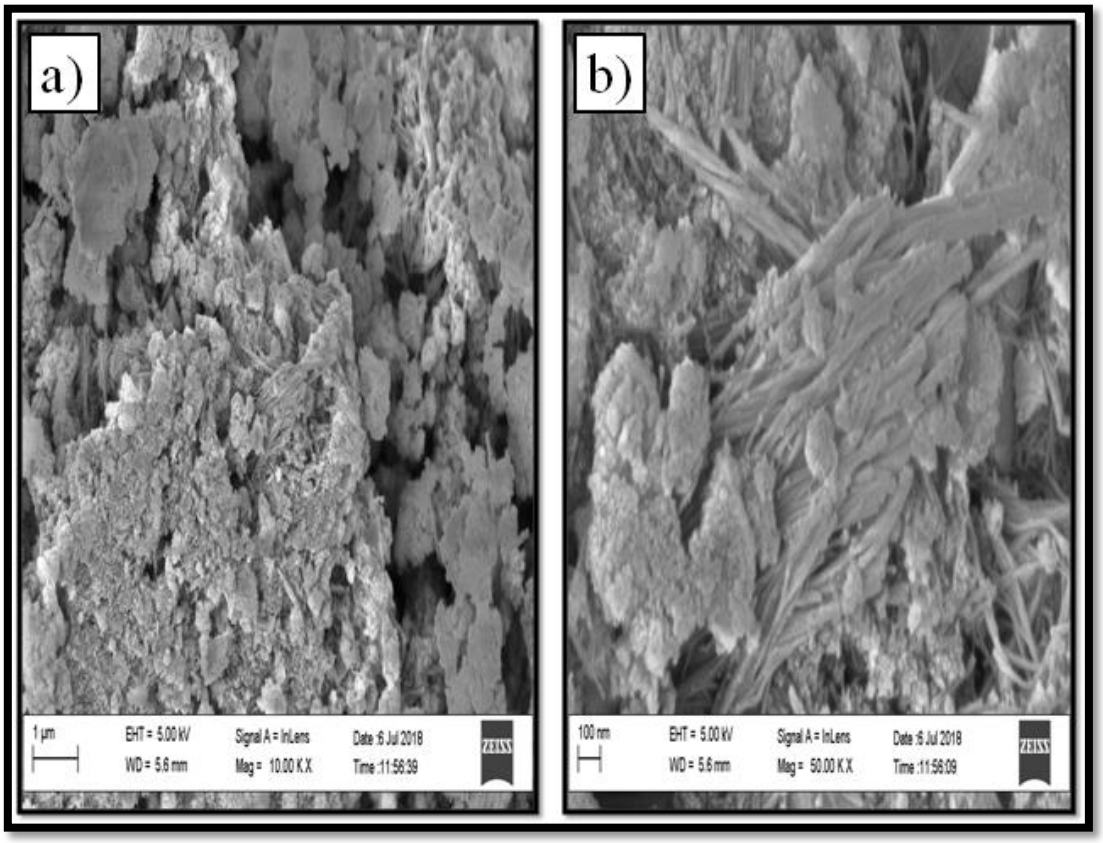

Figure 4.1: SEM images of the pristine Mn_3O_4 electrode material viewed at a scale of a), 1 μm and b), 100 nm.

The SEM micrographs of the spinel $CuMn_2O_4$ material, portrayed in **Fig. 4.2**, displayed morphologies that are closely consistent with that of the pristine Mn_3O_4 material. The Mn_3O_4 nanoparticles displayed plate-like nanostructures, whereas the $CuMn_2O_4$ material portrayed confined nanocrystallites, thus exhibiting exceptional crystallinity [145]. The $CuMn_2O_4$ average particle size calculations revealed sizes ranging between 75-120 nm. Elaborating more on the confinement existing between the $CuMn_2O_4$ nanoparticles, **Fig. 4.2** displayed the $CuMn_2O_4$ nanoparticles as clusters of geometric crystals bound together [146].

This confinement (also termed as quantum confinement) could have possibly been a result of the van der Waals and capillary adhesive forces occurring within the citric acid monohydrate ($C_6H_8O_7.H_2O$) reagent precursor [146-147]. These strong molecular forces contribute towards strong molecular bonding between the elemental constituents of the spinel $CuMn_2O_4$ electrode material, thus promoting excellent structural stability [148]. However, the electrode material's thermal stability properties might not be as good as its structural stability. Therefore, in addition to providing improved electronic conductivity to the spinel system, the incorporated multi-walled carbon nanotube (MWCNT) structures would also provide enhanced thermal stability, as experimentally proven by thermo-gravimetric analysis (TGA) later illustrated in this chapter.

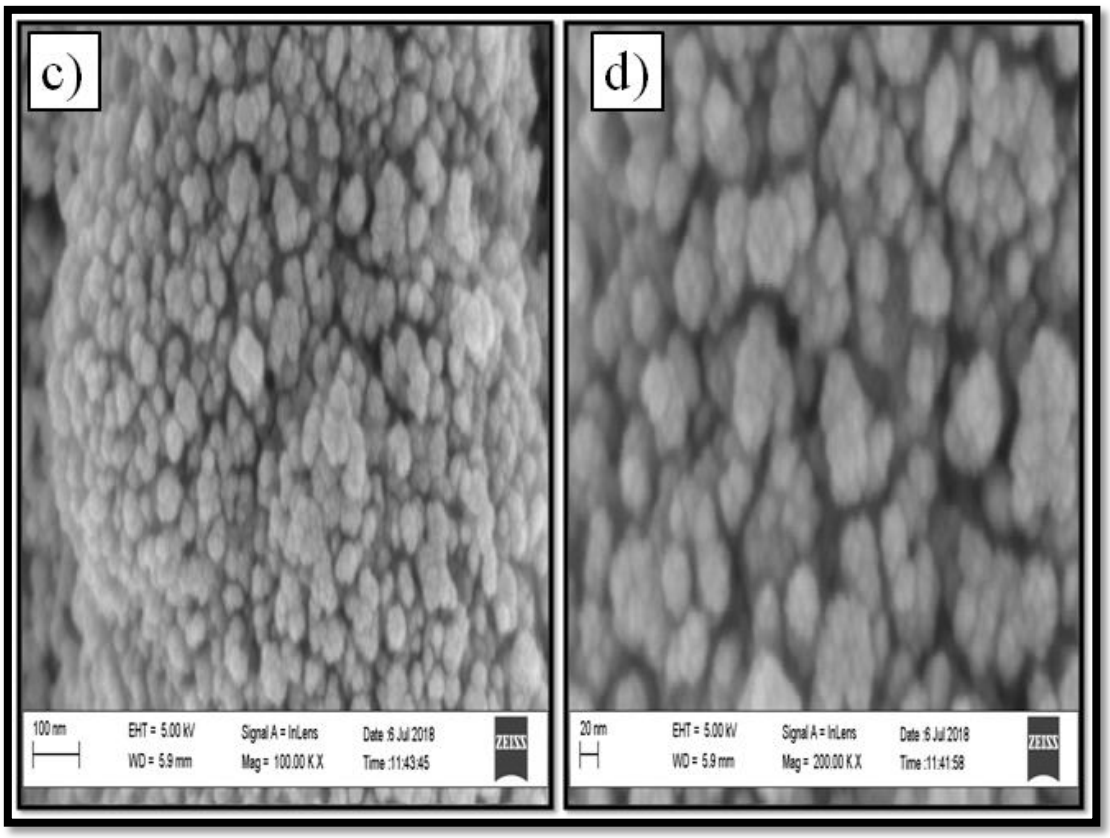

Figure 4.2: SEM images of the spinel $CuMn_2O_4$ electrode material viewed at a scale of c), 100 nm and d), 20 nm.

The confined $CuMn_2O_4$ nanocrystal clusters were anchored to the surface of multi-walled carbon nanotubes (MWCNTs) for the development of the hybrid $CuMn_2O_4$/MWCNT nanocomposite material. Prior to this, SEM and HRTEM images were obtained displaying acid-treated MWCNTs.

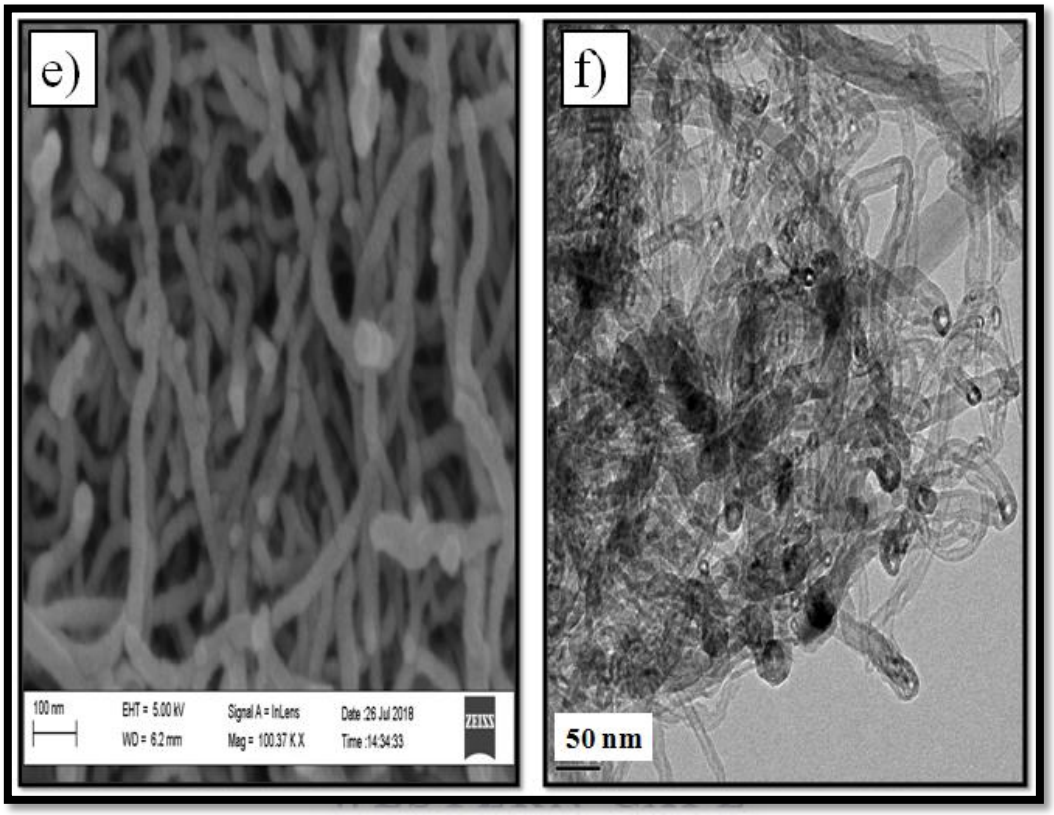

Figure 4.3: Purified MWCNT images: e), SEM and f), HRTEM.

The morphology of the $CuMn_2O_4$/MWCNT nanocomposite material is exhibited in the SEM images below titled **Fig. 4.4**. These images positively displayed optimal incorporation of the spinel $CuMn_2O_4$ nanoparticles to the purified MWCNT network. The purpose of the MWCNT network was to provide a three-dimensional support structure for the spinel $CuMn_2O_4$ nanoparticles, thus increasing its surface area and preventing agglomeration [149]. This statement can be verified from SAXS analysis, which illustrated that the hybrid $CuMn_2O_4$/MWCNT material exhibited no aggregation as compared to the pristine and spinel materials (which exhibited aggregation at a certain degree). Additionally, during electrochemical analysis, the 3D MWCNT network would also help minimize the occurrence

of energy dissipation due to concentration polarisation processes occurring at the electrode surface [150-151]. The structural morphology of the MWCNTs, illustrated in **Fig. 4.4**, displayed lengthy and narrow intertwined entanglements with the spinel $CuMn_2O_4$ nanoparticles [149]. This observation successfully implied the generation of a strong atomic attraction between the 3D MWCNT network and $CuMn_2O_4$ nanoparticles.

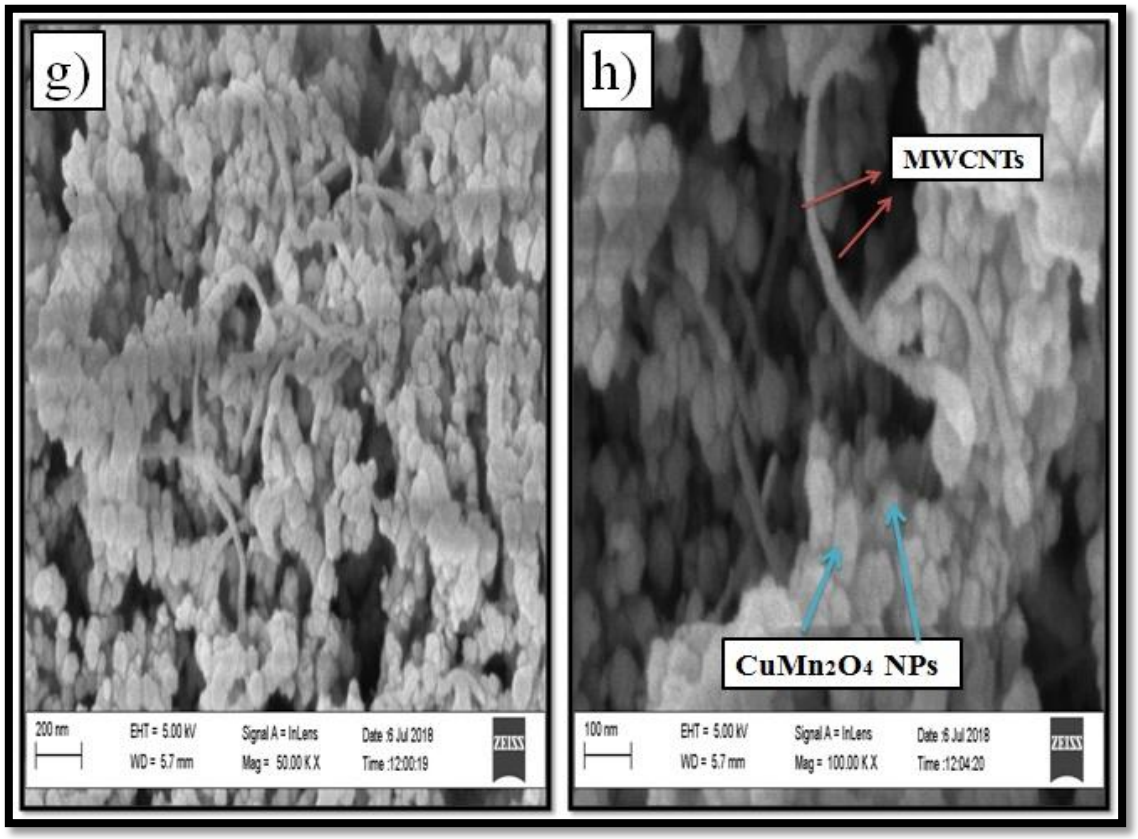

Figure 4.4: SEM images of the hybrid $CuMn_2O_4$/MWCNT electrode material viewed at a scale of g), 200 nm and h), 100 nm.

4.1.2 High-Resolution Transmission Electron Microscopic analysis

In order to obtain a more in depth perception of the inner crystal structure of the synthesized electrode materials, HR-TEM analysis was carried out [152]. **Figs. 4.5a)** and **4.5b)** display 20 and 10 nm scale magnification HR-TEM images of the pristine Mn_3O_4 material, respectively. In **Fig. 4.5b)**, the dark and light lines that appear on one of the crystal planes are called lattice fringes. These periodic fringes are formed by diffracted waves that are transmitted from the atomic lattice planes of the crystalline material [152]. The outline of the particle marked in **Fig. 4.5a)**, displays a generic body-centered tetragonal (BCT) geometrical model of the Mn_3O_4 crystal structure. This outlined projection resembled a rectangular box shape with atomic lattice planes represented by lattice fringes.

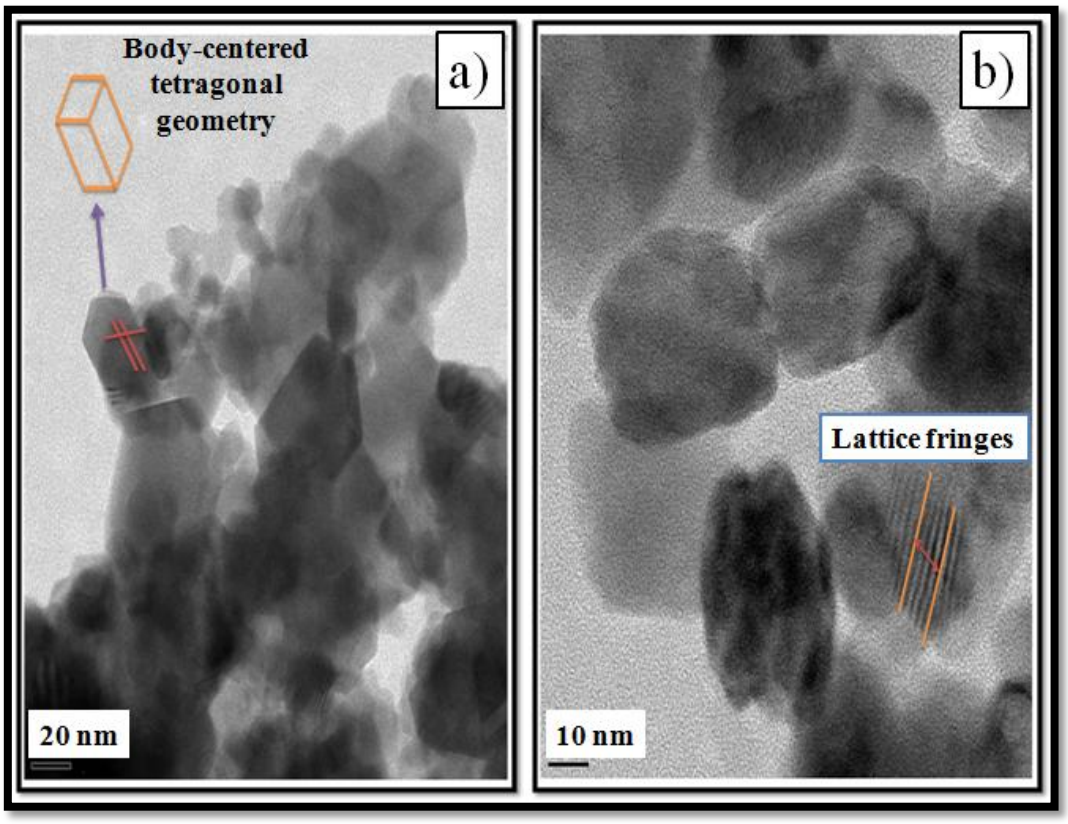

Figure 4.5: HR-TEM images of the pristine Mn_3O_4 electrode material viewed at a scale of a), 20 nm and b), 10 nm.

The selected area electron diffraction (SAED) pattern in **Fig. 4.6d)** displayed a regular sequence of scattered dots, which is a characteristic aspect of the Mn_3O_4 nanocrystal [152]. The lattice fringe lines displayed in **Fig. 4.6c)**, evidently illustrated atomic crystal lattice planes indexed with inter-planar spacing distances of 0.275 nm, 0.248 nm, and 0.236 nm respectively. In conjunction with XRD analysis, these lattice distances are correspondent to the (103) and (202) atomic lattice planes of the Mn_3O_4 crystal structure. However, the (211) plane is correspondent with the MnO_2 atomic crystal structure as confirmed by XRD data. This phenomenon was attributed due to additional phases such as MnO_2 and Mn_2O_3, present within the crystal structure of the Mn_3O_4 material.

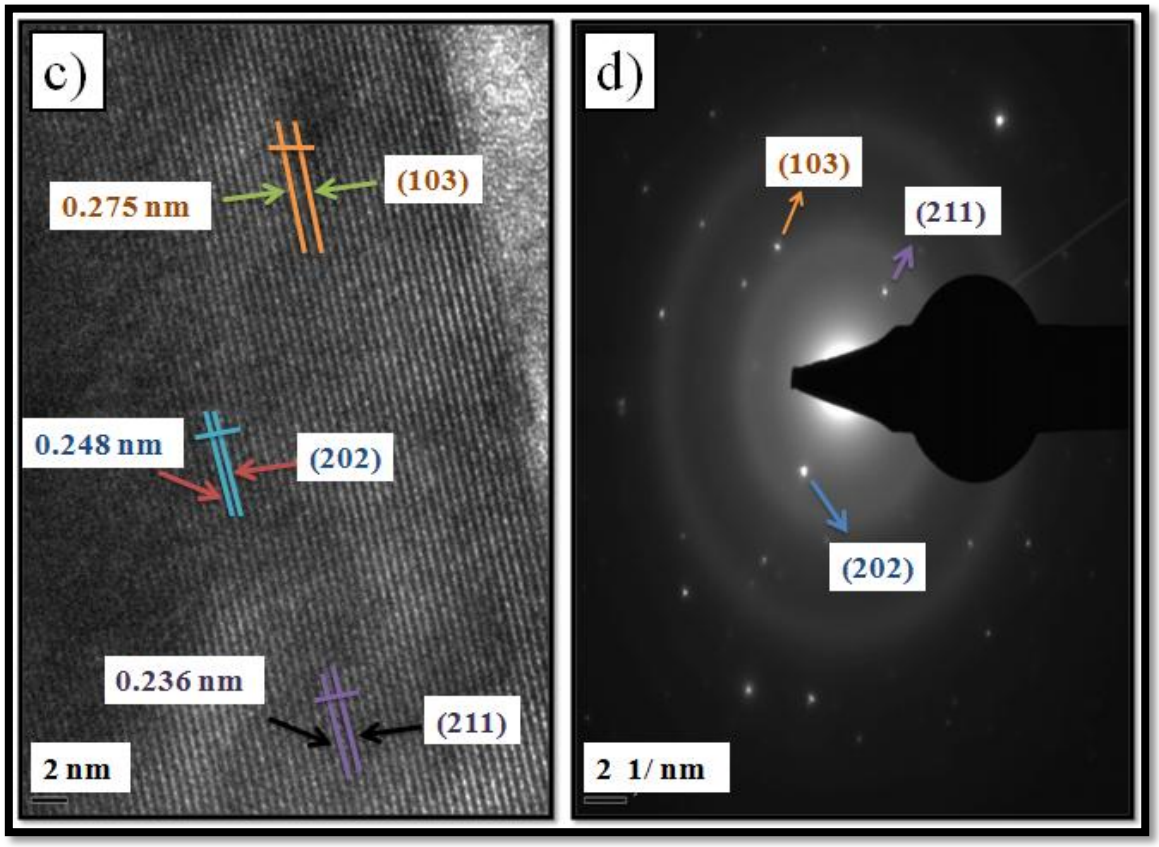

Figure 4.6: c), HR-TEM image and d), SAED image of the pristine Mn_3O_4 electrode material viewed at a 2 nm scale.

The energy dispersive X-ray spectrum, shown in **Fig 4.7**, for the pristine Mn_3O_4 electrode material reveals its elemental composition data. The expected elements, of which Mn_3O_4 is composed of, are displayed in the spectrograph below. However, the copper and nickel signals are due to the copper-nickel grid onto which the Mn_3O_4 material was drop casted during HR-TEM sample preparation. Additionally, the carbon signal on the spectrograph is consequentially due to the carbon black adhesive material coated on the copper-nickel grid before sample analysis [116]. This additional carbon coating process is necessary to make the active electrode material more conductive for obtaining images with high resolution [116]. The potassium signal could be a result of the un-reacted potassium permanganate ($KMnO_4$) residues that may have been present within the Mn_3O_4 structural morphology. Unfortunately, there is no reasonable statement explaining the presence of the silicon (Si) signal, unless it was attributed to contamination occurrence during synthesis.

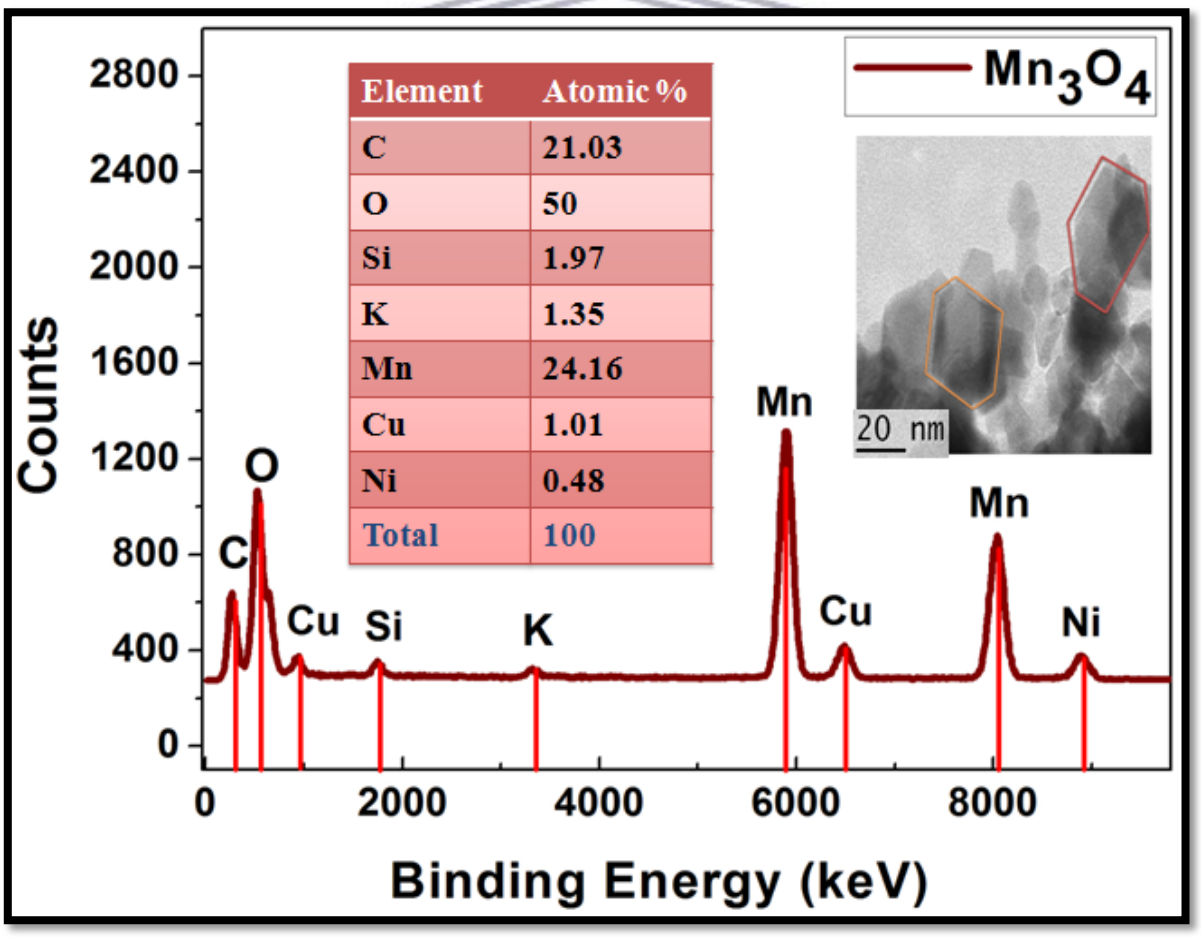

Figure 4.7: Energy Dispersive X-ray (EDS) spectrum of the pristine Mn_3O_4 electrode material obtained from HR-TEM analysis.

The HR-TEM image displayed in **Fig. 4.9g)** illustrated well-defined lattice fringes on the micrograph image, thus indicating good crystallinity retained by the spinel $CuMn_2O_4$ material. The $CuMn_2O_4$ particles are displayed in **Fig. 4.8** as cubic shaped nanostructures with particle sizes ranging between 95-140 nm [153]. A two-dimensional crystal lattice image of one of the cubic $CuMn_2O_4$ nanostructures [153] is shown in **Fig 4.8f)**. The 2D projection is indexed with three distinctive atomic crystal lattice planes: (002), (220), and (222) [154]. These detected atomic planes are in correlation with the indexed miller indices from the spinel $CuMn_2O_4$ XRD data plot.

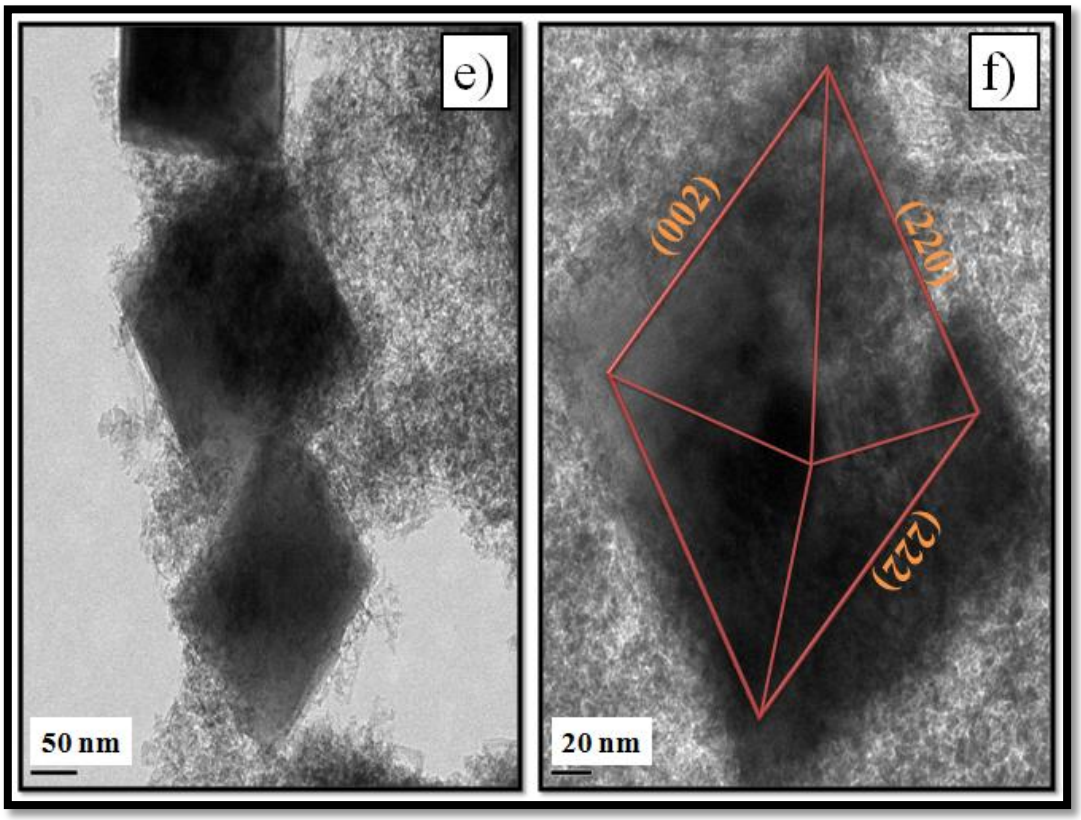

Figure 4.8: HR-TEM images of the spinel $CuMn_2O_4$ electrode material viewed at a scale of e), 50 nm and f), 20 nm.

The distance between the specifically oriented lattice fringes displayed in **Fig. 4.9g)**, was calculated to be 0.234 nm, 0.293 nm, and 0.271 nm for the indexed (002), (220), and (222) atomic lattice planes, respectively. The fringe spacing of the (222) plane is in good agreement with the inter-planar lattice spacing distance of the most intense peak (222) calculated by XRD analysis. The SAED scanned image indexed with the three-lattice planes, indicated diffraction dots that are characteristic of a spinel $CuMn_2O_4$ face-centered cubic crystalline material. The EDS spectrum of the spinel $CuMn_2O_4$ material, displayed in **Fig. 4.10**, shows the presence of the desired elements without the occurrence of unwanted contaminants or residues. This is an indication of a purely synthesized electrode material.

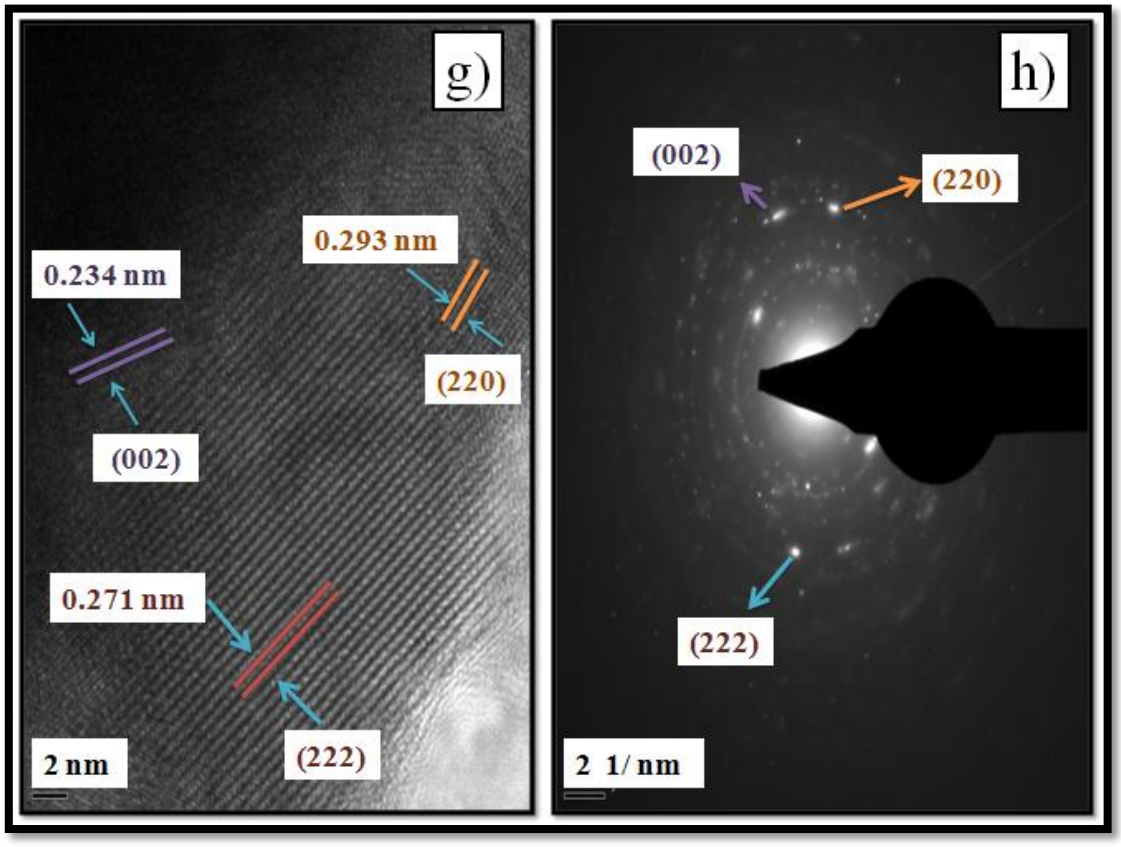

Figure 4.9: g), HR-TEM image and h), SAED image of the spinel $CuMn_2O_4$ electrode material viewed at a 2 nm scale.

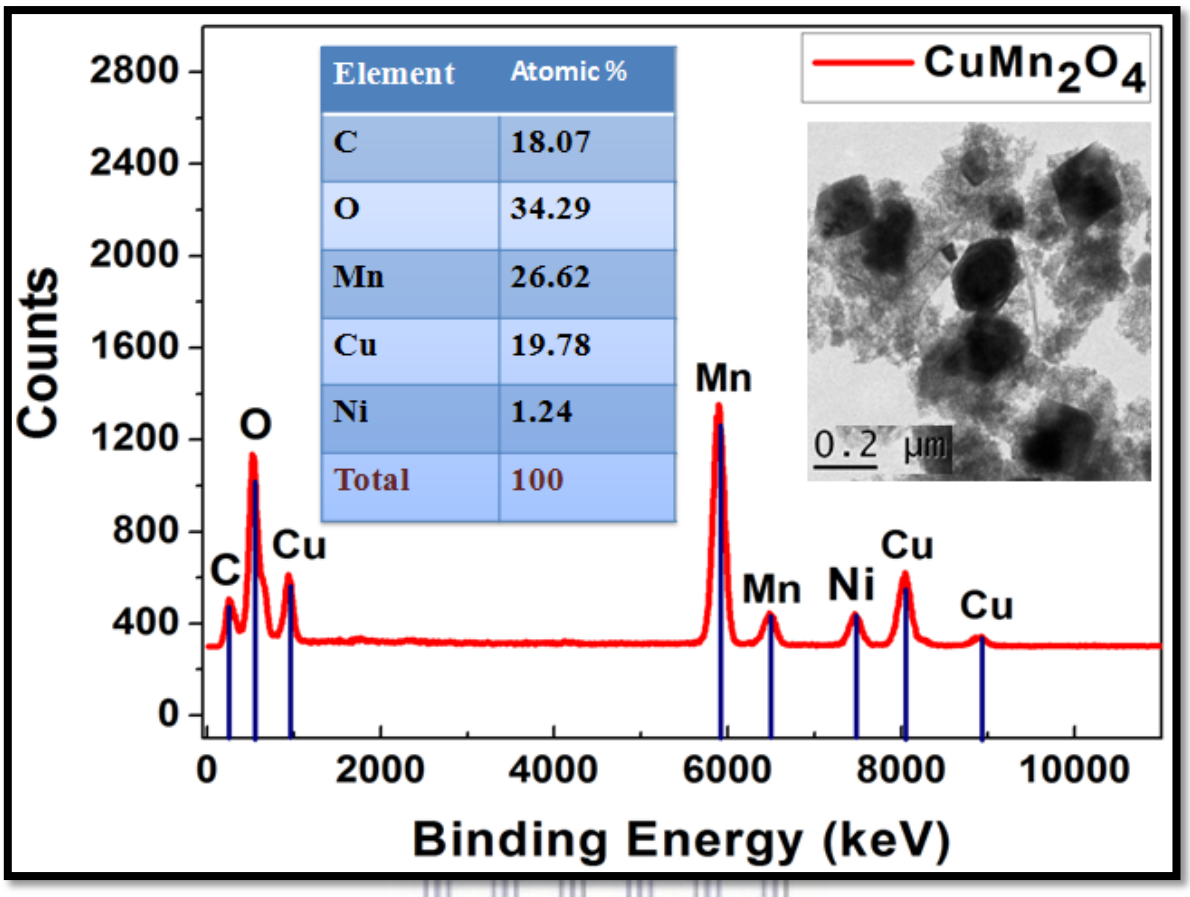

Figure 4.10: Energy Dispersive X-ray (EDS) spectrum of the spinel $CuMn_2O_4$ electrode material obtained from HR-TEM analysis.

Semi-quantitative research of the spinel $CuMn_2O_4$ electrode material was performed through employing HR-TEM EDS analysis, which provided a spectrum that illustrated the presence of the desired elemental constituents of the spinel $CuMn_2O_4$ phase material with no unwanted contaminants [155]. This implied that the designed temperature controlled hydrothermal synthetic procedure, used as the development schematic of the spinel $CuMn_2O_4$ electrode material, resulted in the formation of a purely synthesized spinel $CuMn_2O_4$ binary metal oxide compound. However, despite the promising elemental composition data, it is analytically evident from XRD analysis that there existed additional structural phases such as Mn_2O_3 and CuO, within the spinel $CuMn_2O_4$ crystal structure. Since EDS is mostly useful for when identifying the elements that form the building blocks of the synthesized material, XRD analysis provide a better insight on the material's crystal structure and elemental phase [156].

The HR-TEM images displayed in **Fig. 4.11** illustrated cubic structured spinel $CuMn_2O_4$ nanoparticles, anchored to the outer walls of the MWCNTs [157]. After performing image processing analysis from ImageJ, the average particle sizes of the $CuMn_2O_4$/MWCNT nanocomposite electrode material was obtained as a range of 50 – 108 nm. This result is in good correspondence with the average particle size data obtained from XRD and SAXS analysis. The ionic bonding of sp^2 hybridized carbon atoms, of the acid functionalized MWCNTs, with the tetrahedral Cu^{2+} atoms, of the spinel $CuMn_2O_4$, was confirmed via Raman and FT-IR analysis [158]. An intriguing correlation between the hybrid material observed at the 0.2 µm scale, displayed in **Fig. 4.11(k)**, and it's SAXS analyzed data indicated that a uniformly defined distribution of $CuMn_2O_4$ nanoparticles across the MWCNT network surface were formulated after fabrication.

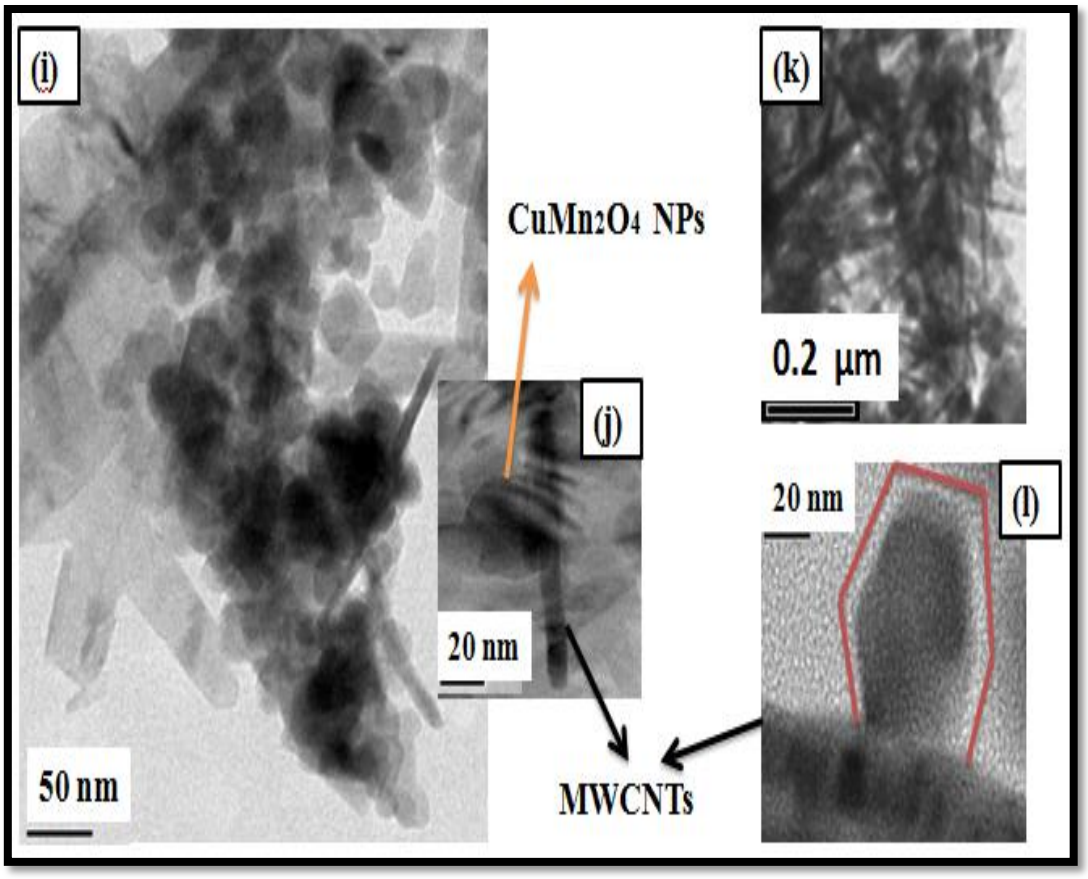

Figure 4.11: HR-TEM images of the hybrid $CuMn_2O_4$/MWCNT electrode material viewed at a scale of (i) 50 nm, (j) 20 nm, (k) 0.2 µm, and (l) 10 nm.

The HR-TEM image, showed in **Fig. 4.12**, clearly displayed atomic lattice fringes indexed as (002), (220), (311), and (100), in conjunction with XRD analysis [159]. These atomic lattice planes are correspondent to the MWCNT and spinel $CuMn_2O_4$ crystalline nanostructures [160]. The respective diffraction angles of the indexed atomic lattice planes, obtained from the XRD data plot, were used to calculate the d-spacing distance between the individually labelled lattice fringes. The calculated distance between the specifically oriented lattice fringes were obtained as 0.294 nm, 0.246nm, 0.227nm, and 0.203 nm for the indexed (002), (220), (311), and (100) atomic lattice planes, respectively. **Fig. 4.12o)** displays the selected area electron diffraction (SAED) pattern of the hybrid $CuMn_2O_4$/MWCNT electrode material, which revealed well-defined scattered dots indicative to the crystalline particles embedded within the $CuMn_2O_4$/MWCNT structure [75]. As seen in the SAED diffraction pattern, the indexed atomic lattice planes were assigned to a Fd3m space group (according to JCPDS pattern no. 00-048-1548), which is characteristic to the spinel face-centered cubic (FCC) crystal lattice structure of the hybrid $CuMn_2O_4$/MWCNT electrode material [114].

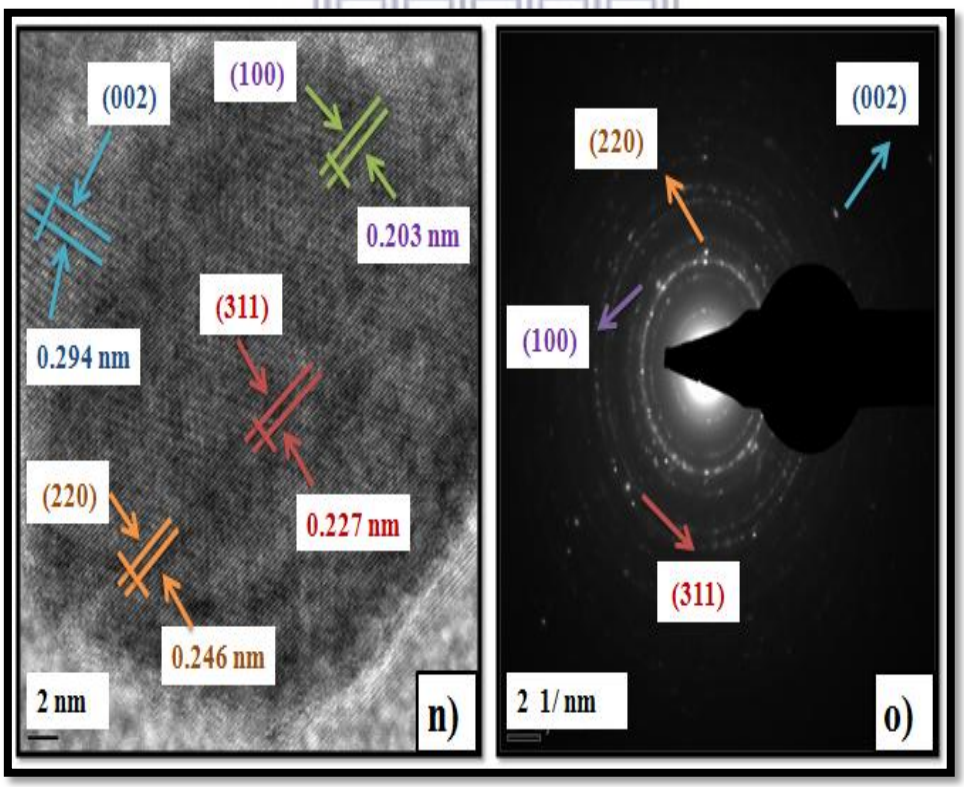

Figure 4.12: n), HR-TEM image and o), SAED image of the hybrid $CuMn_2O_4$/MWCNT electrode material viewed at a 2 nm scale.

Fig. 4.13 illustrates the energy dispersive X-ray (EDS) spectrograph of the investigated hybrid $CuMn_2O_4$/MWCNT electrode material. Chemical analysis confirmed the existence of all the desired elements within the hybrid structured nanocomposite material, however, the presence of a silicon contaminant was identified from the corresponding EDS spectrograph. This purity defect may have been attributed to the employment of the low-temperature reflux heating method used during the electrode material's synthetic procedure [161]. The reflux method was employed to provide a control over the pressure built up during rapid temperature increase, which is difficult to achieve inside a sealed hydrothermal reactor vessel. The high intensity carbon peak illustrated an atomic weight percent of 21.26 % of the entire hybrid $CuMn_2O_4$/MWCNT composite electrode material, thus indicating a uniform distribution of spinel $CuMn_2O_4$ nanoparticles on the MWCNT network.

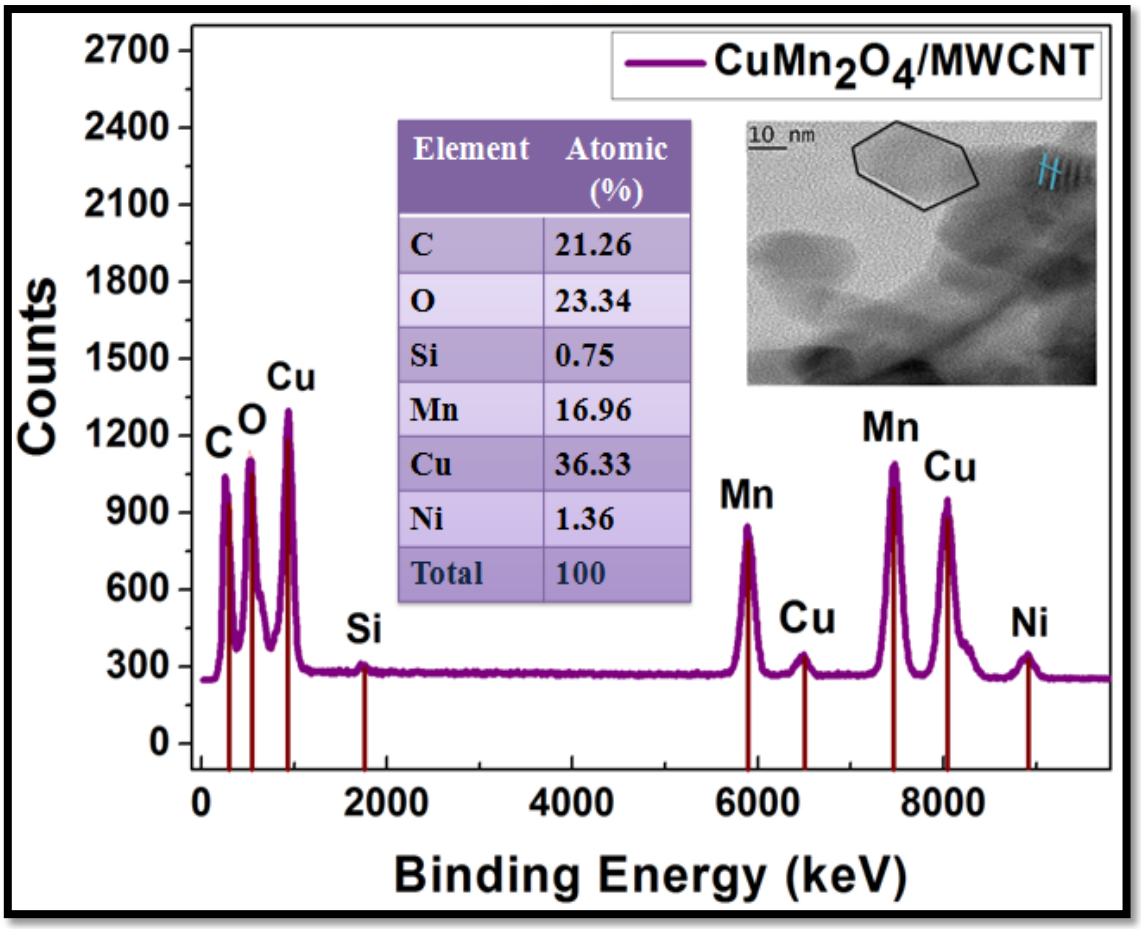

Figure 4.13: Energy Dispersive X-ray (EDS) spectrum of the hybrid $CuMn_2O_4$/MWCNT electrode material obtained from HR-TEM analysis.

4.2 Structural and Spectroscopic Techniques

4.2.1 XRD analysis and interpretation

XRD analysis was performed in order to investigate and identify the crystal structures and average crystallite size of the synthesized electrode materials. The XRD graphs of the pristine Mn_3O_4, spinel $CuMn_2O_4$, and hybrid $CuMn_2O_4$/MWCNT electrode materials displayed sharp and intense Bragg peaks, thus indicating the crystalline nature of the electrode materials. According to the Joint Committee on Powder Diffraction Standards (JCPDS) data file obtained after XRD analysis of the pristine Mn_3O_4 electrode material, it indicated that the material exhibited a body-centered tetragonal crystal structure. The XRD graph of the pristine Mn_3O_4 material is shown in **Fig 4.14**, additionally displaying its crystal structure 3D model.

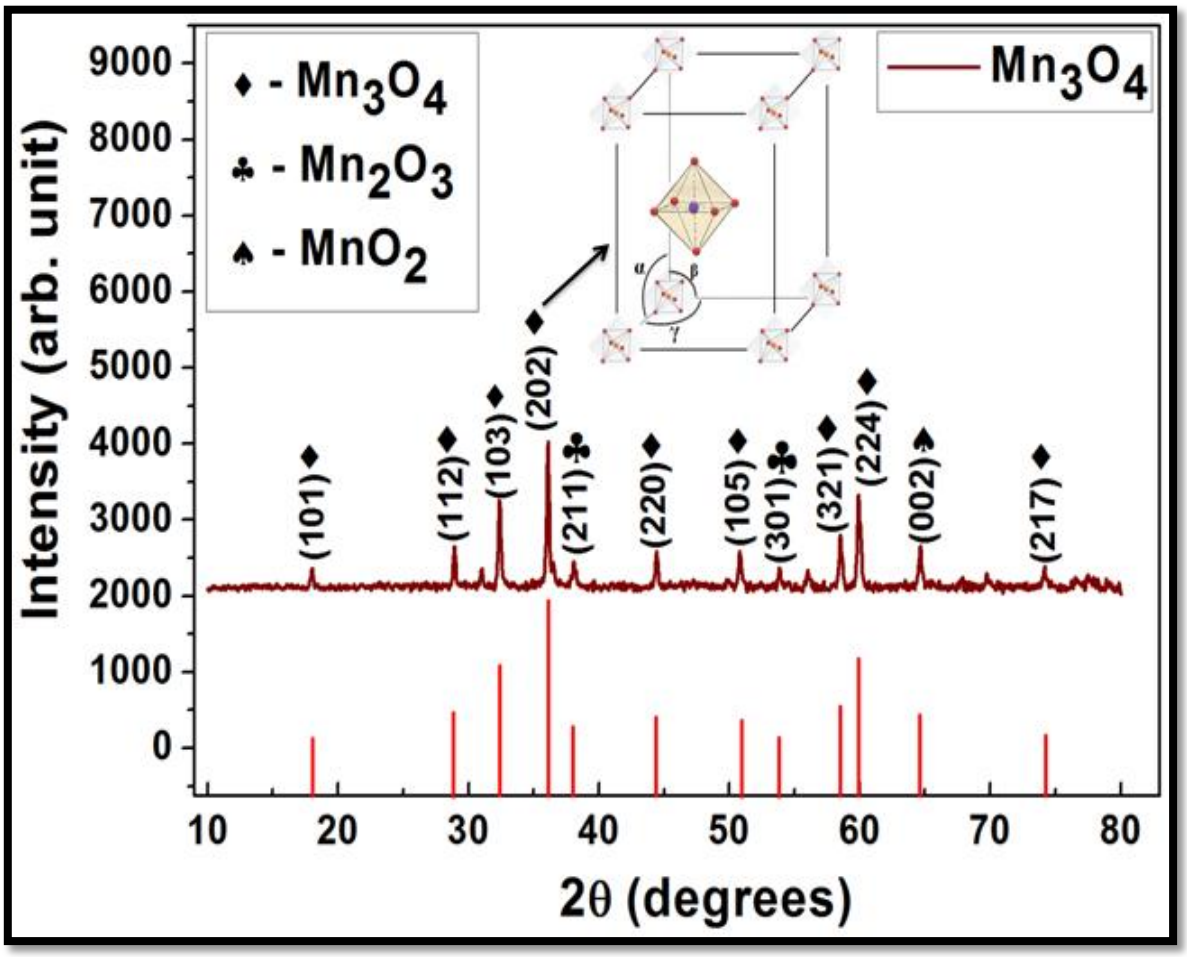

Figure 4.14: XRD pattern of the pristine Mn_3O_4 electrode material.

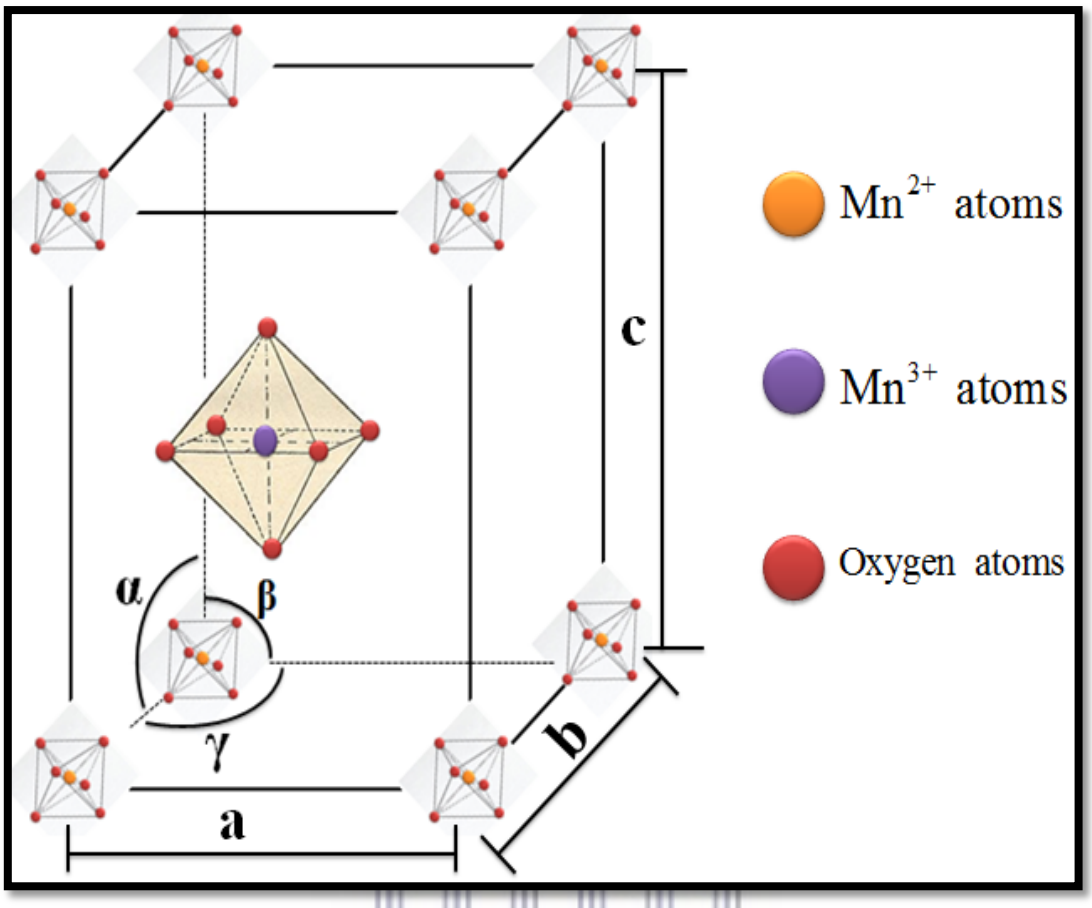

Figure 4.15: Body-centered tetragonal crystal structure of the pristine Mn_3O_4 material [162-163].

The figure above shows an expanded drawing of the crystal structure type obtained from the XRD JCPDS data file (JCPDS pattern: 00-024-0734). Although the figure was not drawn to scale, it can be noted that $a = b \neq c$, and $\alpha = \beta = \gamma = 90°$. Bragg's Law was used to calculate the inter-planar spacing (d) of each X-ray diffraction peak (Bragg peak) at its specific diffraction angle.

$$n\lambda = 2d\sin(\theta) \qquad (4.1 \text{ \& } 4.2)$$

$$\lambda = 2d\sin(\theta)$$

Where n, in this case, is considered as first order reflection $(n=1)$. The given parameters include $\lambda = 0.1540598$ nm, and the X-ray diffraction peaks at their specific 2θ positions (e.g. 2θ = 18.0° indicating the position of the first diffraction peak on the XRD plot). Therefore, from Bragg's Law, the equation below was used to calculate the inter-planar spacing for each diffraction peak at their respective 2θ positions.

$$d = \frac{\lambda}{2\sin(\theta)} \tag{4.3}$$

In the research of body-centered tetragonal crystal structures, it was reported that the only reflections allowed for this type of crystal system is when the sum of the (*h,k,l*) values, essentially being the miller indices, is equal to an even number (e.g 2, 4, 6, ..., etc) [164].

The XRD pattern of the Mn_3O_4 material in **Fig 4.14**, additionally identifies Bragg peaks indexed with miller indices that obeys the rules of crystallography for body-centered tetragonal crystal systems. The unit cell size (a) of the crystal lattice structure is also a lattice parameter that was calculated. This was achieved by relating the inter-planar spacing distance (d), with the miller indices of a specific Bragg diffraction peak illustrated in the Mn_3O_4 XRD graph.

$$\frac{1}{d^2} = \frac{h^2 + k^2}{a^2} + \frac{l^2}{c^2} \tag{4.4}$$

Where (d) = Inter-planar spacing and (a) = Unit cell size. The equation above is only valid for a body-centered tetragonal system (BCT), and in order to calculate the lattice parameters, it was best to use the following two reflections:

- The reflection (*h*, *k*, 0) can be used to calculate the unit cell size (a), and
- The reflection (0, 0, *l*) can be used to calculate the value of (c).

The value of (c) is known as the number of numerical constraints on the lattice parameters of the body-centered tetragonal (BCT) system.

The calculation for the value of (a – unit cell size) was performed with the use of the reflection $(220) \Rightarrow (hkl)$. **Equation (4.4)** was then rearranged by making (a) the subject of the formula, knowing that the value for *l* will substitute to zero.

$$\frac{1}{d^2} = \frac{h^2 + k^2}{a^2} + \frac{l^2}{c^2}$$ From equation (4.4)

Becomes zero

$$\frac{1}{d^2} = \frac{h^2 + k^2}{a^2} + \frac{(0)}{c^2} \qquad (4.5)$$

The zero substituted for *l* cancels out the $\left(\frac{l^2}{c^2}\right)$ term, thus leaving the expression in the following form:

$$a = \sqrt{d^2\left(h^2 + k^2\right)} \qquad (4.6)$$

The inter-planar spacing value (d) of the Bragg peak $(44.441° = 2\theta)$ at miller indices (220), was determined according to the illustrated calculation below:

$$d = \frac{0.1540598 \text{ nm}}{2\sin\left(\frac{44.441°}{2}\right)} \tag{4.7}$$

$$\therefore\ d = 0.2037 \text{ nm} \tag{4.8}$$

From this value, the unit cell size (a) was obtained by using **equation** (**4.6**).

$$a = \sqrt{(0.2037 \text{ nm})^2 (2^2 + 2^2)} \tag{4.9}$$

$$\therefore\ a = 0.5762 \text{ nm} \tag{4.10}$$

The number of numerical constraints (c) on the lattice parameters is mostly considered as one. However, for this structural system it was considered as 2, since the Bragg peak used to calculate the value (c) had miller indices (002). The following expression illustrates the calculation for the value of (c).

$$c = \sqrt{d^2 (l^2)} \tag{4.11}$$

$$c = \sqrt{(0.2037 \text{ nm})^2 (2^2)} = 0.4074 \text{ nm} \tag{4.12}$$

The average crystallite size (D) was lastly calculated from the Bragg peak $2\theta = 36.086°$, which is displayed as the most intense peak, having miller indices (211). Scherrer's equation was used to perform the following objectified calculation.

$$D_{(211)} = \frac{K\lambda}{\beta \cos(\theta)} \tag{4.13}$$

The Scherrer equation states that the average crystallite size (D) is equivalent to the product of the shape factor constant $(K = 0.89)$ and the wavelength of the X-rays (λ), divided by the product of the full width at half-maximum $(\text{FWHM} = \beta)$ height with the cosine of the angle of reflection $\left(\theta = \frac{2\theta}{2}\right)$, for the diffraction peak of interest. From the FWHM value obtained as 0.002059 after systematically calculating it using origin 8, the calculation for the average crystallite size $(D_{(211)})$ progresses in accordance to Scherrer's equation below.

$$D_{(211)} = \frac{(0.89)(0.1540598 \text{ nm})}{(0.002059)\cos\left(\frac{36.086°}{2}\right)} \tag{4.14}$$

$$\therefore \; D_{(211)} = 70.0362 \text{ nm} \tag{4.15}$$

The morphology obtained from the HR-TEM images of the pristine Mn_3O_4 material is correspondent to its crystallography data obtained from XRD analysis. The phase of the material was identified from its JCPDS file as Mn_3O_4 (Hausmannite, body-centered tetragonal crystal system) in an I41/*amd* space-group. The calculated lattice parameter $a = 0.5762$ nm, provided the indication that the Mn_3O_4 nanocrystals were of appropriate size to allow a variety of accepted electrolytes for transition metal oxides [165].

The ion dimension of K^+ and Li^+ in water is estimated to be 0.138 nm and 0.076 nm respectively [17]. Therefore, KOH and LiOH were used as suitable electrolytes during electrochemical measurements. The XRD plot of the synthesized $CuMn_2O_4$ nanoparticles in **Fig 4.16**, illustrated high intensities of (222), (311), (002), (044), and (311) diffraction patterns indexed into a face-centered cubic (FCC) Fd3m space-group spinel structure (according to the JCPDS data file no. 00-035-1030). The XRD pattern also revealed the presence of a few additional compound phases such as CuO and Mn_2O_3, within the spinel $CuMn_2O_4$ material. These residue peaks could have been attributed due to a low thermal energy subjected to the material during calcination treatment. This therefore caused some of the copper precursors to not completely bind with the manganese oxide precursors. In the study of spinel systems, it was reported that for the spinel compound $Cu_xMn_{3-x}O_4$ where $x = 1$, upon thermal treatment below 700 ℃ resulted in the formation of the spinel compound followed by additional phases [166]. Despite these additional phases being present in the XRD pattern, they do exhibit low intensities, thus allowing them to be ignored when performing the necessary lattice parameters and average crystallite size calculations of the purely phased spinel $CuMn_2O_4$.

According to the rules of crystallography for face-centered cubic (FCC) crystal systems, the only reflections permitted for this type of crystal system is when the Bragg diffraction peaks are indexed with miller indices that are either all even or all odd [167]. These primitive conditions are evidently obeyed and observed in the XRD pattern of the spinel $CuMn_2O_4$ material. The equation used in the calculation of the lattice parameters for this type of crystal system is less complex than that of tetragonal or orthorhombic systems.

$$\frac{1}{d^2} = \frac{\left(h^2 + k^2 + l^2\right)}{a^2} \tag{4.16}$$

$$\Rightarrow \; a^2 = d^2 . \left(h^2 + k^2 + l^2\right) \tag{4.17}$$

The most intense Bragg diffraction peak indexed with miller indices (222) was used for the calculation of the inter-planar spacing (d), unit cell size (a), and average crystalline size (D). The XRD graph, in **Fig. 4.16**, additionally indicated a 2θ position of $33.027°$ at which the Bragg diffraction peak occurred.

Inter-planar spacing calculation:

$$d = \frac{\lambda}{2\sin(\theta)} \tag{4.18}$$

$$d = \frac{0.1540598 \text{ nm}}{2\sin\left(\frac{33.027°}{2}\right)} \tag{4.19}$$

$$\therefore \ d = 0.2710 \text{ nm} \tag{4.20}$$

Unit cell size calculation:

$$a = \sqrt{d^2.\left(h^2 + k^2 + l^2\right)} \tag{4.21}$$

$$a = \sqrt{(0.2710 \text{ nm})^2 \left(2^2 + 2^2 + 2^2\right)} \tag{4.22}$$

$$\therefore \ a = 0.9388 \text{ nm} \tag{4.23}$$

Average crystalline size calculation:

$$D_{(222)} = \frac{K\lambda}{\beta\cos(\theta)} \tag{4.24}$$

Where the $\beta \Rightarrow$ FWHM value of the (222) Bragg peak was calculated as 0.001835

$$D_{(222)} = \frac{(0.89)(0.1540598\ \text{nm})}{(0.001835)\cos\left(\frac{33.027°}{2}\right)} \tag{4.25}$$

$$\therefore\ D_{(222)} = 77.9357\ \text{nm} \tag{4.26}$$

The calculation results of the lattice parameters indicated that the unit cell size $(a = 0.9388\ \text{nm})$ of the spinel $CuMn_2O_4$ FCC structured material is larger than the unit cell size $(a = 0.5762\ \text{nm})$ of the pristine Mn_3O_4 BCT structured material. This is attributable to the spinel $CuMn_2O_4$ FCC crystal structure containing 8 tetrahedral and 4 octahedral interstitial sites within the unit cell, at which the Cu^{2+} and Mn^{3+} cations are positioned. The structural design of the pristine and spinel materials obtained from XRD analysis is correspondent to the HRTEM images, which displayed the general shape of the materials. The average crystalline size of the spinel $CuMn_2O_4$ electrode material was additionally calculated as 77.9357 nm, which is slightly greater than that of the pristine Mn_3O_4 electrode material (70.0362 nm). The XRD graph of the $CuMn_2O_4$ electrode material, illustrated in **Fig. 4.16**, displayed Bragg diffraction bands at higher intensities compared to the band intensities exhibited by the Mn_3O_4 electrode material. These results are in good agreement with Raman and small-angle X-ray scattering (SAXS) analysis data, which also illustrated greater peak intensities exhibited by the spinel $CuMn_2O_4$ compared to that of the pristine Mn_3O_4 electrode material.

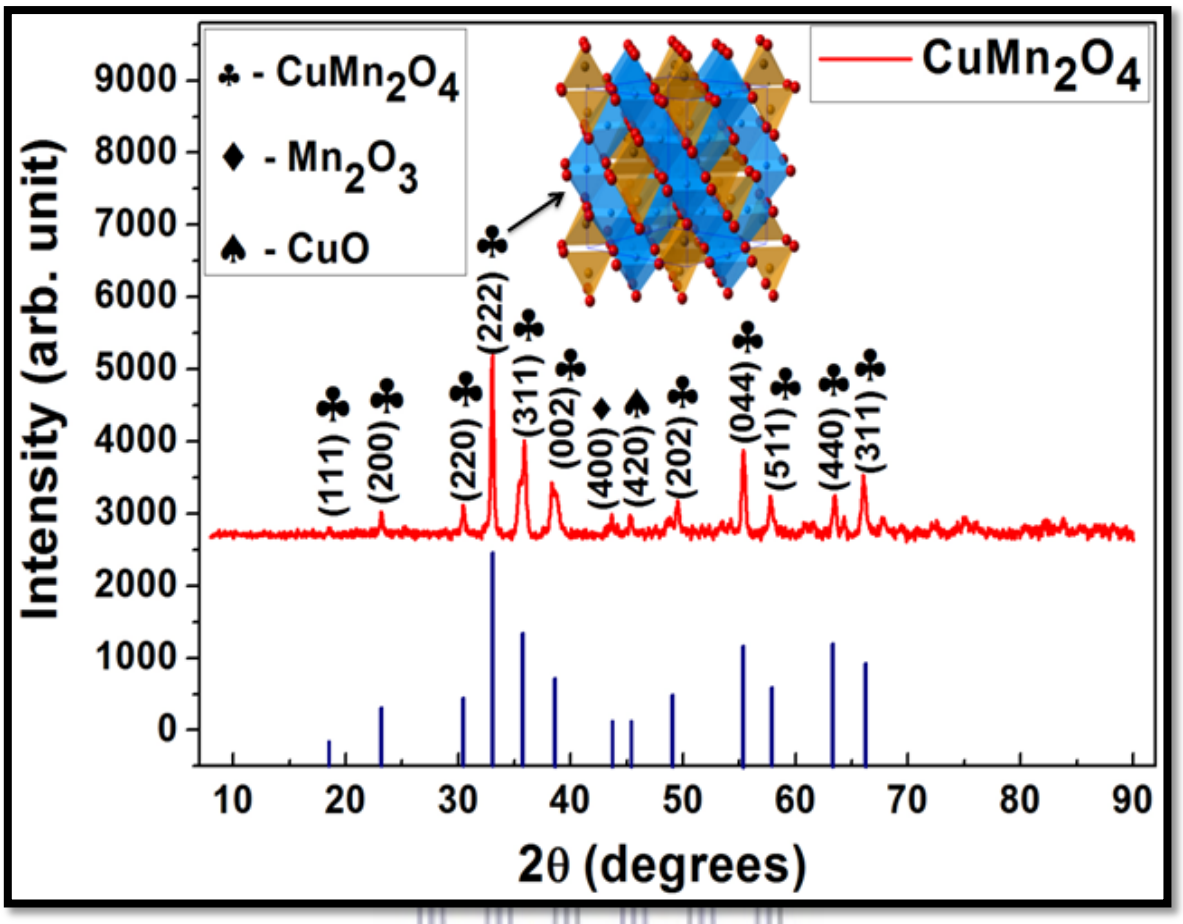

Figure 4.16: XRD pattern of the spinel $CuMn_2O_4$ electrode material.

The main Bragg diffraction bands located at approximate 2θ positions of 33°, 36°, 38°, 55°, and 66°, for the spinel $CuMn_2O_4$ phase, were displayed as sharper and stronger peaks compared to the most intense Bragg diffraction bands of the pristine Mn_3O_4 phase [168]. This observation implied that the spinel $CuMn_2O_4$ electrode material possessed a more stable crystallinity and an increased average particle size, confirmed by the calculated lattice parameters. As mentioned before, as well as displayed in **Fig. 4.16**, there are additional phases (Mn_2O_3 and CuO) within the FCC spinel $CuMn_2O_4$ structured material. However, the Mn_2O_3 phase is also present within the body-centered tetragonal (BCT) Mn_3O_4 crystal structure, as confirmed by the material's XRD graph. Comparing the Mn_3O_4 pattern with that of $CuMn_2O_4$ and identifying the location of the Mn_2O_3 phase, indicated that the assigned Mn_2O_3 Bragg diffraction band indexed as (400) on the $CuMn_2O_4$ pattern, slightly shifted to a higher diffraction angle. This intriguing observation is ascribed to the attachment of Cu^{2+} ions onto the Mn^{3+} octahedral interstitial sites, thus formulating a larger spinel-type unit cell, and hence providing additional ionic vacancies [169]. The crystal structure model of the spinel

$CuMn_2O_4$ material displays Cu^{2+} tetrahedral atomic structures on the 6-faces and 8-corners of the FCC unit cell. Additionally, the Mn^{3+} octahedral atomic sites, originating from the BCT Mn_3O_4 crystal structure, is situated inside the unit cell, as well as in-between the 8-corner Cu^{2+} interstitial sites [170]. As observed from the 2D structural representation of the hybrid $CuMn_2O_4$/MWCNT electrode material, the Cu^{2+} tetrahedral and Mn^{3+} octahedral interstitial sites bind to the MWCNT structures during synthetic protocol, which is microscopically confirmed by SEM and HR-TEM analysis. The XRD graph of the hybrid $CuMn_2O_4$/MWCNT electrode material is illustrated in **Fig. 4.18**, together with an inset pattern of the functionalized MWCNTs.

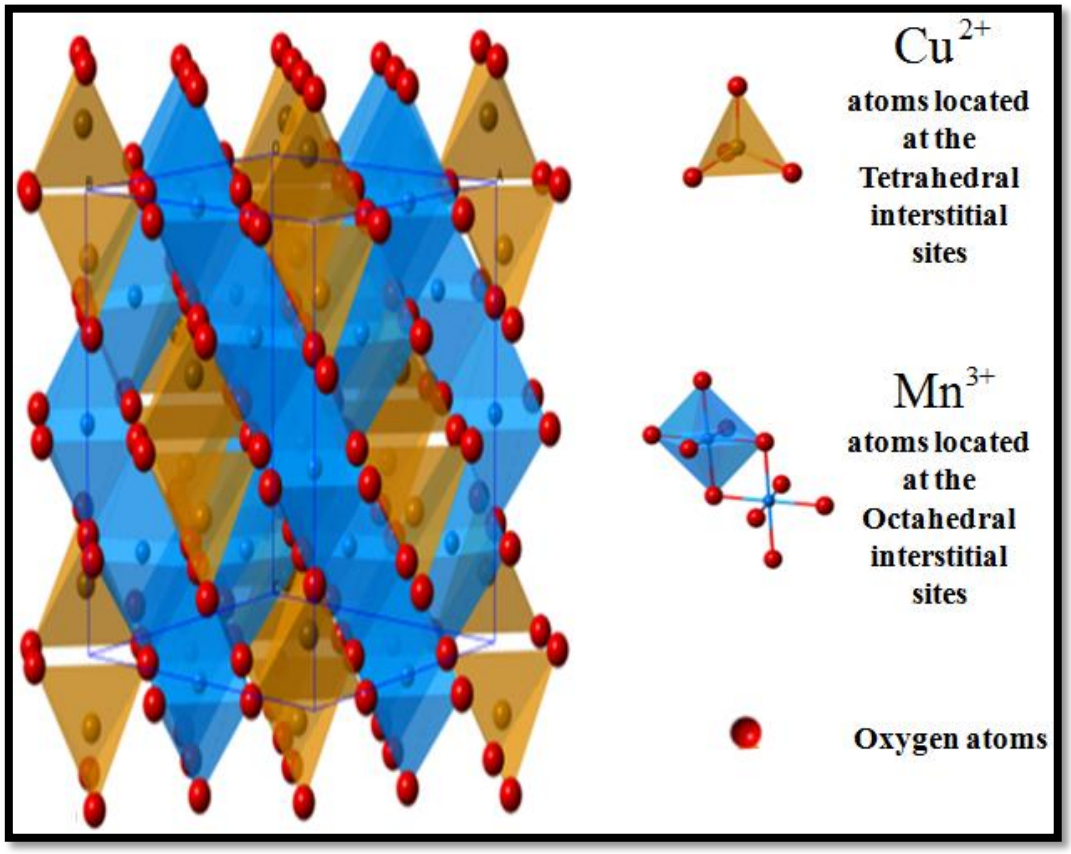

Figure 4.17: Spinel face-centered cubic crystal structure of $CuMn_2O_4$ material [171-174].

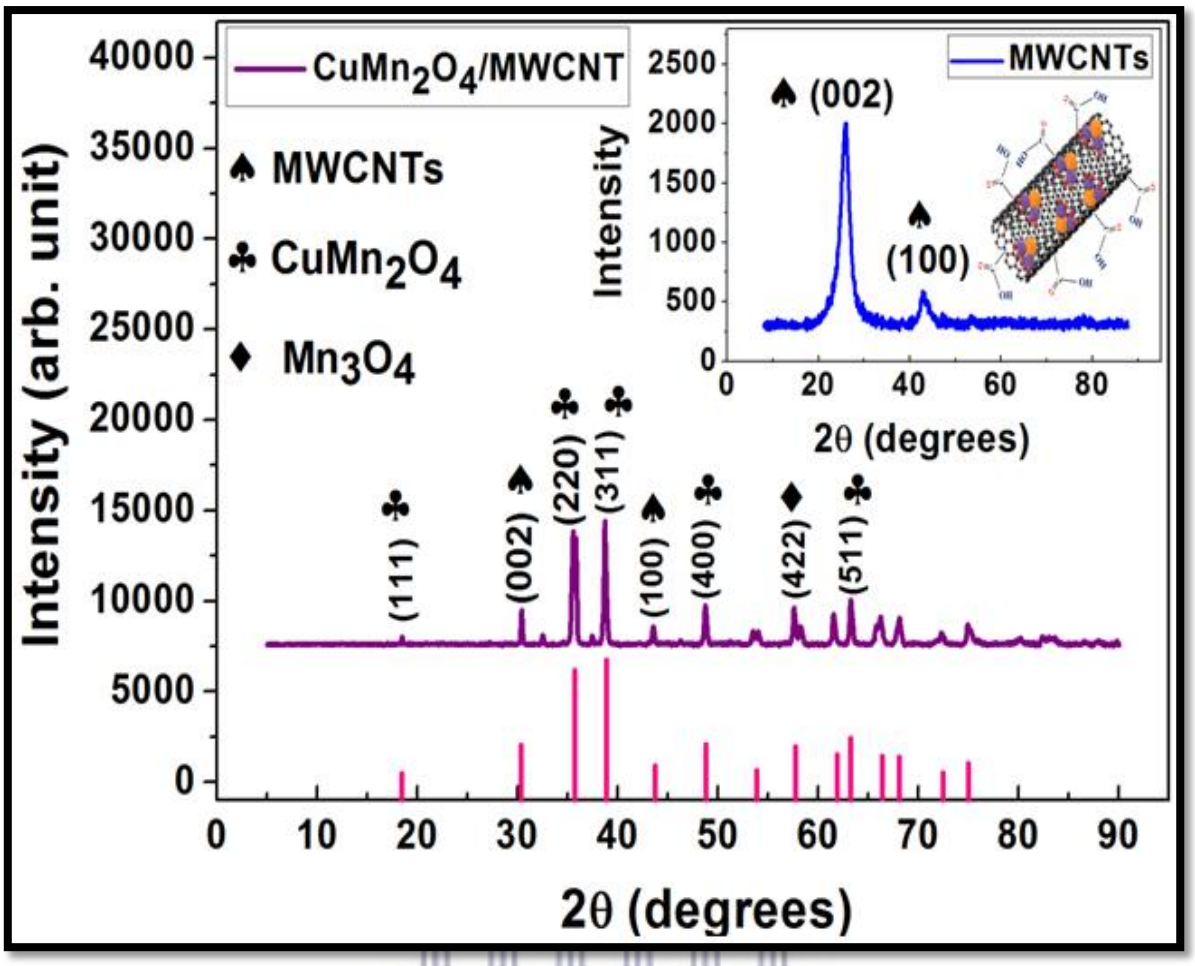

Figure 4.18: XRD pattern of the hybrid $CuMn_2O_4$/MWCNT electrode material.

The XRD graph of the as synthesized hybrid $CuMn_2O_4$/MWCNT electrode material illustrated high intensity Bragg diffraction peaks at 2θ reflection angles of 30,425°, 35.592°, 38.706°, 48.643°, 57.752°, and 63.350° assigned to their respective miller indices (002), (220), (311), (400), (422), and (511). These atomic crystalline planes are indexed according to the existence of a $Cu_{1.4}Mn_{1.6}O_4$/MWCNT phase (Joint Committee on Powder Diffraction Standards, JCPDS pattern no. 00-048-1548), with a Fd3m space group characteristic to FCC crystal systems [175]. The inter-planar spacing distance (d), unit cell size (a), and average crystalline size (D), for the hybrid $CuMn_2O_4$/MWCNT electrode material, was calculated by using the most intense Bragg diffraction band with indexed miller indices (311). The calculated values were obtained as d = 0.2324 nm, a = 0.7708 nm, and $D_{(311)}$ = 51.2610 nm, respectively. The small crystalline size of the $CuMn_2O_4$/MWCNT composite compared to that of the spinel $CuMn_2O_4$ material, is ascribed to the broad and high intensity XRD diffraction bands. Notably, the diffraction peaks indicating the spinel $CuMn_2O_4$ phase within

the hybrid $CuMn_2O_4$/MWCNT composite marginally shifted towards greater reflection angles, thus suggesting the occurrence of structural distortion [176]. This result could additionally be attributed to the stoichiometric mole fraction of the Cu^{2+} and Mn^{2+} constituents. The calculated average crystalline particle size for the hybrid composite electrode material is in good agreement with microscopic (HR-TEM) and spectroscopic (SAXS) analysis results. It is illustrated in **Fig. 4.19** below, displaying a 2D-model of the hybrid $CuMn_2O_4$/MWCNT structure, that the Cu^{2+} ions from the spinel $CuMn_2O_4$ complex strongly interacts with the sp^2 and sp^3 hybridized carbon atoms of the MWCNTs. This pictorial representation of the hybrid $CuMn_2O_4$/MWCNT structure is spectroscopically confirmed by the D and G bands, indicating the presence of sp^3 (C-C) and sp^2 (C=C) hybridized atoms within the analyzed $CuMn_2O_4$/MWCNT material, appearing on the obtained $CuMn_2O_4$/MWCNT Raman spectrograph.

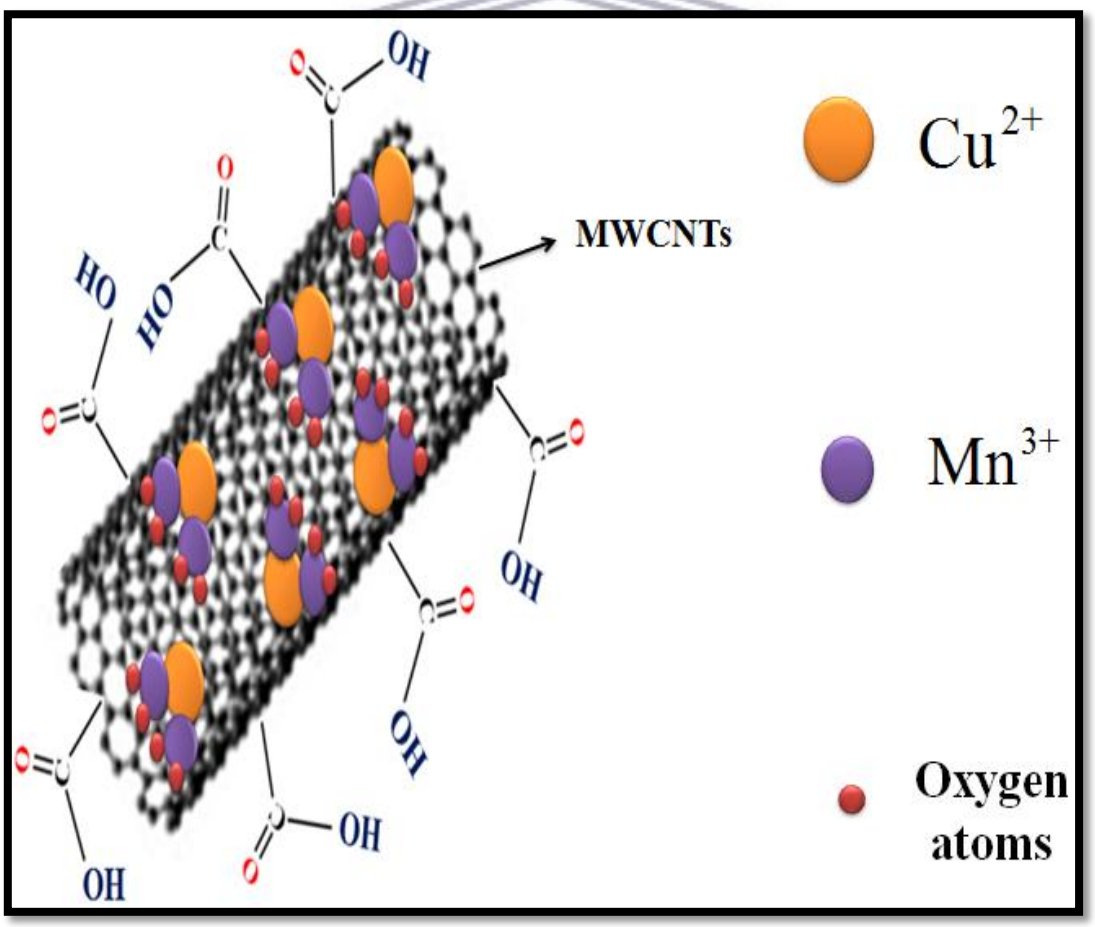

Figure 4.19: Structural model of the hybrid $CuMn_2O_4$/MWCNT electrode material [110].

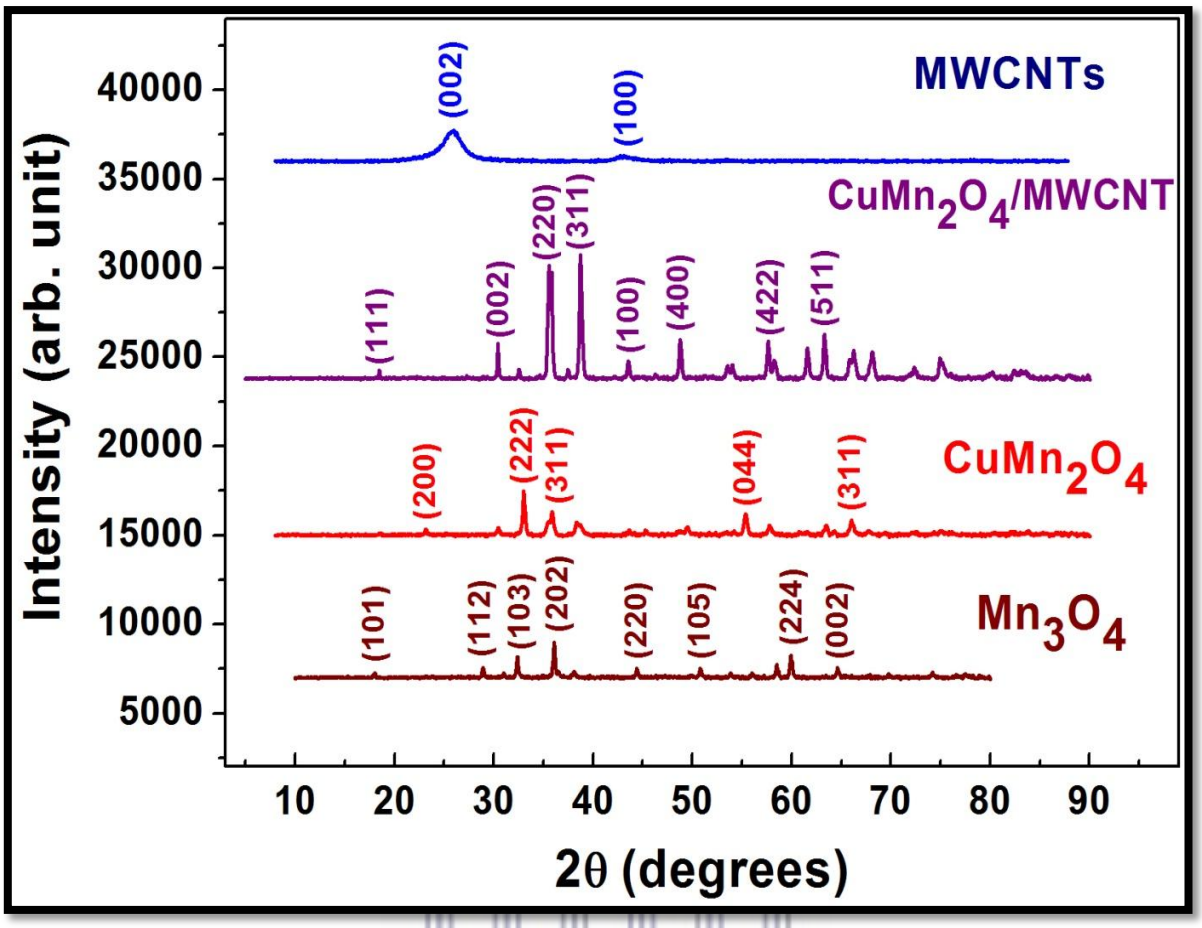

Figure 4.20: Comparative XRD patterns of the pristine Mn_3O_4, spinel $CuMn_2O_4$, and hybrid $CuMn_2O_4$/MWCNT electrode materials.

Table 4.1: Summary of the crystallographic parameters calculated from the XRD patterns of the pristine Mn_3O_4, spinel $CuMn_2O_4$, and hybrid $CuMn_2O_4$/MWCNT electrode materials.

Parameter	Pristine Mn_3O_4	Spinel $CuMn_2O_4$	Hybrid $CuMn_2O_4$/MWCNT
Average crystallite size D, (nm)	74.0362	77.9357	51.2610
Inter-planar spacing $d_{h,k,l}$, (nm)	0.2037	0.2710	0.2324
Unit cell size a, (nm)	0.5762	0.9388	0.7708

4.2.2 Fourier Transform-Infrared Spectroscopic Studies

FT-IR spectroscopy was used to evaluate the various functional groups present within the pristine Mn_3O_4, spinel $CuMn_2O_4$, and hybrid $CuMn_2O_4$/MWCNT electrode materials in order to obtain additional information regarding their specific structure. The FT-IR spectra of the pristine, spinel, and hybrid materials are presented in **Fig. 4.21**. For the pristine Mn_3O_4 electrode material, the broad band within the region of 3660 – 3000 cm^{-1} can be ascribed to the symmetric and asymmetric stretching vibration modes of the hydroxyl (O – H) group from the solvent residual ultra – pure water [171, 177]. The intense absorption bands within the low wave number range of 400 – 700 cm^{-1} are correspondent to the presence of the Mn – O bonds, which appear consistently in each spectra, indicating good quality synthesized electrode materials [178]. The absorption band peaks at 1023 cm^{-1} and 1620 cm^{-1} are present as a result of the C – O stretching vibrations, possibly from the un-reacted residual diethylene glycol used during the pristine Mn_3O_4 electrode material synthetic procedure [179].

The FT-IR spectrograph of the synthesized spinel $CuMn_2O_4$ nanoparticles displayed absorption band peaks at 531 cm^{-1}, 592 cm^{-1}, 668 cm^{-1}, 1421 cm^{-1}, 1640 cm^{-1}, and 3430 cm^{-1}, as illustrated in the plot of **Fig. 4.21**. The broad absorption band, which appeared within the wave-number range of 3000 – 3700 cm^{-1}, is analogous to the stretching vibration modes of the hydroxyl (O – H) group originating from the ultra – pure water (H_2O) molecules physically adsorbed onto the electrode material surface [179]. This adsorption of water molecules improve the wettability of the electrode material, which deals with the surface tension between the electrolyte solution (containing K^+/OH^- or Li^+/OH^- electrolyte ions) and the solid electrode material surface. The enhanced wettability of the electrode material would then subsequently strengthen the intermolecular force interactions between the electrolyte ions and the electrode material surface during ionic-diffusion processes. The absorption bands observed at approximately 531 cm^{-1} and 688 cm^{-1} in the FT-IR spectrum is characteristic to the vibration modes of tetrahedral Cu^{2+} - O^{2-} and octahedral Mn^{3+} - O^{2-} site groups, respectively. The final absorption band accounted for is the one observed at 1640 cm^{-1}, which is correspondent to the (C=O) carbonyl group probably resulting from small quantities of un-reacted citric acid monohydrate ($C_6H_8O_7$. H_2O) used during the material synthetic procedure. The FT-IR spectrograph for the hybrid $CuMn_2O_4$/MWCNT electrode material displayed the essential absorption bands corresponding to the hydroxyl (O – H) and

metal precursor (Mn – O, Cu – O) functional groups [180]. However, in order to identify the absorption band analogous to the incorporated multi-walled carbon nanotube (MWCNT) structure, it was necessary to perform FT-IR analysis on the acid treated MWCNTs alone. The FT-IR spectrum for the acid treated MWCNTs, displayed as an inset to the plot of the hybrid $CuMn_2O_4$/MWCNT material, illustrated the generic broad hydroxyl (O – H) group band at approximately 3440 cm^{-1}. The absorption band observed around 1630 cm^{-1} is correspondent to the (C = C) vibration bonds, arising from the sp^2 hybridized carbon atoms of the acid functionalized MWCNTs. The two spectrographs additionally resembled the absorption band located at 1630 cm^{-1} (indicating the presence of {C = C} symmetric stretching), which provided the indication of strong molecular bonding between the MWCNT structures and the spinel $CuMn_2O_4$ nanoparticles.

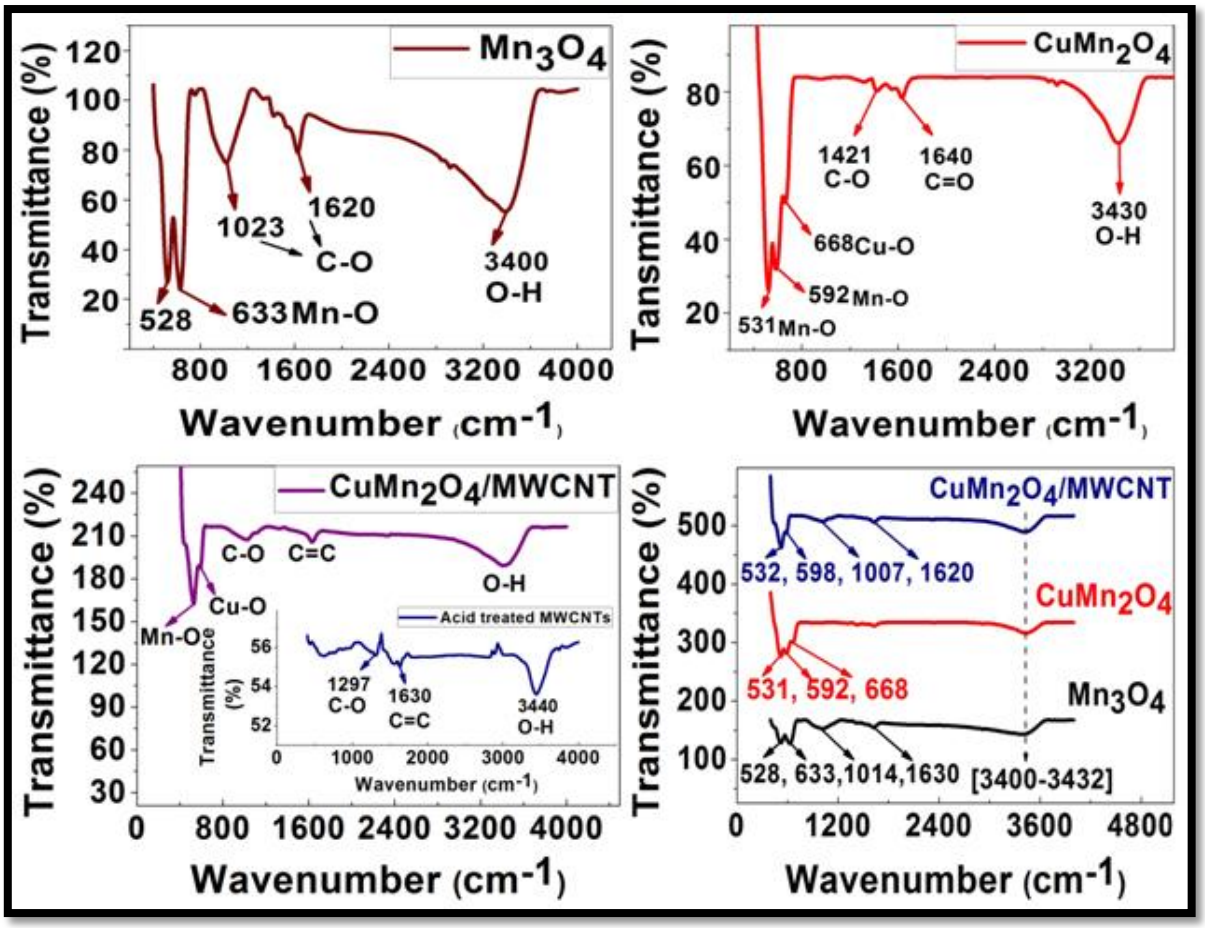

Figure 4.21: FT-IR spectrographs of the pristine Mn_3O_4, spinel $CuMn_2O_4$, and hybrid $CuMn_2O_4$/MWCNT electrode materials.

4.2.3 Raman Spectroscopy

Raman spectroscopy is a spectroscopic technique where a Raman spectrograph is obtained after analysis, which provides the molecular fingerprint of the specified electrode material sample. Raman spectroscopy was used to obtain bond vibration and rotation information of particular molecules that are present within the pristine Mn_3O_4, spinel $CuMn_2O_4$, and hybrid $CuMn_2O_4$/MWCNT electrode materials. The Raman spectrum of the pristine Mn_3O_4 electrode material displayed a low intensity Raman band at approximately 485 cm^{-1}, which is attributed to the Mn – O stretching and vibration modes of the octahedral MnO_6 sub-lattices within the Mn_3O_4 body-centered tetragonal (BCT) crystal structure [180]. This peak is related to the A_{1g} stretching mode, which corresponds to the symmetric stretching of the basal oxygen atoms of the octahedral MnO_6 sub-lattices [180-181]. The Raman spectrum of the spinel $CuMn_2O_4$ electrode material displayed almost similar active band positions to that of the pristine material, as well as with greater Raman intensities. The increased Raman intensities over that of the pristine Mn_3O_4 electrode material is attributed to the more stable face-centered cubic (FCC) crystal structure of the spinel $CuMn_2O_4$ electrode material [182]. The Raman band located at approximately 90 cm^{-1}, can be correspondent to a distortion of atoms and molecules occurring within the spinel $CuMn_2O_4$ FCC structure due to a phenomenon known as the Jahn-Teller effect [183]. This Raman active band is indexed as (Cu – O) due to the Cu^{2+} ions evidently being the cause of the Jahn-Teller distortion occurrence, which unfortunately leads towards the formation of a less asymmetric crystal lattice structure [184]. The peak may additionally be ascribed to the t_{2g} stretching mode due to it having a lower Raman intensity [185].

The hybrid composite, $CuMn_2O_4$/MWCNT, electrode material displays more intense Raman active bands on its spectrograph than that of the pristine and spinel electrode materials. This is attributed to the crystal structure of the $CuMn_2O_4$/MWCNT material being more stable, thus allowing improved charge/discharge rate capabilities [186]. The Raman bands situated at 340 cm^{-1} and 488 cm^{-1} is representative of the Cu(II) (t_{2g}) and Mn – O (A_{1g}) stretching/vibration modes, respectively [187]. The plot displayed as an inset to the Raman spectrum of the hybrid electrode material is an enlarged representation of the two partially distinctive peaks indicating the incorporation of multi-walled carbon nanotubes (MWCNTs) to the spinel $CuMn_2O_4$ FCC structure. These two relatively distinctive Raman bands

positioned at 1467 cm^{-1} and 1529 cm^{-1} is ascribed to the D and G-bands of the MWCNTs within the hybrid electrode material matrix [188]. The D-band represents the disorder of sp^3 (C-C) hybridized carbon atoms within the complex MWCNTs network of the hybrid $CuMn_2O_4$/MWCNT electrode material [189]. The superior structural stability of the hybrid electrode material over that of the pristine and spinel electrode materials is represented by the increased Raman peak intensities as well as the G-band, which indicates the sp^2 (C=C) hybridized carbon atoms of the MWCNT lattice structures [190]. The sp^2 carbon hybridized atoms is what mainly contributes towards the structural stability of the hybrid material matrix. This statement is evident from the plot of the hybrid $CuMn_2O_4$/MWCNT electrode material, since the intensity of the G-band (150 a.u) is slightly greater than that of the D-band (137 a.u). The Raman band vibration peaks occurring within the shift range of (2430-2435 cm^{-1}) for each material is a result of the required gel used during sample preparation [191].

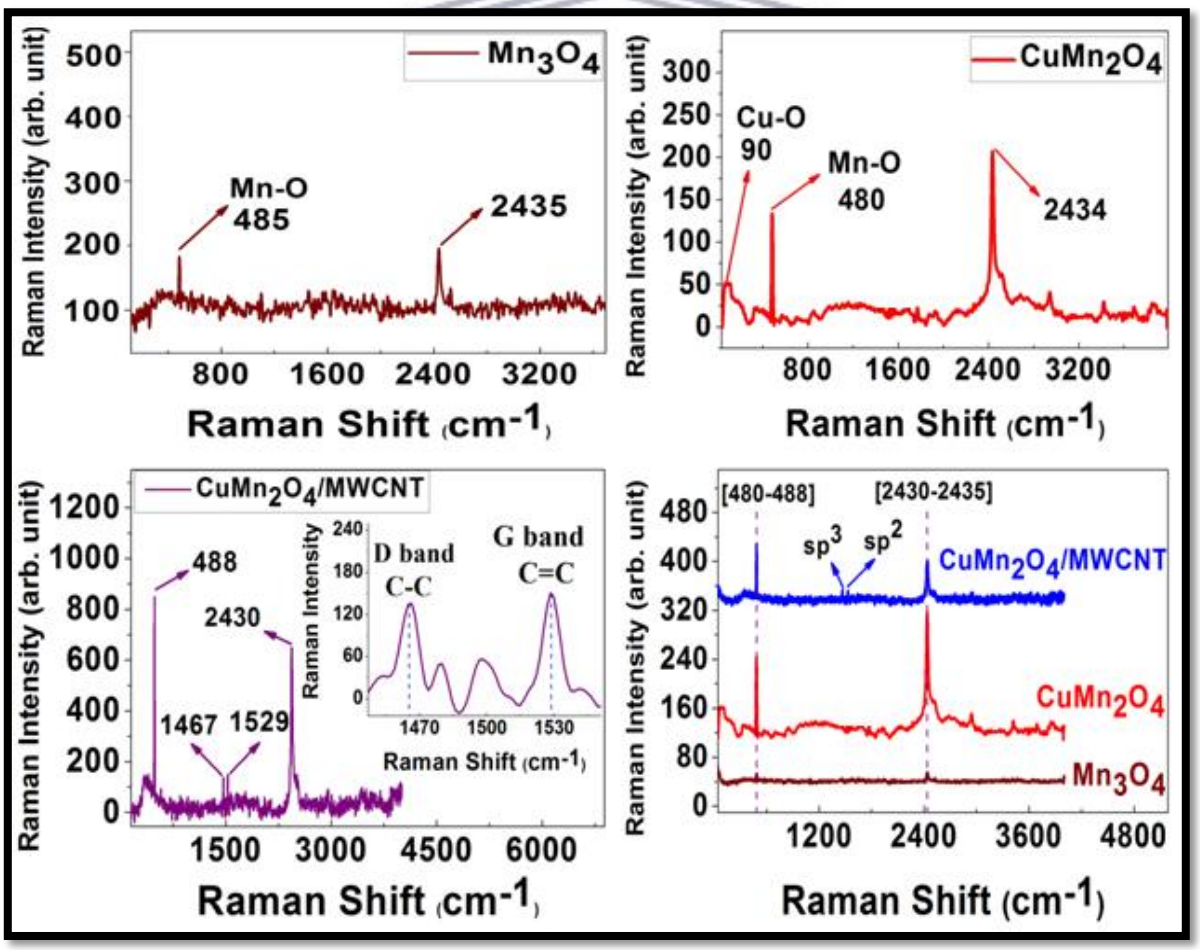

Figure 4.22: Raman spectrographs of the pristine Mn_3O_4, spinel $CuMn_2O_4$, and hybrid $CuMn_2O_4$/MWCNT electrode materials.

4.2.4 Small – Angle X – ray Scattering (SAXS) analysis

The Small – Angle X – ray Scattering (SAXS) technique is an analytical method used to determine the structure of particle systems concerning their average particle sizes or shapes [192]. SAXS was used to perform the analysis of the nanoparticle size distribution of the pristine Mn_3O_4, spinel $CuMn_2O_4$, and hybrid $CuMn_2O_4$/MWCNT composite electrode materials. **Fig. 4.23 (a)** illustrates the pair-distance distribution function (PDDF) of the investigated electrode materials. This function is represented as a histogram of atomic distances, indicating the average particle sizes of the nanoparticles present within the electrode material structure [193]. Firstly, apart from average particle sizes, the PDDF curve additionally provides information concerning the particle shape, according to some classified key features of various PDDF curves that are indicative to specific particle shapes [194]. The PDDF curve of the pristine Mn_3O_4 electrode material illustrated a rather poly-dispersed distribution of spherical/globular nanoparticles over a distance domain of 50 – 160 nm. It is noted that particle shape information extracted from SAXS analysis is often considered as ambiguous data and requires additional information from electron microscopic techniques to absolutely confirm the shape of the nanoparticles [194]. The majority of uniformly distributed spherical shaped Mn_3O_4 nanoparticles illustrated small-angle scattering patterns with average particle sizes ranging between 60 – 90 nm [75]. However, a decrease in the scattering fraction number (P) was observed within the average size range of 110 – 160 nm, thus indicating aggregation occurrence of the bigger Mn_3O_4 nanoparticles [75]. The condensation and aggregation of nanoparticles is a result of the Van-der-Waals interactions between the particles, thus causing them to be attracted to one another once they have reached a minimum inter-particle space distance [194].

The PDDF profile of the spinel $CuMn_2O_4$ electrode material displayed less aggregation, which is attributed to the more stable FCC crystal structure of the $CuMn_2O_4$ material complex confirmed from XRD analysis. The curve additionally indicated spherical shaped nanoparticles with average particle sizes ranging between 70 – 110 nm. These results implied that the spinel $CuMn_2O_4$ nanopaticles had bigger particle sizes compared to the pristine Mn_3O_4 nanoparticles, which was confirmed by microscopic (SEM and HR-TEM) and structural (XRD) analysis. The PDDF profile of the hybrid $CuMn_2O_4$/MWCNT electrode material illustrated a bell shaped almost symmetrical peak, with average particle sizes

ranging between 50 – 108 nm. All-inclusive, the hybrid $CuMn_2O_4$/MWCNT electrode material illustrated the best nanoparticle-distance distribution with justifiable average particle sizes. **Fig. 4.23 (b)** represents the SAXS particle size distribution by number function of the synthesized electrode materials. The function indicated that the smaller particles at small-scale scattering angles exhibited greater intensities than that of the bigger particles at large-scale scattering angles. This, therefore, implied that the intensity of smaller particles eclipsed that of larger particles, which is attributed to the occurrence of agglomeration/aggregation within the larger particles [195]. This result was similarly obtained in the SAXS particle size distribution by volume function, **Fig. 4.23 (c)**, but with greater intensities. However, the opposite result was obtained in **Fig. 4.23 (d)**, representing the size distribution by intensity function, due to the larger particles exhibiting dominated intensities over that of the smaller particles.

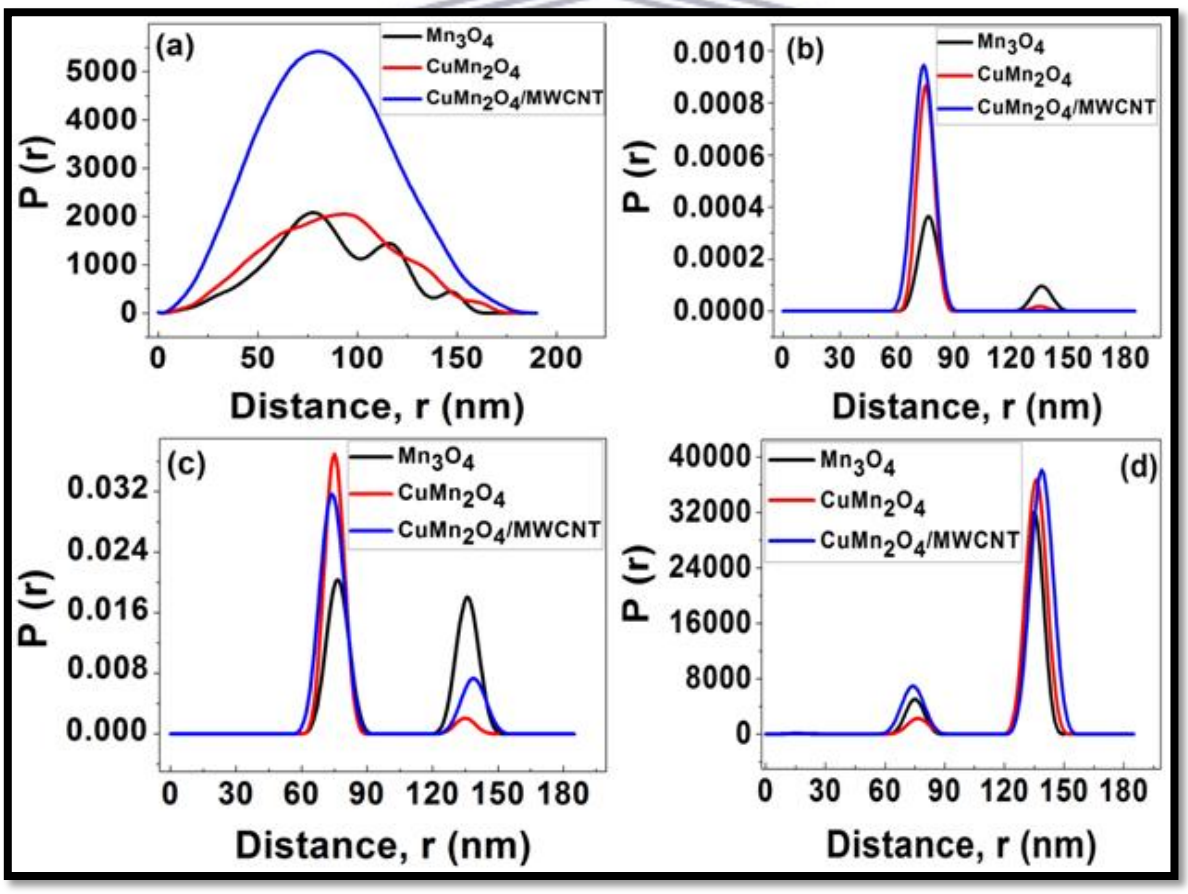

Figure 4.23: SAXS particle size distribution in (a) PDDF profiles, (b) size by number, (c) size by volume, and (d) size by intensity of the pristine Mn_3O_4, spinel $CuMn_2O_4$, and hybrid $CuMn_2O_4$/MWCNT electrode materials.

4.2.5 Thermo-Gravimetric Analysis (TGA)

The thermal stability and phase transformation of the synthesized powder-form pristine Mn_3O_4, spinel $CuMn_2O_4$, and hybrid $CuMn_2O_4$/MWCNT electrode materials were investigated by employing thermo-gravimetric analysis (TGA), as shown in **Fig. 4.25**. TGA experiments were conducted by rapidly heating the sample materials from room temperature up to 900 ℃ with a ramping heating rate of 15 ℃/min under continuous nitrogen gas flow. The TGA analysis plot of the pristine Mn_3O_4 electrode material indicated an initial weight loss of 2.3% within a temperature range of 140 – 300 ℃. This inceptive weight loss percentage is ascribed to the volatilization of weakly adsorbed water molecules from the surface of the Mn_3O_4 nanoparticles [196]. An exothermic peak located at 485 ℃ is correspondent to the phase transformation of the pristine electrode material from Mn_3O_4 to Mn_2O_3, as a result of oxidation/reduction processes occurring at high temperatures [197]. The consequential liberation of oxygen atoms resulting from the oxidation of Mn_3O_4 to Mn_2O_3 yielded a considerable weight loss of 54.7% from the initial 2.3% weight loss. The weight loss of the pristine Mn_3O_4 electrode material remained constant at temperatures greater than 600 ℃, thus indicating the completion of thermal stability analysis for the investigated material sample [198].

The TGA analyzed plot of the spinel $CuMn_2O_4$ electrode material displayed decomposition peaks within the temperature range of 103 – 501 ℃, which is surprisingly lower than the decomposition temperature range of 94 – 600 ℃ exhibited by the pristine Mn_3O_4 electrode material. This typically implied that the spinel $CuMn_2O_4$ electrode material exhibited a lower thermal stability than that of the pristine Mn_3O_4 electrode material. However, it was expected for the introduction of MWCNTs to the $CuMn_2O_4$ nanoparticle surface to improve its physical and thermal stability, as well as its electrochemical performance [199]. Similar to the TGA plot of the pristine Mn_3O_4 electrode material; the TGA profile of the spinel electrode material illustrated an initial weight loss of approximately 7.5%, attributed to moisture and adsorbed water molecules across the electrode material's surface area [200]. The second decomposition peak, illustrating weight loss, can be observed from 240 ℃ to 518 ℃, which is assigned to the oxidation of $CuMn_2O_4$ to CuOOH + 2MnOOH as confirmed by CV analysis. The weight loss of the spinel $CuMn_2O_4$ electrode material remained constant at temperatures beyond 500 ℃, thus providing additional confirmation of the decrease in

thermal stability exhibited by the spinel electrode material. The TGA thermograph of the hybrid $CuMn_2O_4$/MWCNT electrode material displayed a broader temperature domain with no indication of constant weight loss at temperatures greater than 800 ℃. From this result, it was positively confirmed that the hybrid composite electrode material possessed a greater thermal and structural stability than that of the pristine and spinel electrode materials [201]. The hybrid $CuMn_2O_4$/MWCNT TGA thermograph, much like the TGA graphs of the pristine and spinel materials, displayed an initial weight loss of 0.53 %, attributed to the release of adsorbed water molecules, as well as un-reacted polyvinylpyrrolidone (PVP) from the electrode material surface. The second significant weight loss occurring within the temperature range of 492 – 897 ℃ is attributed to the thermal decomposition of carbon, in the form of carbon dioxide (CO_2), from the acid functionalized MWCNT network structures [202].

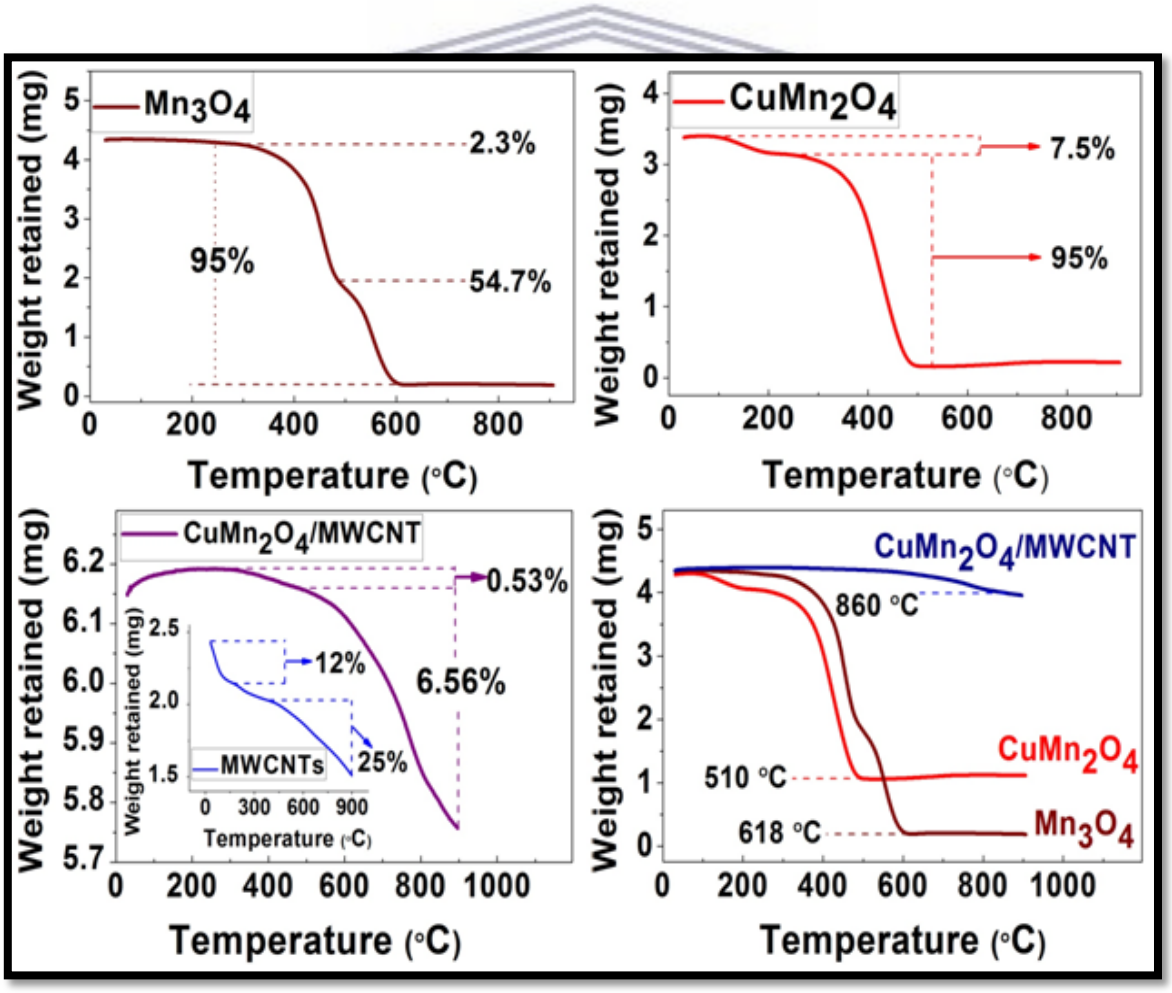

Figure 4.24: TGA thermographs of the pristine Mn_3O_4, spinel $CuMn_2O_4$, and hybrid $CuMn_2O_4$/MWCNT electrode materials.

4.3 Electrochemical Characterization

4.3.1 Cyclic Voltammetry analysis and interpretation

4.3.1.1 Electrochemical studies of half cell (three-electrode) system with 3 M KOH electrolyte

The cyclic voltammetry technique was used to perform the specific charge and discharge capacitance calculations for each of the synthesized materials, starting from the pristine manganese oxide/trimanganese tetraoxide (Mn_3O_4) to the hybrid $CuMn_2O_4$/MWCNT electrode material. However, in order to perform the calculation, it was initially required to determine the integrated area under the anodic reduction peak at the lowest scan rate run (which was 5 mV/s). The calculation was done from CV experimental data run at a low scan rate, as low scan rates provide sufficient time for ions to be transferred between the electrolyte and the electrode surface.

From the definition of capacitance, which states that the capacitance (F) is the ability to store an electric charge, it was possible to calculate the specific discharge capacity from the integrated area value of the cathodic reductive current verses potential peak.

$$C = \frac{Q}{\Delta V} \tag{4.27}$$

Where C = the calculated specific discharge capacitance, Q = the total charge stored on the electrode surface after the charging process, and ΔV is the potential window $(\Delta V = V_f - V_i)$. Since $Q = It$, we can substitute it into the above equation to form a new specific capacitance expression illustrated below.

$$C = \frac{I\Delta t}{\Delta V} \tag{4.28}$$

The electrochemical cell device, which is the three-electrode assembly, consisted of the working electrode (nickel foam current collector onto which active electrode material was coated) against the Ag/AgCl (3 M KCl) reference electrode and counter (platinum wire) electrode. The cell device additionally contained a 3 M KOH aqueous electrolyte solution, and was operated within a potential window of 0-0.65 V. The low selected potential window was merely initiated for test purposes; however, it was gradually increased over further experimental analysis. The actual mass of the active electrode material coated on the nickel foam current collector was obtained by initially subtracting the mass of the bare non-coated Ni-foam substrate, from the mass of the coated Ni-foam electrode. Since the active material makes up 70% of the entire slurry paste mixture, the mass of the coated slurry mixture from the previous subtraction calculation was then multiplied by 70% to obtain the active material mass within the slurry mixture. This mass calculation is required as it is involved in the specific capacitance equation illustrated below.

$$C_{sp} = \frac{Q_E}{\Delta V \text{ x } M_E} \tag{4.29}$$

Where C_{sp} = the specific charge/discharge capacitance, Q_E = the total charge stored on the electrode surface, and M_E = the mass of the active electrode material coated on the Ni-foam current collector. From these identified parameters, the following strategy was employed for the C_{sp} calculation. The specific capacitance of the Mn_3O_4 material was calculated by initially finding the integrated area of the anodic peak at the lowest selected scan rate (which was run at 5 mV/s). An integration tool, which is available with the EC-Lab analysis and data processing software on the computer system, was used to obtain the integral value. This program does not change the raw data file after performing the mathematical analysis. The integrated area value, measured in Ampere-Volt (AV), indicates the total amount of current that flows through the electrode during the oxidation process of the active material at the electrode surface. The integral area value of a selected trace between two points on the anodic peak curve was calculated as 0.00075 AV from **equation (4.30)**.

$$\text{Total Charge}\left(Q_{\text{Total}}\right)=\frac{\left|\int_{E_1}^{E_2} i.dV\right|}{\text{Scan rate}\left(\frac{\text{V}}{\text{s}}\right)} \tag{4.30}$$

The total quantity of charge accumulated on the surface of the electrode during oxidation processes was obtained as illustrated in the calculation below.

$$Q=\frac{0.00075(\text{AV})}{0.005\left(\frac{\text{V}}{\text{s}}\right)}=0.15\,\text{As}=0.15\text{ Coulombs} \tag{4.31}$$

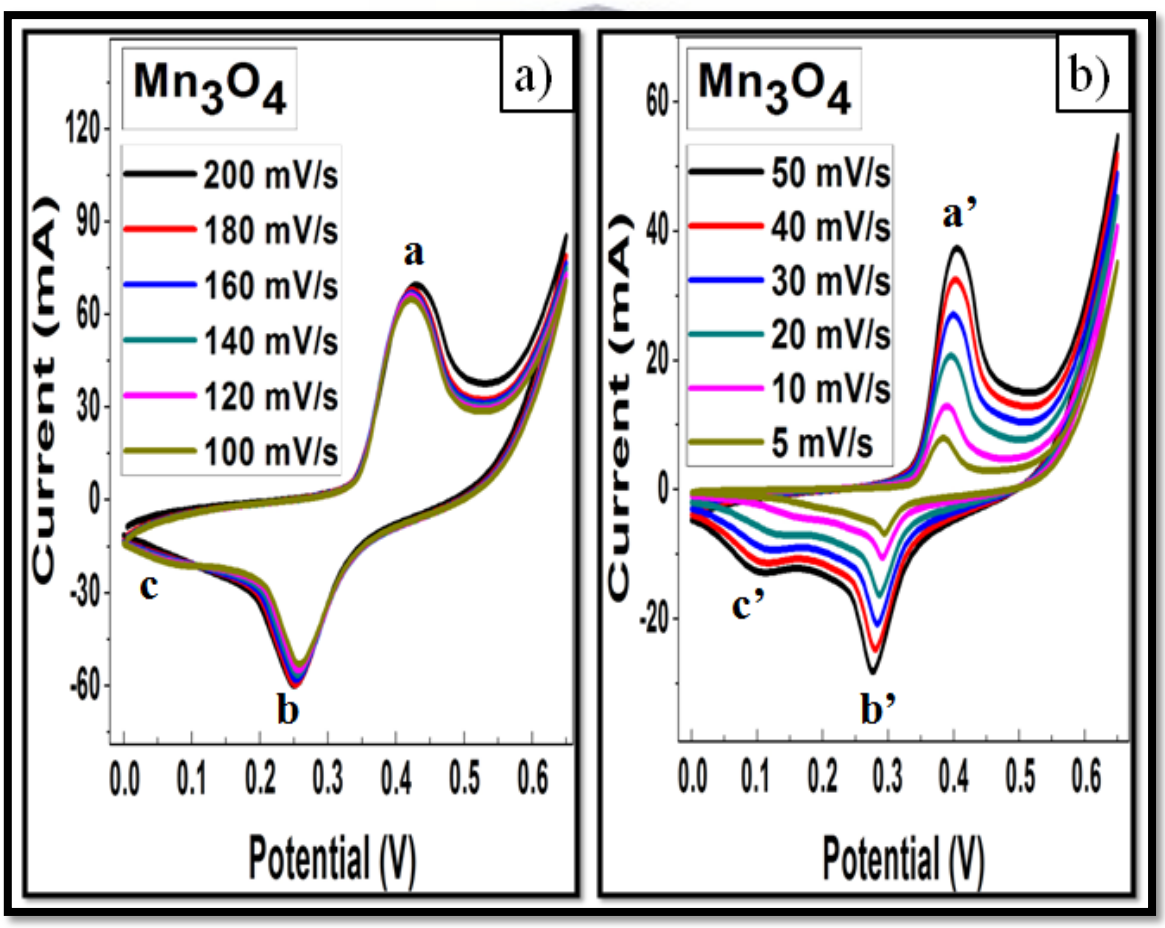

Figure 4.25: Cyclic Voltammograms of the pristine Mn_3O_4 electrode material run at a), high scan rates (100-200 mV/s) and b), low scan rates (5-50 mV/s) in a 3 M KOH electrolyte solution.

The mass of the Mn_3O_4 active electrode material was additionally calculated, as illustrated below, before commencing towards the final specific capacitance calculation.

$$\text{Slurry mixture}\left(\text{mg}\right)=\text{Coated electrode}\left(\text{mg}\right)-\text{Bare electrode}\left(\text{mg}\right) \tag{4.32}$$

$$\therefore\ \text{Slurry mixture}\left(\text{mg}\right)=47.0\,\text{mg}-43.7\,\text{mg}=3.3\,\text{mg} \tag{4.33}$$

The active Mn_3O_4 material mass is 70% of the slurry mixture mass, thus making it 2.31 mg. The calculation below illustrates the final specific capacitance of the Mn_3O_4 electrode material obtained at the lowest scan rate of 5 mV/s.

From **equation (4.29)**, the calculation proceeds as follows:

$$C_{sp}=\frac{0.15\,\text{C}}{\left(0.6\,\text{V}\right)\text{x}\left(2.31\text{x}10^{-3}\,\text{g}\right)} \tag{4.34}$$

$$\therefore\ C_{sp}=108.225\,\text{CV}^{-1}\text{g}^{-1} \tag{4.35}$$

It is essential to note that 1 Coulomb per volt $\left(\text{CV}^{-1}\right)$ is equivalent to 1 Farad.

$$\therefore\ C_{sp}=108.225\,\text{F/g} \tag{4.36}$$

This calculated specific capacitance value, 108.225 F/g, is defined as the charge specific capacitance of the electrode material; as the total charge was calculated from the integrated area under the anodic peak curve. The calculation for the discharge specific capacitance was done in a similar manner; however, the absolute value of the integrated area under the cathodic peak curve was used to perform the calculation.

The total charge (Q) for the discharge specific capacitance at 5 mV/s scan rate was obtained from the following calculation below:

$$Q = \frac{0.0006(\mathrm{AV})}{0.005\left(\mathrm{V}/\mathrm{s}\right)} \tag{4.37}$$

$$\therefore \quad Q = 0.12\,\mathrm{As} = 0.12\ \mathrm{Coulombs} \tag{4.38}$$

After obtaining all the required parameters for **equation (4.29)**, the discharge specific capacitance computation proceeded as follows:

$$\text{Discharge } C_{sp} = \frac{0.12\,\mathrm{C}}{(0.6\,\mathrm{V})\,\mathrm{x}\left(2.31\mathrm{x}10^{-3}\,\mathrm{g}\right)} \tag{4.39}$$

$$\Rightarrow \quad \text{Discharge } C_{sp} = 86.580\,\mathrm{CV^{-1}g^{-1}} \tag{4.40}$$

$$\therefore \quad \text{Discharge } C_{sp} = 86.580\,\mathrm{F/g} \tag{4.41}$$

The percentage Coulombic Efficiency (C_{Eff}) of the material, within the conducted experimental parameters and conditions, was also calculated using the following equation:

$$C_{Eff} = \frac{\text{Discharge Capacitance}}{\text{Charge Capacitance}} \text{x} 100\% \quad (4.42)$$

$$\Rightarrow \frac{86.580\,\text{F/g}}{108.255\,\text{F/g}} \text{x } 100\% \quad (4.43)$$

$$\therefore \; C_{Eff} = 80\% \quad (4.44)$$

This Mn_3O_4 material exhibited a percentage capacitance loss of 20 %, thus indicating a solid platform for improvement through structural modification. **Table 4.2** shows a data schematic of all the charge/discharge specific capacitance and coulombic efficiency values for the respected scan rates portrayed in the CV plots of **Fig 4.25**.

The variation in scan rates was employed to investigate the reversibility of the pristine Mn_3O_4 electrode material. The 5mV/s scan of the cyclic votammogram b) in **Fig. 4.25**, indicated an anodic oxidation peak at the (E_{pa}; I_{pa}) co-ordinate of (0.384 V; 8.2 mA), and a cathodic reduction peak at the (E_{pa}; I_{pc}) co-ordinate of (0.294 V; -6.7 mA). These anodic and cathodic peaks also exhibited a formal potential (E^0) of 0.340 V and a peak-to-peak separation (ΔE_p = E_{pa} – E_{pc}) of 0.09 V. The pairs of anodic and cathodic peaks at different scan rates, corresponds to the electrochemical transformation of Mn^{2+}/Mn^{3+} in the charge/discharge processes occurring at the electrode surface. The additional reduction peak (c') observed at 0.096 V in **Fig. 4.25**, is associated with the reduction of MnO_2 to Mn_2O_3 (Mn^{4+} to Mn^{3+}). This implies that the reduction process of the Mn_3O_4 electrode material involves two cathodic half reactions. The corresponding oxidation and reduction half reactions can be illustrated as follows:

Oxidation half reaction at peak (a'):

$$2Mn_3O_4 + 2OH^- \rightarrow 3Mn_2O_3 + H_2O + 2e^- \quad (4.45)$$

Reduction half reaction at peak (b'):

$$3Mn_2O_3 + H_2O + 2e^- \rightarrow 2Mn_3O_4 + 2OH^- \quad (4.46)$$

Second reduction half reaction at peak (c'):

$$6MnO_2 + 3H_2O + 6e^- \rightarrow 3Mn_2O_3 + 6OH^- \quad (4.47)$$

The additional meta-stable MnO_2 phase is formed from the assistance of the Mn^{4+} cations contained within tetragonal crystal structure of the Mn_3O_4 material [203]. These additional phases were confirmed to be part of the multi-phased Mn_3O_4 structure from XRD analysis. The data illustrated in **Table 4.2** and ragone plot (c) in **Fig. 4.26**, indicated an increase in specific capacitance at low scan rates. This implies that at slow scan rates, more time was available for the KOH electrolyte ions to diffuse to the electrode surface containing the electrode material [75].

The evaluation of the reversibility of the pristine Mn_3O_4 electrode material was done by relating the change in peak potentials (ΔE_p) with the scan rates. From the data illustrated in **Table 4.3**, ΔEp was observed to increase with the increase in scan rate and was calculated to be 90 mV, which is greater than 59 mV for an ideal Nernstian process [150]. However, due to the presence of the additional reduction peak (c') in **Fig. 4.25**, the electrochemical process demonstrated by the pristine Mn_3O_4 material was considered to be quasi-reversible [116]. This could be explained by observing the appearance and disappearance of the reduction peak (c') at high and low scan rates, respectively. At a scan rate of 50 mV/s, the peak (c') is clearly distinguishable on the cyclic voltammogram. However, at 5 mV/s, the peak (c) is no longer visible, thus only displaying the small anodic and cathodic peaks. This observation therefore concludes the fact that the Mn_3O_4 electrode material behaved reversibly at low scan rates and irreversibly at high scan rates, thus exhibiting a quasi-reversible system [114, 116].

Table 4.2: Illustrating data obtained from the charge/discharge specific capacitance and coulombic efficiency calculations of the pristine Mn_3O_4 electrode material.

Scan rate (mV/s)	Specific charge capacitance (F/g)	Specific discharge capacitance (F/g)	Coulombic efficiency (%)
200	27.201	25.902	95.224
180	30.764	29.778	96.795
160	35.426	34	95.975
140	39.930	35.276	88.345
120	46.573	41.564	89.245
100	52.872	49.329	93.3
50	59.076	53.463	90.5
40	64.141	55.957	87.233
30	69.288	61.760	89.135
20	79.978	69.517	86.920
10	93.795	83.189	88.692
5	108.225	86.580	80

Fig. 4.26d) illustrates the linear relationship between the peak current and the square root of the scan rate for the Mn_3O_4 electrode material. This plot was used to calculate the diffusion coefficient at the electrode/electrolyte interface by employing the Randles-Sevcik equation (under ambient conditions) [204].

$$I_p = \left(2.69 \times 10^5\right) n^{3/2} A D^{1/2} C v^{1/2} \quad (4.48)$$

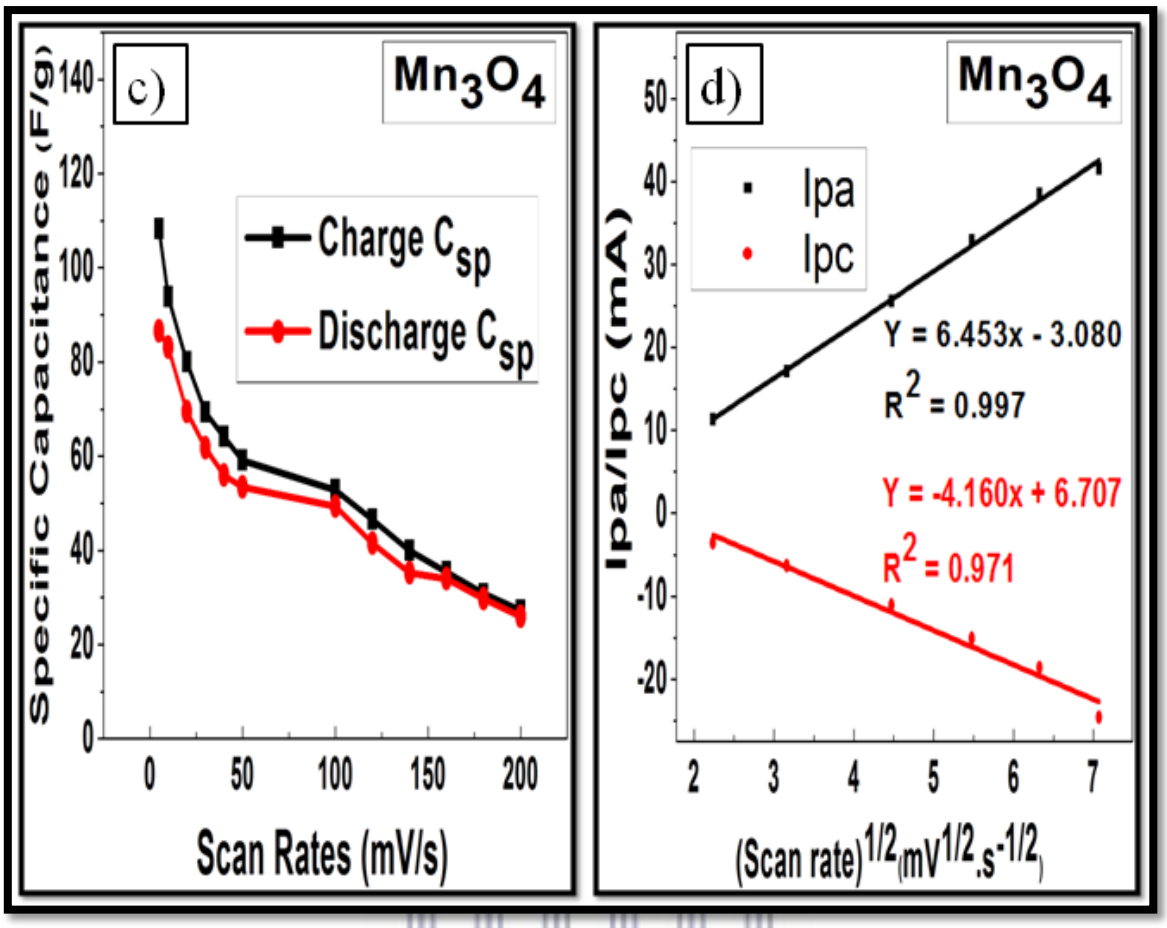

Figure 4.26: Illustrating c), a ragone plot comparing the specific capacitance at various scan rates, and d), a linear relationship between the peak current (I_{pa} and I_{pc}) and the square root of the scan rate for the Mn_3O_4 electrode material.

The parameters of the Randle Sevcik equation include the following values and definitions. n = 2 is defined as the number of electrons transferred during the oxidation-reduction processes. A = 0.5 cm^2 is the area of the nickel foam onto which the slurry paste (containing the active material) was coated. C = 3 x 10^{-3} mol/cm^3 is the concentration of the electrolyte solution. $I_{pa}/v^{1/2}$ = 6.453 x 10^{-3} A $s^{1/2}/mV^{1/2}$ is the slope of the I_{pa} versus $v^{1/2}$ linear plot (from **Fig. 4.26d)**) for the Mn_3O_4 material. The diffusion coefficient, D, was calculated to be the value 2.378 x 10^{-3} cm^2/s. The calculation is additionally illustrated below and this result was intriguingly found to be fairly close to reported electrochemical analysis of Mn_3O_4 operated in a 1 mol/L $LiPF_6$ electrolyte solution. Due to this discovery, it was interesting to investigate how the Mn_3O_4 material would operate in a different selected electrolyte (in this case 3M LiOH).

Table 4.3: Illustrating redox parameters obtained from the cyclic voltammograms of the pristine Mn_3O_4 electrode material at high and low scan rates.

Scan rate (mV/s)	E_{pa} (V)	E_{pc} (V)	I_{pa} (mA)	I_{pc} (mA)	ΔE_p (V)	E^0 (V)
200	0.420	0.241	75.6	-54.3	0.179	0.331
180	0.417	0.250	73.3	-58.6	0.167	0.334
160	0.410	0.247	77.2	-53.0	0.163	0.329
140	0.420	0.257	66.2	-52.5	0.163	0.339
120	0.418	0.258	65.2	-49.9	0.160	0.338
100	0.415	0.264	59.4	-44.3	0.151	0.340
50	0.400	0.274	38.9	-27.2	0.126	0.337
40	0.401	0.279	33.4	-24.2	0.122	0.340
30	0.398	0.282	27.9	-20.2	0.116	0.340
20	0.394	0.286	21.3	-16.0	0.108	0.340
10	0.388	0.291	13.5	-10.2	0.097	0.340
5	0.384	0.294	8.2	-6.7	0.09	0.340

Diffusion Coefficient calculation:

$$D = \sqrt{\frac{I_{pa}}{v^{1/2}} \text{x} \frac{1}{\left(2.69 \text{x} 10^5\right) n^{3/2} AC}} \tag{4.49}$$

$$D = \sqrt{\frac{6.453 \text{x} 10^{-3}\ \text{As}^{1/2}/\text{mV}^{1/2}}{\left(2.69 \text{x} 10^5\right)(2)^{3/2}\left(0.5 \text{cm}^2\right)\left(3 \text{x} 10^{-3}\ \text{mol/cm}^3\right)}} \tag{4.50}$$

$$\therefore\ D = 2.378 \text{x} 10^{-3}\ \text{cm}^2/\text{s} \tag{4.51}$$

Copper manganese oxides ($CuMn_2O_4$) are spinel structured materials that have mostly been applied in the field of catalysis, due to their high catalytic activity and remarkable magnetic properties. However, $CuMn_2O_4$ have barley been studied in literatures according to its electrochemical properties for use in supercapacitors [205]. The XRD analysis interpretation provides a detailed study on the crystal structure of the $CuMn_2O_4$ material. In summary, within the FCC crystal structure of the $CuMn_2O_4$ material, copper cations and manganese cations occupy tetrahedral and octahedral stacking interstices respectively [145]. The main advantage of this material is driven by its spinel structure, which offers a three-dimensional pathway for the complete adsorption and desorption of electrolyte ions at the electrode/electrolyte interface [145].

The cyclic voltammograms for the $CuMn_2O_4$ material, displayed in **Fig. 4.27**, was used to study and determine its capacitive response. The CV curve, at a scan rate of 5 mV/s, showed a current response value greater than that of the pristine Mn_3O_4 material, and all the curves displayed approximately symmetric anodic (oxidation) and cathodic (reduction) peaks [146]. This observation unveiled quality capacitive performance exhibited by the $CuMn_2O_4$ material [146]. Additionally, the voltammogram also displayed an anodic oxidation peak (illustrating the E_{pa}; I_{pa} co-ordinate) at approximately (0.382 V; 20.9 mA) and a cathodic reduction peak (indicating the E_{pc}; I_{pc} co-ordinate) at about (0.296 V; -9.6 mA). This data extrapolation indicates the possible occurrence of a reversible system, which could provide a prominent pseudocapacitive contribution factor [146, 206]. These anodic and cathodic peaks also exhibited a formal potential (E^0) of 0.341 V and a peak-to-peak separation ($\Delta E_p = E_{pa} - E_{pc}$) of 0.086 V [146, 207]. The comparison of **Table 4.3** to **Table 4.4** indicated an increase in the peak current values (I_{pa} and I_{pc}) at a high scan rate (200 mV/s) and a low scan rate (5 mV/s) for the spinel $CuMn_2O_4$ compared to the pristine Mn_3O_4. The data illustrated in **Table 4.4** also indicated that the spinel $CuMn_2O_4$ material exhibited a smaller peak-to-peak separation (ΔE_p) as compared to the pristine Mn_3O_4 material. This smaller ΔE_p value implied that the spinel $CuMn_2O_4$ material processed an improved electrochemical reversibility than the pristine Mn_3O_4 material. The small ΔE_p value may have been attributed due to the tetrahedral and octahedral sites present within the spinel $CuMn_2O_4$ FCC crystal structure. These sites could have occupied additional electrolyte ions and provide a shorter pathway for electrons to diffuse across the electrode surface.

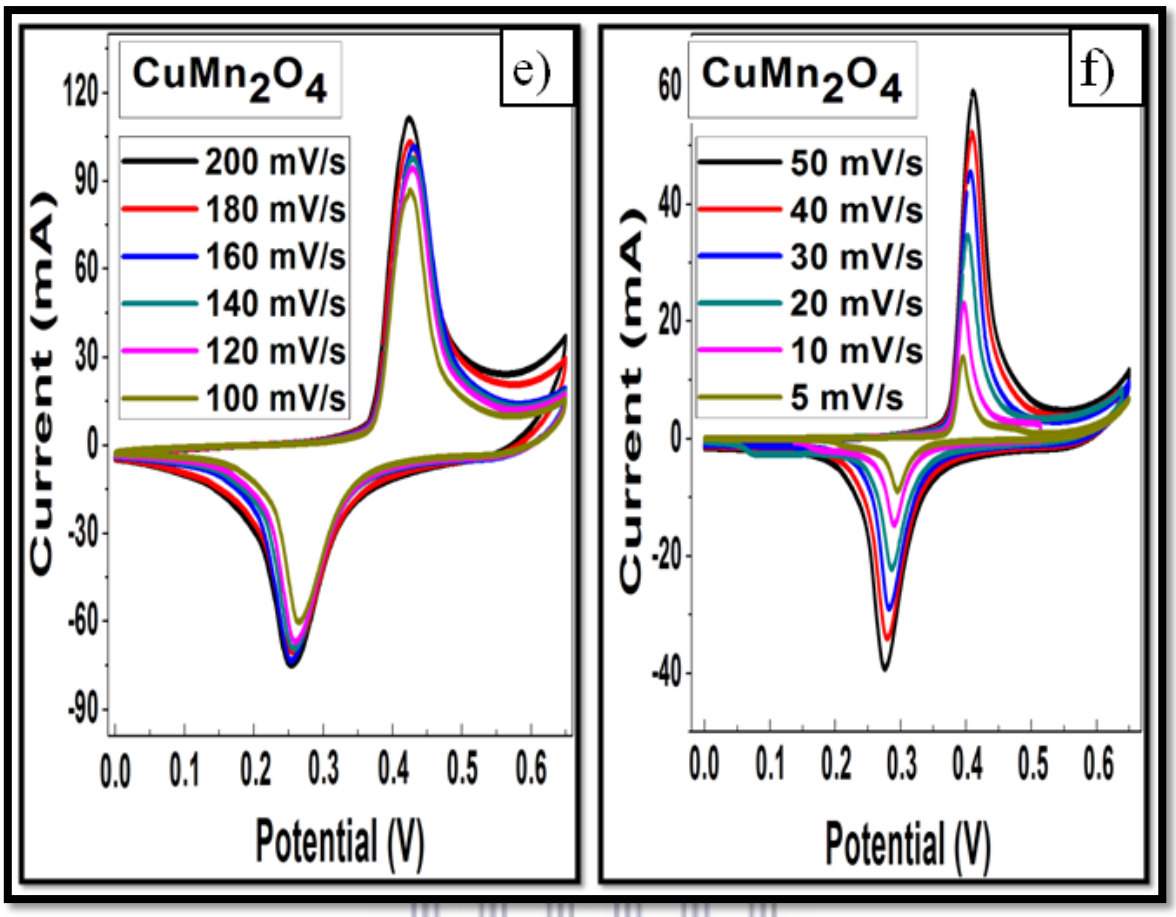

Figure 4.27: Cyclic Voltammograms of the spinel $CuMn_2O_4$ electrode material run at e), high scan rates (100-200 mV/s) and f), low scan rates (5-50 mV/s) in a 3 M KOH electrolyte solution.

The ragone plot in **Fig. 4.28g)** of the $CuMn_2O_4$ material illustrated greater charge/discharge specific capacitances at the various scan rates as compared to that of the pristine Mn_3O_4 material. Although the ragone plots of the two respective pristine and spinel materials appeared graphically similar, it was also observed that the CV plots of the two electrode materials displayed a similar curve shape. The only difference was that the $CuMn_2O_4$ material exhibited higher and sharper peak currents at lower peak-to-peak separation potentials. The rate at which the electrolyte ions diffuse across each section of the $CuMn_2O_4$ coated electrode surface was additionally investigated in order to fully understand the reversible nature portrayed in the $CuMn_2O_4$ CV plots. The anodic and cathodic half reactions were initially investigated and obtained in order to schematically observe the oxidation and reduction mechanism of the spinel $CuMn_2O_4$ material at the I_{pa} and I_{pc} peaks .

Table 4.4: Illustrating redox parameters obtained from the cyclic voltammograms of the spinel $CuMn_2O_4$ electrode material at high and low scan rates.

Scan rate (mV/s)	E_{pa} (V)	E_{pc} (V)	I_{pa} (mA)	I_{pc} (mA)	ΔE_p (V)	E^0 (V)
200	0.421	0.264	114	-78.6	0.157	0.343
180	0.422	0.254	113	-74.0	0.168	0.338
160	0.430	0.240	110	-77.9	0.190	0.335
140	0.427	0.251	107	-69.9	0.176	0.339
120	0.424	0.256	100	-61.0	0.168	0.340
100	0.418	0.258	96.1	-50.7	0.160	0.338
50	0.407	0.272	64.5	-33.9	0.135	0.339
40	0.405	0.275	56.8	-29.3	0.130	0.340
30	0.403	0.278	50.2	-24.0	0.125	0.341
20	0.398	0.282	39.5	-17.1	0.116	0.340
10	0.394	0.287	25.5	-12.0	0.107	0.341
5	0.382	0.296	20.9	-9.6	0.086	0.341

The anodic oxidation and cathodic reduction half reactions are illustrated below.

Anodic oxidation half reaction:

$$CuMn_2O_4 + OH^- + H_2O \rightarrow CuOOH + 2MnOOH + e^- \quad (4.52)$$

Cathodic reduction half reaction:

$$CuOOH + 2MnOOH + e^- \rightarrow CuMn_2O_4 + OH^- + H_2O \quad (4.53)$$

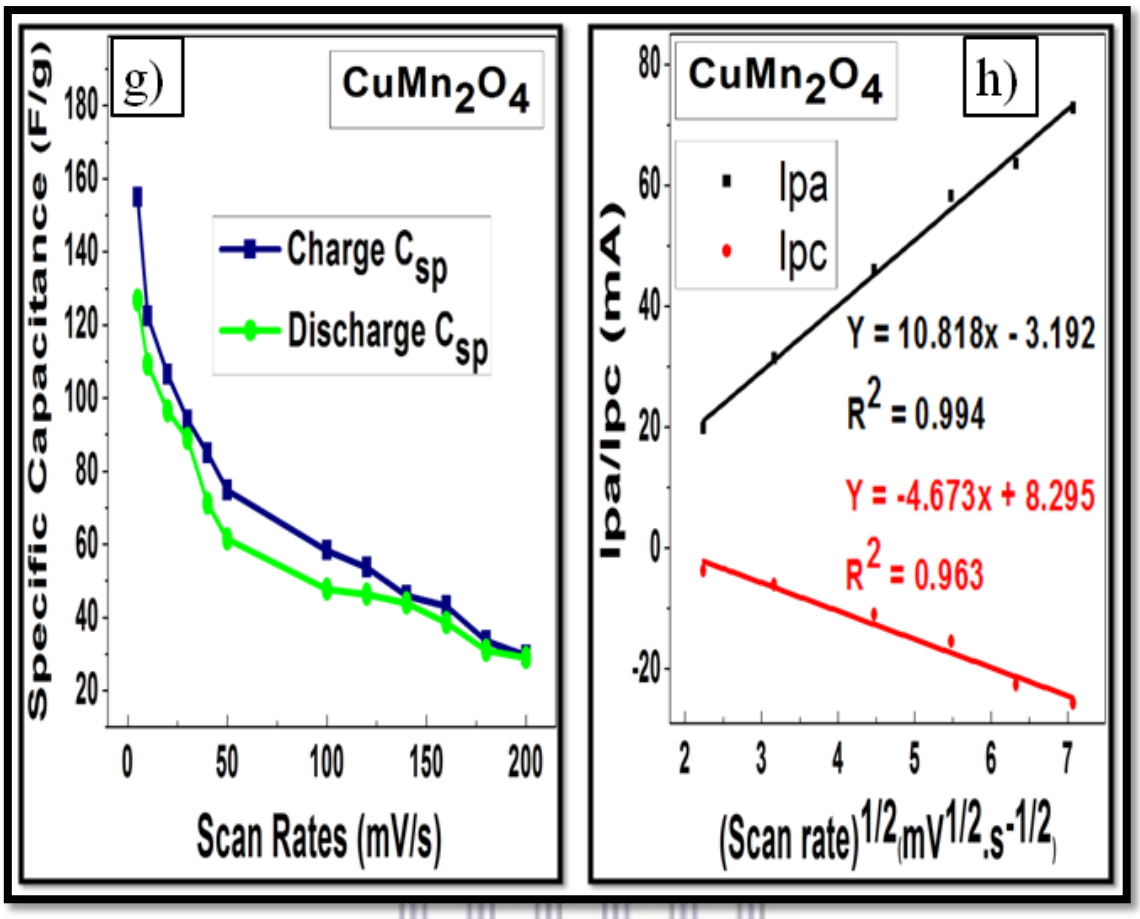

Figure 4.28: Illustrating g), a ragone plot comparing the specific capacitance at various scan rates, and d), peak current (I_{pa} and I_{pc}) as a function of the square root of the scan rate for the $CuMn_2O_4$ electrode material.

The diffusion coefficient calculated for the spinel $CuMn_2O_4$ material was 5.178 x 10^{-3} cm^2/s, which is approximately 2 orders of magnitude greater than the diffusion coefficient for the pristine Mn_3O_4 material. The increase in the diffusion coefficient of the spinel $CuMn_2O_4$ material, as previously mentioned, is attributed due to the electrolyte ions occupied within the tetrahedral (Cu^{2+}) and octahedral (Mn^{3+}) interstitial sites, thus improving the diffusion rate of ions and electrons across the $CuMn_2O_4$ coated electrode surface. This improvement signified that the structural property of the spinel material obtained from XRD analysis, contributed towards its rate capability. This improved rate capability allows the storage of sufficient electrolyte ions on the electrode surface during charge/discharge processes, thus yielding greater specific capacitance values. The charge storage mechanism of the $CuMn_2O_4$ nanoparticles is based on the adsorption and desorption of electrolyte anions (OH^-) and

cations (K^+) on the surface of the $CuMn_2O_4$ electrode material [208]. During electrochemical analysis of the full cell (two-electrode) system, the electrolyte anions and cations adsorb on the spinel $CuMn_2O_4$ and activated carbon electrodes, respectively. The $CuMn_2O_4$ was tested as the positive electrode material against activated carbon in a two-electrode system. Nevertheless, in the half cell (three-electrode) system, electrolyte anions adsorb only to the partially positive spinel $CuMn_2O_4$ material. The one impediment observation made when comparing the data obtained in **Table 4.5** to that of galvanostatic charge/discharge (GCD), was that GCD data displayed lower specific capacitance values from the same three-electrode configuration with the 3 M KOH electrolyte solution [209]. However, additional two-electrode full cell electrochemical analysis with a different electrolyte species (3 M LiOH), illustrated improved supercapacitive performance exhibited by all synthesized electrode materials.

Table 4.5: Illustrating data obtained from the charge/discharge specific capacitance and coulombic efficiency calculations of the spinel $CuMn_2O_4$ electrode material.

Scan rate (mV/s)	Specific charge capacitance (F/g)	Specific discharge capacitance (F/g)	Coulombic efficiency (%)
200	29.645	28.881	97.423
180	33.594	30.907	92.002
160	43.167	38.470	89.119
140	45.775	43.758	95.594
120	53.640	46.296	86.310
100	58.324	47.607	81.625
50	74.727	61.462	82.249
40	84.956	71.134	83.730
30	93.940	88.792	94.520
20	106.473	96.411	90.550
10	122.236	109.181	89.320
5	154.869	126.780	81.863

The cyclic voltammograms of the hybrid $CuMn_2O_4$/MWCNT material illustrated integrated CV area values greater than that of both the pristine Mn_3O_4 and spinel $CuMn_2O_4$ electrode materials [210]. The increase in integrated area values resulted in an increase in the total amount of charge stored during charge/discharge processes, thus indicating improved electron transport exhibited mechanisms. This result additionally provided the indication that the incorporated MWCNT network enhanced the electrochemical performance of the spinel $CuMn_2O_4$ electrode material. The reason for this result is ascribed to the unique structure, high conductivity, and high surface area of the MWCNTs [210]. This large surface area provides additional sites for oxidation-reduction reactions.

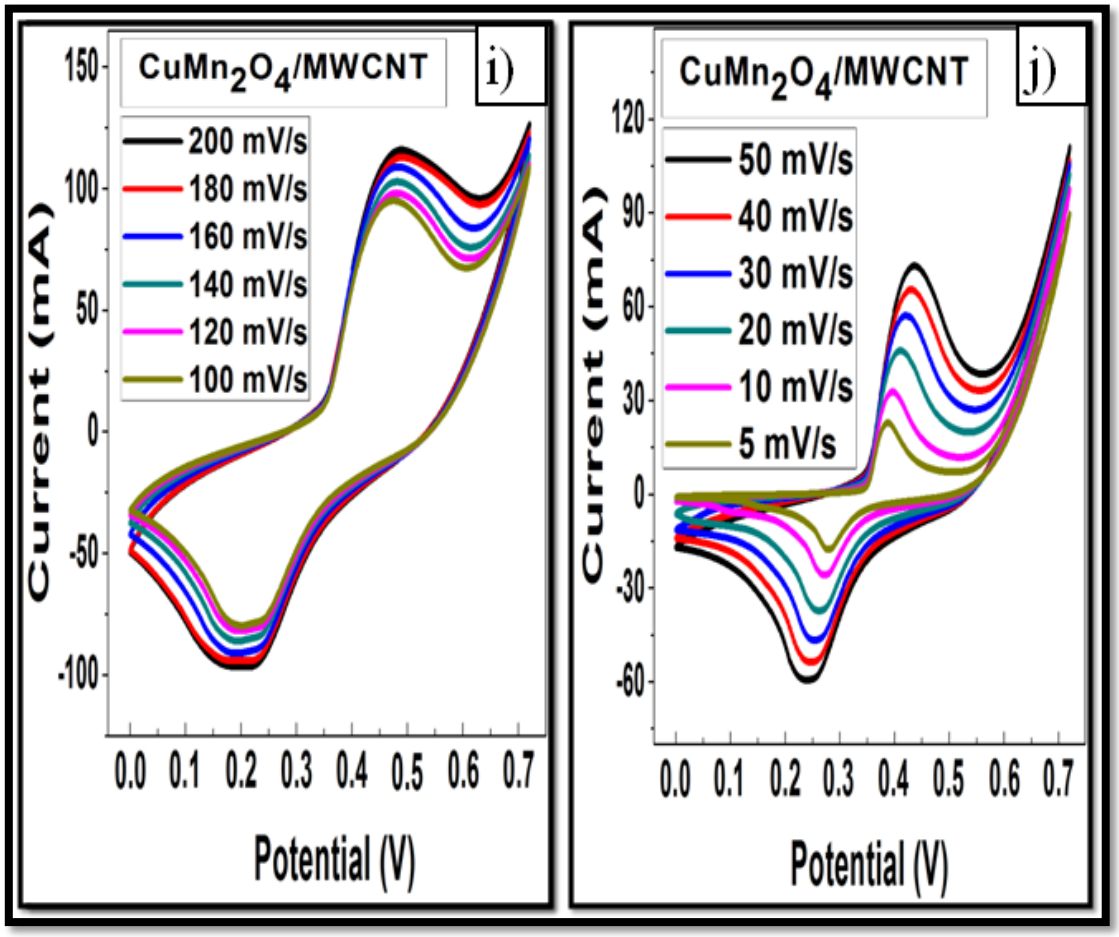

Figure 4.29: Cyclic Voltammograms of the hybrid $CuMn_2O_4$/MWCNT electrode material run at e), high scan rates (100-200 mV/s) and f), low scan rates (5-50 mV/s) in a 3 M KOH electrolyte solution.

Table 4.6: Illustrating redox parameters obtained from the cyclic voltammograms of the hybrid $CuMn_2O_4$/MWCNT electrode material at high and low scan rates.

Scan rate (mV/s)	E_{pa} (V)	E_{pc} (V)	I_{pa} (mA)	I_{pc} (mA)	ΔE_p (V)	E^0 (V)
200	0.477	0.205	130	-87.9	0.272	0.341
180	0.471	0.196	126	-81.6	0.275	0.334
160	0.480	0.198	113	-86.1	0.282	0.339
140	0.474	0.197	109	-81.6	0.277	0.336
120	0.470	0.219	107	-88.5	0.251	0.345
100	0.465	0.202	102	-72.8	0.263	0.334
50	0.434	0.238	74.9	-57.1	0.196	0.336
40	0.426	0.246	68.6	-49.9	0.180	0.336
30	0.417	0.254	60.3	-42.5	0.163	0.336
20	0.407	0.261	48.6	-35.5	0.146	0.334
10	0.393	0.270	34.6	-24.4	0.123	0.332
5	0.387	0.279	22.9	-17.7	0.108	0.333

The data displayed in **Table 4.6** indicated that the hybrid material exhibited a larger peak-to-peak separation (ΔE_p = 0.108 V), and a larger diffusion coefficient ($D = 5.581 \times 10^{-3}$ cm^2/s) as compared to the spinel and pristine materials. The increased ΔE_p value is a result of the decrease in electrochemical reversibility of the hybrid material. However, the increased D value is assigned to the additional electroactive sites for electrolyte ions to occupy during oxidation-reduction processes. The data from the ragone plot and **Table 4.7** indicated that the hybrid material exhibited higher charge/discharge specific capacitance values as compared to the pristine and spinel materials. The MWCNT attachement to the spinel $CuMn_2O_4$ nanoparticles therefore increased its electrical conductivity and rate capability. The CV curves displayed in **Fig. 4.29** additionally illustrated that with an increase in scan rate, the anodic and cathodic peaks increased in area and shifted towards the more positive and negative electrode potentials, respectively. This therefore resulted in a faster ion-electron

transport throught the electrode material [211]. It was reported in small-angle X-ray scattering (SAXS) spectroscopic analysis that the formation of the hybrid $CuMn_2O_4$/MWCNT composite electrode material resulted in less agglomoration of spinel $CuMn_2O_4$ nanoparticles [212]. This, therefore, provided the indication that the majority of Cu^{2+}-oxide tetrahedral interstitial sites were effectively utilized for the occupation of electrolyte ions, as well as for efficient electron transport, during electrochemical analysis [213]. In addition to promoting an improved conductivity towards the electrode material, the incorporated MWCNT networks also had synergistic effects with the spinel $CuMn_2O_4$ particles regarding enhancement in the specific capacitance of the hybrid electrode material [214].

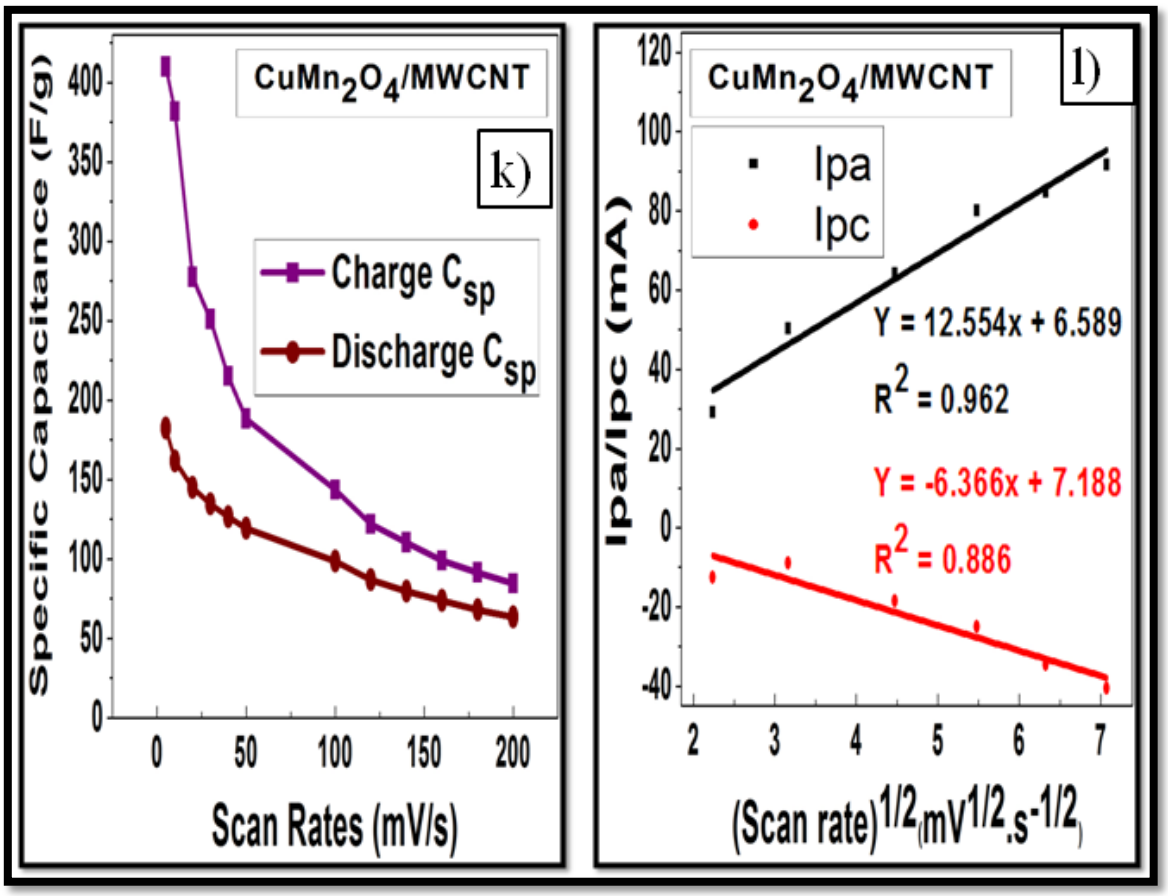

Figure 4.30: Illustrating k), a ragone plot comparing the specific capacitance at various scan rates, and l), peak current (I_{pa} and I_{pc}) as a function of the square root of the scan rate for the $CuMn_2O_4$/MWCNT electrode material.

Table 4.7: Illustrating data obtained from the charge/discharge specific capacitance and coulombic efficiency calculations of the hybrid $CuMn_2O_4$/MWCNT material.

Scan rate (mV/s)	Specific charge capacitance (F/g)	Specific discharge capacitance (F/g)	Coulombic efficiency (%)
200	84.431	63.481	75.187
180	91.519	67.938	74.234
160	98.881	73.783	74.618
140	110.306	79.520	72.090
120	121.815	87.073	71.480
100	143.454	98.612	68.741
50	188.384	119.132	63.240
40	214.980	126.691	58.932
30	250.811	134.549	53.646
20	277.410	145.072	52.295
10	381.547	161.672	42.373
5	409.705	182.482	44.540

The following set of cyclic voltammetry analysis results is based on the utilization of an aqueous 3 M LiOH electrolyte solution. One of the main reasons for using LiOH, apart from comparing it with KOH, was to see whether the insertion/extraction of Li^+ ions in the metal oxide electrode materials are associated with a reversible charge storage mechanism during charge transfer processes at the electrode/electrolyte interface [215]. An additional valued reason would be that very few reports have been made in literature concerning the utilization of LiOH as a potential electrolyte solution for high-performance supercapacitors [215]. Despite it being anticipated to exhibit a superior performance over that of the 3 M KOH electrolyte, due to its smaller ionic radii, the 3 M LiOH electrolyte solution could also have electrochemical diffusion defects involved during electrochemical analysis at the electrode surface. This essentially implies that the continuous build up of electrolyte ions on the electrode material during cycling, would eventually reduce the efficiency of the electrochemical cell device. This electrochemical phenomenon is known as electrode concentration polarisation [216].

4.3.1.2 Electrochemical studies of half cell (three-electrode) system with 3 M LiOH electrolyte

In literature, it is often reported that the performance of a supercapacitor is equally dependent on the electrolyte of choice, as it is on the active electrode material [217]. It was expected for the LiOH electrolyte to provide superior supercapacitive properties over the KOH electrolyte, due to Li^+ having a smaller ionic radii than K^+ [217]. The smaller ionic radii of the Li^+ ion would allow it to efficiently intercalate into the multi-walled carbon nanotube structure of the hybrid $CuMn_2O_4$/MWCNT electrode material [218]. This would undoubtedly enhance the material's supercapacitive performance. The cyclic voltammograms displayed in **Fig. 4.31**, illustrated that the pristine Mn_3O_4 material, analyzed in 3M LiOH aqueous electrolyte, demonstrated a quasi-reversible, much like the material analyzed in 3 M KOH, electrochemical process [116]. This is therefore said to be one similarity between the two electrolyte CV tests. However, the calculated diffusion coefficient for the Mn_3O_4 material in 3 M LiOH electrolyte was 2.918 x 10^{-3} cm^2/s, which is slightly greater than (D) calculated for the 3 M KOH electrolyte analysis. The increase in calculated diffusion coefficient (D) is attributed to the increase in intercalation efficiency exhibited by Li^+ ions. This was expected since the ionic radii of Li^+ (0.076 nm) is smaller than that of K^+ (0.138 nm) [217].

The data illustrated in **Table 4.8** showed the indication of anodic and cathodic peak currents (I_{pa} & I_{pc}) that are greater in magnitude than the pristine material run in 3 M KOH electrolyte. This result yielded larger integrated peak areas, thus providing a greater quantity of total charge stored. The increased quantity of total charge stored would then ultimately generate an enhanced specific charge/discharge capacitance. This statement is confirmed by the specific capacitance data illustrated in the ragone plot of **Fig. 4.32o)**, as well as in **Table 4.9**. An additional and intriguing comparative observation made from **Table 4.9** was that the Mn_3O_4 material exhibited a lower energy loss (7.4 %) in LiOH electrolyte as compared to it analyzed in the KOH (which exhibited 20% energy loss) aqueous electrolyte solution. These results and observations therefore evidently conclude that 3 M LiOH would be the most suitable electrolyte solution for the full cell (two-electrode system) electrochemical analysis.

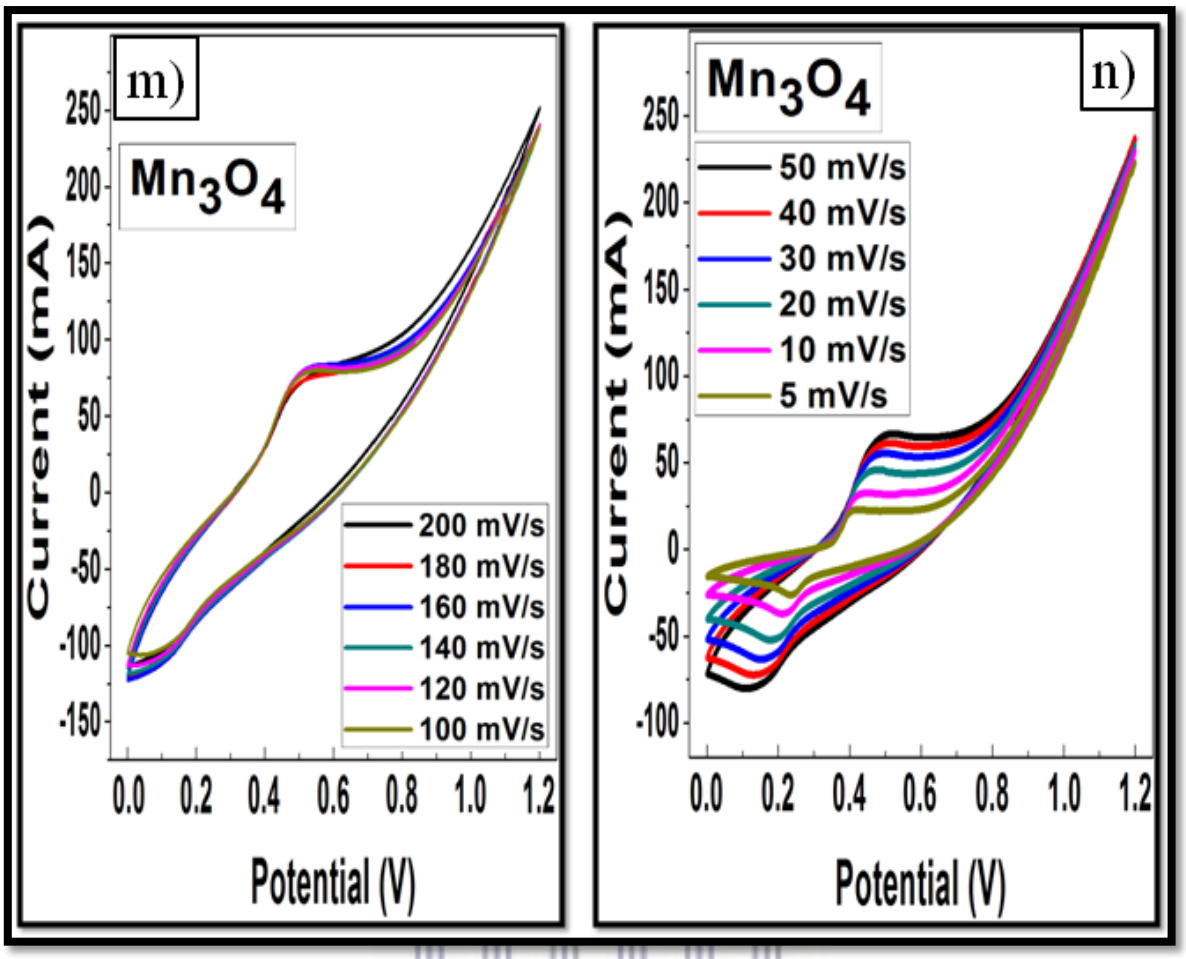

Figure 4.31: Cyclic Voltammograms of the pristine Mn_3O_4 electrode material run at m), high scan rates (100-200 mV/s) and n), low scan rates (5-50 mV/s) in a 3 M LiOH electrolyte solution.

The figure above, **Fig. 4.31**, also indicated that the operating potential range $(0 \rightarrow 1.2\ \text{V})$ was increased from $(0 \rightarrow 0.7\ \text{V})$. This analysis parameter input was initialized in order to investigate whether there might have been additional oxidation or reduction peaks at potentials greater than 0.7 V. The anodic and cathodic peaks only occurred within the potential range of $(0 \rightarrow 0.8\ \text{V})$. This implied that with an increase in the potential window, the oxidation/reduction processes was not affected in any way. However, the result did provide the possibility of the electrode material possessing a potentially improved electrochemical stability, while being operated in a 3 M LiOH aqueous electrolyte solution.

Table 4.8: Illustrating redox parameters obtained from the cyclic voltammograms of the pristine Mn_3O_4 electrode material at high and low scan rates in a 3 M LiOH electrolyte solution.

Scan rate (mV/s)	E_{pa} (V)	E_{pc} (V)	I_{pa} (mA)	I_{pc} (mA)	ΔE_p (V)	E^0 (V)
200	0.486	0.0948	89.7	-87.7	0.391	0.290
180	0.457	0.102	84.6	-89.4	0.355	0.280
160	0.475	0.112	88.7	-95.8	0.363	0.294
140	0.471	0.0937	88	-96.8	0.377	0.282
120	0.471	0.0917	92.4	-90.5	0.380	0.281
100	0.468	0.086	86.5	-90.4	0.382	0.277
50	0.457	0.112	75.8	-69.6	0.345	0.285
40	0.479	0.146	69.9	-63.5	0.333	0.313
30	0.439	0.154	61.9	-53.6	0.285	0.297
20	0.433	0.182	52.8	-43.7	0.251	0.308
10	0.401	0.196	38.7	-30.6	0.205	0.300
5	0.393	0.221	28.5	-20.7	0.172	0.307

The results illustrated in **Table 4.8** represented a ΔE_p value of 0.172 V at the lowest scan rate of 5 mV/s. Compared to the Mn_3O_4 material operated in 3 M KOH electrolyte, these calculated results represent ΔE_p values that are greater in magnitude at a variety of scan rates. These findings constitute towards a decrease in electrochemical reversibility exhibited by the 3 M LiOH electrolyte operated cell for the Mn_3O_4 material. In literature, it was reported that the cations Li^+ and K^+ within the respected electrolyte solutions tend to formulate hydrated OH^- anions with different ionic radii [217]. The reported literature stated that during electrochemical analysis of the two electrolytes, smaller cations (Li^+ = 0.076 nm) formed larger hydrated anions (OH^- = 0.382 nm) [217]. This implied that during discharge processes, the deintercalation of Li^+ ions occured at lower efficiencies to that of the intercalated Li^+ ion efficiency during charge processes [219]. It can also be explained by the large ionic size of

the hydrated anions causing a strain on the movement of the intercalated Li^+ ions during reduction processes of the electrode material [220]. However, this minor disadvantage did not attribute towards a poor electrochemical performance, as illustrated in the plot of **Fig. 4.32o)**. Galvanostatic charge/discharge analysis revealed an approximate 31% increase in specific capacitance, as compared to the corresponding CV data. Nontheless, the pristine Mn_3O_4 particle aggregation results ilustrated from SAXS analysis, could be the reason behind the decrease in electrochemical reversibility exhibited by the electrode material.

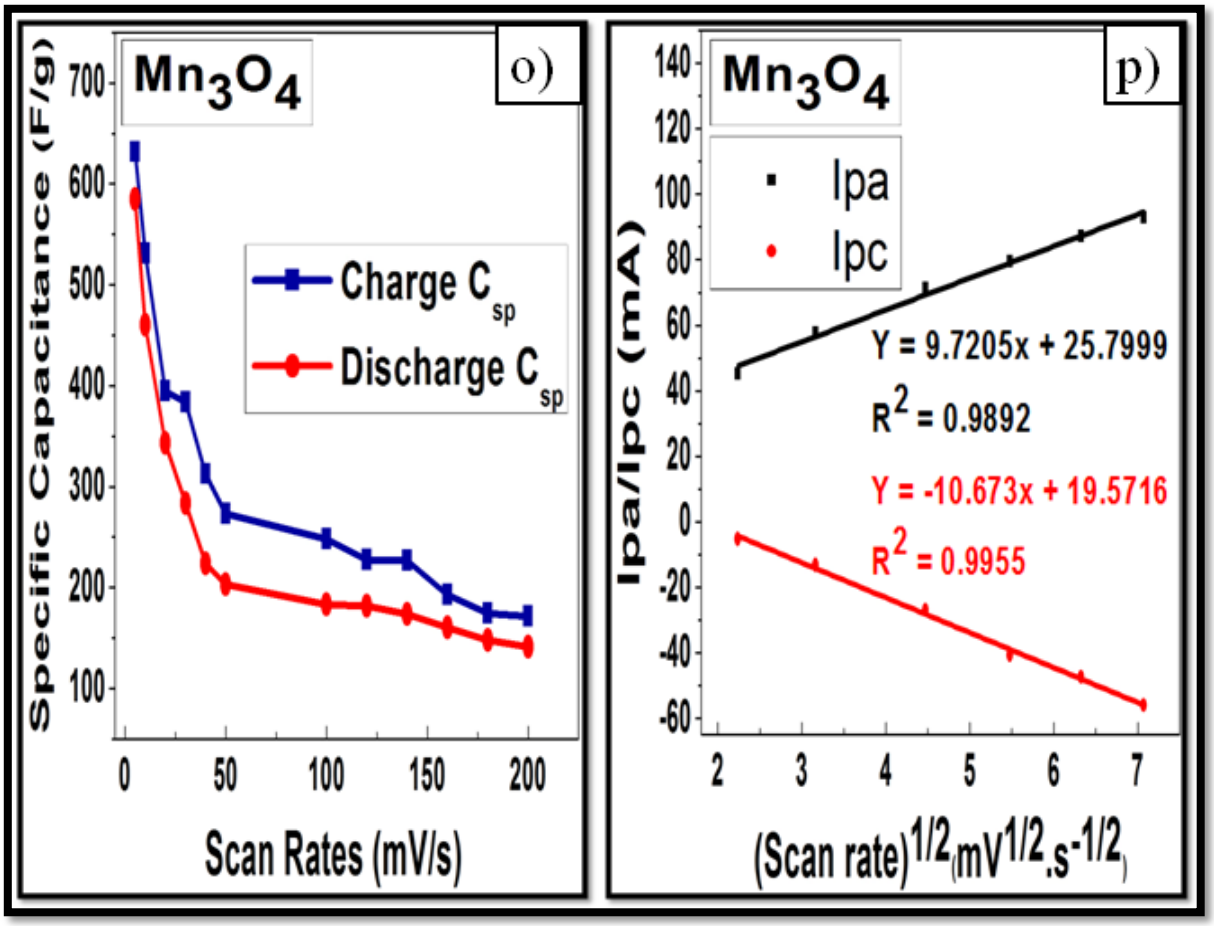

Figure 4.32: Illustrating o), a ragone plot comparing the specific capacitance at various scan rates, and p), peak current (I_{pa} and I_{pc}) as a function of the square root of the scan rate for the Mn_3O_4 electrode material in a 3 M LiOH electrolyte solution.

Table 4.9: Illustrating data obtained from the charge/discharge specific capacitance and coulombic efficiency calculations of the pristine Mn_3O_4 material in a 3 M LiOH electrolyte solution.

Scan rate (mV/s)	Specific charge capacitance (F/g)	Specific discharge capacitance (F/g)	Coulombic efficiency (%)
200	171.625	141.365	82.369
180	174.270	147.682	84.743
160	192.568	159.938	83.055
140	226.320	173.650	76.728
120	227.208	181.366	79.824
100	248.125	183.187	73.829
50	273.013	202.718	74.252
40	312.471	223.696	71.589
30	383.867	283.230	73.783
20	394.517	343.348	87.030
10	530.970	460.022	86.638
5	631.696	584.982	92.605

The calculated charge/discharge specific capacitance results, as illustrated in **Table 4.9**, indicateded a substantial increase compared to the electrochemical data obtained from using the 3 M KOH aqueous electrolyte solution. The Mn_3O_4 material analyzed in the 3 M LiOH electrolyte solution exhibited a specific charge/discharge capacitance of approximately 6 and 7 orders of magnitude greater than that exhibited by the material when analyzed in the 3 M KOH electrolyte solution, respectively. Comparing the CV plots shown in **Fig. 4.33** to that in **Fig. 4.31**; it was clearly observed that the plots of the two materials, pristine Mn_3O_4 and spinel $CuMn_2O_4$, portrayed a similar CV curve shape. This subsequently implied that the materials additionally exhibited a similar electrochemical reversibility, which was previously determined to be quasi-reversible for the pristine Mn_3O_4 electrode material. However, on the contrary, the increased peak-to-peak separation values (ΔE_p) from the data illustrated in **Table 4.10**, compared to that in **Table 4.8**, suggested that the spinel $CuMn_2O_4$ material demonstrated a lower electrochemical reversibility to that of the pristine Mn_3O_4 material. As

mentioned previously in the XRD analysis section, the spinel $CuMn_2O_4$ electrode material contains Cu^{2+} and Mn^{3+} atoms located at the tetrahedral and octahedral interstitial sites, respectively. These sites were occupied by the Li^+ electrolyte ions during oxidation processes, thus resulting in the occurrance of efficient Li^+-ion intercalation within those sites. This additionally implied that more electrolyte ions where diffused across the surface of the electrode material; as a result of the number of interstitial sites and the small ionic radii of Li (0.076 nm) compared to Cu (0.145 nm) and Mn (0.161 nm).

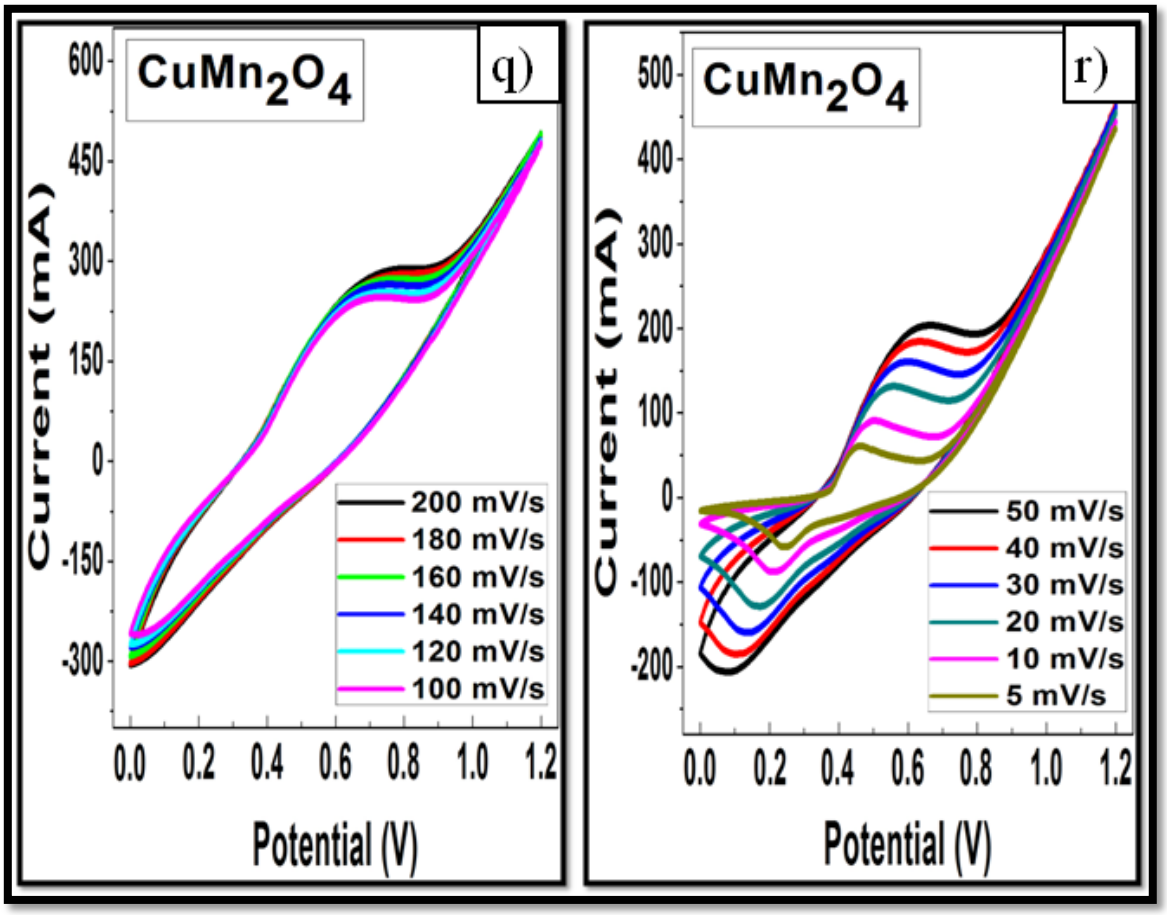

Figure 4.33: Cyclic Voltammograms of the spinel $CuMn_2O_4$ electrode material run at m), high scan rates (100-200 mV/s) and n), low scan rates (5-50 mV/s) in a 3 M LiOH electrolyte solution.

Table 4.10: Illustrating redox parameters obtained from the cyclic voltammograms of the spinel $CuMn_2O_4$ electrode material at high and low scan rates in a 3 M LiOH electrolyte solution.

Scan rate (mV/s)	E_{pa} (V)	E_{pc} (V)	I_{pa} (mA)	I_{pc} (mA)	ΔE_p (V)	E^0 (V)
200	0.592	0.067	278	-229	0.525	0.330
180	0.574	0.070	272	-215	0.504	0.322
160	0.579	0.047	253	-230	0.532	0.313
140	0.570	0.028	260	-223	0.542	0.300
120	0.584	0.033	253	-209	0.551	0.310
100	0.588	0.056	237	-201	0.532	0.322
50	0.554	0.061	218	-184	0.493	0.308
40	0.542	0.085	194	-167	0.457	0.314
30	0.538	0.118	173	-144	0.420	0.328
20	0.513	0.155	141	-118	0.358	0.334
10	0.480	0.20	100	-79.8	0.280	0.340
5	0.449	0.236	67.6	-53.0	0.213	0.343

The comparison of the CV curves illustrated in **Fig. 4.31** and **4.33**, indicated that the spinel $CuMn_2O_4$ electrode material displayed much larger current response values at various high (100-200 mV/s) and low (5-50 mV/s) scan rates [179]. These results, therefore, provided the indication of the spinel $CuMn_2O_4$ electrode material possessing a strong pseusocapacitive nature, thus leading towards a good electrochemical performance [221]. However, the reason for the spinel $CuMn_2O_4$ material exhibiting a decreased electrochemical reversibility, indicated from the increased peak-to-peak separation values (ΔE_p) illustrated in **Table 4.10**, may have been due to the internal resistance (R_{ir}) of the electrode material [62]. This internal resistance impede the motion of electrolyte ions within the porous crystal structures of the spinel $CuMn_2O_4$ electrode material [222]. Despite it's contained internal resistance, the spinel $CuMn_2O_4$ material did, however, exhibit a higher diffusion coefficient (8.434×10^{-3} cm^2/s)

compared to that of the pristine Mn_3O_4 material. This, therefore, implied that the diffusion of electrolyte ions across the electrode material surface occured at a faster rate, thus leading towards a larger quantity of charge stored on the electrode surface during charge/discharge processes. The increase in the total quantity of charge stored would then ultamitely yield an increase in specific capacitance. The less agglomeration of spinel $CuMn_2O_4$ nanoparticles illustrated from SAXS analyzed data, additionally contributed towards a reasonably uniform distribution of electrolyte ions across the electrode material surface during diffusion processes [223].

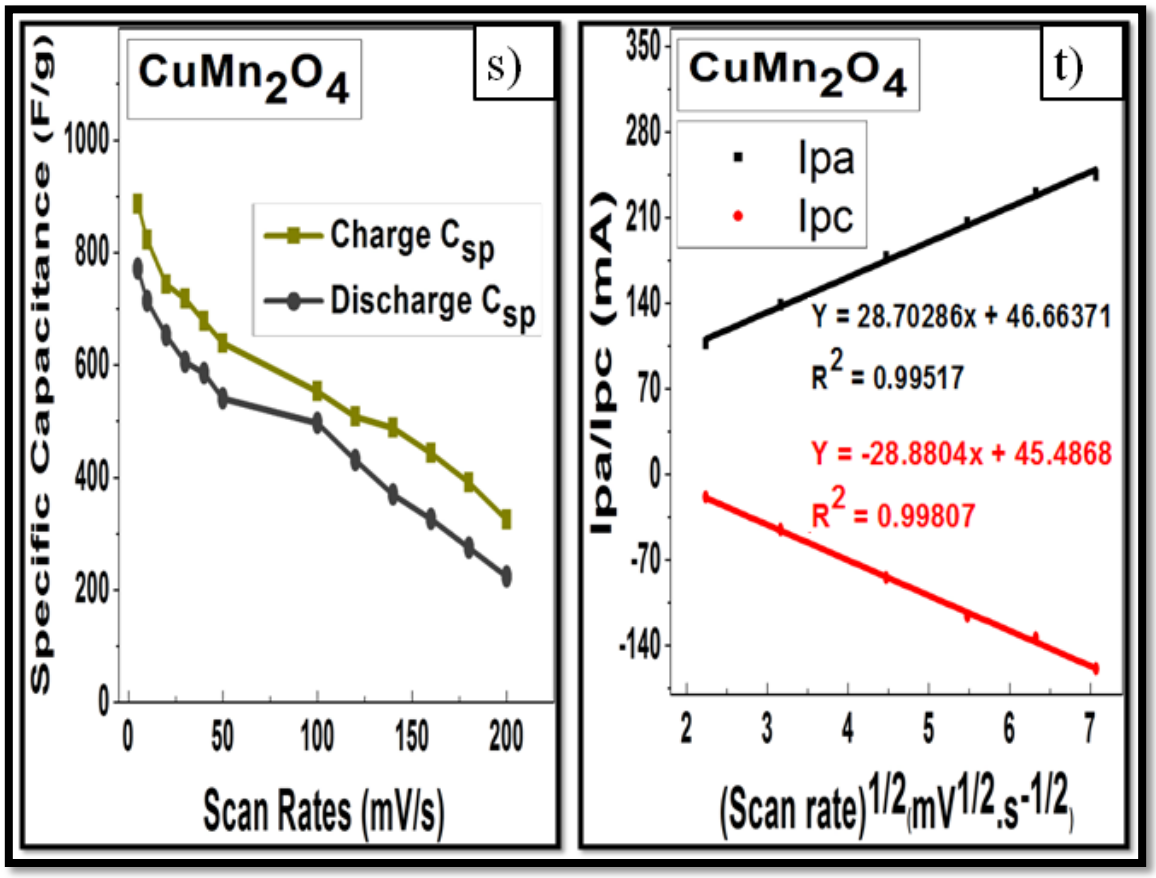

Figure 4.34: Illustrating s), a ragone plot comparing the specific capacitance at various scan rates, and t), peak current (I_{pa} and I_{pc}) as a function of the square root of the scan rate for the $CuMn_2O_4$ electrode material in a 3 M LiOH electrolyte solution.

Table 4.11: Illustrating data obtained from the charge/discharge specific capacitance and coulombic efficiency calculations of the spinel $CuMn_2O_4$ material in a 3 M LiOH electrolyte solution.

Scan rate (mV/s)	Specific charge capacitance (F/g)	Specific discharge capacitance (F/g)	Coulombic efficiency (%)
200	324.257	223.252	68.850
180	390.671	274.521	70.269
160	443.091	325.328	73.422
140	487.547	369.396	75.766
120	508.003	430.467	84.737
100	553.056	496.950	89.855
50	638.171	540.528	84.700
40	677.203	585.360	86.438
30	717.354	605.350	84.387
20	743.169	652.534	87.804
10	821.910	714.363	86.915
5	886.017	771.596	87.086

The GCD analyzed data illustrated discharge specific capacitance values of 1189 – 764 F/g at current densities ranging from 0.5 – 4 A/g, respectively, for the spinel $CuMn_2O_4$ electrode material investigated within a 3 M LiOH electrolyte solution. This result revealed much improvement from that of CV, as indicated in **Table 4.11**. However, the CV specific charge/discharge data indicated an enhanced electrochemical performance at lower scan rates, much like the GCD data represented at lower current densities. The cyclic voltammograms of the hybrid $CuMn_2O_4$/MWCNT electrode material, displayed in **Fig. 4.35**, illustrated remarkable anodic and cathodic current responses of (380 mA; -314 mA) and (244 mA; -203 mA) at high and low scan rates, respectively. This implied that a subsequent quantity of charge, derived from electrolyte ion diffusion, accumulated on the electrode material surface during charge/discharge experimentation [224]. However, no additional oxidation/reduction peaks were observed at potentials beyond 0.9 V for this electrochemical system. In addition, the homogenous colour of the electrolyte solution began to alter due to

the increased oxidation/reduction level of the hybrid electrode material; and at operating potentials exceeding 1.2 V, resulted in the electrode material becoming electrochemically unstable. This situation was fortunately solved through employing the two-electrode full cell system for electrochemical analysis, as illustrated in its following results revealing operating potentials up to 2 V for all investigated electrode materials [225]. Comparing the CV data of the three-electrode system with that of the two-electrode full cell device revealed that the full cell exhibited a 29% increase in specific capacitance for the hybrid $CuMn_2O_4$/MWCNT electrode material. GCD analysis of the full cell supercapacitor device reveals additional astonishing aspects of electrochemical data such as cycling stability [226].

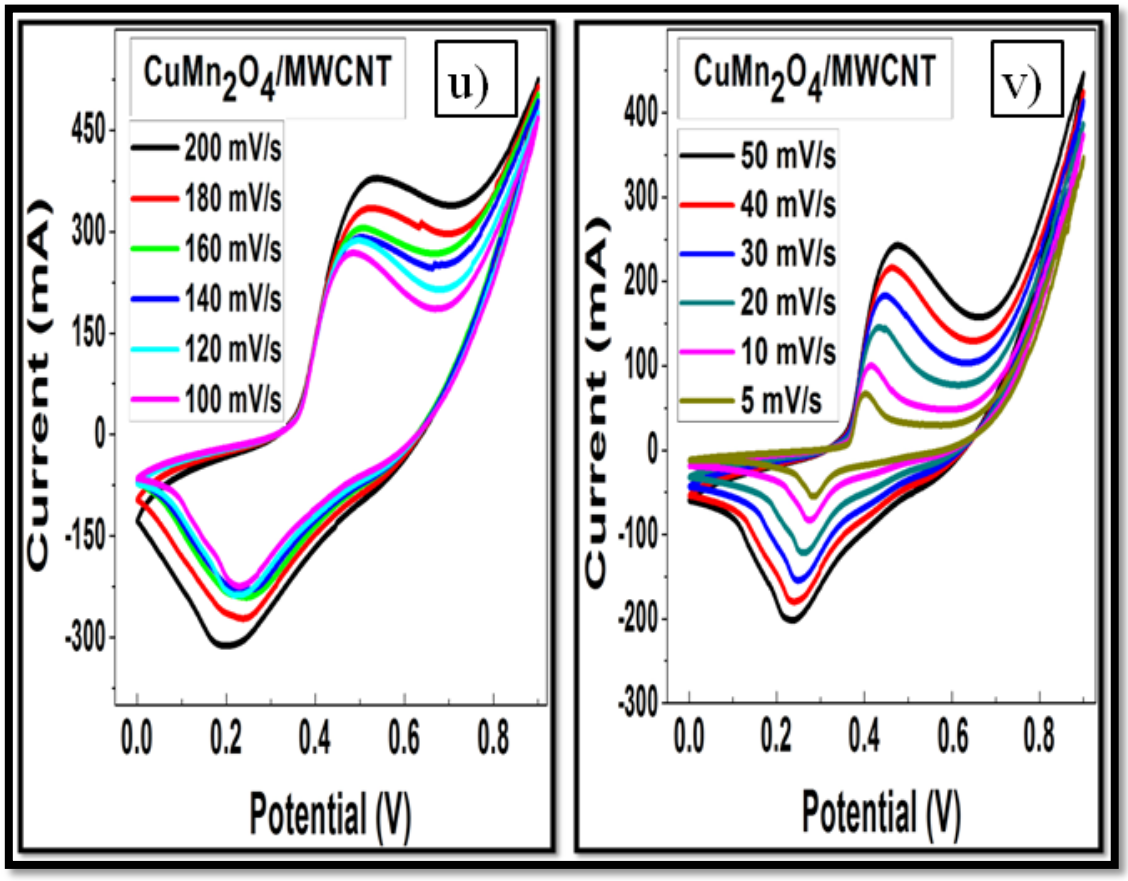

Figure 4.35: Cyclic Voltammograms of the hybrid $CuMn_2O_4$/MWCNT electrode material run at u), high scan rates (100-200 mV/s) and v), low scan rates (5-50 mV/s) in a 3 M LiOH electrolyte solution.

Table 4.12: Illustrating data obtained from the charge/discharge specific capacitance and coulombic efficiency calculations of the hybrid $CuMn_2O_4$/MWCNT material in a 3 M LiOH electrolyte solution.

Scan rate (mV/s)	Specific charge capacitance (F/g)	Specific discharge capacitance (F/g)	Coulombic efficiency (%)
200	372.141	269.504	72.420
180	437.980	289.954	66.203
160	492.615	311.760	63.287
140	521.860	330.782	63.385
120	582.026	360.539	61.946
100	623.112	471.313	75.639
50	681.564	582.279	85.433
40	745.607	650.424	87.234
30	865.806	733.767	84.750
20	906.312	782.253	86.312
10	973.657	815.860	83.793
5	1067.427	923.903	86.554

The oxidation/reduction parameters results, illustrated in **Table 4.13**, indicated that the hybrid $CuMn_2O_4$/MWCNT electrode material exhibited a superior electrochemical reversibility, as compared to both the pristine Mn_3O_4 and spinel $CuMn_2O_4$ electrode materials. This result was identified by the lower peak-to-peak separation values (ΔE_p) of 0.320 – 0.118 V exhibited by the hybrid electrode material from high (200 mV/s) to low (5 mV/s) scan rates [227]. The diffusion coefficient value (D) for the hybrid $CuMn_2O_4$/MWCNT electrode material was calculated from the extrapolated data of its corresponding peak current (I_{pa} and I_{pc}) versus square root of scan rate ($v^{1/2}$) linear function, illustrated in **Fig. 4.36**. The value was calculated as 9.682 x 10^{-3} cm^2/s, thus indicating an improvement from the standard/un-modified spinel $CuMn_2O_4$ electrode material [228]. The improved diffusion capabilities exhibited by the hybrid $CuMn_2O_4$/MWCNT electrode material, additionally confirmed its enhanced electrochemical reversibility over that of the pristine Mn_3O_4 and spinel $CuMn_2O_4$ electrode materials [229].

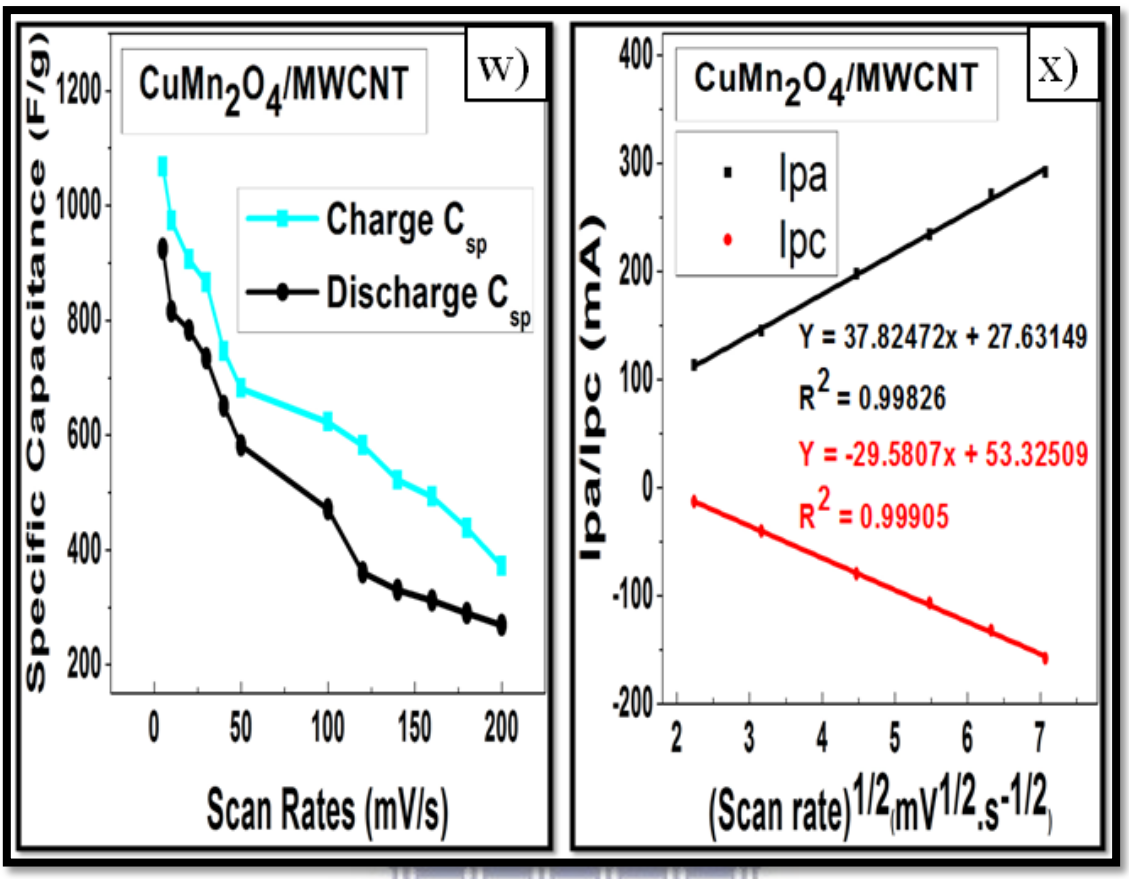

Figure 4.36: Illustrating w), a ragone plot comparing the specific capacitance at various scan rates, and x), peak current (I_{pa} and I_{pc}) as a function of the square root of the scan rate for the $CuMn_2O_4$/MWCNT electrode material in a 3 M LiOH electrolyte solution.

The performance comparison of various spinel-type composite electrode materials to that of the findings reported in this work is presented in **Table 4.14**. The $LiMn_2O_4$/CNTs/GO composite material, operated within a 1.0 M Li_2SO_4 aqueous electrolyte solution, provided some innovative ideas for future prospects. The incorporation of graphene oxide (GO) to the hybrid $CuMn_2O_4$/MWCNT composite matrix would undoubtedly boost its conductivity, thus improving its overall electrochemical performance. The use of Li_2SO_4 would also be a better-suited aqueous electrolyte solution than LiOH due to its sulphate ions having a greater electronegativity than OH^- ions, thus inducing ions with a smaller ionic radius causing faster diffusion kinetics [230].

Table 4.13: Illustrating redox parameters obtained from the cyclic voltammograms of the hybrid $CuMn_2O_4$/MWCNT electrode material at high and low scan rates in a 3 M LiOH electrolyte solution.

Scan rate (mV/s)	E_{pa} (V)	E_{pc} (V)	I_{pa} (mA)	I_{pc} (mA)	ΔE_p (V)	E^0 (V)
200	0.500	0.180	422	-279	0.320	0.340
180	0.490	0.216	375	-241	0.274	0.353
160	0.470	0.221	346	-209	0.249	0.346
140	0.465	0.221	332	-201	0.244	0.343
120	0.461	0.204	319	-211	0.257	0.333
100	0.457	0.215	289	-206	0.242	0.336
50	0.452	0.219	264	-185	0.233	0.336
40	0.443	0.224	238	-162	0.219	0.334
30	0.427	0.233	206	-136	0.194	0.330
20	0.420	0.249	161	-109	0.171	0.335
10	0.408	0.267	108	-75.8	0.141	0.338
5	0.396	0.278	72.5	-50.4	0.118	0.337

Table 4.14: Specific capacitance comparison of various spinel-type composites [231].

Electrode material	Electrolyte	Specific capacitance (F/g)	Reference
MWCNTs	1.0 M H_2SO_4	55	[232]
$CuMn_2O_4$/MWCNT	3 M LiOH	923.903	This work
$LiMn_2O_4$/CNTs/GO	1.0 M Li_2SO_4	676.660	[233]
$NiCo_2O_4$/rGO	2 M KOH	777.100	[234]
$NiCo_2O_4$/CNTs	1 M KOH	220	[235]
$MnCo_2O_4$/Ag NPs	6 M KOH	942	[236]
CNTs/C/$NiMoO_4$	2 M KOH	1037	[237]

4.3.1.3 Electrochemical studies of the full cell (two-electrode) system with 3 M LiOH aqueous electrolyte solution

The three-electrode system is a useful configuration for determining specific material electrochemical properties, where as the two-electrode system is the ideal configuration for testing an electrode material's true capacitive performance [238]. The two-electrode configuration essentially imitates the internal voltages and charge transfer processes that occur within a commercialized supercapacitor cell [238]. It is, therefore, an important design employed for testing the application performance of the researched electrode material. In this research study, electrochemical performance reports of an asymmetric supercapacitor cell configuration were conducted, utilizing commercial grade activated carbon as the negative electrode and the synthesized active material as the positive electrode [239]. Initially, the three-electrode system was used to test the potential range of the activated carbon against all three synthesized electrode materials, as portrayed in **Fig. 4.37**.

The activated carbon CV curve displayed a generic rectangular shaped voltammogram with a more negative potential window, as compared to the three electrode materials of interest. This result, therefore, evidently confirmed the necessary use of activated carbon as the negative electrode during the assembly of the two-electrode full cell device. In the case of a full cell Swagelok device, the specific capacitance value of the positive active material electrode is commonly different to that of the negative activated carbon electrode [240]. Therefore, from this the total capacitance of the full cell was mathematically obtained by relating the electrode configuration of the cell to that of an equivalent electrical circuit containing two identical parallel electrode capacitors connected in series [241]. This train of thought made it easier to derive the equation used to calculate the specific capacitance (C_{sp}) for the full cell Swagelok device. The analogous expression for the total capacitance, calculated in Farad (F), of two asymmetric capacitor systems in series is illustrated below as follows:

$$\frac{1}{C_{\text{Total}}} = \frac{1}{C_1} + \frac{1}{C_2} \tag{4.54}$$

$$\Rightarrow \frac{1}{C_{\text{Total}}} = \frac{2}{C_{\text{Electrode}}} \tag{4.55}$$

$$\therefore \; 2C_{\text{Total}} = C_{\text{E}} \tag{4.56}$$

The expression above was related to **equation (4.29)** from the earlier reported studies of this section, as the C_E variable denotes the combined accumulated charge from the two electrode surfaces [242]. **Equation (4.29)**, however, is only valid for a half cell (three-electrode) system. The full cell asymmetric system employs a mass balance ratio of the two electrodes in order to maximize its operating voltage [243]. The initial three-electrode cyclic voltammetry analysis was a useful experimental procedure to perform, as it aided in selecting a suitable operating potential for the two-electrode system. The potential window is already compensated for in the mass balance ratio calculation, as it is not involved in the final specific capacitance formula [244].

$$C_{\text{sp}} = \frac{2Q_{\text{Total}}}{M_{\text{E}}} \tag{4.57}$$

The M_E variable in **equation (4.59)** denotes the total mass of the two electrodes of the system, including the masses of the positive and negative electrode materials coated on the nickel foam current collectors. This mass is considered as a ratio of the two electrodes as a result of the interfacial charge transfer processes occurring during the diffusion of electrolyte anions (OH^-) and cations (Li^+) across the electrode surface [150, 245]. The expression for the total electrode mass of the two-electrode system is illustrated below.

$$M_{\text{E}_1} + M_{\text{E}_2} = 2M_{\text{E}} \tag{4.58}$$

$$\Rightarrow \quad M_{\mathrm{E}} = \frac{M_{\mathrm{Total}}}{2} \tag{4.59}$$

The expression for the M_E variable was then substituted into **equation (4.57)**, thus obtaining the final derived specific capacitance formula for a full cell (two-electrode) system from cyclic voltammetry analysis [246].

$$C_{\mathrm{sp}} = \frac{2Q_{\mathrm{Total}}}{\frac{M_{\mathrm{Total}}}{2}} \tag{4.60}$$

$$\therefore \quad C_{\mathrm{sp}} = \frac{4Q_{\mathrm{Total}}}{M_{\mathrm{Total}}} \tag{4.61}$$

The specific capacitance of the activated carbon material was calculated from the CV plot in **Fig. 4.37** at a scan rate of 5 mV/s. This C_{sp} value was used to obtain the mass balance ratio for each electrode material. The mass balance ratio calculation, according to the illustrated equation below [247], proceeds as follows:

$$C_{\mathrm{sp}_+} \text{ x } m_+ \text{ x } \Delta V_+ = C_{\mathrm{sp}_-} \text{ x } m_- \text{ x } \Delta V_- \tag{4.62}$$

$$\Rightarrow \quad \frac{m_+}{m_-} = \frac{C_{\mathrm{sp}_-} \text{ x } \Delta V_-}{C_{\mathrm{sp}_+} \text{ x } \Delta V_+} \tag{4.63}$$

$$\frac{M_{\mathrm{Mn_3O_4}}}{M_{\mathrm{AC}}} = \frac{112.454\,\mathrm{F/g} \text{ x } 1\mathrm{V}}{584.982\,\mathrm{F/g} \text{ x } 0.9\,\mathrm{V}} \tag{4.64}$$

$$\frac{M_{Mn_3O_4}}{M_{AC}} = 0.214 \quad (4.65)$$

$$\therefore \; M_{Mn_3O_4} = 0.214 M_{AC} \quad (4.66)$$

The optimal mass ratio of the positive (m_+) and negative (m_-) electrodes for the $CuMn_2O_4||AC$ and $CuMn_2O_4/MWCNT||AC$ supercapacitor assembly was calculated to be 0.149 and 0.133, respectively. The operating voltage for the full cell devices was selected as 2 V.

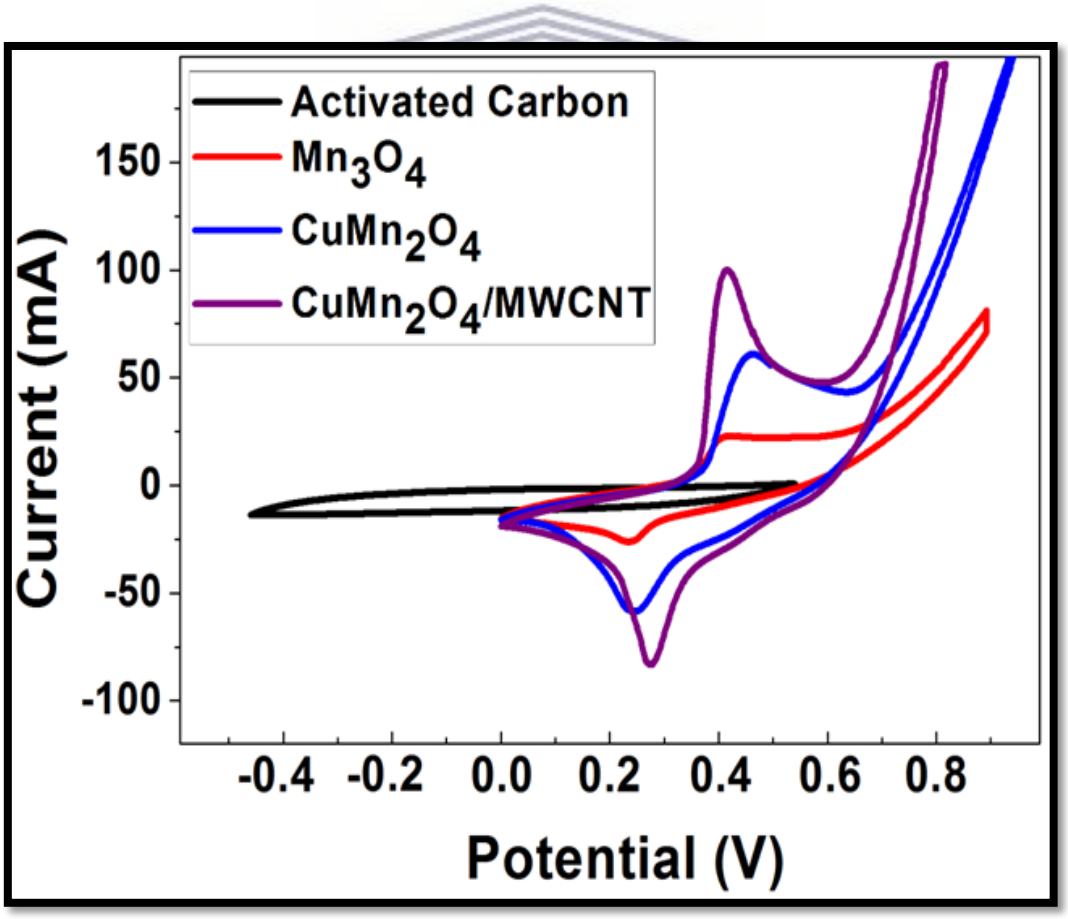

Figure 4.37: Correlative cyclic voltammograms of activated carbon and all three (pristine Mn_3O_4, spinel $CuMn_2O_4$, and hybrid $CuMn_2O_4$/MWCNT) electrode materials at a scan rate of 5 mV/s, in an aqueous 3 M LiOH electrolyte solution.

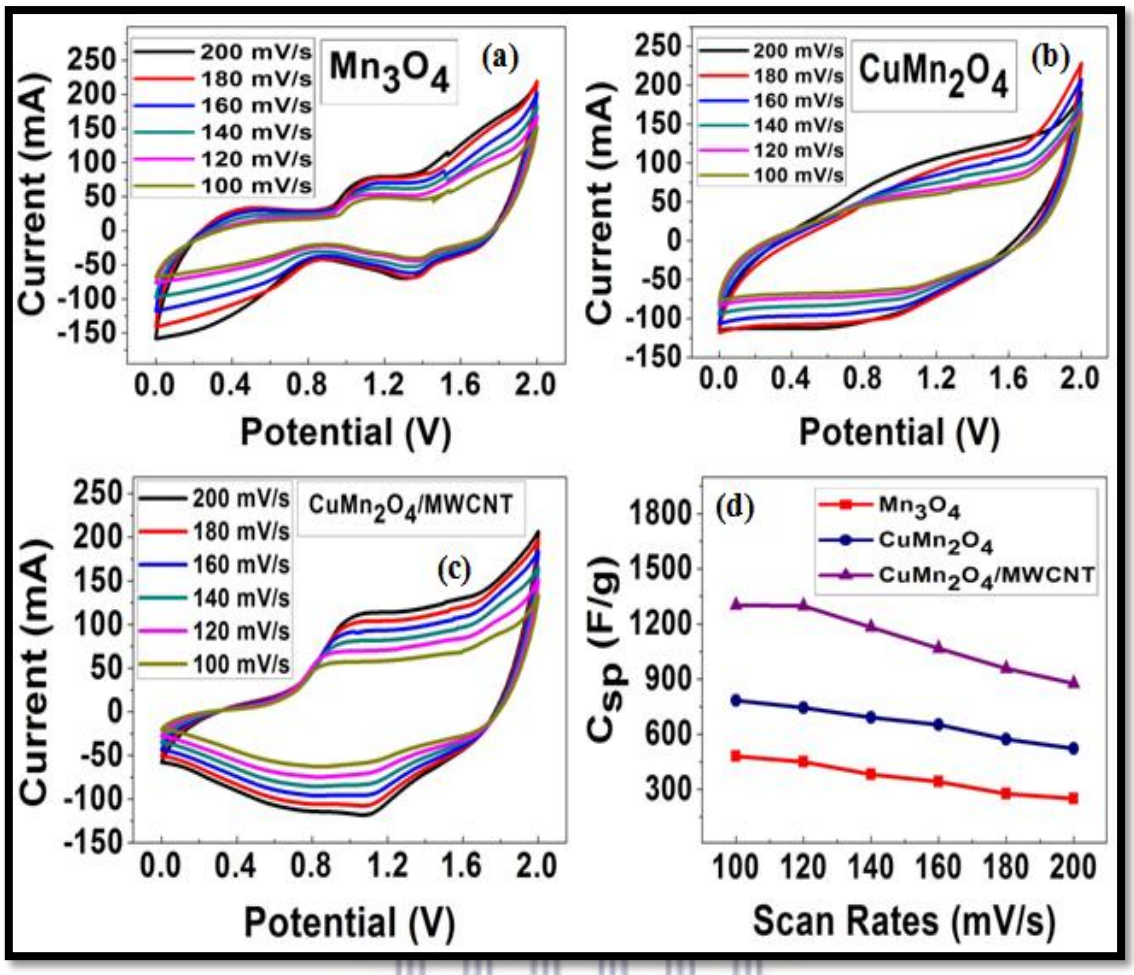

Figure 4.38: The correlation of cyclic voltammetry for (a) Mn_3O_4 ‖ AC, (b) $CuMn_2O_4$ ‖ AC, (c) $CuMn_2O_4$/MWCNT ‖ AC, and (d) rate capability of supercapacitor cells at high scan rates (100-200 mV/s).

Fig. 4.38 and **4.39** are observed as comparative CV curves for the Mn_3O_4 ‖ AC, $CuMn_2O_4$ ‖ AC, and $CuMn_2O_4$/MWCNT ‖ AC supercapacitor cells. These figures also display how the supercapacitive performances of the cell devices compare to one another. The CV curves in **Fig. 4.38(a), (b),** and **(c)** displayed a relatively rectangular shape within the potential ranges of 0-1 V for **(a)** and **(b)**, and approximately 0-0.8 V for **(c)**. This is a result of the activated carbon material exhibiting an electrical double layer capacitive property [75, 248]. The approximate irregular shape of the CV curves observed within the voltage ranges of 1-2 V and 0.8-2 V is attributed to the Faradic pseudocapacitive characteristic exhibited from the reduction/oxidation reactions of the electrode materials [114, 204]. An additional observation made from the shape of the CV curves for each electrode material was that they retained their

original shape regardless of an increase in scan rate [249]. This therefore revealed the occurrence of exceptional rate capability, as proven from **Fig. 4.38(d)** and **Fig. 4.39(h)** [250]. The synergistic effects that occur between the spinel $CuMn_2O_4$ nanoparticles and the MWCNT nano-networks attribute the superior specific capacitance exhibited by the hybrid $CuMn_2O_4$/MWCNT electrode material, compared to that of the pristine Mn_3O_4 and spinel $CuMn_2O_4$ electrode materials [251].

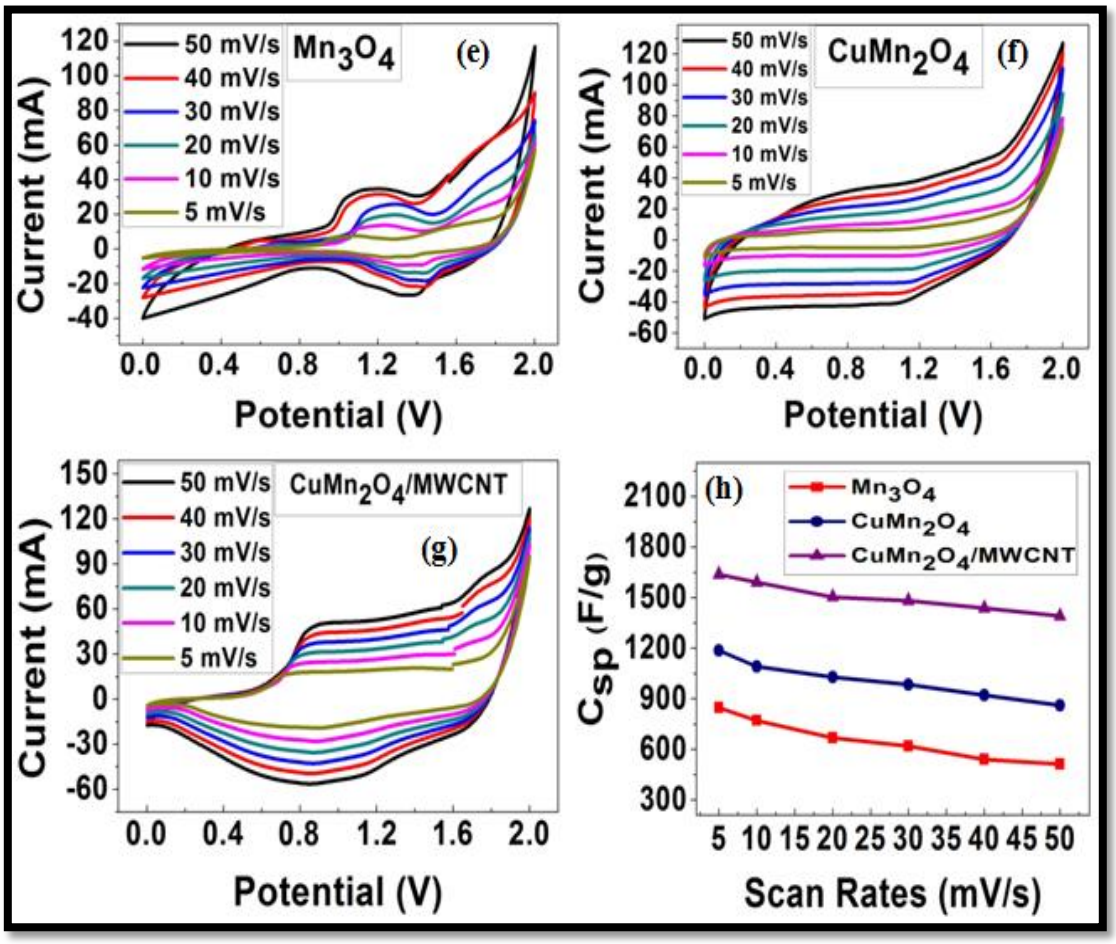

Figure 4.39: The correlation of cyclic voltammetry for (e) Mn_3O_4 ‖ AC, (f) $CuMn_2O_4$ ‖ AC, (g) $CuMn_2O_4$/MWCNT ‖ AC, and (h) rate capability of supercapacitor cells at low scan rates (5-50 mV/s).

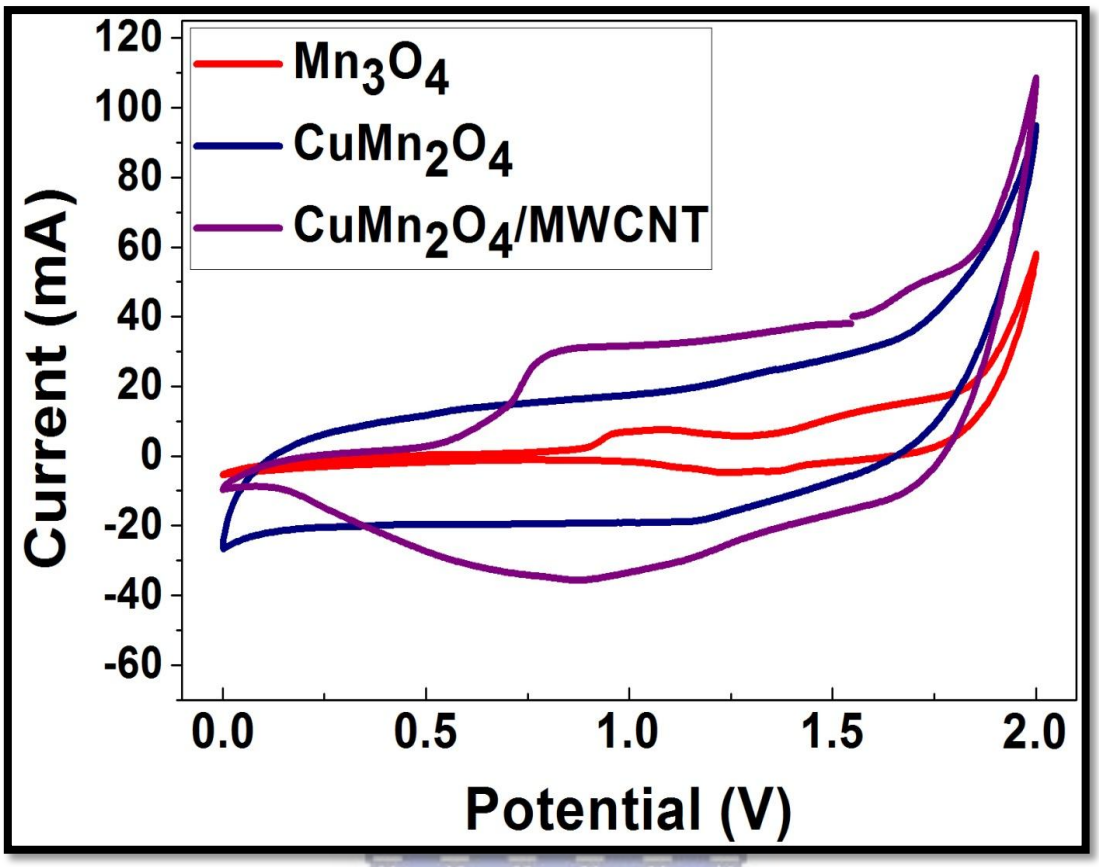

Figure 4.40: Final correlative cyclic voltammograms for the Mn_3O_4 ‖ AC, $CuMn_2O_4$ ‖ AC, and $CuMn_2O_4$/MWCNT ‖ AC supercapacitor cells at a scan rate of 5 mV/s, in an aqueous 3 M LiOH electrolyte solution.

The CV profile for the $CuMn_2O_4$/MWCNT ‖ AC electrochemical cell device appeared to be much broader compared to that of the Mn_3O_4 ‖ AC and $CuMn_2O_4$ ‖ AC cells. This result implied that the hybrid $CuMn_2O_4$/MWCNT composite material processed a lower charge transfer and solution resistance compared to that of the pristine Mn_3O_4 and spinel $CuMn_2O_4$ materials. Electrochemical impedance spectroscopy (EIS) was conducted in order to prove/disprove this scientific statement made.

4.3.2 Electrochemical Impedance Spectroscopy (EIS) analysis and interpretation

The electrochemical impedance spectroscopy (EIS) technique allows one to assess and extract data revealing information about the electronic and ionic conductivity of the analyzed electrode materials [252]. This technique was also used to investigate how the impedance data readings of the circuit elements, which are involved in the correctly constructed equivalent circuit model displayed in the EIS spectrographs, change with an applied frequency signal ranging from high to low frequencies (100 mHz to 200 kHz). The EIS experiments were conducted using the BioLogic Science electrochemical instrument, with built in EC-Lab analysis and interpretation software. The applied DC potential obtained from CV experimental analysis was 0.324 V, at a 10 mV (Vrms) sinus AC amplitude.

In a typical electrochemical impedance spectrograph, the diameter of the semi-circle of impedance is equivalent to the charge-transfer resistance (R_{ct}) within a high frequency region; and the slanted line in the low frequency region reveals the Warburg impedance (W_s). The resistance value signifies the occurrence of the electron transfer kinetics at the electrode/electrolyte interface. **Fig. 4.41** represents the Nyquist Impedance plots for the pristine Mn_3O_4, spinel $CuMn_2O_4$, and hybrid $CuMn_2O_4$/MWCNT electrode materials operated in a 3 M KOH aqueous electrolyte solution. The figure also shows the equivalent circuit model (inset) used to perform the EIS data fittings from the spectrographs. The intercept of the semi-circle in a high frequency regime with the Re(Z')/Ω-axis, indicates the identification of the electrochemical series resistance (ERS) or solution resistance (R_s), which is defined as the resistance between the working electrode and the reference electrode. The R_{ct} and R_s values of the Mn_3O_4, $CuMn_2O_4$, and $CuMn_2O_4$/MWCNT electrode materials were obtained after performing the Randles equivalent circuit model data fitting, using the EC-Lab EIS data analysis Z-fit software. The correspondent parameters of the series resistance (R_s) and the charge-transfer resistance (R_{ct}) data illustrated in **Table 4.15** are relatively low in magnitude. These captivating low R_s and R_{ct} values could be a result of the distinctive structure and morphology of the electrode materials, contributing towards improved percolation and movement of electrolyte ions to and from the electrode surface during diffusion [252-253].

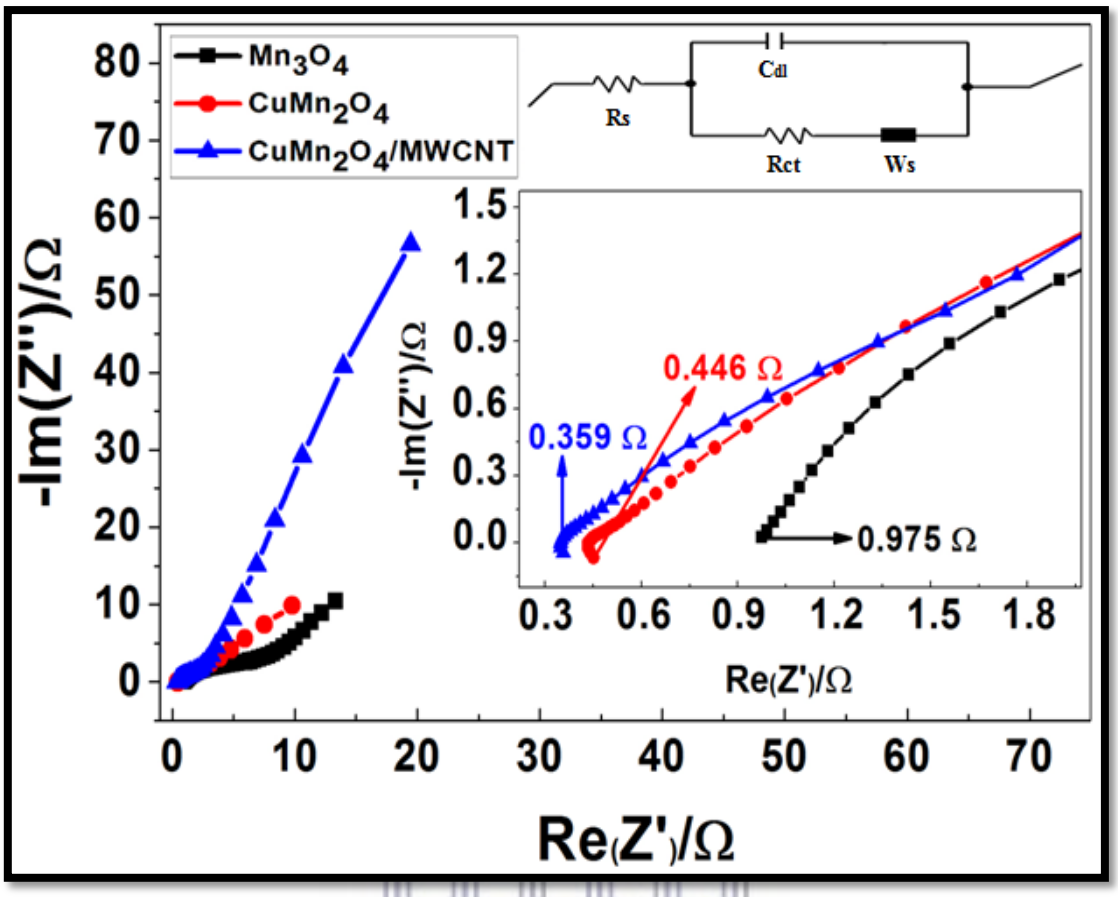

Figure 4.41: Comparative Nyquist plots of the pristine Mn_3O_4, spinel $CuMn_2O_4$, and hybrid $CuMn_2O_4$/MWCNT electrode materials obtained at a frequency range of 100 mHz-200 kHz with a 3M KOH aqueous electrolyte solution.

Table 4.15: EIS fitted data of the Mn_3O_4, $CuMn_2O_4$, and $CuMn_2O_4$/MWCNT electrode materials with a 3 M KOH aqueous electrolyte solution.

Electrode materials	R_s [Ω]	C_{dl} [F]	R_{ct} [Ω]	W_s [$\Omega.s^{-1/2}$]
Mn_3O_4	0.455	2.582×10^{-3}	1.293	0.381
$CuMn_2O_4$	0.225	4.635×10^{-3}	0.827	0.327
$CuMn_2O_4$/MWCNT	0.121	7.292×10^{-3}	0.633	0.300

The low R_s and R_{ct} values of the pristine Mn_3O_4, spinel $CuMn_2O_4$, and hybrid $CuMn_2O_4$/MWCNT electrode materials showed a valid indication of a solid electrochemical platform for the enhancement of its electronic conductivity and energy performance [254]. The double layer capacitance (C_{dl}) parameter, which is a result of the surface morphology of the electrode materials, is modelled by the constant phase element (CPE). The impedance and capacitance data readings, shown in **Table 4.15**, were used to calculate fundamental kinetic parameters involved in the electron transfer process. These parameters include the time constant (τ), which can be calculated from the angular frequency (ω_{max}) recorded at the maximum imaginary impedance of the semi-circle. The (ω_{max}) value was calculated according to the following equation:

$$\omega_{max} = \frac{1}{R_{ct} C_{dl}} \tag{4.67}$$

From the angular frequency (ω_{max}), the time constant (τ) could then be calculated according to the following equation:

$$\tau = \frac{1}{\omega_{max}} \tag{4.68}$$

The following important kinetic parameter would be the exchange current (I_0), which is defined as a measure of the rate at which charges are exchanged between the oxidized and reduced species at any equilibrium potential without an overall net change [150]. The equation for calculating this parameter is presented as follows:

$$I_0 = \frac{RT}{nFR_{ct}} \tag{4.69}$$

Where: R is the molar gas constant = 8.314 J/mol/K [255]; T is the room temperature = 293 K [255]; n is the number of transferred electrons; F is Faraday's constant = 96485 C/mole [256]. The heterogeneous rate constant of electron transfer $\left(k_{et}\right)$ [257], which is the third kinetic parameter, was additionally calculated conforming to the equation below:

$$k_{et} = \frac{I_0}{nFAC} \tag{4.70}$$

Where: A is the area of the nickel foam substrate (0.5 cm^2) and C is the concentration of the metal Cu^{2+} and Mn^{3+} ions within the Mn_3O_4, $CuMn_2O_4$, and $CuMn_2O_4$/MWCNT matrix [258]. The mass of the Mn_3O_4, $CuMn_2O_4$, and $CuMn_2O_4$/MWCNT electrode materials that was coated on their individual nickel foam substrates was 2.31 mg, 3.15 mg, and 3.85 mg, respectively. Another vital element is the volume of electrolyte used, and during experimentation, 5 ml of 3 M KOH was used. From all this information, the concentration of the metal ions was able to be obtained. Finally, having obtained all the variables in **equation (4.70)**, the value of k_{et} for all the synthesized electrode materials was obtained. The Warburg coefficient (σ), which is defined by the diffusion coefficient of electrolyte ions across the electrode interface, was determined in consonance with the following equation [257, 259]:

$$\sigma = \left(R_s + R_{ct}\right).\omega^{1/2} \tag{4.71}$$

The equation for the apparent diffusion coefficient $\left(D_{app}\right)$, an additional kinetics parameter, is derived from the equation of the Warburg coefficient (σ) in its original form [260].

$$D_{app} = \frac{2\left(RT\right)^2}{\left(\sigma n^2 F^2 AC\right)^2} \tag{4.72}$$

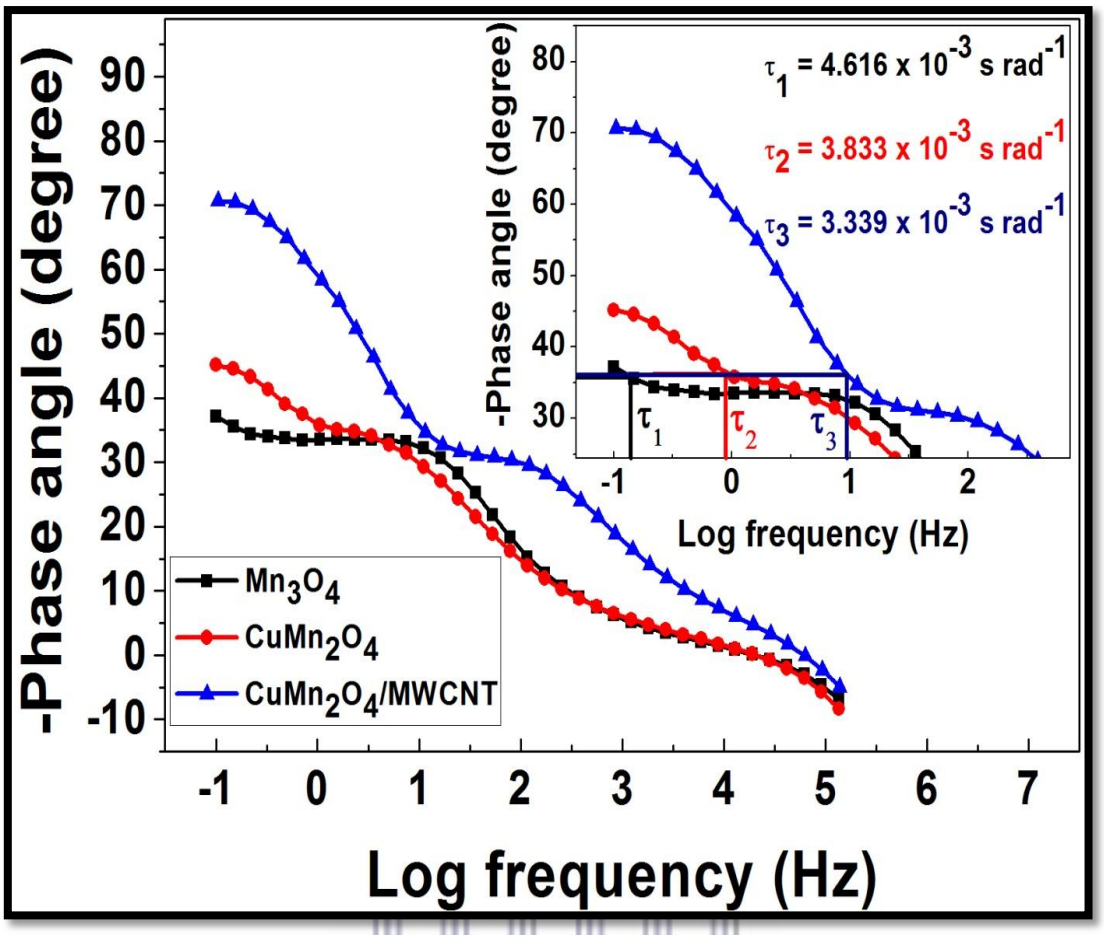

Figure 4.42: Comparative Bode plots of the pristine Mn_3O_4, spinel $CuMn_2O_4$, and hybrid $CuMn_2O_4$/MWCNT electrode materials obtained with a 3M KOH aqueous electrolyte solution.

Table 4.16: Kinetic parameters of the pristine Mn_3O_4, spinel $CuMn_2O_4$, and hybrid $CuMn_2O_4$/MWCNT electrode materials, calculated from EIS data obtained at 298 K.

Electrode materials	τ $[s\,rad^{-1}]$	I_0 [A]	σ $[\Omega s^{-1/2}]$	k_{et} $[cm\,s^{-1}]$	D_{app} $[cm^2\,s^{-1}]$
Mn_3O_4	4.616×10^{-3}	0.02	30.253	2.343×10^{-4}	2.34×10^{-10}
$CuMn_2O_4$	3.833×10^{-3}	0.03	16.992	2.591×10^{-4}	2.69×10^{-10}
$CuMn_2O_4$/MWCNT	3.339×10^{-3}	0.04	11.098	4.509×10^{-4}	1.315×10^{-9}

The EIS Nyquist plots, illustrated in **Fig. 4.41**, displayed distinctive single semi-circle curves in the high frequency regime and slanted straight line curves in the low frequency region. The inclined straight-line curves are attributed to the Warburg impedance (W_s), which is associated with the diffusion of electrolyte ions in the bulk of the electrode material [261]. The diffusion kinetics of the electrolyte ions is controlled by the Warburg impedance in the low frequency region, where as the charge transfer processes is controlled by the resistance in the high frequency region [262]. The charge-transfer resistance (R_{ct}), illustrated in **Table 4.15**, for the pristine Mn_3O_4, spinel $CuMn_2O_4$, and hybrid $CuMn_2O_4$/MWCNT electrode materials were obtained to be 1.293 Ω, 0.827 Ω, and 0.633 Ω, respectively. The smaller charge-transfer resistance exhibited by the hybrid $CuMn_2O_4$/MWCNT electrode material indicated the promotion of faster electrolyte ion diffusion kinetics at the electrode/electrolyte interface [263]. This statement is further confirmed by the shorter response-time (τ) illustrated in the Bode plots of **Fig. 4.42** and calculated kinetic parameters data in **Table 4.16**.

The fast ionic-diffusion through the hybrid $CuMn_2O_4$/MWCNT electrode material matrix is a result of the $CuMn_2O_4$/MWCNT structure. XRD analysis results previously revealed that the spinel $CuMn_2O_4$ material possessed Cu^{2+} tetrahedral and Mn^{3+} octahedral interstitial sites, whereby electrons and/or ions presumably occupy during electrochemical processes. In addition to the improved conductivity provided by the MWCNTs, it also assisted the hybrid material's ionic-diffusion by inducing a low ionic-diffusion resistance [264]. The phase angle, from the Bode plots illustrated in **Fig. 4.42**, obtained for the pristine Mn_3O_4, spinel $CuMn_2O_4$, and hybrid $CuMn_2O_4$/MWCNT electrode materials were 37°, 45°, and 71°, respectively. The higher phase angle exhibited by the hybrid $CuMn_2O_4$/MWCNT electrode material provided the indication that it was the most conductive of the three synthesized electrode materials. In literature, it was reported that an electrode material synthesized for an ideal Electrical Double Layer Capacitor (EDLC) system, exhibited a phase angle close to 90° (i.e, within the range of 80 – 90°) [265]. This would imply that electrode materials exhibiting phase angles below 80° possess pseudocapacitive properties, as a result of faradaic oxidation/reduction reactions occurring at the electrode/electrolyte interface during electrochemical analysis [75]. The hybrid $CuMn_2O_4$/MWCNT electrode material also exhibited a higher apparent diffusion coefficient $\left(D_{app}\right)$ implying that a larger surface area of electrolyte ions were diffused at the electrode/electrolyte interface.

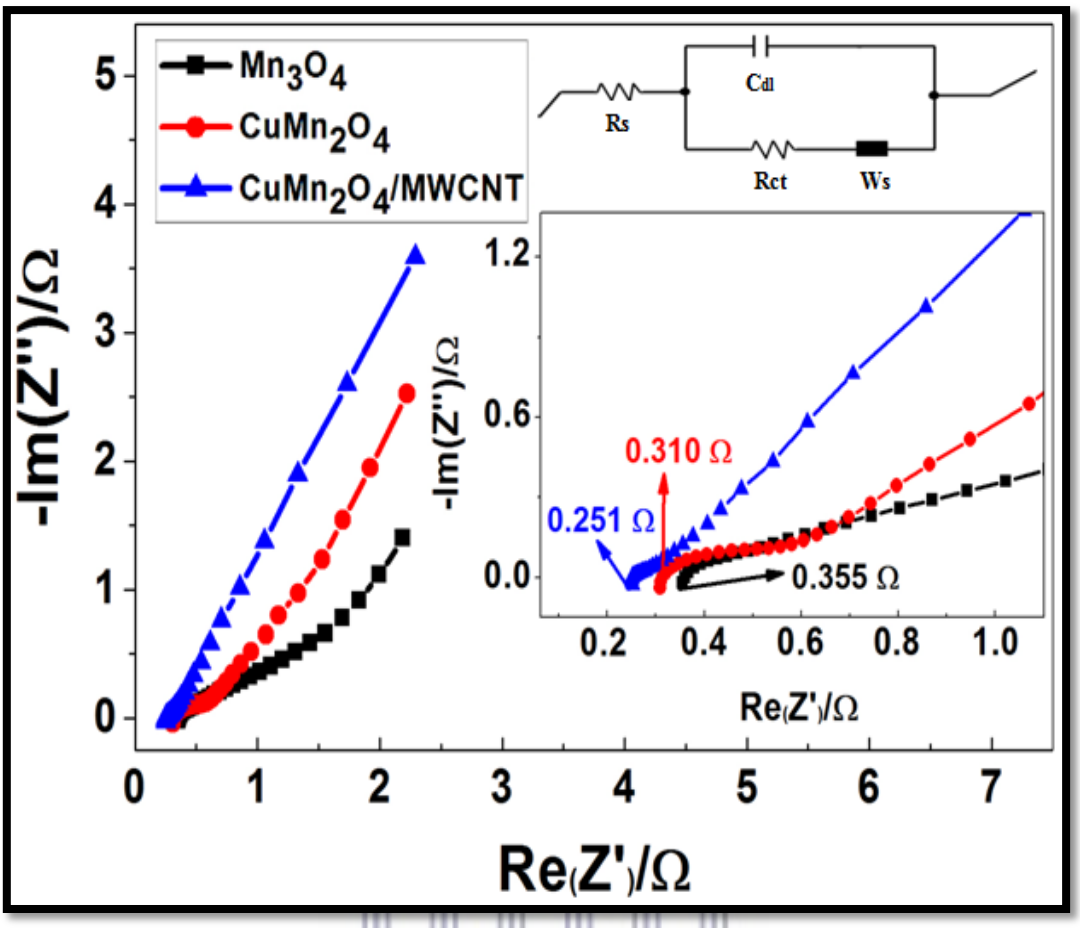

Figure 4.43: Comparative Nyquist plots of the pristine Mn_3O_4, spinel $CuMn_2O_4$, and hybrid $CuMn_2O_4$/MWCNT electrode materials obtained at a frequency range of 100 mHz-200 kHz with a 3M LiOH aqueous electrolyte solution.

Table 4.17: EIS fitted data of the Mn_3O_4, $CuMn_2O_4$, and $CuMn_2O_4$/MWCNT electrode materials with a 3 M LiOH aqueous electrolyte solution.

Electrode materials	R_s [Ω]	C_{dl} [F]	R_{ct} [Ω]	W_s [$\Omega.s^{-1/2}$]
Mn_3O_4	0.356	3.160×10^{-3}	0.516	4.978
$CuMn_2O_4$	0.212	5.660×10^{-3}	0.476	2.86
$CuMn_2O_4$/MWCNT	0.086	7.872×10^{-3}	0.350	0.861

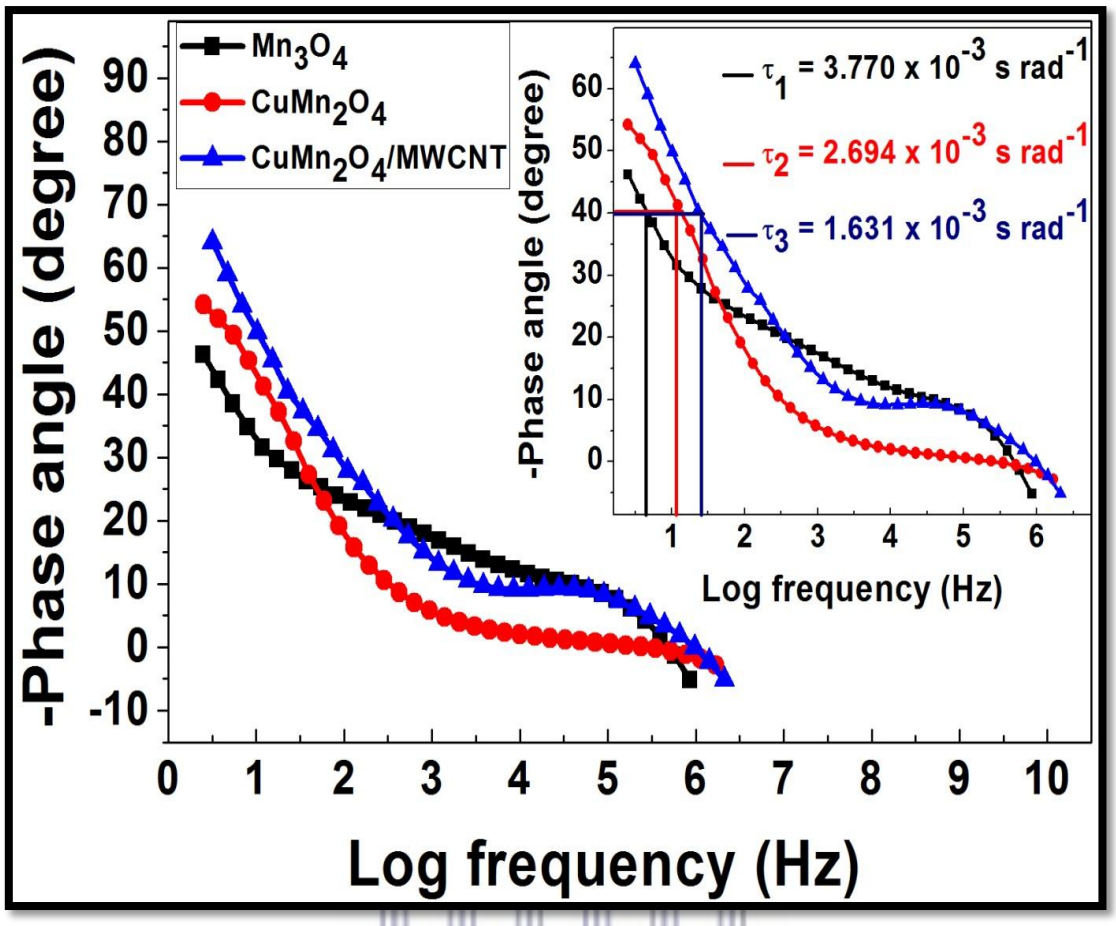

Figure 4.44: Comparative Bode plots of the pristine Mn_3O_4, spinel $CuMn_2O_4$, and hybrid $CuMn_2O_4$/MWCNT electrode materials obtained with a 3M LiOH aqueous electrolyte solution.

Table 4.18: Kinetic parameters of the pristine Mn_3O_4, spinel $CuMn_2O_4$, and hybrid $CuMn_2O_4$/MWCNT electrode materials, calculated from EIS data obtained at 298 K.

Electrode materials	τ $[s\,rad^{-1}]$	I_0 [A]	σ $[\Omega s^{-1/2}]$	k_{et} $[cm\,s^{-1}]$	D_{app} $[cm^2\,s^{-1}]$
Mn_3O_4	3.770×10^{-3}	0.049	21.595	4.139×10^{-4}	4.43×10^{-10}
$CuMn_2O_4$	2.694×10^{-3}	0.053	13.255	6.348×10^{-4}	4.59×10^{-10}
$CuMn_2O_4$/MWCNT	1.631×10^{-3}	0.072	8.757	8.116×10^{-4}	5.768×10^{-9}

EIS experiments for the electrode materials in a 3 M LiOH aqueous electrolyte solution were conducted in order to investigate, whether or not, the Li^+ ions would easily undergo ionic-diffusion at a faster response-time [145]. The EIS spectrograph of the electrode materials analyzed with a 3 M LiOH aqueous electrolyte solution is presented in **Fig. 4.43**. The analyzed data obtained from the EIS spectrograph indicated that the electrode materials exhibited lower charge-transfer resistance (R_{ct}) values, compared to that obtained after electrochemical analysis with the 3 M KOH aqueous electrolyte solution. From these results, it was certain that a greater surface area of Li^+ ions were diffused at a faster rate, as confirmed by the apparent diffusion coefficient (D_{app}) and response-time (τ) values calculated from the Bode plots in **Fig. 4.44** [266-267]. It is previously mentioned in CV analysis that the main reason for Li^+ ions diffusing faster and easier than that of K^+ ions, is a result of its smaller ionic radii (Li^+ = 0.076 nm) over that of potassium (K^+ = 0.138 nm) [217]. This, therefore, enabled the Li^+ ions to intercalate within the atomic spaces of the metal oxide and carbon based electrode materials [268].

Comparing the electrochemical impedance results for the three electrode materials analyzed in the 3 M KOH and 3 M LiOH aqueous electrolyte solutions; it was observed that the 3 M LiOH electrolyte analysis exhibited a lower electrochemical resistance and, therefore, a greater capacitive performance. The full cell two-electrode cell configuration was then assembled using the 3 M LiOH aqueous electrolyte solution, where EIS measurements were performed at a sinusoidal frequency range of 100 mHz-200 kHz [252, 268-269]. After fitting the Nyquist plots with the equivalent circuit model, also illustrated as an inset of **Fig. 4.45**, the data obtained indicated that the R_{ct} value for the $CuMn_2O_4$/MWCNT ‖ AC cell device was lower than that of the other assembled supercapacitor cell devices [270-271]. The R_{ct} values for the Mn_3O_4 ‖ AC, $CuMn_2O_4$ ‖ AC, and $CuMn_2O_4$/MWCNT ‖ AC two-electrode cells were obtained as 0.457 Ω, 0.310 Ω, and 0.156 Ω, respectively. The lower R_{ct} value exhibited by the $CuMn_2O_4$/MWCNT ‖ AC supercapacitor cell device is due to the faster transport of charges through the pores of the hybrid $CuMn_2O_4$/MWCNT composite electrode material matrix [268]. The Nyquist plots, indicated in **Fig. 4.45**, correspond with the Bode phase-impedance plots, in **Fig. 4.46**, where the phase angle values were obtained as (Mn_2O_4 ‖ AC: 16°; $CuMn_2O_4$ ‖ AC: 51°; and $CuMn_2O_4$/MWCNT ‖ AC: 70°) at low frequency regimes [114, 272].

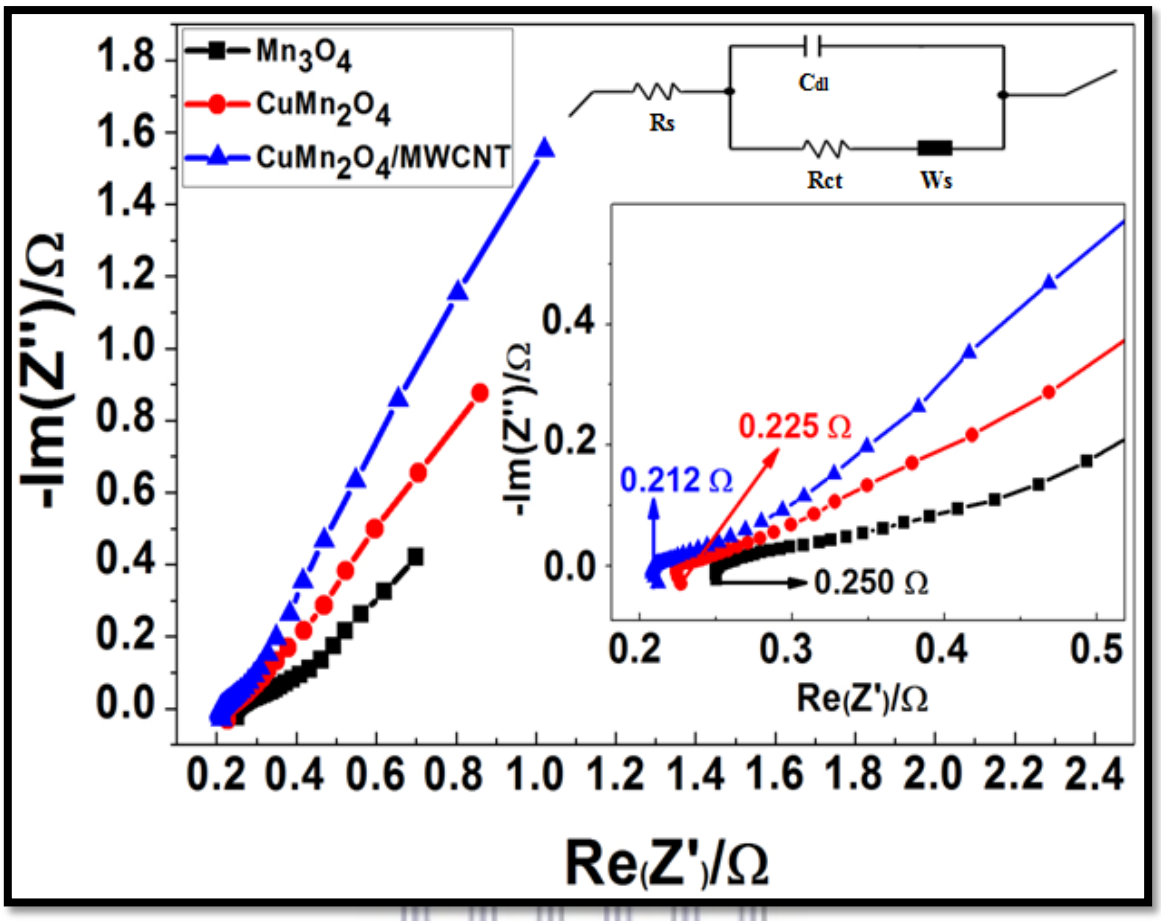

Figure 4.45: Comparative Nyquist plots of the Mn_3O_4 ‖ AC, $CuMn_2O_4$ ‖ AC, and $CuMn_2O_4$/MWCNT ‖ AC supercapacitor cells obtained at a frequency range of 100 mHz-200 kHz with a 3M LiOH aqueous electrolyte solution.

Table 4.19: EIS fitted data of the Mn_3O_4 ‖ AC, $CuMn_2O_4$ ‖ AC, and $CuMn_2O_4$/MWCNT ‖ AC full cell devices with a 3 M LiOH aqueous electrolyte solution.

Electrode materials	R_s [Ω]	C_{dl} [F]	R_{ct} [Ω]	W_s [$\Omega.s^{-1/2}$]
Mn_3O_4	0.604	1.210×10^{-3}	0.457	5.317
$CuMn_2O_4$	0.321	0.480×10^{-3}	0.310	3.317
$CuMn_2O_4$/MWCNT	0.459	0.365×10^{-3}	0.156	3.383

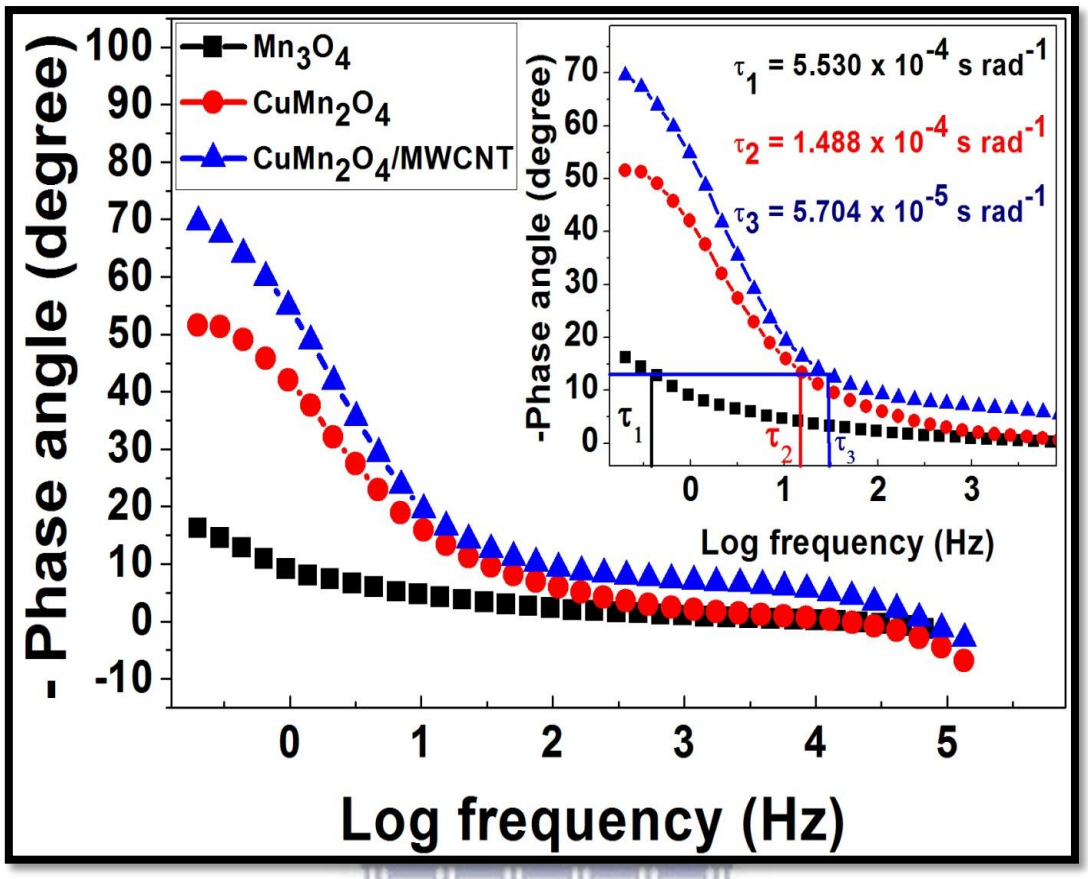

Figure 4.46: Comparative Bode plots of the Mn_3O_4 ‖ AC, $CuMn_2O_4$ ‖ AC, and $CuMn_2O_4$/MWCNT ‖ AC supercapacitor cells obtained with a 3M LiOH aqueous electrolyte solution.

Table 4.20: Kinetic parameters of the Mn_3O_4 ‖ AC, $CuMn_2O_4$ ‖ AC, and $CuMn_2O_4$/MWCNT ‖ AC supercapacitor cell devices, calculated from EIS data obtained at 298 K.

Electrode materials	τ $[s\,rad^{-1}]$	I_0 [A]	σ $[\Omega s^{-1/2}]$	k_{et} $[cm\,s^{-1}]$	D_{app} $[cm^2\,s^{-1}]$
Mn_3O_4	5.530×10^{-4}	0.055	81.431	1.562×10^{-4}	3.84×10^{-12}
$CuMn_2O_4$	1.488×10^{-4}	0.081	51.728	2.716×10^{-4}	5.05×10^{-12}
$CuMn_2O_4$/MWCNT	5.704×10^{-5}	0.162	45.120	1.071×10^{-3}	8.43×10^{-12}

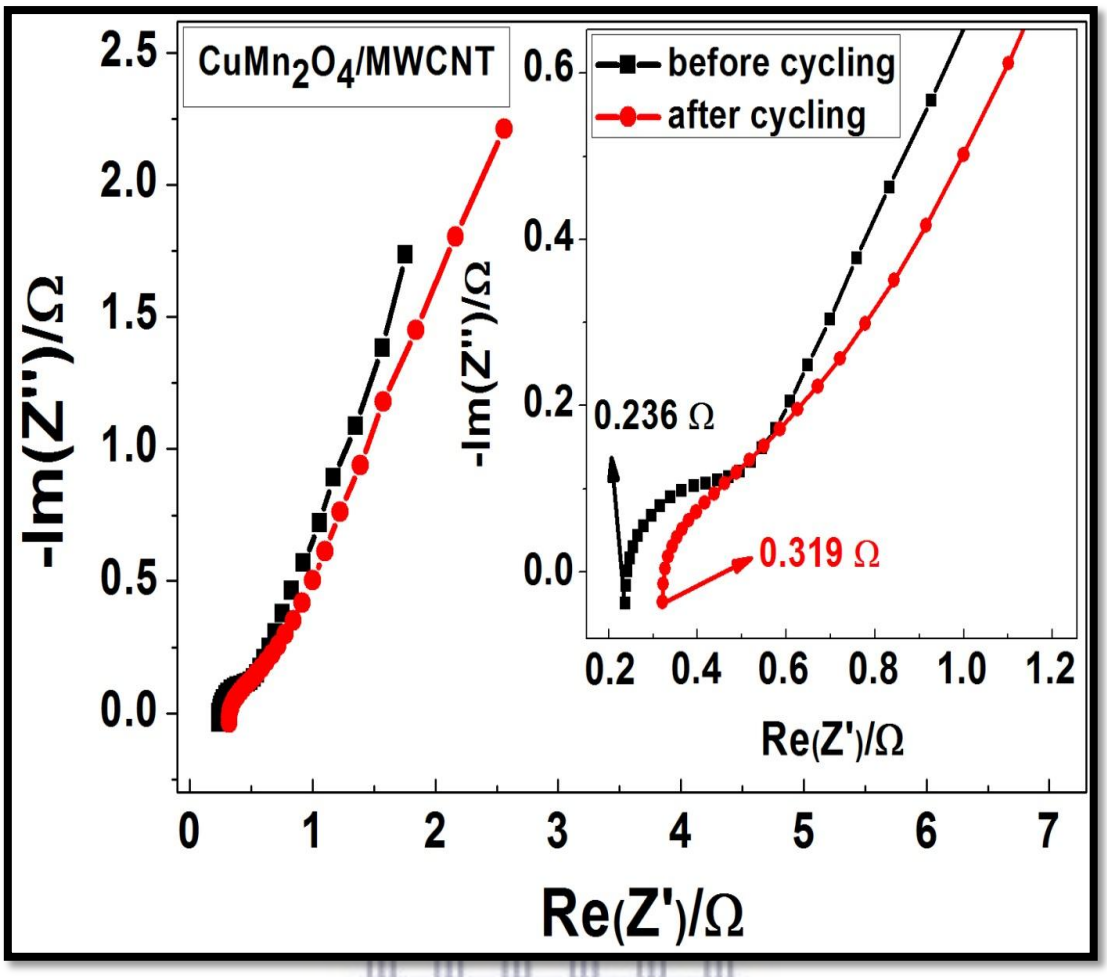

Figure 4.47: Nyquist plot for the $CuMn_2O_4$/MWCNT ‖ AC supercapacitor cell before and after cycling in a 3M LiOH aqueous electrolyte solution.

Cycling stability tests were conducted on the full cell two-electrode $CuMn_2O_4$/MWCNT ‖ AC electrochemical capacitor, and EIS data was obtained in order to investigate the behaviour of the electrode material prior and post to cycling experiments, as illustrated in **Fig. 4.47** and **4.48**. The cycling stability test results obtained after performing GCD analysis of the $CuMn_2O_4$/MWCNT ‖ AC supercapacitor cell, revealed exceptional stability data as the device retained a specific capacitance of 460 F/g (i.e., approximately 91% of its initial capacitance of 507 F/g) for 3000 cycles at a 1 A/g current density [62]. The analyzed EIS data obtained after performing cycling stability tests indicated that the cell device exhibited a charge-transfer resistance (R_{ct}) of 0.252 Ω, which is slightly higher than the R_{ct} value of 0.156 Ω obtained prior to cycling experiments. This result implied that the electrochemical capacitor (EC) cell device would still operate optimally after a greater number of cycles. However, in order to obtain a more accurate set of electrochemical data regarding the

stability of the supercapacitor cell device, a minimum of 5000 cycles should be implemented during cycling stability experiments [273]. This statement is included in the list of recommended future electrochemical research prospects. In addition to cycling analysis, it was also reported that a different technique called voltage-holding (also known as "float test"), can be deemed useful when investigating the performance of the EC-cell over extended time-periods [273]. The Bode-phase impedance plot in **Fig. 4.48**, illustrated that the $CuMn_2O_4$/MWCNT ‖ AC full cell device exhibited a 30% decrease in conductivity after cycling, as illustrated by the lower phase angle. This percentage is less than half, thus giving the impression that the cell device could be tested at extended time-periods and increased cycle number. These experimental proposals are currently being pursued for a future manuscript potentially to be published.

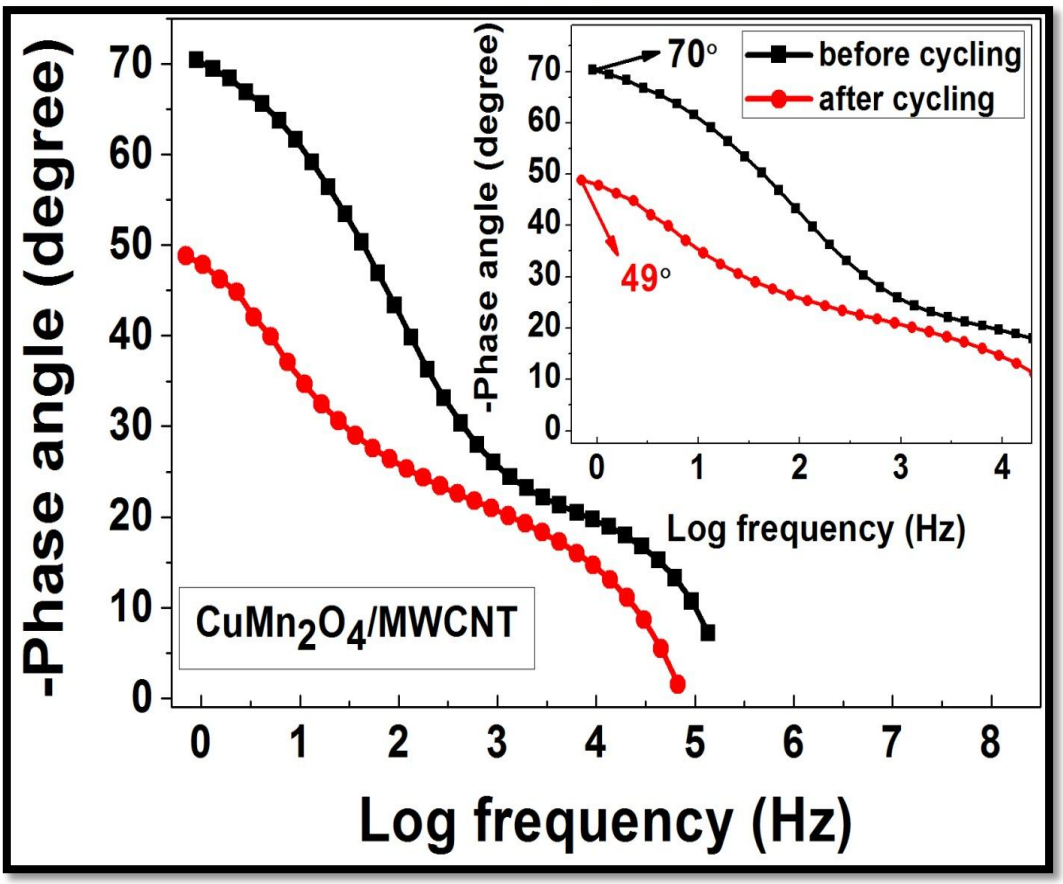

Figure 4.48: Bode phase-impedance plot for the $CuMn_2O_4$/MWCNT ‖ AC supercapacitor cell before and after cycling in a 3M LiOH aqueous electrolyte solution.

4.3.3 Galvanostatic charge/discharge (GCD) analysis

4.3.3.1 Electrochemical studies of half cell (three-electrode) system with 3 M KOH electrolyte

The galvanostatic charge/discharge technique is one of the most dependable methods used to test and evaluate the electrochemical specific capacitance of electrode materials for supercapacitor devices. In this technique, the specifically selected current density and applied potential variables are controlled, whereas the time variable is measured. Apart from the specific capacitance, two additional parameters can be calculated and obtained from galvanostatic charge/discharge data. These parameters are called the maximum specific power density (P_{max}) and the specific energy density (E_{sp}). The mathematical equations for calculating each of these parameters is presented as follows:

The slope of the charge/discharge curves was used for the specific capacitance calculations, as per following the equation below:

$$C_{sp} = \frac{4I\Delta t}{m\Delta V} \tag{4.73}$$

Where I is the discharge current (mA), Δt is the charge/discharge time interval (s), m is the mass (g) of the active material on each electrode surface, and ΔV is the potential window of charge and discharge occurrence [274]. The galvanostatic charge/discharge plot, with current densities ranging between 0.5 - 4 A/g, for all the electrode materials in the 3 M KOH electrolyte solution is illustrated in **Fig. 4.49**. The charge/discharge curves, from the plots, displayed approximate linearity, thus indicating pseudocapacitive behaviour exhibited from the electrode materials [148, 275]. The specific capacitance for the electrode materials was obtained through conforming to **equation (4.73)** above, by initially calculating the applied current from the electrode material mass and selected current density. The two pertinent parameters, maximum specific power density (P_{max}) and specific energy density (E_{sp}), were obtained from **equation (4.74)** and **(4.75)**, respectively.

$$P_{max}\left(\mathrm{W}/\mathrm{kg}\right)=\frac{V^2}{4mR_{ir}} \tag{4.74}$$

$$E_{sp}\left(\mathrm{Wh}/\mathrm{kg}\right)=\frac{CV^2}{2m} \tag{4.75}$$

Where C (F/g) is the specific capacitance calculated from **equation (4.73)**, V is the maximum operating potential, m (kg) is the mass of the active electrode material, and R_{ir} (Ω) is the internal resistance of the electrochemical cell. The internal resistance (R_{ir}) was calculated from the voltage drop (ΔV_{iR}) that occurs at the initial downward step of the discharge curve [62].

$$R_{ir}\left(\Omega\right)=\frac{\Delta V_{iR}}{2i} \tag{4.76}$$

As displayed in **Fig. 4.49**, the three electrode materials were analyzed under various selected current densities within the range of 0.5 – 4 A/g. The hybrid $CuMn_2O_4$/MWCNT electrode material exhibited the largest specific capacitance of 123.406 F/g, followed by the spinel $CuMn_2O_4$ material with a specific capacitance of 76.313 F/g, and lastly the pristine Mn_3O_4 material, which exhibited the lowest specific capacitance of 56.580 F/g. The analyzed GCD data were all evaluated at a current density of 0.5 A/g in an aqueous 3 M KOH electrolyte solution. Comparing the data obtained from GCD to that of CV, it was observed that the specific capacitance values calculated from CV data far out performed that calculated from GCD data. This unfortunate observation could have been rectified by selecting current densities preferably lower than 0.5 A/g. However, the data analysis for the 3 M LiOH electrolyte solution illustrated a relatively acceptable improvement. It was clearly notified that the larger specific capacitance exhibited by the hybrid electrode material, was attributed by the additional conductivity contributed by the multi-walled carbon nanotube structures [276]. The analyzed data presented in **Fig. 4.49**, as well as **equation (4.74)**, **(4.75)**, and **(4.76)** were utilized to computationally evaluate the energy and power densities of the

electrochemical cell. **Fig. 4.50** illustrates a Ragone plot displaying the relationship between the energy and power densities of all three investigated electrode materials. The data analysis portrayed in the Ragone plot indicated that the hybrid $CuMn_2O_4$/MWCNT electrode material exhibited the largest maximum energy and power density values of 48.171 Wh/kg and 596.602 W/kg, respectively, as compared to that of the pristine Mn_3O_4 and spinel $CuMn_2O_4$ electrode materials. These calculated results were performed at a current density of 0.5 A/g. This trend of superior pseudocapacitive performance displayed by the hybrid material over the others indicated that it was the best-suited cathode electrode material for a supercapacitor full cell (two-electrode) device.

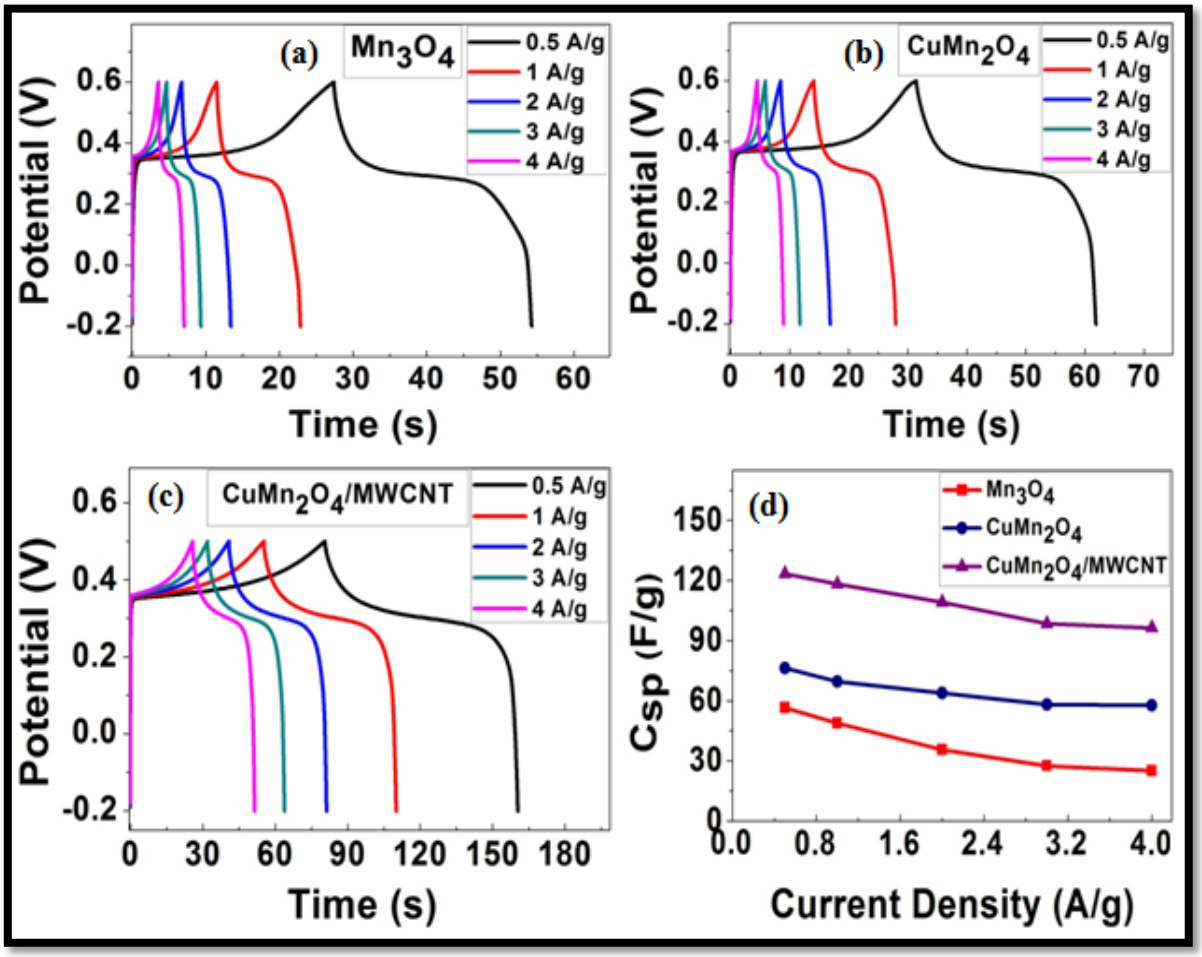

Figure 4.49: Galvanostatic charge/discharge curves (obtained using a 3M KOH electrolyte solution) of (a) pristine Mn_3O_4, (b) spinel $CuMn_2O_4$, and (c) hybrid $CuMn_2O_4$/MWCNT electrode materials at various current densities; as well as (d) the specific capacitance against current density ragone plot for all synthesized materials.

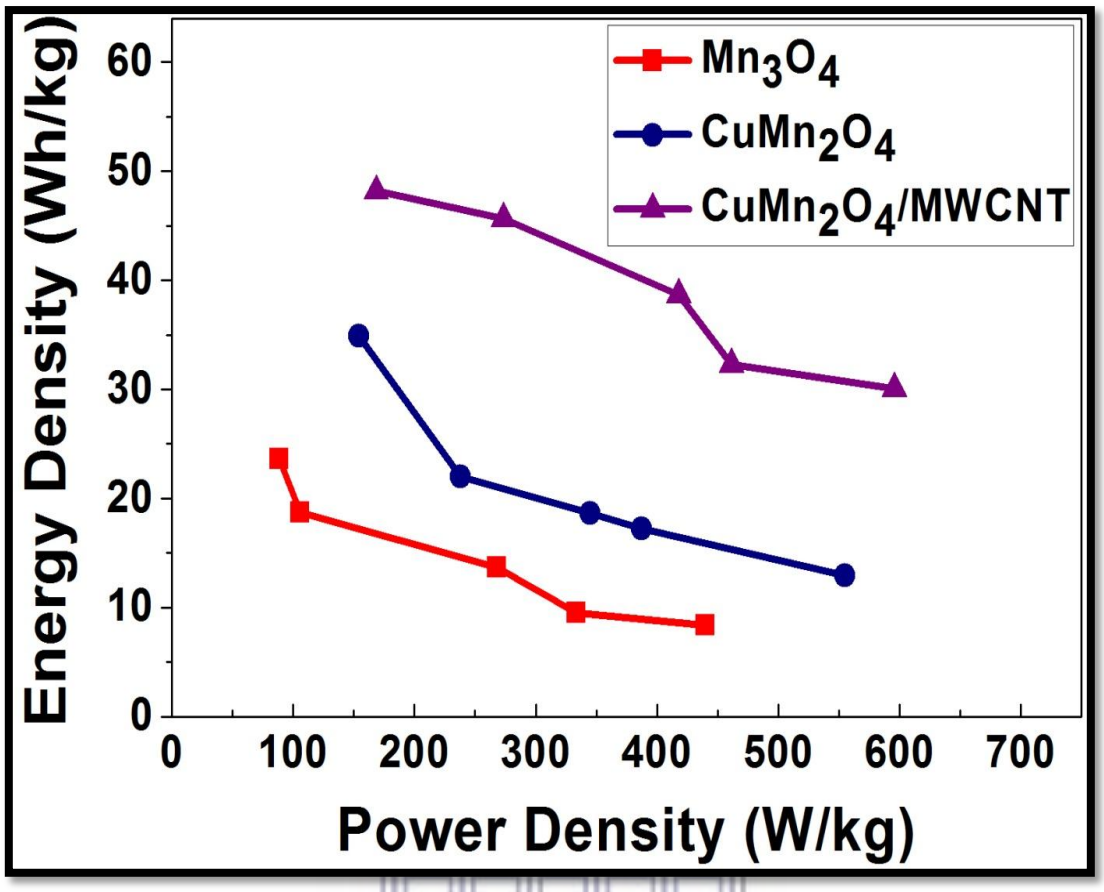

Figure 4.50: Ragone plot illustrating Energy against Power Densities for the pristine Mn_3O_4, spinel $CuMn_2O_4$, and hybrid $CuMn_2O_4$/MWCNT electrode materials obtained using the 3 M KOH aqueous electrolyte solution.

The superior pseudocapacitive performance trend exhibited by the hybrid $CuMn_2O_4$/MWCNT electrode material is evidently shown in the rate capability plots from CV and GCD analysis. The data analysis in the plot of **Fig. 4.50** also illustrated maximum energy and power density values of 23.620 Wh/kg and 441.468 W /g, respectively, for the pristine Mn_3O_4 electrode material. The maximum energy and power density values for the spinel $CuMn_2O_4$ electrode material were obtained as 34.920 Wh/kg and 554.688 W/kg, respectively. From studies documented in literature, it was identified and hypothesized through comparison that the asymmetric $CuMn_2O_4$/MWCNT ‖ AC supercapacitor system would be a suitable electrochemical device for energy storage applications [277]. The three synthesized electrode materials were also tested with a 3 M aqueous LiOH electrolyte solution, and from the analyzed results, the materials exhibited longer response times.

4.3.3.2 Electrochemical studies of half cell (three-electrode) system with 3 M LiOH electrolyte

The results obtained after analyzing the electrode materials in the 3 M LiOH aqueous electrolyte solution, indicated some quite remarkable performance results. After performing the prescribed calculations, it was obtained that the electrode material's specific capacitance values increased by 80.105 %, 66.338 %, and 64.042 %, for the hybrid, spinel, and pristine electrode materials, respectively, from the results obtained after electrochemical analysis with 3 M KOH aqueous electrolyte solution. It can be seen in **Fig. 4.49** and **4.51** that the operating potential for the hybrid material was initialized at a low voltage, as the charging process became unstable at high potentials. This, however, did not occur during the two-electrode full cell analysis as this configuration is designed for maintaining its electrode stability at high operating potentials.

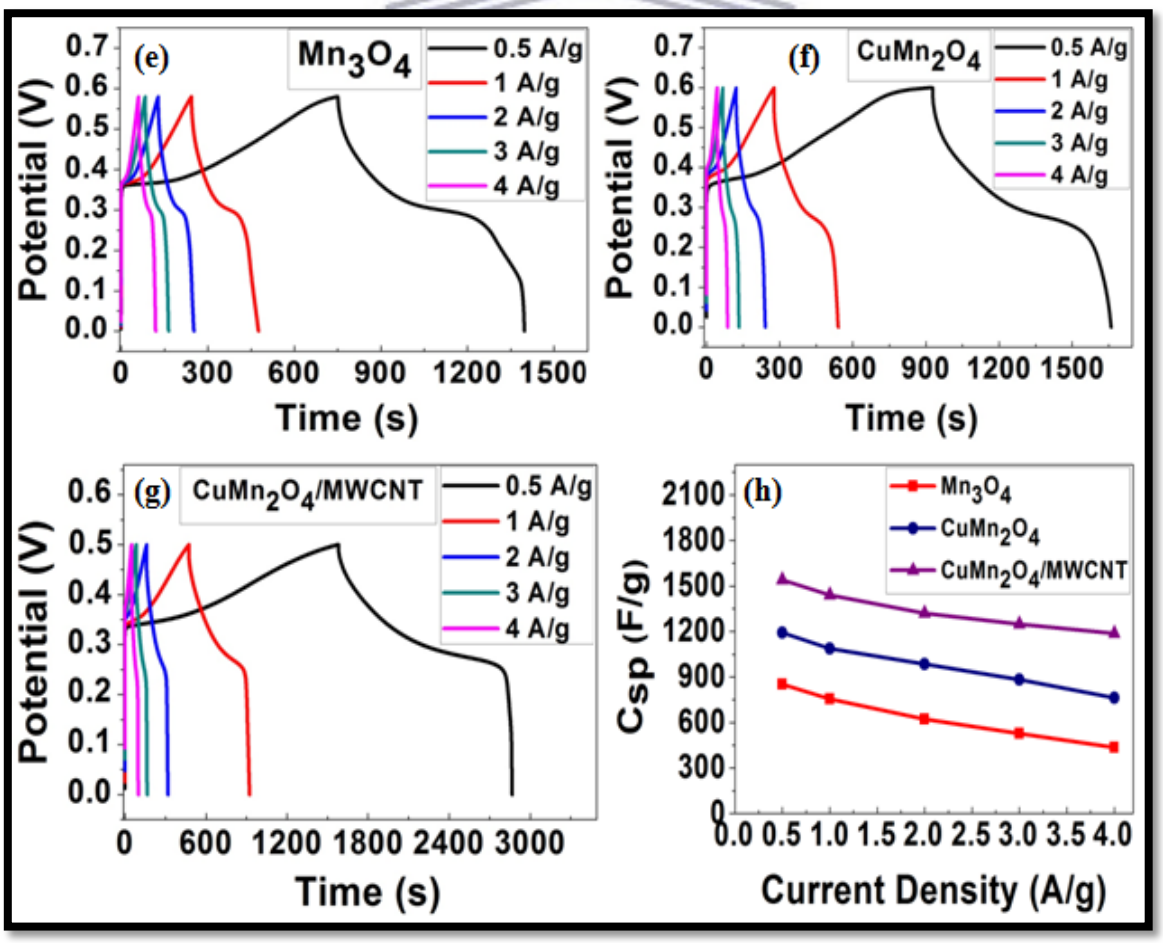

Figure 4.51: Galvanostatic charge/discharge curves, as well as the specific capacitance against current density plot for all synthesized materials in 3 M LiOH electrolyte.

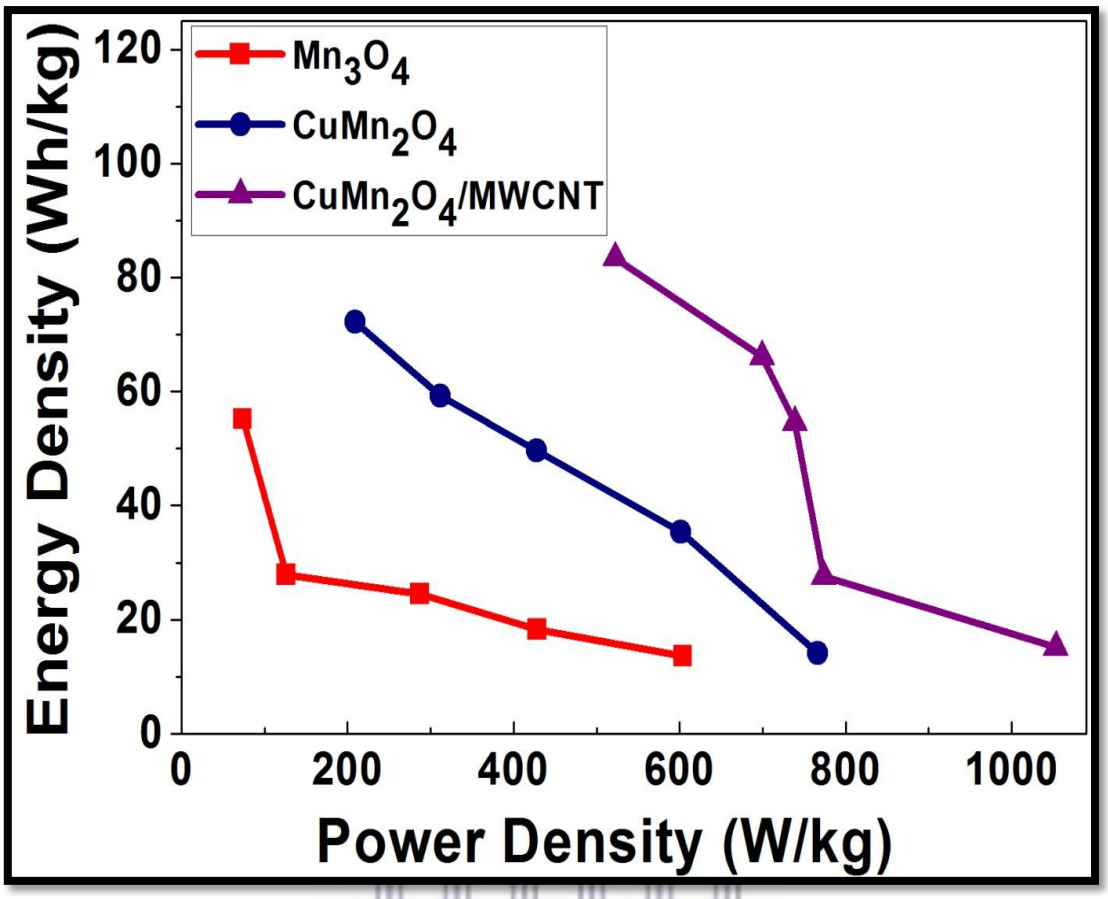

Figure 4.52: Ragone plot illustrating Energy against Power Densities for all the electrode materials obtained using the 3 M LiOH aqueous electrolyte solution.

It is evidently displayed in **Fig. 4.52** that the electrode materials analyzed in 3 M LiOH electrolyte exhibited maximum energy and power densities of 55.160 Wh/kg and 605.817 W/kg (for Mn_3O_4), 72.189 Wh/kg and 766.367 W/kg (for $CuMn_2O_4$), and 83.597 Wh/kg and 1053.800 W/kg (for $CuMn_2O_4$/MWCNT), respectively. It was also additionally deduced that the energy and power density values for the electrode materials were quite close to each other, thus revealing that the calculated results were quite accurate for manual input of data into the equations to perform each computation. The impressive energy and power density exhibited by the hybrid $CuMn_2O_4$/MWCNT material is attributed to the porous architecture of the multi-walled carbon nanotube structures [278]. The porous nature of the hybrid material is beneficial for the penetration of electrolyte ions, during intercalaction processes, into the material's atomic spaces. This would then also advance electrolyte ion diffusion through the electrode material surface at the electrode/electrolyte interface [279].

4.3.3.3 Electrochemical studies of full cell (two-electrode) system with 3 M LiOH electrolyte

The GCD plots in **Fig. 4.53** for all the synthesized electrode materials assembled in a full cell supercapacitor system, illustrated longer charge/discharge response times than that of the three-electrode configuration. It was also additionally operated at a higher potential window of 1.2 V. The maximum specific capacitance values for the Mn_3O_4 ‖ AC, $CuMn_2O_4$ ‖ AC, and $CuMn_2O_4$/MWCNT ‖ AC supercapacitor cell devices were obtained to be 994.373 F/g, 1608.523 F/g, and 2234.460 F/g, respectively. This improved specific capacitance values may have been a result of the greater operating voltage used. Nevertheless, the specific capacitance values for the $CuMn_2O_4$/MWCNT ‖ AC cell device at various current densities, additionally illustrated a 60% retention, thus indicating good rate capability [279].

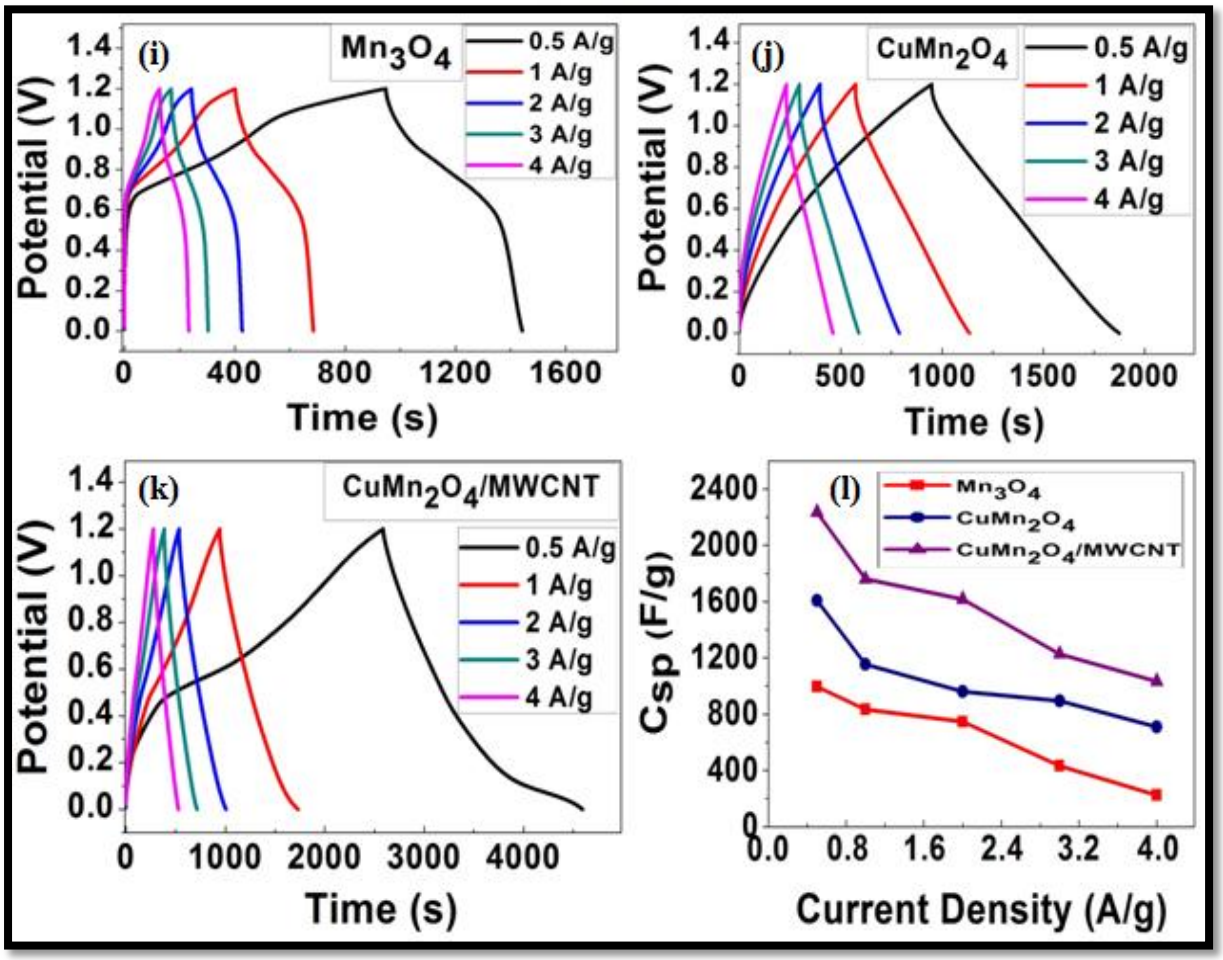

Figure 4.53: The correlation of GCD plots for (i) Mn_3O_4 ‖ AC, (j) $CuMn_2O_4$ ‖ AC, (k) $CuMn_2O_4$/MWCNT ‖ AC, and (l) rate capability of supercapacitor cells at various current densities (0.5 – 4 A/g).

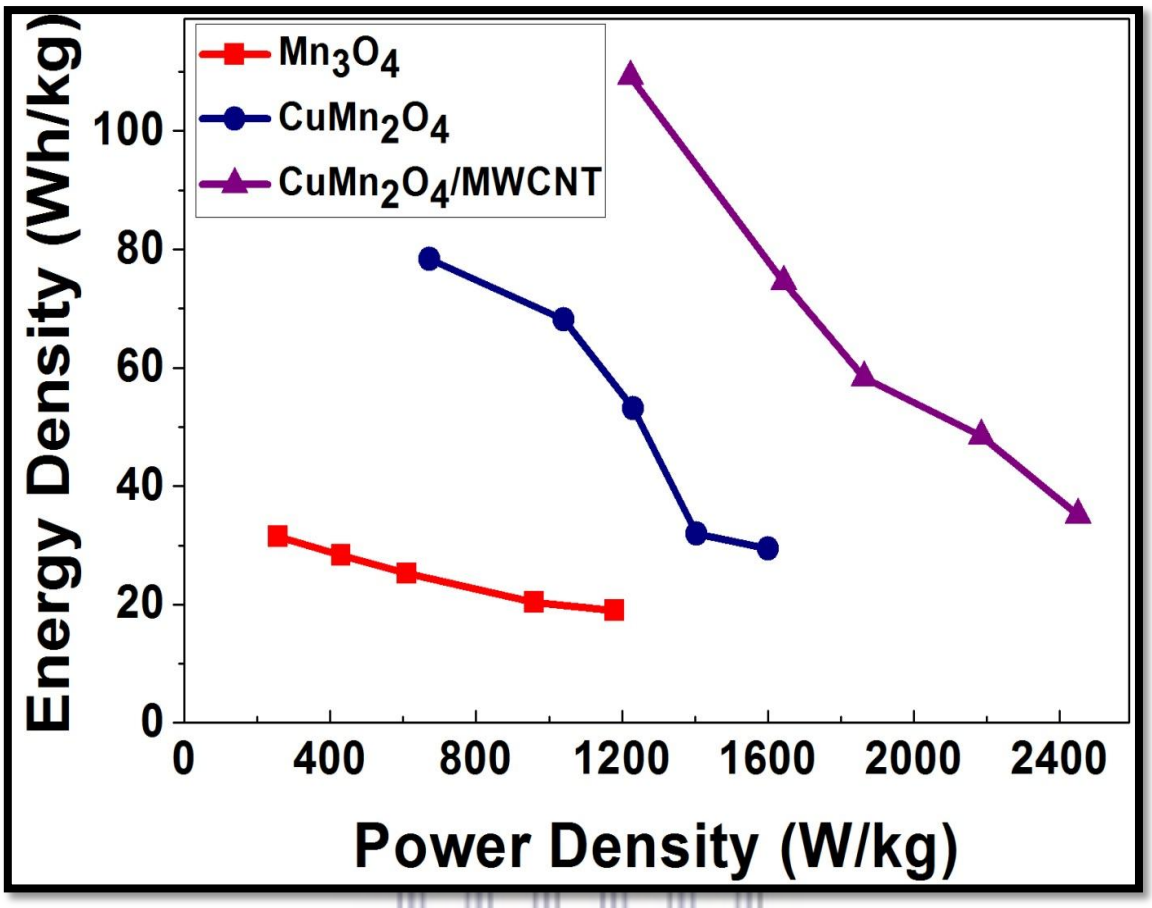

Figure 4.54: Ragone plot illustrating Energy against Power Densities of all the asymmetric supercapacitor cells obtained using 3 M LiOH aqueous electrolyte solution.

The operational performance of the fabricated Mn_3O_4 ‖ AC, $CuMn_2O_4$ ‖ AC, and $CuMn_2O_4$/MWCNT ‖ AC supercapacitor cells were obtained through energy and power density calculations, where the results are illustrated in **Fig. 4.54**. As can be observed in the ragone plot, the maximum energy density of the asymmetric $CuMn_2O_4$/MWCNT ‖ AC cell device is 109.197 Wh/kg at a power density of 1221.324 W/kg. The plot also illustrated that the cell device retained a relatively high energy density of 35.068 Wh/kg at a maximum power density of 2449.942 W/kg. The calculated energy density values of the asymmetric $CuMn_2O_4$/MWCNT ‖ AC supercapacitor cell device were higher than most values reported in resent literature [280-282]. However, the unfortunate characteristic of the device performance was that it exhibited an unusually low power density, compared to other reported cell devices [283]. This could very well be a result of the hindered stability nature of the hybrid $CuMn_2O_4$/MWCNT electrode material structure at high operating voltages. The

charge/discharge curves of the Mn_3O_4 ‖ AC, $CuMn_2O_4$ ‖ AC, and $CuMn_2O_4$ ‖ AC supercapacitor cells at 1 A/g current density, were compared with one another, as displayed in **Fig. 4.55**. The discharge profiles of the respected supercapacitor devices illustrated symmetrical corresponding charge profiles, thus indicating enhanced electrochemical reversibility exhibited by the full cell devices. All the electrode materials exhibited a decrease in specific capacitance (C_{sp}) with an increase in current density. This is due to the diffusion kinetic limitations of the electrolyte ions on the electrode surface [284]. The diffusion kinetic limitation arises due to the high internal resistance (R_{ir}) experienced by the electrochemical cell during charge/discharge processes. The $CuMn_2O_4$/MWCNT ‖ AC supercapacitor cell displayed the best performance due to the result of a lower experienced internal resistance.

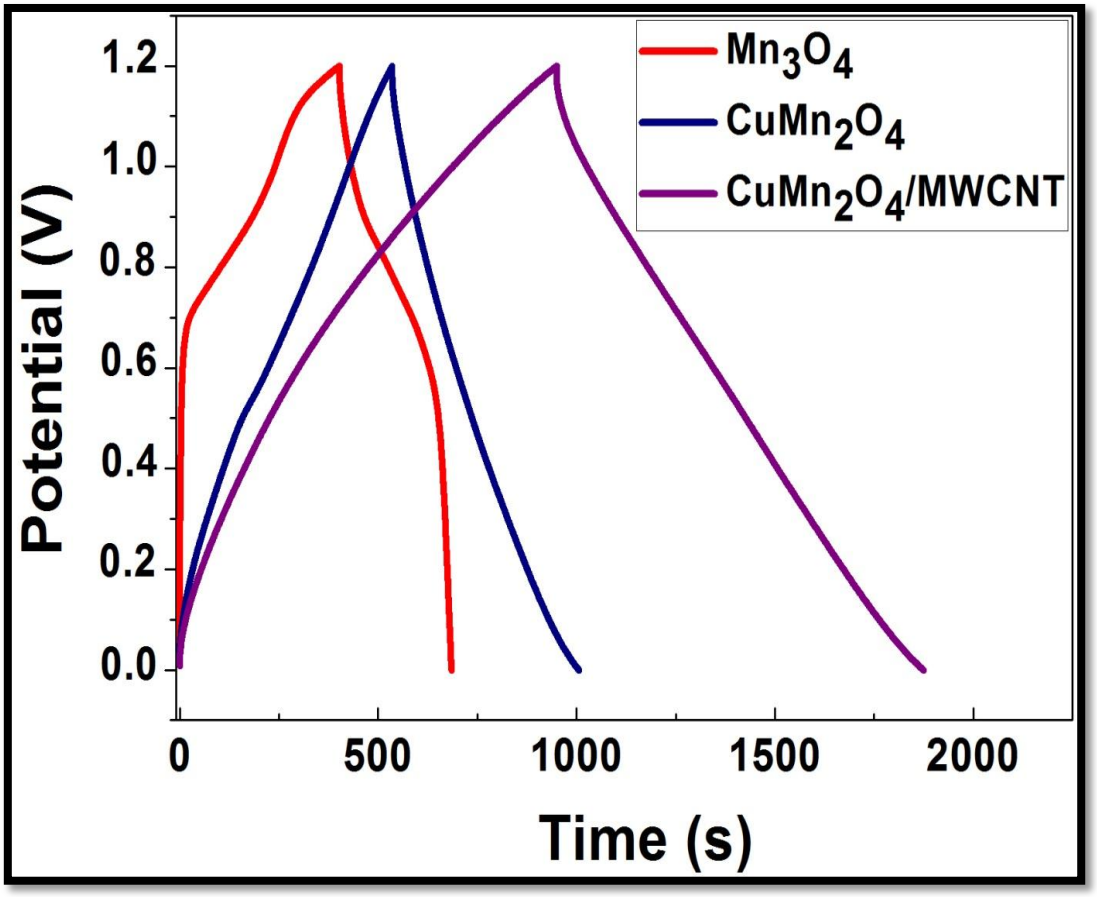

Figure 4.55: Final comparative galvanostatic charge/discharge curves for the Mn_3O_4 ‖ AC, $CuMn_2O_4$ ‖ AC, and $CuMn_2O_4$/MWCNT ‖ AC supercapacitor cells at a current density of 1 A/g, in an aqueous 3 M LiOH electrolyte solution.

The life cycle of a supercapacitor's electrode material is a crucial aspect to investigate, as it provides data on how long the device will sustain its operational use [63]. The galvanostatic charge/discharge technique was used to test the cycle life of the Mn_3O_4 ‖ AC, $CuMn_2O_4$ ‖ AC, and $CuMn_2O_4$/MWCNT ‖ AC supercapacitor cells at a current density of 1 A/g, as illustrated in **Fig. 4.56**. The hybrid $CuMn_2O_4$/MWCNT ‖ AC supercapacitor cell device, impressively exhibited a specific capacitance of 948.388 F/g and a capacitance retention and coulombic efficiency of 88.571% and 92%, respectively after 3000 cycles. Additionally, the pristine Mn_3O_4 ‖ AC and spinel $CuMn_2O_4$ ‖ AC cell devices exhibited specific capacitances of 416.165 F/g and 763.656 F/g, respectively, as well as a capacitance retention and coulombic efficiency of (80.310%, 62%) and (87.059%, 74%), individually after 3000 cycles. This outstanding cycling performance of the hybrid $CuMn_2O_4$/MWCNT ‖ AC full cell indicated that the device would retain its stability, during charging/discharging, for extended time-periods without experiencing any significant electrode material deterioration [105].

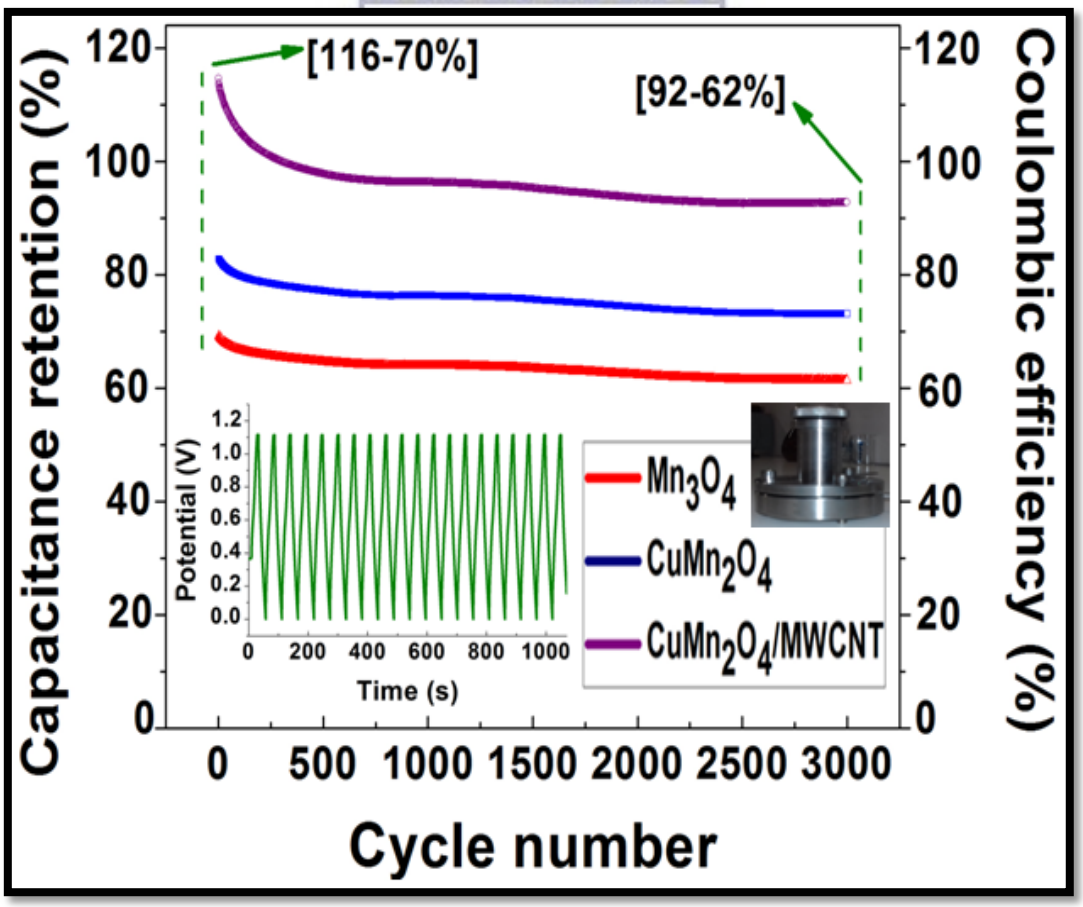

Figure 4.56: Cycling performance of the Mn_3O_4 ‖ AC, $CuMn_2O_4$ ‖ AC, and $CuMn_2O_4$/MWCNT ‖ AC supercapacitor cells at a current density of 1 A/g.

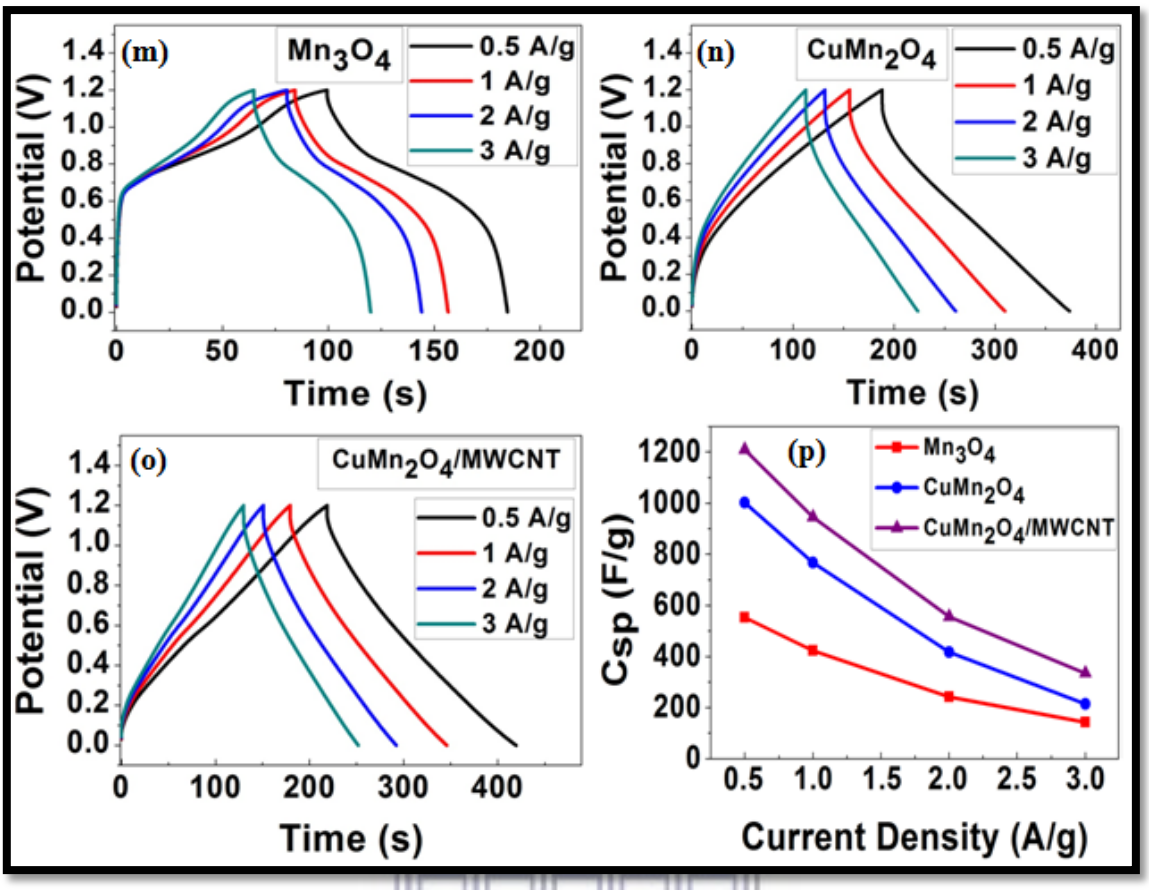

Figure 4.57: GCD analysis of electrode materials after 3000 cycles.

Table 4.21: Comparison of maximum specific capacitance values for various electrode materials operated within a LiOH aqueous electrolyte solution [285].

Electrode material	Electrolyte	Specific capacitance (F/g)	Reference
$CuMn_2O_4$/MWCNT	3 M LiOH	2234.5 at 0.5 A/g	This work
$LiMnPO_4$	2 M LiOH	170 at 0.5 A/g	[286]
$LiMnPO_4$/rGO	1 M LiOH	464.5 at 0.5 A/g	[287]
$NiCo_2O_4$ ‖ MoO_2-C	1 M LiOH	571.5 at 0.5 A/g	[288]
Ni-P@$NiCo_2O_4$	0.7 M LiOH	1240 at 0.5 A/g	[289]
Li-doped CuO/RGO	1.2 M LiOH	399.8 at 0.5 A/g	[290]
α-Fe_2O_3@C	1 M LiOH	443.2 at 0.5 A/g	[291]
Cu_3SbS_4/Ni	1 M LiOH	835.243 at 0.5 A/g	[292]

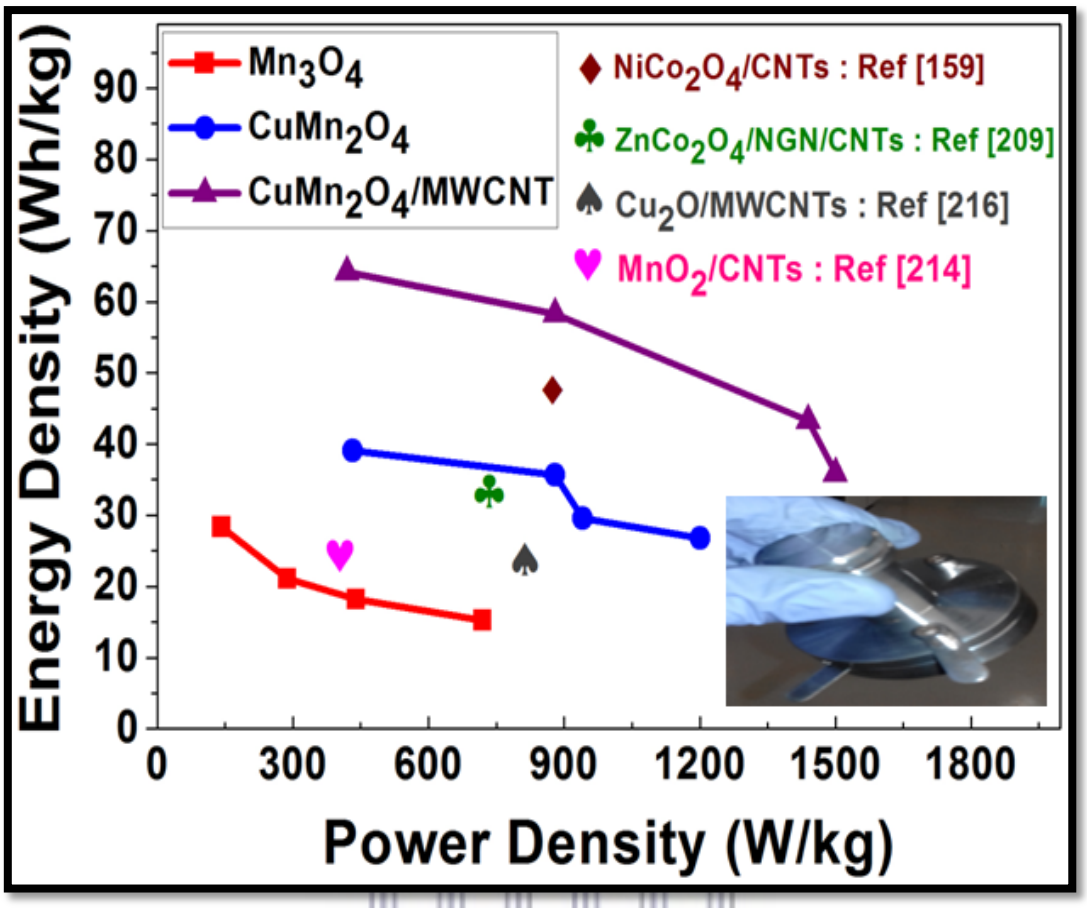

Figure 4.58: Ragone plot illustrating Energy versus Power Densities of all electrode materials after 3000 cycles.

The two-electrode full cell devices were additionally tested for specific capacitance, energy, and power density performance after employing 3000 cycles, of which the results are illustrated in **Fig. 4.57**. The data from the plot revealed specific capacitance values of 549.392 F/g, 1004.015 F/g, and 1210.037 F/g, exhibited by the pristine, spinel, and hybrid composite asymmetric cells. The electrochemical cells also exhibited impressive energy and power densities, as portrayed in the ragone plot **Fig. 4.58**, of which the hybrid $CuMn_2O_4$/MWCNT asymmetric pseudocapacitor cell device exhibited energy and power densities equivalent to 35.828 Wh/kg and 1497.830 W/kg, respectively. These performance results were unexpectedly high after having performed cycling analysis for 3000 cycles, which took approximately 3 days to reach completion, thus implied that additional cycling analysis could be conducted on this research work for future prospects [293].

CHAPTER 5

5.0 Conclusion and Recommendations

5.1 Conclusion

The objective of this research project was to investigate the physical and electrochemical properties of the pristine Mn_3O_4, spinel $CuMn_2O_4$, and hybrid $CuMn_2O_4$/MWCNT composite electrode materials. The pristine and spinel materials were synthesized via a temperature controlled high-pressure hydrothermal method, where as the hybrid composite material was produced using a reflux heating system. Electrochemical analysis was performed using both three-electrode (half cell) and two-electrode (full cell) devices, were the half cells were tested with 3 M KOH and 3 M LiOH aqueous electrolyte solutions, of which the best performance electrolyte was used for the full cell analysis.

As mentioned before, the purpose of integrating copper nanoparticles to the pristine Mn_3O_4 crystal structure was to induce a more stable crystal lattice with increased reactive sites for electrolyte ion diffusion. XRD analysis confirmed that the pristine Mn_3O_4 material had a hausmannite-type body-centered tetragonal (BCT) crystal system, with an I41/*amd* space-group. This confirmation was supported with HR-TEM analysis, which displayed images of rectangular box shaped nanoparticles, resembling that of a BCT crystal structure, for the pristine material. Structural analysis of the spinel $CuMn_2O_4$ material illustrated that it possessed a face-centered cubic (FCC) crystal structure, with an Fd3m space-group. This result was evidently supported with HR-TEM images displaying two-dimensional cubic shaped $CuMn_2O_4$ nanostructures. The three-dimensional model of the spinel $CuMn_2O_4$ unit cell, shown in XRD analysis, displayed the structure containing Cu^{2+} tetrahedral and Mn^{3+} octahedral interstitial sites, thus making the lattice structure much bigger and crystalline compared to that of the pristine Mn_3O_4 BCT structure. The average crystallite size for the individual pristine Mn_3O_4 and spinel $CuMn_2O_4$ electrode materials were calculated as 74.0362 nm and 77.9357 nm, respectively. The incorporation of multi-walled carbon nanotubes (MWCNTs) to the spinel $CuMn_2O_4$ nanostructures, apart from increasing its

conductivity, was to reduce its average crystalline size and particle distribution. The average crystalline size calculated for the hybrid $CuMn_2O_4$/MWCNT composite material was determined as 51.2610 nm, thus confirming the reduced crystalline size effect of the $CuMn_2O_4$ nanoparticles induced by the attachment of MWCNTs. The pair-distance distribution function (PDDF) for the hybrid $CuMn_2O_4$/MWCNT electrode material, displayed in SAXS analysis, illustrated average particle sizes ranging between 50-108 nm confirmed by microscopic (SEM and HR-TEM) and structural (XRD) analysis.

Extensive interpretation of FT-IR results for the pristine Mn_3O_4 and spinel $CuMn_2O_4$ electrode materials illustrated the presence of tetrahedral Cu^{2+} - O^{2-} and octahedral Mn^{3+} - O^{2-} vibration modes occurring at frequencies approximately 531 cm^{-1} and 688 cm^{-1}, respectively. The FT-IR spectrum of the MWCNTs alone compared to that of the hybrid $CuMn_2O_4$/MWCNT composite material, resembled vibration bands identified as O-H, C=C, and C-O functional groups occurring at vibration frequencies of 3440 cm^{-1}, 1630 cm^{-1}, and 1297 cm^{-1}, respectively. The C=C symmetric stretching band, illustrated on the hybrid $CuMn_2O_4$/MWCNT composite FT-IR spectrum, confirmed the intra-molecular attraction between the MWCNT networks and the spinel $CuMn_2O_4$ nanostructures. The FT-IR results of the electrode materials were correspondent with its Raman analysis data. Raman spectrographs of the individual pristine Mn_3O_4 and spinel $CuMn_2O_4$ electrode materials, illustrated Raman bands situated at 340 cm^{-1} and 488 cm^{-1}, representative of the Cu(II) (t_{2g}) and Mn – O (A_{1g}) stretching/vibration modes, respectively. The Raman spectrum of the hybrid $CuMn_2O_4$/MWCNT composite electrode material revealed two relatively distinctive Raman bands positioned at 1467 cm^{-1} and 1529 cm^{-1}, characteristic to the D (C-C) sp^3 and G (C=C) sp^2 hybridized carbon atoms from the MWCNT nanostructures. Thermo-gravimetric analysis (TGA) additionally confirmed the increase in thermal stability of the spinel $CuMn_2O_4$ electrode material through MWCNT fabrication. The TGA results revealed that the hybrid $CuMn_2O_4$/MWCNT composite electrode material retained 92.91 % of its total weight after being subjected to high temperatures up to 900 ℃. These results were corroborated with electrochemical stability performance data obtained from galvanostatic charge/discharge (GCD) cycling analysis conducted for 3000 cycles.

Electrochemical analysis of the three synthesized electrode materials, conducted in both 3 M KOH and 3 M LiOH aqueous electrolyte solutions, illustrated that the hybrid $CuMn_2O_4$/MWCNT composite material exhibited the best overall performance. The half cell (three-electrode) configuration was employed to test for the best performing electrolyte solution and results indicated that 3 M LiOH was the best suited for this analysis, as it generated a specific capacitance value of 1067.427 F/g for the hybrid $CuMn_2O_4$/MWCNT composite electrode material. This result was hypothesized, since it was aware that Li^+ has a smaller ionic radii (0.076 nm) compared to that of K^+ (0.138 nm), thus allowing Li^+ ions to intercalate/deintercalate within the hybrid $CuMn_2O_4$/MWCNT composite matrix during charging/discharging processes. This statement is scientifically correct as it is possible for the hybrid $CuMn_2O_4$/MWCNT composite electrode material to processes both faradaic/redox and intercalation pseudocapacitance mechanisms for storing energy in the form of charge. The potential window for the two-electrode (full cell) analysis was increased from 0.7 V, during three-electrode analysis, to 2 V, which in-turn generated enhanced specific capacitances, energy and power densities for the analyzed electrode materials.

Electrochemical impedance spectroscopy (EIS), conducted on all electrode materials configured in both two and three-electrode cells, illustrated the hybrid $CuMn_2O_4$/MWCNT composite material exhibiting the lowest charge transfer resistance (R_{ct}) of 0.156 Ω, compared to the pristine and spinel materials. This result was correspondent to the large diffusion coefficient value of 5.581 x 10^{-3} cm^2/s calculated for the hybrid $CuMn_2O_4$/MWCNT composite material. This result also provided the implication that the improved specific capacitance and internal resistance of the hybrid composite material was attributed to the conductive MWCNT networks, which provided additional diffusion channels for electrolyte ions and electrons to move. GCD cycling performance analysis on the hybrid $CuMn_2O_4$/MWCNT ‖ AC full cell device, impressively exhibited a capacitance retention and coulombic efficiency of 88.571 % and 92 %, respectively after 3000 cycles. The results also revealed that the cell device retained a relatively high energy density of 35.068 Wh/kg at a maximum power density of 2449.942 W/kg. The work presented in this research on supercapacitor electrode materials sets us one-step closer to developing a superior ultra-capacitor device, capable of retaining energy densities comparable to that of lithium ion batteries.

5.2 Recommendations

An additional technique recommended for further investigation of elemental composition, regarding the electrochemical oxidation states of the elemental constituents present within the electrode materials, is X-ray photoelectron spectroscopy (XPS). This analysis would additionally confirm the data obtained from EDS analysis in HR-TEM. Another recommended technique is the employment of solid-state nuclear magnetic resonance (SS-NMR) analysis to provide assistance in the confirmation of quadrupolar-interactions between the MWCNT networks and spinel $CuMn_2O_4$ nanostructures. In addition to asymmetric full cell device analysis of the active electrode materials, symmetric full cell analysis is also required in order to attain full knowledge and understanding of the materials electrochemical performance. Another recommended electrochemical testing method, which is in-line with symmetric and asymmetric Swagelok devices, is the coin cell assembly. This assembly is advantageous for practical analysis as the electrode substrates used, onto which the active material is coated, is small in surface area, thus requiring small amounts of synthesized material. This research work is also aimed at providing a stable research platform of exploring additional electrolytic species such as ionic liquids, organic and non-neutral aqueous electrolyte within improved supercapacitor development. In relation to the utilized synthetic procedure during electrode material manufacturing, it is recommended to use the more time and energy efficient microwave assisted method. One final future recommendation, after this research work proves to be successful, is to test the developed cell device against a light-emitting diode (LED).

REFERENCES

1. Ander González, E.G., Jon Andoni Barrena, Roman Mysyk, *Review on supercapacitors: Technologies and materials.* Renewable and Sustainable Energy Reviews, 2016. **58**: p. 1189-1206.

2. Subramanian Yuvaraj, R.K.S., and Yun Sung Lee, *An overview of AB_2O_4- and A_2BO_4-structured negative electrodes for advanced Li-ion batteries.* RSC Advances, 2016. **6**(26): p. 21448-21474.

3. G.Pratibha, I.S., K.V.Rao, Arun K.Shanker, B.M.K.Raju, Deepak K.Choudhary, K.Srinivas Rao, Ch.Srinivasarao, M.Maheswari, *Net global warming potential and greenhouse gas intensity of conventional and conservation agriculture system in rainfed semi arid tropics of India.* Atmospheric Environment, 2016. **145**: p. 239-250.

4. Hooven, T.A. and R.A. Polin, *Pneumonia.* Seminars in Fetal and Neonatal Medicine, 2017. **4**(22): p. 206-213.

5. Woldeyohannes, A.D., D.E. Woldemichael, and A.T. Baheta, *Sustainable renewable energy resources utilization in rural areas.* Renewable and Sustainable Energy Reviews, 2016. **66**: p. 1-9.

6. Aliyu, A.K., B. Modu, and C.W. Tan, *A review of renewable energy development in Africa: A focus in South Africa, Egypt and Nigeria.* Renewable and Sustainable Energy Reviews, 2018. **81**: p. 2502-2518.

7. Jain, S. and P.K. Jain, *The rise of Renewable Energy implementation in South Africa.* Energy Procedia, 2017. **143**: p. 721-726.

8. Pegels, A., *Renewable energy in South Africa: Potentials, barriers and options for support.* Energy Policy, 2010. **38**(9): p. 4945-4954.

9. Hadjipaschalis, I., A. Poullikkas, and V. Efthimiou, *Overview of current and future energy storage technologies for electric power applications.* Renewable and Sustainable Energy Reviews, 2009. **13**(6): p. 1513-1522.

10. Alotto, P., M. Guarnieri, and F. Moro, *Redox flow batteries for the storage of renewable energy: A review.* Renewable and Sustainable Energy Reviews, 2014. **29**: p. 325-335.

11. Viswanathan, B., *Chapter 13 - Supercapacitors*, in *Energy Sources*. 2017, Elsevier: Amsterdam. p. 315-328.

12. Mauro C dos Santos, L.S.P., Felipe De Moura Souza, José Camargo Junior, and Tuani Gentil, *Fuel Cells: Hydrogen and Ethanol Technologies.* Materials Science and Materials Engineering, 2017.

13. Xiong, P., J. Zhu, and X. Wang, *Recent advances on multi-component hybrid nanostructures for electrochemical capacitors.* Journal of Power Sources, 2015. **294**: p. 31-50.

14. Shen-Ming Chen, R.R., Veerappan Mani, Ramiah Saras Wathi, *Recent Advancements in Electrode Materials for the High performance Electrochemical Supercapacitors: A Review.* International Journal of Electrochemical Science, 2014. **9**: p. 4072-4085.

15. Long Zhang, L.D., Mengxiong Li, Peng Wang, Jiajia Zhang, Hongbin Lu, *Ultra-high-rate, ultra-long-life asymmetric supercapacitors based on few-crystalline, porous $NiCo_2O_4$ nanosheet composites.* Journal of Materials Chemistry A, 2018. **6**(4): p. 1412-1422.

16. Saravanakumar, B., S.M. Lakshmi, G. Ravi, V. Ganesha, A. Sakunthala, R. Yuvakkumar, *Electrochemical properties of rice-like copper manganese oxide ($CuMn_2O_4$) nanoparticles for pseudocapacitor applications.* Journal of Alloys and Compounds, 2017. **723**: p. 115-122.

17. Hu, Y., *Controllable structure transitions of Mn_3O_4 nanomaterials and their effects on electrochemical properties.* Nanoscale Horizons, 2017. **2**(6): p. 326-332.

18. Mirzaeian, M., *Electrode and electrolyte materials for electrochemical capacitors.* International Journal of Hydrogen Energy, 2017. **42**(40): p. 25565-25587.

19. Brien, D.O., *Power electronics, EC Capacitors Deliver High Capacitance in a Small Size, Single-cell EC capacitors can reach 50,000 + farads.* North American Capacitor Corp., Greencastle, Ind, 2001.

20. Ke, Q. and J. Wang, *Graphene-based materials for supercapacitor electrodes – A review*. Journal of Materiomics, 2016. **2**(1): p. 37-54.

21. Black, L., ed. *Physics for Scientists and Engineers with modern physics*. Second Edition ed., ed. S. Kusch. 1986, Raymond A, Serway: New York City. page 574.

22. Frost, P., *Physics: Why aren't wires capacitors?*, in *Electrical Engineering Stack Exchange*, C. Diagram, Editor. 2014.

23. Dufresne, S., *Capacitance of cylindrical capacitors*, in *rimstar.org*, C.f.a. calculators, Editor. 2011.

24. Bidgood, F.E., ed. *Physics*. First Edition ed. 1985, Susan Farnsworth Ohanian: New York City and London. Page 612.

25. Nave, C.R. *HyperPhysics*. 2016 [cited 2018 8 May 2018].

26. Dupont, M.F., *Effect of electrolyte cation on the charge storage mechanism of manganese dioxide for electrochemical capacitors.* Electrochimica Acta, 2018. **271**: p. 337-350.

27. Bailey, A.G., *The charging of insulator surfaces.* Journal of Electrostatics, 2001. **51-52**: p. 82-90.

28. Arfken, G.B., *chapter 29 - CAPACITANCE AND CAPACITORS*, in *International Edition University Physics*. 1984, Academic Press. p. 536-556.

29. Langton, N.H., *The parallel-plate capacitor with symmetrically placed unequal plates.* Journal of Electrostatics, 1981. **9**(4): p. 289-305.

30. Xiang, Y., *The electrostatic capacitance of an inclined plate capacitor.* Journal of Electrostatics, 2006. **64**(1): p. 29-34.

31. Xiang, Y., *Further study on electrostatic capacitance of an inclined plate capacitor.* Journal of Electrostatics, 2008. **66**(7): p. 366-368.

32. Joseph, N. *Parallel Plate Capacitor*. Electromagnetics 2013 [cited 2018 17 May 2018].

33. Smith, A., *Capacitance and Dielectrics*, in *Chapter 5* 2010, Massachusetts Institute of Technology: Cambridge, Massachusetts, United States.

34. Mobini, S., F. Meshkani, and M. Rezaei, *Surfactant-assisted hydrothermal synthesis of $CuCr_2O_4$ spinel catalyst and its application in CO oxidation process.* Journal of Environmental Chemical Engineering, 2017. **5**(5): p. 4906-4916.

35. Saunders, ed. *Physics for Scientists and Engineers with Modern Physics*. 3 rd Edition ed. 1990, Raymond A. Serway: New York. 1230.

36. Campbell, J., ed. *Calculus: Concepts and Contexts, Fourth Edition, Metric International Edition.* 4th edition ed. Metric International Edition, James Stewart, ed. J. Lawless. Vol. 978. 2010, Richard Stratton: Belmont USA. 1200.

37. Black, L., ed. *Physics for Scientists and Engineers with modern physics*. ed. S. Kusch. 1986, Raymond A, Serway: New York. 1102.

38. Shahbaaz, *Physics: Spherical Conducting Shells, Potential*, in *Electrical Engineering Stack Exchange*, S.C. Diagram, Editor. 2016.

39. Pengxi Li, C.R., Jing Xu, and Yibing Xie. , *A high-performance asymmetric supercapacitor electrode based on a three-dimensional $ZnMoO_4$/CoO nanohybrid on nickel foam.* Nanoscale, 2019.

40. Aoki., K.J., *Frequency-dependence of electric double layer capacitance without Faradaic reactions.* Journal of Electroanalytical Chemistry, 2016. **779**(15): p. 117-125.

41. D.A. Harrington, P.v.d.D., *Equivalent circuits for some surface electrochemical mechanisms.* Journal of Electroanalytical Chemistry, 2004. **567**(2): p. 153-166.

42. Mohammed Kechadi, L.C., Bernard Tribollet, Jean Gamby. , *Dielectric impedance spectroscopy of polymer-coated microelectrodes for adsorption monitoring of proteins within polymer microchannels.* Journal of Electroanalytical Chemistry, 2015. **737**(15): p. 108-113.

43. Casao, R. *Capacitance*. Physics 2016 [cited 2018 2018/08/24]; Commercial electrostatic capacitor designs].

44. Roueche, C. *Itseo.Info*. Electrical Diagrams and Ideas 2017 [cited 2018 2018/08/20]; The power of applied intelligence].

45. Po-Hsin Wang, T.-L.W., Wen-Churng Lin, Hung-Yin Lin, Mei-Hwa Lee, Chien-Hsin Yang., *Enhanced supercapacitor performance using molecular self-assembling polyaniline onto carbon nanoparticles.* Journal of Electroanalytical Chemistry, 2018. **810**(1): p. 145-153.

46. Madhav Singh, J.K., Horst Hahn., *A systematic study of thick electrodes for high energy lithium ion batteries.* Journal of Electroanalytical Chemistry, 2016. **782**(1): p. 245-249.

47. Swagatika Rout, A.K.N., Jhansi L. Varanasi, Debabrata Pradhan, Debabrata Das., *Enhanced energy recovery by manganese oxide/reduced graphene oxide*

nanocomposite as an air-cathode electrode in the single-chambered microbial fuel cell. Journal of Electroanalytical Chemistry, 2018. **815**(15): p. 1-7.

48. Litong Zhang, Y.Z., Weidong Zhao, Lu Zhang, Xiangrong Ye, Jiu-Ju Feng., *Facile one-step synthesis of three-dimensional freestanding hierarchical porous carbon for high energy density supercapacitors in organic electrolyte.* Journal of Electroanalytical Chemistry, 2018. **818**(1): p. 51-57.

49. Szymon Sollami Delekta, K.H.A., Nejla Benyahia Erdal, Minna Hakkarainen, Mikael Ostling, and Jiantong Li. , *Fully inkjet printed ultrathin microsupercapacitors based on graphene electrodes and a nano-graphene oxide electrolyte.* Nanoscale, 2019. **21**(11): p. 10172-10177.

50. Meng Zhang, S.Y., Yiyong Mai, Shaodong Zhang, and Yongfeng Zhou., *A single-ion conducting hyperbranched polymer as a high performance solid-state electrolyte for lithium ion batteries.* Chemical Communications, 2019. **47**(55): p. 6715-6718.

51. Yongging Wang, H.Z., and Hongbing Ji., *A promising Mo-based lithium-rich phase for li-ion batteries.* RSC Advances, 2019. **31**(9): p. 17852-17855.

52. Shao., Z.W.a.G., *High-capacity cathodes for magnesium lithium chlorine tri-ion batteries through chloride intercalaction in layered MoS_2: a computational study.* Journal of Materials Chemistry A, 2018. **16**(6): p. 6830-6839.

53. Sergej Repp, E.H., Seda Gurgen, Mike Castellano, Nora Kremer, Nils Pompe, Jakob Worner, Anke Hoffmann, Ralf Thomann, Fatih M. Emen, Stefan Weber, Kasim Ocakoglu, and Emre Erdem., *Synergetic effects of Fe^{3+} doped spinel $Li_4Ti_5O_{12}$ nanoparticles on reduced graphene oxide for high surface electrode hybrid supercapacitors.* Nanoscale, 2018. **4**(10): p. 1877-1884.

54. Qing Xu, P.X., Yuyan Xu, Deli Jiang, and Min Chen, *Hierarchical urchin-like Co_9S_8@$Ni(OH)_2$ heterostructures with superior electrochemical performance for hybrid supercapacitors.* New Journal of Chemistry, 2019. **22**(43): p. 8444-8451.

55. Perkin., C.S.P.-M.a.S., *Surface forces generated by the action of electric fields across liquid films.* Soft Matter, 2019. **21**(15): p. 4255-4265.

56. Tarugu Anitha, A.E.R., Ikkurthi Kanaka Durga, S. Srinivasa Rao, Hyeon Wook Nam, Hee-Je Kim., *Facile synthesis of $ZnWO_4@WS_2$ cauliflower-like structures for supercapacitors with enhanced electrochemical performance.* Journal of Electroanalytical Chemistry, 2019. **841**(15): p. 86-93.

57. Jinwen Lin, J.H., *A mean-field model for the double layer of stepped platinum single-crystal electrodes.* Journal of Electroanalytical Chemistry, 2019. **846**(1): p. 113-136.

58. Pilon., H.W.a.L., *Accurate Simulations of Electric Double Layer Capacitance of Ultramicroelectrodes.* Physical Chemistry C, 2011. **115**(13): p. 16711-16719.

59. Pech, D.B., M; Durou, H; Huang, P; Mochalin, V; Gogotsi, Y; Taberna, P.L; Simon, P., *Ultrahigh-power micrometre-sied supercapacitors based on onion-like carbon.* Nature Nanotechnology, 2010. **5**: p. 651-654.

60. Yue Zhao, M.D., Depeng Zhao, Li Xiao, Xiang Wu, and Fei Liu. , *Asymmetric pseudo-capacitors based on dendrite-like MnO_2 nanostructures.* CrystEngComm, 2019. **21**: p. 3349-3355.

61. K. Tonurist, T.T., A. Janes, T. Romann, V. Sammelselg, E. Lust., *Influence of separator properties on electrochemical performance of electrical double-layer capacitors.* Journal of Electroanalytical Chemistry, 2013. **689**(15): p. 8-20.

62. Makgopa, K., *Effects of carbon nanomaterials on the performance of symmetric pseudocapacitors.*, in *Chemistry Department*. 2016, University of Pretoria: Pretoria. p. 270.

63. Xuli Chen, R.P., and Liming Dai, *Carbon-based supercapacitors for efficient energy storage.* Journal of Materials Science: National Science Review., 2017. **4**: p. 453-489.

64. Yuanlong Shao, M.F.E.-K., Jingyu Sun, Yaogang Li, Qinghong hang, Meifang Zhu, Hongzhi Wang, Bruce Dunn, and Richard B. Kaner. , *Design and Mechanisms of Asymmetric Supercapacitors.* Chemical Reviews, 2018. **118**(18): p. 9233-9280.

65. Veronica Augustyn, P.S., and Bruce Dunn., *Pseudocapacitive oxide materials for high-rate electrochemical energy storage.* Energy & Environmental Science, 2014. **7**(5): p. 1597-1614.

66. Henri-Louis Girard, H.W., Anna L.d' Entremont, Laurent Pilon. , *Enhancing Faradaic Charge Storage Contribution in Hybrid Pseudocapacitors.* Electrochimica Acta, 2015. **182**(10): p. 639-651.

67. Gogotsi, Y.P., R. M., *Energy Storage in Nanomaterials-Capacitive, Pseudocapacitive, or Battery-like?* ACS Nano, 2018. **12**: p. 2081-2083.

68. Balducci, A.B., D.; Brousse, T.; Long, J.W.; Sugimoto, W., *Perspective-A Guidline for Reporting Performance Metrics with Electrochemical Capacitors: From Electrode Materials to Full Devices.* Journal of Electrochemical Society, 2017. **164**: p. A1487-1488.

69. Bidhan Pandit, N.K., Pankaj M. Koinkar, Babasaheb R. Sankapal. , *Solution processed nanostructured cerium oxide electrode: Electrochemical engineering towards solid-state symmetric supercapacitor device.* Journal of Electroanalytical Chemistry, 2019. **839**(15): p. 96-107.

70. Ying-Chu Chen, J.-H.H., Yan-Gu Lin, Yu-Kuei Hsu., *Synthesis of Fe_2O_3 nanorods/silver nanowires on coffee filter as low-cost and efficient electrodes for supercapacitors.* Journal of Electroanalytical Chemistry, 2017. **801**(15): p. 65-71.

71. Lukatskaya, M.R., B. Dunn, and Y. Gogotsi, *Multidimensional materials and device architectures for future hybrid energy storage.* Nature Communications, 2016. **7**: p. 12647.

72. Binbin Liu, J.H., Tingting Zhang, Caixia Xu, and Hong Liu. , *A three-dimensional multilevel nanoporous $NiCoO_2$/Ni hybrid for highly reversible electrochemical energy storage.* Journal of Materials Chemistry A, Advance Article, 2019. **28**.

73. Yuanyi Zhu, S.A., Jinlong Cui, Hengrui Qiu, Xuejiao Sun, Yonggiang Zhang, and Wenxiu He. , *Improving the specific capacity of nickel hydroxide nanocrystals via yttrium doping for application in hybrid supercapacitors.* CrystEngComm, Advance Article, 2019. **26**.

74. Xin Guo, R.G., Nan Qin, Liming Jin, Junsheng Zheng, Qiang Wu, Jim P. Zheng. , *The influence of electrode matching on capacity decaying of hybrid lithium ion capacitor.* Journal of Electroanalytical Chemistry, 2019. **845**(15): p. 84-91.

75. Hlongwa, N.W., *Thermochemical Storage and Lithium Ion Capacitors Efficiency of Manganese-Graphene Framework*, in *Chemistry Department*. 2018, University of the Western Cape: Cape Town. p. 192.

76. Jin Zhang, J.W., Zhiqiang Shi, Zhiwei Xu. , *Electrochemical behaviour of lithium ion capacitor under low temperature.* Journal of Electroanalytical Chemistry, 2018. **817**(15): p. 195-201.

77. Mojtaba Mirzaeian, Q.A., Abraham Ogwu, Peter Hall, Mark Goldin, Marjan Miraeian, Hassan Fathinejad Jirandehi., *Electrode and electrolyte materials for electrochemical capacitors.* International Journal of Hydrogen Energy., 2017. **42**(22): p. 25565-25587.

78. Shasha Wang, Y.u., Meifang Yan, Zuozhao Zhai, Bin Ren, Lihui Zhang, Zhenfa Liu., *Comparative study of metal-doped carbon aerogel: Physical properties and electrochemical performance.* Journal of Electroanalytical Chemistry, 2018. **809**(15): p. 111-116.

79. Yang, H., *Graphene-based Supercapacitors for Energy Storage.*, in *Graduate Program in Electrical and Computer Science.* 2013, Ohio State University. p. 88.

80. Byong Chol Bai, E.A.K., Chul Wee Lee, Young-Seak Lee, Ji Sun Im. , *Effects of surface chemical properties of activated carbon fibers modified by liquid oxidation for CO_2 adsorption.* Applied Surface Science, 2015. **353**(30): p. 158-164.

81. Renyuan Li, L.Z., and Peng Wang., *Rational design of nanomaterials for water treatment.* Nanoscale, 2015. **21**(7): p. 17167-17194.

82. Sun., C.L.a.K., *The preparation of 3D network pore structure activated carbon as an electrode material for supercapacitors with long-term cycle stability.* RSC Advances, 2016. **62**(6): p. 57075-57083.

83. R.W. Pekala, J.C.F., C.T. Alviso, T.D. Tran, S.T. Mayer, J.M. Miller, B. Dunn. , *Carbon aerogels for electrochemical applications.* Journal of Non-Crystalline Solids. , 1998. **225**: p. 74-80.

84. H. Pröbstle, M.W., and J. Fricke. , *Carbon Aerogels for Electrochemical Double Layer Capacitors.* Journal of Porous Materials, 2003. **10**(4): p. 213-222.

85. John Chmiola, C.L., Pierre-Louis Taberna, Patrice Simon, and Yury Gogotsi. , *Monolithic Carbide-Derived Carbon Films for Micro-Supercapacitors.* Science, 2010. **328**(23): p. 480-483.

86. Carlos R. Pérez, S.-H.R., Julie Ségalini, Volker Presser-Louis Taberna, Patrice Simon, Yury Gogotsi. , *Structure and Electrochemical Performance of Carbide-Derived Carbon Nanopowders.* Advanced Functional Materials, 2012. **23**(8): p. 1081-1089.

87. Lars Borchardt, F.H., Martin R. Lohe, Martin Oschatz, Fran Schmidt, Emanuel Kockrick, Christopher iegler, Tristan Lescouet, Alicja Bachmatiuk, Bernd Büchner, David Farrusseng, Peter Strasser, Stefan Kaskel. , *Transition metal loaded silicon carbide-derived carbons with enhanced catalytic properties.* Carbon, 2012. **50**(5): p. 1861-1870.

88. Salunkhe RR, L.Y., Chang KH, Li JM, Simon P, Tang J. , *Nanoarchitectured graphene-based supercapacitors for next-generation energy-storage applications.* Chem A Eur J, 2014. **43**(20): p. 13838-13852.

89. Hu. J, K.Z., Li. F, Huang. X., *Graphene with three-dimensional architecture for high performance supercapacitor.* Carbon, 2014. **67**: p. 221-229.

90. A. Iadi-Najafabadi, S.Y., K. Kobashi, T. Yamada, D.N. Futaba, H. Hatori, M. Yumura, S. Iijima, and K. Hata. , *Extracting the full potential of single-walled carbon nanotubes as durable supercapacitor electrodes operable at 4V with high power and energy density.* Advanced Functional Materials, 2010. **22**(35): p. 235-241.

91. Ji Chen, Y.Z., Miao Zhang, Bowen Yao, Yingru Li, Liang Huang, Chun Li, and Gaoquan Shi. , *Water-enhanced oxidation of graphite to graphene oxide with controlled species of oxygenated groups*. Chemical Science, 2016. **7**(3): p. 1874-1881.

92. Afsaneh Dorri Moghadam, E.O., Pradeep L. Menezes, Pradeep K. Rohatgi. , *Mechanical and tribological properties of self-lubricating metal matrix nanocomposites reinforced by carbon nanotubes (CNTs) and graphene-A review.* Composites Part B: Engineering, 2015. **77**(3): p. 402-420.

93. Dr. Changzhou Yuan, H.B.W., Prof. Yi Xie, Prof. Xiong Wen (David) Lou. , *Mied Transition-Metal Oxides: Design, Synthesis, and Energy-Related Applications.* German Chemical Society: Angewandte Chemie, 2014. **53**(6): p. 1488-1504.

94. Bo-Hye Kim, C.H.K., Do Geum Lee. , *Mesopore-enriched activated carbon nanofiber web containing RuO_2 as electrode material for high-performance supercapacitors.* Electroanalytical Chemistry, 2016. **760**(1): p. 64-70.

95. Rahul R. Salunkhe, Y.V.K., and Yusuke Yamauchi. , *Metal-Organic Framework-Derived Nanoporous Metal Oxides toward Supercapacitor Applications: Progress and Prospects.* ACS Nano, 2017. **11**(6): p. 5293-5308.

96. Jiayi Yang, Y.Y., Jinle Lan, Yunhua Yu, Xiaoping Yang., *Polyaniline-manganese dioxide-carbon nanofiber ternary composites with enhanced electrochemical performance for supercapacitors.* Journal of Electroanalytical Chemistry, 2019. **843**(15): p. 22-30.

97. Haijun Peng, H.F., Li Ning, Weijia Wang, Jianan Sui., *Templated manganese oxide by pyrolysis route as a promising candidate cathode for asymmetric supercapacitors.* Journal of Electroanalytical Chemistry, 2019. **843**(15): p. 54-60.

98. E. Kowsari, A.E., S. Assadi, R. Safari. , *Influence of different N-benoyl derivatives of isoleucine on electrochemical properties and pseudocapacitance performance of conductive polymer electroactive film: Electrochemical and theoretical study.* Journal of Electroanalytical Chemistry, 2018. **826**(1): p. 65-75.

99. lewis M. Cowen, J.A., Matthew J. Carnie, Derya Baran, and Bob C. Schroeder. , *Review-Organic Materials for Thermoelectric Energy Generation.* ECS Journal of Solid State Science and Technology. , 2017. **6**(3): p. N3080-N3088.

100. Sarkar., S., *Electronic Structure of Complex Crystalline Solids.* , in *Depapartment of Physics*. 2012, University of Calcutta: Kolkata, India. p. 129.

101. Xia., Y.W.a.Y., *Recent Progress in Supercapacitors: From Materials Design to System Construction.* Advanced Materials, 2013. **25**(37): p. 5336-5342.

102. Qi Lu, M.W.L., Yunpeng Chen, Dr. Xiaoming Kou, Dr. Wanfeng Li, Dr. Xin Fan, Prof. Dr. Karl M. Unruh, Prof. Dr. Jingguang G. Chen, Prof. Dr. John Q. Xiao. , *Supercapacitor Electrodes with High-Energy and Power Densities Prepared from Monolithic NiO/Ni Nanocomposites.* Journal of the German Chemical Society: Angewandte Chemie. , 2011. **50**(30): p. 6847-6850.

103. Van Chinh Tran, S.S., Jinho Hwang, Van Quang Nguyen, Jae-Jin Shim. , *Poly(aniline-co-pyrrole)-spaced graphene aerogel for advanced supercapacitor electrodes.* Journal of Electroanalytical Chemistry, 2018. **810**(1): p. 154-160.

104. Maria R. Lukatskaya, B.D., and Yury Gogotsi., *Multidimensional materials and device architectures for future hybrid energy storage.* Nature Communications, 2016. **12647**(7): p. 13.

105. Abolhassan Noori, M.F.E.-K., Mohammad S. Rahmanifar, Richard B. Kaner, and Mir F. Mousavi, *Towards establishing standard performance metrics for batteries, supercapacitors and beyond.* Journal of Chemical Society Reviews, 2019. **48**(5): p. 1272-1341.

106. Ahmed, K.A.M. and K. Huang, *Formation of Mn_3O_4 nanobelts through the solvothermal process and their photocatalytic property.* Arabian Journal of Chemistry, 2014.

107. Ramsay, S. *Energy-efficient fabrication of a novel multivalence Mn_3O_4-MnO_2 heterojunction for dye degradation under visible light irradiation-Scientific Figure on ResearchGate*. Schematic illustration of the fabrication process of Mn_3O_4-MnO_2 2016 [cited 2018 3 September]; Image for Mn_3O_4 synthetic schematic].

108. Wang, X., *Structure–Activity Relationships of AMn_2O_4 (A = Cu and Co) Spinels in Selective Catalytic Reduction of NOx: Experimental and Theoretical Study.* The Journal of Physical Chemistry C, 2017. **121**(6): p. 3339-3349.

109. Rasha Yousef, A.A.-Z., Nasser Sad-Din, *A Study of Structural Properties of $CuMn_2O_4$ Synthesized by Solid State Method.* Advances in Physics Theories and Applications, 2018. **71**: p. 7.

110. Hamidreza Sadeqh, K.Z., Behnam Maazinejad, Ramin Shahryari-ghoshekandi, Inderjeet Tyagi, Shalpi Agarwal, Vinod Kumar, *Synthesis of MWCNT-COOH-Cysteamine composite and its application for dye removal.* Journal of Molecular Liquids, 2016. **215**: p. 221-228.

111. Vasilios Goergakilas, V.T., Dimitrios Gournis, and Dimitrios Petridis, *Attachment of Magnetic Nanoparticles on Carbon Nanotubes and their soluble derivatives.* Chemistry of Materials, 2005. **17**: p. 5.

112. Yujing Yang, Q.M., Lei Han, and Kai Tao. , *Zeolitic imidazolate framework-derived Co_3S_4@$Co(OH)_2$ nanoarrays as self-supported electrodes for asymmetric supercapacitors.* Inorganic Chemistry Frontiers., 2019(6): p. 1398-1404.

113. R.Juškėnas, V.K., V.Pakštas, A.Selskis, V.Kapočius, *Electrochemical and XRD studies of Cu-Zn coatings electrodeposited in solution with D-mannitol.* Journal of Electroanalytical Chemistry, 2007. **602**(2): p. 237-244.

114. Hlongwa, N.W., *Nanoparticles-Infused Lithium Manganese Phosphate Coated With Magnesium-Gold Composite Thin film - A possible Novel Material for Lithium Ion Battery Olivine Cathode*, in *Chemistry Department*. 2014, University of the Western Cape Cape Town. p. 104.

115. Goldstein, J., *Scanning electron microscopy and X-ray microanalysis: a text for biologists, material scientists, and geologists*. Springer Science and Business Media, 2012. **7**(12).

116. Ndipingwi, M.M., *Designing next generation high energy density lithium-ion battery with manganese orthosilicate-capped alumina nanofilm*, in *Chemistry*. 2015, University of the Western Cape: Cape Town. p. 102.

117. Nzaba, S.K.M., *Lithium Manganese Oxide Modified with Copper-Gold Nanocomposite Cladding - a Potential Novel Cathode Material for Spinel Type Lithium-ion Bateries*, in *Chemistry Department*. 2014, University of the Western Cape: Cape Town. p. 119.

118. Terry Yuan-Fang Chen, T.-C.C., Fa-Yen Cheng, Ang-Ting Tsai, Ming-Tzer Lin, *Digital image correlation of SEM images for surface deformation of CMOS IC.* Microelectronic Engineering, 2018. **201**: p. 16-21.

119. Bao Liu, C.Y.W., Yongqiang Chen, Baozhong Ma., *Electrochemical behaviour and corrosion mechanism of Ti/IrO_2-RuO_2 anodes in sulphuric acid solution.* Journal of Electroanalytical Chemistry, 2019. **15**(837): p. 175-183.

120. Xin Wang, Q.K., Yiping Han, Yawen Tang, Xiaojun Wang, Xiaohua Huang, Tianhong Lu., *Construction of Ir-Co/C nanocomposites and their application in ammonia oxidation reaction.* Journal of Electroanalytical Chemistry, 2019. **838**(1): p. 101-106.

121. Congli Qin, A.F., Xin Zhang, Xiaoping Dai, Hui Sun, Danhua Ren, Zhun Dong, Yao Wang, Chenglong Luan, Jin-Yu Ye, and Shi-Gang Sun., *The in situ etching assisted synthesis of Pt-Fe-Mn ternary alloys with high-index facets as efficient catalysts for electroxidation reactions.* Nanoscale, 2019. **19**: p. 1-34.

122. Xing Liao, M.P., Kui Liang, *Enhanced electrochemical performance of SiO anode material via nitrogen-doped carbon coating in a facile and green route.* Journal of Electroanalytical Chemistry, 2019. **841**(15): p. 79-85.

123. Gh. Barati Darband, M.A., A. Sabour Rouhaghgam., *Three-dimensional porous Ni-CNT composite nanocones as high performance electrocatalysts for hydrogen evolution reaction.* Journal of Electroanalytical Chemistry, 2018. **829**(15): p. 194-207.

124. Muhammad Rashid, A.H., Muhammad Shoaib, Muhammad Abdul Basit, Hammad Khan, Yong Shin Kim., *An amperometric hydrogen sensor based on Pt nanoparticles supported multi-wall carbon nanotubes.* Journal of Electroanalytical Chemistry, 2019. **833**(15): p. 173-180.

125. Sekar Shankar, N.S.K.G., S. Abraham John., *Synthesis of albumin capped gold nanoparticles and their direct attachment on glassy carbon electrode for the determination of nitrite ion.* Journal of Electroanalytical Chemistry, 2018. **828**(1): p. 33-40.

126. Camila S. Inagaki, M.M.O., Marcio F. Bergamini, Luiz H. Marcolino-Junior, Aldo J.G. Zarbin., *Facile synthesis and dopamine sensing application of three component nanocomposite thin flims based on polythiophene, gold nanoparticles and carbon nanotubes.* Journal of Electroanalytical Chemistry, 2019. **840**(1): p. 208-217.

127. Ting-ting Lv, Z.-g.Z., Yan-wei Li, Sheng-yu Li, Yan-jiao Zhang., *Hydrothermal synthesis of high specific capacity Al/Na co-doped V_6O_{13} cathode material for lithium-ion battery.* Journal of Electroanalytical Chemistry, 2018. **829**(15): p. 42-50.

128. Assumpta C Nwanya, C.A., Daniel Obi, Kumar Raju, Kenneth I. Ozoemena Rose U. Osuji, Andreas Ruediger, Malik Maaza, Federico Rosei, Fabian I. Ezema., *Nanoporous copper-cobalt mixed oxide nanorod bundles as high performance pseudocapacitive electrodes.* Journal of Electroanalytical Chemistry, 2017. **787**(15): p. 24-35.

129. Lichao Tan, D.G., Jingyan Liu, Xiumei Song, Qi Liu, Rongrong Chen, Jun Wang., *In-situ calcination of polyoxometallate-based metal organic framework/reduced graphene oxide composites towards supercapacitor electrode with enhanced performance.* Journal of Electroanalytical Chemistry, 2019. **836**(1): p. 112-117.

130. Jianjun Tang, Y.S., Xueli Miao, Hao Qin, Dan dan Song, Yanting Li, Yuning Qu, Zhen Yin, Jiahao Ren, Lili Wang, Bing Wang., *Template-directed growth of hierarchically structured MOF-derived LDH cage hybrid arrays for supercapacitor electrode.* Journal of Electroanalytical Chemistry, 2019. **840**(1): p. 174-181.

131. Ruey-Chi Wang, P.-H.H., Ping-Chang Chuang, Yu-Cheng Lin., *Enhanced rate capability of pseudocapacitive CuO by incorporation of Li for excellent composite electrode.* Journal of Electroanalytical Chemistry, 2019. **839**(15): p. 160-165.

132. X. Zhou, Y.Y.Z., S.R. Kim, M. Elimelech, S. Hu, J.H. Kim., *Controlled TiO_2 Growth on Reverse Osmosis and Nanofiltration Membranes by Atomic Layer Deposition: Mechanisms and Potential Applications.* Journal of Environmental Science & Technology, 2018. **52**: p. 14311-14320.

133. Juan Corchado-García, C.M., Nicolás Alonso-Vante, Carlos R.Cabrera., *Probing ethanol oxidation mechanism with in-situ FT-IR spectroscopy via photodeposited Pt nanoparticles onto titania.* Journal of Electroanalytical Chemistry, 2017. **799**(15): p. 228-234.

134. Keiser, G., *Spectroscopic Methodologies*, in *Biophotonics: Concepts to Applications*. 2016, Springer Singapore: Singapore. p. 259-290.

135. Renata, J., *Micro and nanocapsules as supports for Surface-Enhanced Raman Spectroscopy (SERS).* Physical Sciences Reviews, 2016. **1**(1): p. 1-16.

136. P. Nagaraju, A.A., A. Alswieleh, R. Jayavel. , *Facile in-situ microwave irradiation synthesis of TiO_2/graphene nanocomposite for high-performance supercapacitor applications.* Journal of Electroanalytical Chemistry, 2018. **808**(1): p. 90-100.

137. Yamamoto, K., *Grazing-Incidence Small Angle X-Ray Scattering in Polymer Thin Films Utilizing Low-Energy X-rays.* 2017, IntechOpen.

138. Sabrina Schindler, T.B., *Mechanistic insights into the electrochemical oxidation of dopamine by cyclic voltammetry*. Journal of Electroanalytical Chemistry, 2019. **836**(1): p. 94-101.

139. Das, D.S.d., *Cyclic Voltammetry*, in *Urrjaa*. 2013.

140. Yuki Uchida, E.K., Richard G. Compton., *Cyclic voltammetry with non-triangular waveforms: Electrochemically irreversible and quasi-reversible systems.* Journal of Electroanalytical Chemistry, 2018. **810**(1): p. 135-144.

141. Debasish Mandal, P.R., Ashok K. Mahato, and K. Nandi. , *Electrochemically modified graphite paper as an advanced electrode substrate for supercapacitor application.* Journal of Materials Chemistry A Advanced Article. , 2019.

142. Karuppasamy Dharmaraj, Z.N., Heike Kahlert, Fritz Scholz., *The electrochemistry of DPPH in three-phase electrode systems for ion transfer and ion association studies.* Journal of Electroanalytical Chemistry, 2018. **823**(15): p. 765-772.

143. Debarshi Saha, D.S., Rahul Pal., *Effect of carbon on galvanically deposited cuprous oxide as flexible charge storage electrode.* Journal of Electroanalytical Chemistry, 2016. **776**(1): p. 34-39.

144. Du, W., *Advanced metal-organic frameworks (MOFs) and their derived electrode materials for supercapacitors.* Journal of Power Sources, 2018. **402**: p. 281-295.

145. Jiang, G., *$CuMn_2O_4$/graphene nanosheets as excellent anode material for Litium-ion battery.* ScienceDirect Materials Research Bulletin, 2018. **104**: p. 53-59.

146. Zhongxing Wang, J.Z., Ping Sun, Pengyu Zhang, *Nanostructured Mn-Cu binary oxides for supercapacitors.* Journal of Alloys and Compounds, 2014. **598**(ScienceDirect): p. 166-170.

147. Xia, L., *Fe_3O_4 nanoparticles embedded in cellulose nanofibre/graphite carbon hybrid aerogels as advanced negative electrodes for flexible asymmetric supercapacitors.* Journal of Materials Chemistry A, 2018. **36**(6): p. 17378-17388.

148. Mondal, C., *Mn_3O_4 nanoparticles anchored to multiwall carbon nanotubes: a distinctive synergism for high-performance supercapacitors.* New Journal of Chemistry, 2015. **39**(11): p. 8373-8380.

149. Tuantuan Zhou, W.G., Yanshan Gao, Qiang Wang, Ahmad Umar, *Co_3O_4 nanoparticles/MWCNTs composites: a potential scafforld for hydrazine and glucose electrochemical detection.* Royal Society of Chemistry, 2017. **7**(50087): p. 10.

150. Ikpo, D.C., *Development of high performance composite lithium ion battery cathode systems with carbon nanotubes functionalised with bimetallic inorganic nanocrystal alloys*, in *Chemistry*. 2011, University of the Western Cape Cape Town. p. 156.

151. McGraw-Hill, *Handbook of Batteries*, a.T.B.R. Linden D, Editor. 2002.

152. Taotao Li, C.G., Bo Sun, Ting Li, Yonggang Li, Lifeng Hou, Yinghui Wei, *Well-shaped Mn_3O_4 tetragonal bipyramids with good performance for lithium ion batteries.* Journal of Materials Chemistry A, 2015. **14**(3): p. 7248-7254.

153. Xingfu Tang, J.L., Jiming Hao, *Synthesis and characterization of spinel Co_3O_4 octahedra enclosed by the {111} facets.* ScienceDirect: Materials Research Bulletin, 2007. **43**: p. 2912-2918.

154. Massimo Nespolo, T.K., Hiroshi Takeda, and Giovanni Ferraris, *Periodic intensity distribution (PID) of mica polytypes: Symbolism, structural model orientation and axial settings.* Act crystallographica. Section A, Foundations of crystallography, 1999. **55**: p. 659-676.

155. Mauricio A. P. Papi, M.F.B., Luiz H. Marolino-Junior., *Electrochemical behaviour of a cation-exchange resin modified with copper ions on non-enzymatic glucose determination.* Journal of Electroanalytical Chemistry, 2019. **835**(15): p. 248-253.

156. Shahram Ghasemi, S.R.H., Monire Moalem-Banhangi, *Preparation of electrochemically reduced graphene oxide/bimetallic copper-platinum nanohybrid as counter electrode for fabrication of dye-sensitized solar cell.* Journal of Electroanalytical Chemistry, 2019. **833**(15): p. 242-250.

157. Dalia M. El-Gendy, N.A.A.G., Nageh K. Allam, *Green, single-pot synthesis of functionalized Na/N/P co-doped graphene nanosheets for high-performance supercapacitors.* Journal of Electroanalytical Chemistry, 2019. **837**(15): p. 30-38.

158. Raji Atchudan, T.N.J.I.E., Suguna Perumal, Asrafali Shakila Parveen, Yong Rok Lee., *Electrocatalytical and energy storage performance of bio-derived sulphur-nitrogen-doped carbon.* Journal of Electroanalytical Chemistry, 2019. **833**(15): p. 357-369.

159. Zhong Jie Zhang, X.Y.C., *Nitrogen-doped nanoporous carbon materials derived from folic acid: Simply introducing redox additive of p-phenylenediamine into KOH electrolyte for greatly improving the supercapacitor.* Journal of Electroanalytical Chemistry, 2016. **764**(1): p. 45-55.

160. M. Mondal, B.D., P. Howli, N.S. Das, K.K. Chattopadhyay, *Porosity-tuned NiO nanoflaks: Effect of calcination temperature for high performing supercapacitor application.* Journal of Electroanalytical Chemistry, 2018. **813**(15): p. 116-126.

161. Jiao Chen, J.Q., Bin Wang, Huixia Feng, Yanling Yu, Eiichi Sakai, *Polyaniline/sugarcane bagasse derived biocarbon composites with superior performance in supercapacitors.* Journal of Electroanalytical Chemistry, 2017. **801**(15): p. 360-367.

162. Fang, D., *Effect of $CuMn_2O_4$ spinel in Cu–Mn oxide catalysts on selective catalytic reduction of NOx with NH_3 at low temperature.* RSC Advances, 2014. **4**(49): p. 25540-25551.

163. Li, T., *Well-shaped Mn_3O_4 tetragonal bipyramids with good performance for lithium ion batteries.* Journal of Materials Chemistry A, 2015. **14**(3): p. 7248-7254.

164. Dunlap, R.A., *The Symmetry and Packing Fraction of The Body Centered Tetragonal Structure.* European Journal of Physics Education, 2012. (3): p. 6.

165. Prashanth W. Menezes, A.I., Patrick Littlewood, Michael Schwarze, Caren Gobel, Reinhard Schomacker, and Matthias Driess, *Nanostructured Manganese Oxides as Highly Active Water Oxidation Catalysts: A Boost from Manganese Precursor Chemistry*. Chemistry & Sustainability (CHEMSUSCHEM), 2014: p. 10.

166. Fitri Afriani, C., Bambang Hermanto, and Toto Sudiro, *Synthesis of $CuMn_2O_4$ spinel and its magnetic properties characterization.* AIP Conference Proceedings, 2017: p. 7.

167. Sher, D.F., *Crystal Structure Determination*, in *National Workshop on Crystal Structure Determination using Powder XRD* K.S. Society, Editor. 2010, Pakistan Institute of Engineering and Applie Science.

168. Syam G. Krishnan, M.H., Bhupender Pal, Izan Izwan Misnon, Chelladurai Karuppiah, Chun-Chen Yang, Rajan Jose, *Improving the symmetry of asymmetric*

supercapacitors using batter-type positive electrodes and activated carbon negative electrodes by mass and charge balance. Journal of Electroanalytical Chemistry, 2017. **805**(15): p. 126-132.

169. Chun Li, X.H., Fangyi Cheng, Yuxiang Hu, Chengcheng chen, and Chen, *Phase and composition controllable synthesis of cobalt manganese spinel nanoparticles towards efficiency oxygen electrocatalysis.* Nature Communications, 2015(10): p. 1-8.

170. Xiuyun Wang, Z.L., Kai Zhang, Jianjun Chen, Lilong Jiang, and Ruihu Wang, *Structure-Activity Relationships of AMn_2O_4 (A = Cu and Co) spinels in Selective Catalytic Reduction of NO_X: Experimental and Theoretical Study*. The Journal of Physical Chemistry, 2017. **121**(16): p. 3339-3349.

171. Ma, P., *Solution combustion of spinel $CuMn_2O_4$ ceramic pigments for thickness sensitive spectrally selective (TSSS) paint coatings.* Ceramics International, 2016. **42**(10): p. 11966-11973.

172. Rasha Yousef, A.A.-Z., Nasser Sad-Din, *A study of Structural Properties of $CuMn_2O_4$ Synthesized by Solid State Method.* Advances in Physics Theories and Applications 2018. **71**: p. 7.

173. Krishnan Rajeshwar, M.K.H., Robin T. Macaluso, Csaba Janaky, Andras Varga, and Pawel J. Kulesza., *Review-Copper Oxide-Based Ternary and Quaternary Oxides: Where Solid-State Chemistry Meets Photoelectrochemistry.* Journal of The Electrochemical Society, 2018. **165**(4): p. 3192-3206.

174. Hao Ming Chen, C.-S.H., *From the Research of Contract Beamline BL12B2/12XU (NSRRC): Developed in-situ X-ray Spectroscopy to Investigate the Catalyst System toward Oxygen Evolution Reaction.* SPring-8/SACLA, 2017. **22**(4): p. 297-305.

175. Ivan S. Filimonenkov, S.A.U., Ekaterina A. Zhukova, Aida R. Karaeva, Elena A. Skryleva, Vladimir Z. Mordkovich, Galina A. Tsirlina *Carbon nanotube cloth for electrochemical charge storage in aqueous media.* Journal of Electroanalytical Chemistry, 2018. **827**(15): p. 58-63.

176. Raja Noor Amalina Raja Seman, M.A.A., and Mohd Hanafi Ani., *Graphene/transition metal dichalcogenides hybrid supercapacitor electrode: status, challenges, and perspectives.* Nanotechnology, 2018. **29**(8): p. 1-28.

177. D. Gingasu, I.M., L. Patron, *Synthesis of $CuGa_2O_4$ nanoparticles by precursor and self propagating combusion methods.* Ceramics International, 2012. **38**(8): p. 6739-6751.

178. Elbeyli, Y., *Structural, magnetic, electrical and dieletric properties of $Mn_xNi_{1-x}Fe_2O_4$ spinel nanoferrites prepared by PEG assissted hydrothermal method.* Ceramics International, 2013. **39**(4): p. 4221-4230.

179. Apurba Ray, A.R., Monalisa Ghosh, Jesus Alberto Ramos-Ramon, Samik Saha, Umapada Pal, Swapan Kumar Bhattacharya, Sachindranath Das, *Study on charge storage mechanism in working electrodes fabricated by sol-gel derived spinel $NiMn_2O_4$ nanoparticles for supercapacitor application.* Journal of Applied Surface Science, 2019. **463**: p. 513-525.

180. Willenberg, S., *Carbon supported aluminium trifluoride nanoparticles functionalized lithium manganese oxide for the developement of advanced lithium ion battery system*, in *Chemistry*. 2017, University of the Western Cape: Cape Town. p. 78.

181. T. N. Renata Lewwandowska, M.O., *Raman Spectroscopic Applied to the Lithium-ion battery analysis.* Horiba Sci, 2001. **2**: p. 3-4.

182. Fatma M. Ismail, M.R., Ahmed M. Abdellah, Ibrahium Ismail, Nageh K. Allam, *Mesoporous spinel manganese zinc ferrite for high-performance supercapacitors.* Journal of Electroanalytical Chemistry, 2018. **817**(15): p. 111-117.

183. Pura Ram, R.S., Ganpat Chouldhary, Rakesh K. Sharma, *On the key role of Dy^{3+} in spinel $LiMn_2O_4$ cathodes for Li-ion rechargeable batteries.* Journal of Electroanalytical Chemistry, 2017. **802**(1): p. 94-99.

184. Bhamini Bhujun, M.T.T.T., Anandan S. Shanmugam, *Study of mixed ternary transition metal ferrites as potential electrodes for supercapacitor applications.* Results in Physics, 2017. **7**: p. 345-353.

185. John Anthuvan Rajesh, B.-K.M., Jae-Hong Kim, Soon-Hyung Kang, Hyunsoo Kim, Kwang-Soon Ahn., *Facile hydrothermal synthesis and electrochemical supercapacitor performance of hierarchical coral-like $ZnCo_2O_4$ nanowires.* Journal of Electroanalytical Chemistry, 2017. **785**(15): p. 48-57.

186. Yanzhong Wang, Y.L., Kai Xia, Yang Zhang, Jinlong Yang, *$NiCo_2S_4$ nanoparticles anchoring on polypyrrole nanotubes for high-performance supercapacitor electrodes.* Journal of Electroanalytical Chemistry, 2019. **840**(1): p. 242-248.

187. Hongchun Luo, H.L., Jun Qiu, *Carbon fibers surface-grown with helical carbon nanotubes and polyaniline for high-performance electrode materials and flexible supercapacitors.* Journal of Electroanalytical Chemistry, 2018. **828**(1): p. 24-32.

188. Wei Du, X.W., Xiangyu Ju, Ke Xu, Mingjun Gao, Xintao Zhang, *Carbonized Enteromorpha prolifera with porous architecture and its polyaniline composites as high-performance electrode materials for supercapacitors.* Journal of Electroanalytical Chemistry, 2017. **802**(1): p. 15-21.

189. Xiaogang Luo, W.W., Yunxia Liang, Zexu Hu, Yang Zhang, Junlie Yang, Lijun Yang, Shengyuan Yang, Meifang Zhu, Hui-Ming Cheng., *Multifunctional fabrics of carbon nanotube fibers.* Journal of Materials Chemistry A, 2019. **15**(7): p. 8790-8797.

190. Lifeng Zhang, Y.G., Kechao Shen, Jinghao Huo, Yi Liu, and Shouwu Guo, *Ion-matching porous carbons with ultra-high surface area and superior energy storage performance for supercapacitors.* Journal of Materials Chemistry A, 2019. **15**(7): p. 9163-9172.

191. Mengying Jia, L.C., Feng Peng, Yue Li, Lanshu Xu, and Xiaojuan Jin, *Self-assembly design and synthesis of pulp fiber-graphene for flexible and high performance electrode based on polyacrylamide.* New Journal of Chemistry, 2019.

192. Ewa Nazaruk, A.M.-P., Marlena Godlewska, Miroslaw Salamonczyk, Damian Gawel., *Electrochemical and biological characterization of lyotropic liquid crystalline phases-retardation of drug release from hexagonal mesophases.* Journal of Electroanalytical Chemistry, 2018. **813**(15): p. 208-215.

193. Parvin Asen, S.S., Azam Iraji Zad, *Iron-vanadium oxysulfide nanostructures as novel electrode materials for supercapacitor applications.* Journal of Electroanalytical Chemistry, 2018. **818**(1): p. 157-167.

194. Schnablegger, H., *The SAXS Guide*, in *Getting acquanted with the principles of SAXS*, Y. Singh, Editor. 2013, Anton Paar GmnH: Austria. p. 123.

195. Wei Du, X.W., Xueqin Sun, Jie Zhan, Huadong Zhang, Xiangjin Zhao, *Nitrogen-doped hierarchical porous carbon using biomass-derived activated carbon/carbonized polyaniline composites for supercapacitor electrodes.* Journal of Electroanalytical Chemistry, 2018. **827**(15): p. 213-220.

196. A.K.M. Atique Ullah, A.K.M.F.K., M. Akter, M.N.I. Khan, M.A. Maksud, Rumana A. Jahan, *Synthesis of Mn_3O_4 nanoparticles via a facile gel formation route and study of their phase and structural transformation with distinct surface morphology upon heat treatment.* Journal of Saudi Chemical Society, 2017(21): p. 830-836.

197. Ammar Bin Yousaf, R.K., M. Imran, Muhammad Fasehullah, Akif Zeb, Syed Javaid Zaidi, Peter Kasak., *Carbon nitride embedded MnO_2 nanospheres decorated with low-content Pt nanoparticles as highly efficient and durable electrode material for solid state supercapacitors.* Journal of Electroanalytical Chemistry, 2017. **801**(15): p. 84-91.

198. Sheng-Yu Chen, W.T., Junkai He, Ran Miao, Hui-Jan Lin, Wengiao Song, Sibo Wang, Pu-Xian Gao, and Steven L. Suib, *Copper manganese oxide enhanced nanoarray-based monolithic catalysts for hydrocarbon oxidation.* Journal of Materials Chemistry A, 2018. **39**(6): p. 19047-19057.

199. Kurungot, V.K.a.S., *Zirconium-Substituted Cobalt Ferrite Nanoparticle Supported N-doped Reduced Graphene Oxide as an Efficient Bifunctional Electrocatalyst for Rechargeable Zn-Air Battery.* ACS Catalysis, 2018, (8): p. 3715-3726.

200. L. Yang, W.Z., P. Zhang, J. Chen, W.B. Tian, Y.M. Zhang, Z.M. Sun, *MXene/CNTs films prepared by electrophoretic deposition for supercapacitor electrodes.* Journal of Electroanalytical Chemistry, 2018. **831**(1): p. 1-6.

201. Bhagwan, J., *Porous, One dimensional and High Aspect Ratio Mn_3O_4 Nanofibers: Fabrication and Optimization for Enhanced Supercapacitive Properties.* Electrochimica Acta, 2015. **174**: p. 992-1001.

202. Suhui Lu, Y.S., Kunkun Guo, Xuli Chen, Jiajing Xu, Li Zhao, *Effect of aqueous electrolytes on the electrochemical behaviours of ordered mesoporous carbon composites after KOH activation as supercapacitors electrodes.* Journal of Electroanalytical Chemistry, 2018. **818**(1): p. 58-67.

203. S Fritsch, J.S., A Rousset, G.U Kulkarni, *Low-temperature oxidation of Mn_3O_4 hausmannite.* Materials Research Bulletin, 1998. **33**(8): p. 1185-1194.

204. Miranda M.Ndipingwi, C.O.I., Ntuthuko W.Hlongwa, Zolani Myalo, Natasha Ross, Milua Masikini, Suru V. John, Priscilla G. Baker, Wiets D.Roos, and Emmanuel I. Iwuoha *Orthorhombic Nanostructured Li_2MnSiO_4/Al_2O_3 Supercapattery Electrode with Efficient Lithium-Ion Migratory Pathway.* Batteries & Supercaps Articles. ChempubSoc Europe, 2018. **1**: p. 1-14.

205. Meng, X., *Ball-milling synthesized hydrotalcite supported Cu–Mn mixed oxide under solvent-free conditions: an active catalyst for aerobic oxidative synthesis of 2-acylbenzothiazoles and quinoxalines.* Green Chemistry, 2018.

206. Gao, B., *Recent progress in nanostructured transition metal nitrides for advanced electrochemical energy storage.* Journal of Materials Chemistry A, 2018.

207. Thakur, S., *Geometrically intricate sheet-on-pillar/flake hierarchy embracing cobaltosic and manganese oxides over flexible carbon scaffold for binder-free high-energy-density supercapacitor.* CrystEngComm, 2018.

208. B. Saravanakumar, S.M.L., G. Rari, V.Ganesh, A. Sakunthala, R. Yuvakkumar *Electrochemcial properties of rice-like copper manganese oxide ($CuMn_2O_4$) nanoparticles for pseudocapacitor applications.* Journal of Aolloys and Compounds, 2017. **723**(5): p. 115-122.

209. Bhupender Pal, S.G.K., Bincy Lathakumary Vijayan, Midhun Harilal, Chun-Chen Yang, Fabian I. Ezema, Mashitah Mohd Yusoff, Rajan Jose., *In situ encapsulation of tin oxide and cobalt oxide composite in porous carbon for high-performance energy storage applications.* Journal of Electroanalytical Chemistry, 2018. **817**(15): p. 217-225.

210. Jingxuan Xu, Y.Y., Hang Chu, Jianhua Tang, Yuancai Ge, Jianfeng Shen, Mingxin Ye, *Novel $NiCo_2S_4$ @ reduced Graphene Oxide @ Crabon Nanotube Nanocomposites for high Performance Supercapacitors.* Royal Society of Chemistry, 2016. **3**(10): p. 1-8.

211. Ramkrishna Sahoo, A.P.a.T.P., *Proportion of Composition in a Composite does Matter to Behave as an Advanced Supercapacitor.* Journal of Materials Chemistry A, 2016. **721**: p. 1-28.

212. Shaktivel Manavalan, U.R., Shen-Ming Chen, Tse-Wei Chen, R. Jothi Ramalingam, T.Maiyalagan, Anandaraj Sathiyan, Qingli Hao, Wu Lei., *Microwave-assisted synthesis of gadolinium (III) oxide decorated reduced graphene oxide nanocomposite for detection of hydrogen peroxide in biological and clinical samples.* Journal of Electroanalytical Chemistry, 2019. **837**(15): p. 167-174.

213. Ao Xia, W.Y., Jue Yi, Guoqiang Tan, Huijun Ren, Chun Liu., *Synthesis of porous MnO_2 nanosheets and their supercapacitor performance.* Journal of Electroanalytical Chemistry, 2019. **839**(15): p. 25-31.

214. Qiang Li, J.M., Jin Zhou, Yi Zhao, Shuping Zhuo., *Avoiding the use of corrosive activator to produce nitrogen-doped hierarchical porous carbon materials for high-performance supercapacitor electrode.* Journal of Electroanalytical Chemistry, 2019. **832**(1): p. 284-292.

215. Izabela Stepniak, A.C., *New design of electric double layer capacitors with aqueous LiOH electrolyte as a alternative to capacitor with KOH solution.* Journal of Power Sources, 2010. **195**(9): p. 2564-2569.

216. Jie Ma, X.-Y.T., Shi-Xiang Zhou, Xiang-Zhu Song, Lin-Guo, Yao-Wang, Ya-Bo Zhu, Li-Tong Guo, Zhang-Sheng Liu, He-Liang Fan, Xian-Yong Wei., *Facile fabrication of Ag/PANI/g-C_3N_4 composite with enhanced electrochemical performance as supercapacitor electrode.* Journal of Electroanalytical Chemistry, 2019. **835**(15): p. 346-353.

217. Madagonda M. Vadiyar, S.C.B., Sandip K. Patil, Prof. Sanjay S. Kolekar, Prof. Jia-Yaw Chang, Prof. Anil V. Ghule, *Comparative Study of Individual and Mixed Aqueous Electrolytes with $ZnFe_2O_4$ Nao-flakes Thin Film as an Electrode for Supercapacitor Application.* ChemPubSoc Europe Energy Technology & Environmental Science 2016. **222**(11): p. 1604-1615.

218. Chunyang Li, W.W., Shuaishuai Zhang, Liange He, Yusong Zhu, Jing Wang, Lijun Fu, Yuhui Chen, Yuping Wu, and Wei Huang, *A high-voltage aqueous lithium ion capacitor with high energy density from an alkaline-neutral electrolyte.* Journal of Materials Chemistry A, 2019: p. 1-10.

219. Manickam Minakshi, P.S., Melody Cater, and Kathryn Prince, *The Zn-MnO_2 Battery: The Influence of Aqueous LiOH and KOH Electrolytes on the Intercalation Mechanism.* Electrochemical and Solid-State Letters, 2008. **11**(8): p. 145-149.

220. Xiaoyu Gao, C.Z., Xiaoliang Yu, Qinghua Liang, Ruitao Lv, Guosheng Gai, Wanci Shen, Feiyu Kang, and Zheng-Hong Huang., *A high Performance Lithium-Ion Capacitor with Both Electrodes Prepared from Sri Lanka Graphite Ore.* Materials, 2017. **10**(4): p. 414-425.

221. Mohammad S. Rahmanifar, M.H., Abolhassan Noori, Maher F, EI-Kady, Mir F. Mousavi, Richard B. Kaner, *Asymmetric supercapacitors: An alternative to activated carbon negative electrodes based on earth abundant elements.* Materialstoday Energy, 2019. **12**: p. 26-36.

222. Luchao Yue, S.Z., Hanqing Zhao, Yu Feng, Miao Wang, Lulu An, Xiaodan Zhang, Jie Mi, *One-pot synthesis $CoFe_2O_4$/CNTs composite for asymmertric supercapacitor electrode.* Solid State Ionics, 2019. **329**: p. 15-24.

223. Namachivayam Karthik, T.N.J.I.E., Raji Atchudan, Dangsheng Xiong, Yong Rok Lee., *Electro-synthesis of sulfur doped nickel cobalt layered double hydroxide for electrocatalytic hydrogen evolution reaction and supercapacitor applications.* Journal of Electroanalytical Chemistry, 2019. **833**(15): p. 105-112.

224. Van Chinh Hoang, L.H.N., Vincent G. Gomes., *High efficiency supercapacitor derived from biomass based carbon dots and reduced graphene oxide composite.* Journal of Electroanalytical Chemistry, 2019. **832**(1): p. 87-96.

225. W. Zheng, P.G.Z., J. Chen, W.B. Tian, Y.M. Zhang, Z.M. Sun., *Microwave-assisted synthesis of three-dimensional MXene derived metal oxide/carbon nanotube/iron hybrids for enhanced lithium-ions storage.* Journal of Electroanalytical Chemistry, 2019. **835**(15): p. 205-211.

226. Shuo Zhang, S.G., Houcai Dong, Xiuzhen Wang, Min Liu, Yiping Sun, Xiaodong Wu, Jiaqiang Xu, Liwei Chen, Anbao Yuan, Wei Lu., *Mesoporous carbon nanotube microspheres supported microporous pyrolytic carbon for high-performance supercapacitors.* Journal of Electroanalytical Chemistry, 2019. **840**(1): p. 423-429.

227. Qingfeng Zhou, Y.G., Jianhua Lin., *Low temperature synthesis of sponge-like NiV_2O_6/C composite by calcining Ni-V-based coordination polymer for supercapacitor application.* Journal of Electroanalytical Chemistry, 2018. **823**(15): p. 80-91.

228. Qinxing Xie, S.W., Yufeng Zhang, Peng Zhao., *Nitrogen-enriched flexible porous carbon/graphene composite cloth as free-standing electrodes for high performance aqueous supercapacitors.* Journal of Electroanalytical Chemistry, 2017. **801**(15): p. 57-64.

229. Jing Zhao, Y.L., Fengguang Huang, Hongquan Zhang, Junwei Gong, Chenxu Miao, Kai Zhu, Kui Cheng, Ke Ye, Jun Yan, Dianxue Cao, Guiling Wang, Xianfa Zhang., *High-performance asymmetric supercapacitor assembled with three-dimensional, coadjacent graphene-like carbon nanosheets and its composite.* Journal of Electroanalytical Chemistry, 2018. **823**(15): p. 474-481.

230. Suhui Lu, Y.S., Kunkun Guo, Xuli Chen, Jiajing Xu, Li Zhao, *Effect of aqueous electrolytes on the electrochemical behaviours of ordered mesoporous carbon composites after KOH activation as supercapacitors electrodes.* Journal of Electroanalytical Chemistry, 2018. **818**(1): p. 58-67.

231. Hongchun Luo, H.L., Jun Qiu, *Carbon fibers surface-grown with helical carbon nanotubes and polyaniline for high-performance electrode materials and flexible supercapacitors.* Journal of Electroanalytical Chemistry, 2018. **828**(1): p. 24-32.

232. Seyed Hamed Aboutalebi, A.T.C., Maryam Salari, Konstantinoy, David Wexler, Hua Kun Liu, and Shi Xue Dou., *Comparison of GO, GO/MWCNTs composite and MWCNTs as potential electrode materials for supercapacitors.* Journal of Energy and Environmental Science, 2011. **5**(4): p. 1855-1865.

233. Lina Chen, D.L., Xiaowen Zheng, Long Chen, Yamin Zhang, Zhen Liang, Jinkui Feng, Pengchao Si, Jun Lou, Lijie Ci., *Integrated nanocomposite of $LiMn_2O_4$/graphene/carbon nanotubes with pseudocapacitive properties as superior cathode for aqueous hybrid capacitors.* Journal of Electroanalytical Chemistry, 2019. **15**: p. 1-34.

234. Yazi Luo, H.Z., Di Guo, Jianming Ma, Qiuhong Li, Libao Chen, Taihong Wang., *Porous $NiCo_2O_4$-reduced graphene oxide (rGO) composite with superior capacitance retention for supercapacitors.* Electrochimica Acta, 2014. **132**(20): p. 332-337.

235. Nousheen Iqbal, X.W., Aijaz Ahmed Babar, Jianyong Yu, Bin Ding., *Highly flexible $NiCo_2O_4$/CNTs doped carbon nanofibers for CO_2 adsorption and supercapacitor electrodes.* Journal of Colloid and Interface Science., 2016. **475**(15): p. 87-93.

236. Babak Mazinani, M.K., Ghazal Mobarhan, and Mohammadreza Shokouhimehr., *The Combination Synthesis of Ag-Doped $MnCo_2O_4$ Nanoparticles for supercapacitor applications.* Journal of the Minerals, Metals & Materials Society., 2019. **4**(71): p. 1-8.

237. Haicheng Xuan, Y.X., Yongqing Zhang, Hui Li, Peide Han, Youwei Du., *One-step combustion synthesis of porous CNTs/C/$NiMoO_4$ composites for high-performance asymmetric supercapacitors.* Journal of Alloys and Compounds., 2018. **745**(15): p. 135-146.

238. Stoller, M.D. and R.S. Ruoff, *Best practice methods for determining an electrode material's performance for ultracapacitors.* Energy & Environmental Science, 2010. **3**(9): p. 1294-1301.

239. Ruiz-Rosas, R., *Design of hybrid asymmetric capacitors in aqueous electrolyte using ZTC and ultraporous activated carbons*. Journal of Power Sources, 2015. **37**(September 2015): p. 14-19.

240. Liu, L., Z. Niu, and J. Chen, *Unconventional supercapacitors from nanocarbon-based electrode materials to device configurations.* Chemical Society Reviews, 2016. **45**(15): p. 4340-4363.

241. Arie Borenstein, O.H., Ran Attias, Shalom Luski, Thierry Brousse, and Doron Aurbach, *Carbon-based composite materials for supercapacitor electrodes: a review.* Journal of Materials Chemistry A, 2017. **18**(5): p. 12653-12672.

242. Cheng Zhong, Y.D., Wenbin Hu, Jinli Qiao, Lei Zhang, and Jiujun Zhang, *A review of electrolyte materials and compositions for electrochemical supercapacitors.* Journal of Chemical Society Reviews, 2015. **44**: p. 7484-7539.

243. Jenel Vatamanu, O.B., Marco Olguin, Gleb Yushin, and Omitry Bedrov, *Charge storage at the nanoscale: understanding the trends from the molecular scale perspective.* Journal of Materials Chemistry A, 2017. **5**: p. 21049-21076.

244. Lin, K.-C.H.a.L.-Y., *A review of electrode materials based on core-shell nanostructures for electrochemical supercapacitors.* Journal of Materials Chemistry A, 2019. **7**: p. 3516-3530.

245. Jamie C. Wang, S.P.H., Tristan Dilbeck, Omotola O. Ogunsolu, Tanmay Banerjee, and Kenneth Hanson., *Multimolecular assemblies on high surface area metal oxide and their role in interfacial energy and electron transfer.* Journal of Chemical Society Reviews, 2018. **47**: p. 104-148.

246. Sivalingam Ramesh, D.V., Hyun-Seok Kim, Heung Soo Kim, Joo-Hyung Kim, *Electrochemical performance of MWCNT/GO/$NiCo_2O_4$ decorated hybrid nanocomposite for supercapacitor electrode materials.* Journal of Aolloys and Compounds, 2018. **765**: p. 369-379.

247. Cen Jin, Y.C., Guofeng Zhang, Wenhao Luo, Yanxia Liu, Yan Sun, Zhangmin Tian, Wenjun Zheng, *Synthesis of copper-cobalt hybrid oxide microflowers as electrode material for supercapacitors.* Chemical Engineering Journal, 2018. **343**: p. 311-339.

248. Tuan Ngoc Phan, M.K.G., Ranjith Thangavel, Yun Sung Lee, Chang Hyun Ko, *Enhanced electrochemical performance for EDLC using oedered mesopores and mesopore structures.* Journal of Aolloys and Compounds, 2018. **780**: p. 90-97.

249. Guoxiong Zhang, Y.C., Yigang Chen, and Haibo Guo, *Activated biomass carbon made from bamboo as electrode material for supercapacitors.* Materials Research Bulletin, 2018. **102**: p. 391-398.

250. Rui Xu, J.L., Jihuai Wu, Miaoliang Huang, Leqing Fan, Zedong Xu, Zeyu Song, *A high-performance pseudocapacitive electrode material for supercapacitors based on*

the unique $NiMoO_4/NiO$ nanoflowers. Applied Surface Science, 2019. **463**: p. 721-731.

251. Yang Luo, T.Y., Qi Zhao, Mingzhe Zhang, *CeO_2/CNTs hybrid with high performance as electrode materials for supercapacitors.* Journal of Aolloys and Compounds, 2017. **729**: p. 64-70.

252. Wei, H., *Facile synthesis of $NiMn_2O_4$ nanosheet arrays grown on nickel foam as novel electrode materials for high-performance supercapacitors.* ScienceDirect Ceramics International 2016. **42**: p. 14963-14969.

253. Al-Rubaye, S., *$NiFe_2O_4$ nanoparticles coated on 3D graphene capsule as electrode for advanced energy storage applications.* Dalton Transactions, 2018.

254. Jai Bhagwan, A.S., K.L. Yadav, Yogesh Sharma, *Nanofibers of spinel-$CdMn_2O_4$: A new performance material for supercapacitor and Li-ion batteries.* Journal of Alloys and Compounds, 2017. **703**: p. 86-95.

255. Mi, C.H., X.G. Zhang, and H.L. Li, *Electrochemical Behaviours of Solid $LiFePO_4$ and $Li_{0.99}Nb_{0.01}FePO_4$ in Li_2SO_4 Aqueous Electrolyte.* Journal of Electroanalytical Chemistry, 2007. **602(2)**: p. 245-254.

256. Lide, D.R., ed. CRC *Handbook of Chemistry and Physics*, C. Press/Taylor, Editor. 2010, Francis: Boca Raton, FL.

257. Bard, A.J.a.L.R.F., *Electrochemical methods: Fundamentals and Applications*, J. Wiley, Editor. 2001, Sons.Inc.

258. Adams, R.A.R.A., *Calculus: A Complete Course* M.A. Field, Editor. 2006, Pearson Addison Wesley: Canada.

259. Ma, C., *Carbon-coated FeP nanoparticles anchored on carbon nanotube networks as an anode for long-life sodium-ion storage.* Chemical Communications, 2018.

260. Xiang, Y., *Pseudocapacitive behavior of the Fe_2O_3 anode and its contribution to high reversible capacity in lithium ion batteries.* Nanoscale, 2018.

261. Ceilidh F. Armer, J.S.Y., Xu Li, Adrian Lowe, *Electrospun vanadium-based oxides as electrode materials.* Journal of Power Sources, 2018. **395**(15): p. 414-429.

262. Liujun Cao, G.T., Jun Mei, Hao Liu, *Construct hierarchical electrode with $Ni_xCo_{3-x}S_4$ nanosheet coated on $NiCo_2O_4$ nanowire arrays grown on carbon fiber paper for high-performance asymmetric supercapacitors.* Journal of Power Sources, 2017. **359**(15): p. 262-269.

263. Zhichao Qu, M.S., Hanzhao Wu, Yongchao Liu, Jintian Jiang, Chao Yan, *An efficient binder-free electrode with multiple carbonized channels wrapped by $NiCo_2O_4$ nanosheets for high-performance capacitive energy storage.* Journal of Power Sources, 2019. **411**(31): p. 179-187.

264. Xiumei Song, L.T., Xiuli Wang, Lin Zhu, Xiaoqing Yi, Qiang Dong, *Synthesis of CoS@rGO composites with excellent electrochemical performance for supercapacitors.* Journal of Electroanalytical Chemistry, 2017. **794**(1): p. 132-138.

265. M.S. Michael, A.R.K., S.R.S. Prabaharan, *Design of Monolayer Porous Carbon-Embedded hybrid-$LiMnPO_4$ for High Energy Density Li-ion Capacitors.* Journal of Nanoscience and Nanotechnology, 2016. **16**: p. 7314-7324.

266. X. Zhang, X.C., Q. Zhange, *Nanostructured energy materials for electrochemical energy conversion and storage: a review.* J. Energy Chem, 2016. **25**: p. 967-984.

267. K. Chen, Q.W., Z. Niu, J. Chen, *Graphene-based materials for flexible energy storage devices.* J. Energy Chem, 2018. **27**: p. 12-24.

268. Srikant Sahoo, A.K.S., *Electrochemical capacitance properties of cobalt oxide entangled over MWCNT and cobalt oxide AC composites.* Journal of Electroanalytical Chemistry, 2017. **801**(15): p. 416-424.

269. K. Zhang, X.H., Z. Hu, X. Zhang, Z. Tao, J. Chen, *Nanostructured Mn-based oxides for electrochemical energy storage and conversion.* Chem. Soc. Rev, 2015. **44**: p. 699-728.

270. P. J. Hall, M.M., S.I. Fletcher, F. B. Sillars, A. J. R. Rennie, G. O. Shitta-Bey, G. Wilson, A. Cruden, R. Carter, *Energy storage in electrochemical capacitors: designing functional materials to improve performance.* Energy Environ. Sci. , 2010. **3**: p. 1238-1251.

271. Conway, B.E., *Transition from 'supercapacitor' to 'battery' behaviour in electrochemical energy storage.* J. Electrochem. Soc. , 1991. **138**: p. 1539-1548.

272. Ayhan, I.A., *Effect of Mn_3O_4 nanoparticle composition and distribution on graphene as a potential hybrid anode material for lithium-ion batteries.* RSC Advances, 2016. **6**(39): p. 33022-33030.

273. A. Balducci, D.B., T. Brouse, J.W. Long, and W. Sugimoto, *A Guideline for Reporting Performance Metrics with Electrochemical Capacitors: From Electrode Materials to Full Devices.* Journal of The Electrochemical Society, 2017. **164**(7): p. 1487-1488.

274. Po-Hsin Wang, T.-L.W., Wen-Churing Lin, *Enhanced Supercapacitor Performance Using Electropolymerization of Self-Doped Polyaniline on Carbon Film.* Journal of Nanomaterials, 2018. **34**: p. 1-12.

275. Li, K., S. Chen, and J. Zhang, *CHAPTER 9 Functionalization of Chemically Derived Graphene for High-performance Supercapacitors*, in *Chemically Derived Graphene: Functionalization, Properties and Applications*. 2018, The Royal Society of Chemistry. p. 242-278.

276. Yongkun Liu, G.J., Shiqing Sun, Bin Xu, Junyi Zhou, Yang Zhang, Juming Yao, *Growth of $NiCo_2S_4$ nanotubes on carbon nanofibers for high performance flexible supercapacitors.* Journal of Electroanalytical Chemistry, 2017. **804**: p. 212-219.

277. Ning Wei, Q.w., Yue Ma, Limin Raun, Wei Zeng, Dong Liang, Chao Xu, Linsheng Huang, Jinling Zhao, *Asymmetric supercapacitor for sensitive elastic-electrochemical stress sensor.* Journal of Power Sources, 2018. **402**: p. 353-362.

278. Gaurav Lalwani, A.G., Michael D' Agati, Jeyantt Srinivas Sankaran, Stefan Judex, Yi-Xian Qin, and Balaji Sitharaman, *Porous Three-Dimensional Crabon Nanotube Scaffolds for Tissue Engineering.* Journal of biomedical materials research. Part A, 2016. **103**(10): p. 3212-3225.

279. Min Fu, W.C., Xixi Zhu, Qingyun Liu, *One-step preparation of one dimensional nickel ferrites/graphene composites for supercapacitor electrode with excellent cycling stability.* Journal of Power Sources, 2018. **396**(31): p. 41-48.

280. Qingya Zhou, J.H., Cuiyu Li, Zhiwei Lv, Huilin Zhu, and Gang Hu, *Wrapping $CuCo_2S_4$ arrays on nickel foam with $Ni_2(CO_3)(OH)_2$ nanosheets as a high-performance faradaic electrode.* New Journal of Chemistry, 2019: p. 1-10.

281. Periyasamy Sivakumar, M.J., Manikantan Kota, Min Gyu Jung, Aharon Gedanken, *Controllable synthesis of nanohorn-like architectured cobalt oxide for hybrid supercapacitor application.* Journal of Power Sources, 2018. **402**(31): p. 147-156.

282. Xueqin Lang, H.Z., Xin Xue, Chuanlu Li, Xucong Sun, Zitang Liu, Haoshan Nan, Xiaoying Hu, Hongwei Tian, *Rational design of $La_{0.85}Sr_{0.15}MnO_3$@$NiCo_2O_4$ Core-Shell architecture supported on Ni foam for high performance supercapacitors.* Journal of Power Sources, 2018. **402**(31): p. 213-220.

283. Feifei Wang, X.L., Lili Zhang, Hualian Zhang, Yanfang Zhu, Zhufeng Hu, Yuxin Zhang, Junyi Ji, Wei Jiang, *Construction of vertically aligned PPy nanosheets networks anchored on $MnCo_2O_4$ nanobelts for high-performance asymmetric supercapacitors.* Journal of Power Sources, 2018. **393**(31): p. 169-176.

284. Wen Qi, X.L., Ying Wu, Hong Zeng, Chunjiang Kuang, Shaoxiong Zhou, Shengming Huang, Zhengchun Yang., *Flexible electrodes of MnO_2/CNTs composite for enhanced*

performance on supercapacitors. Surface & Coatings Technology, 2017. **18**(320): p. 624-629.

285. L. Yang, W.Z., P. Zhang, J. Chen, W.B. Tian, Y.M. Zhang, Z.M. Sun, *MXene/CNTs films prepared by electrophotoretic deposition for supercapacitor electrods.* Journal of Electroanalytical Chemistry, 2018. **830-831**(1): p. 1-6.

286. S.R.S. Prabaharan, R.A.S., Ajit R. Kulkarni, M.S. Michael, *Nano-composite $LiMnPO_4$ as new insertion electrode for electrochemical capacitors.* Current Applied Physics, 2015. **15**(12): p. 1624-1633.

287. Lin Xu, S.W., Xiao Zhang, Tabin He, Fengxia Lu, Huichang Li, Junhui Ye, *A facile method of preparing $LiMnPO_4$/reduced graphene oxide aerogel as cathodic material for aqueous lithium-ion hybrid supercapacitors.* Applied Surface Science, 2018. **428**(15): p. 977-985.

288. Yuanyuan Li, F.T., Renjie Wang, Chong Wang, and Jinping Liu, *A Novel Dual-Ion Hybrid Supercapacitor Based on $NiCo_2O_4$ Nanowire Cathode and MoO_2-C Nanofilm Anode.* ACS Applied Materials & Interfaces, 2016. **44**(8): p. 30232-30238.

289. Xudong Li, R.D., Lanhua Yi, Wei Shi, Qilei Xu, Enhui Liu, *Mesoporous Ni-P@$NiCo_2O_4$ composite materials for high performance aqueous asymmetric supercapacitors.* Electrochimica Acta, 2016. **222**(20): p. 1169-1175.

290. Ruey-Chi Wang, P.-H.H., Ping-Chang Chuang, Yu-Cheng Lin., *Enhanced rate capability of pseudocapacitive CuO by incorporation of Li for excellent composite electrode.* Journal of Electroanalytical Chemistry, 2019. **839**(15): p. 160-165.

291. Balakrishnan Kirubasankar, S.V., and Subramania Angaiah., *Sonochemical synthesis of a 2D-2D $MoSe_2$/graphene nanohybrid electrode material for asymmetric supercapacitors.* Journal of Sistainable Energy & Fuels., 2019. **2**(3): p. 467-477.

292. Vimal Kumar Mariappan, K.K., Parthiban Pazhamalai, Surjit Sahoo, Swapnil Shital Nardekar, Sang-Jae Kim, *Nanostructured tenary metal chalcogenide-based binder-*

free electrodes for high energy density asymmetric supercapacitors. Nano Energy, 2019. **57**: p. 307-316.

293. Rinki Malik, S.L., Rajender Singh Malik., *Electrochemical behaviour of composite electrode based on sulphonated polymeric surfactant (SPEEK/PSS) incorporated polypyrrole for supercapacitor.* Journal of Electroanalytical Chemistry, 2019. **835**(15): p. 48-59.